CRANFIELD UNIVERSITY

Diego M. Lombetti

TUFTING OF COMPLEX COMPOSITE STRUCTURES

SCHOOL OF AEROSPACE, TRANSPORT AND MANUFACTURING
Enhanced Composites and Structures Centre

PhD-Thesis
Academic Years: 2011 - 2015

Supervisors: Dr Alexandros A. Skordos
Professor Ivana K. Partridge

December 2015

CRANFIELD UNIVERSITY

SCHOOL OF AEROSPACE, TRANSPORT AND MANUFACTURING
Enhanced Composites And Structures Centre

PhD-Thesis

Academic Years 2011 - 2015

Diego M. Lombetti

Tufting of complex composite structures

Supervisors: Dr Alexandros A. Skordos
Professor Ivana K. Partridge

December 2015

ABSTRACT

This study focuses on the effect of tufting on the mechanical and electrical properties of carbon composites using a variety of tuft materials, such as aramid, steel and copper. Several configurations were investigated based on a case study, involving the reinforcement of stiffener-to-skin interfaces of a tail cone. The effect of tuft and base composite material, tufting depth and inclination on the delamination resistance in mode I was evaluated, the associated bridging laws were determined and the failure mechanisms were identified. A simplified superposition model of the delamination response of tufted composites was developed. The electrical performance of tufted composites was determined in simulated lightning strike tests and set against the through-the-thickness electrical conductivity of the materials.

The results of mechanical testing showed that the delamination performance depends strongly on the material response of the tufts, with both the bridging behaviour and final toughness levels influenced directly by the strength, ductility and ultimate strain of the tufts. Interactions between the tufts and the surrounding composite, such as interfacial shear and bridging induced by tuft pull-out, play a significant role in the overall behaviour generating a deviation from a simple superposition of the base material and tuft response. The balance between interfacial shear and tuft elongation results in a decreasing trend of delamination toughness with increasing tufting depth for low ductility materials, whilst the trend is reversed for the high ductility copper tufts. This balance is also affected by the properties of the base material, with tougher matrices leading to dominance of shear effects and a weaker enhancement introduced by tufting. Inclination of tufts leads to an increase in crack energy release rate due to the activation of a ploughing mechanism. Metallic and carbon tufts have a positive effect on lightning strike response, with copper tufting offering strike protection at an improved level compared to standard copper mesh solutions.

Keywords:
Metallic tufts, Through-the-thickness reinforcement, Delamination, Bridging law, Lightning strike protection, Electrical conductivity, Carbon fibres

To my nephew…

Welcome to the world Nahuel!

ACKNOWLEDGEMENTS

I would like to express my deepest gratitude to Dr Alex Skordos for all his guidance, support, patience, advices and caring regardless day and time. Your passion for research, setting the highest standards and discussion about work and life led me through the hard times during the last years. I am also very grateful you introduced me to your football team and it has been a pleasure to play alongside you.

I am extremely grateful to have had Professor Ivana K. Partridge as additional supervisor. Your trust, guidance, advices and caring during your time at Cranfield University and afterwards at University of Bristol helped me to solve many problems I faced during the PhD. I will never forget you trusted me and gave me the chance to do the PhD at Cranfield University. I also want to thank Dr Giuseppe Dell'Anno, who started as my first supervisor, became a friend but, unfortunately, left Cranfield University. I thank you for all your help and advices you gave me during our time together and after leaving.

I also thank the entire Composite team; it has been a pleasure to work alongside you, especially Jim Hurley, who made the time in the composite lab enjoyable. I thank you for all the discussions we had about work and many other topics, all your help and extra hours you spent to get me back on track. My special thanks also go to Dr David Ayre. Your availability, care and interest in my progress were very supportive! Thanks go to the rest of the team: Professor Peter Foote, Mr Andrew Mills, Tassos Mesogitis, Dr Lawrence Cook, Mr Ben Hopper and Mrs Sharon McGuire.

During my time in Cranfield I have had the pleasure to meet many people who became my friends. These people made my time in the UK wonderful and I will never forget them. Thank you: Giuseppe, Marta, Ioanna, Stefan, Ken, Giacomo, Thomas, John, Paul, Sat, Aurele, all my close friends from abroad visiting me, the Cranfield University football team 2012 and everybody I haven't mentioned and shared the time with me. My family: What would I have done without my family?! Thank you for all the support in every manner! THANK YOU! My last thoughts go to my love. Thank you Lara for sharing beautiful moments and bearing me during difficult times, supporting me every day and every minute!

TABLE OF CONTENTS

LIST OF FIGURES

LIST OF TABLES

NOMENCLATURE

Mechanical:

v_f	Fibre volume fraction
N	Number of fabric plies
W_A	Fabric areal weight
h	Half laminate thickness
ρ_f	Fibre density
ρ_t	Areal tuft density
A_t	Cross sectional area of tuft
s_x	Tuft pitch
s_y	Tuft row distance
W_L	Fibre linear weight
C_0	Initial compliance
$G_{Ic,ini}$	Critical crack initiation toughness in mode I
G_{Ic}	Critical crack energy release rate in mode I
F	Vertical load
d	Beam opening displacement at load line
b	Beam width
a	Crack length
Δ	Linear fit intercept
B	Correction factor for reduction of lever arm at large displacements
Q_c	Correction factor compensating rotation at delamination front
C	Compliance
l_1	Distance from centre of loading pin to the mid-plane of specimen
l_2	Distance from load line to end of loading block facing specimen centre
σ	Fracture surface stress
δ^*	Beam opening displacement at crack starter end
x	Position in specimen longitudinal direction
L	Specimen length from load line
E	Young's modulus
I	Moment of inertia
a_0	Initial crack length (at crack starter end)
δ'	Beam opening at first tuft row
t	Distance from crack starter end to first tuft row
A_u	Tuft unit area
σ_{th}	Thread stress
A_{th}	Thread cross sectional area

σ_R	Resin bridging stress
σ_{R+t}	Superimposed bridging stress
σ_t	Tuft bridging stress
a_1, a_2, a_3	Factors for Newton-Raphson method
t_T	Welch's t-test statistical value
df	Degree of freedom
ν_1, ν_2	Degree of freedom associated with variances of batch 1 and 2
$\bar{X}_1, \bar{X}_2$	Mean values of batch 1 and 2
N_1, N_2	Number of values of batch 1 and 2
s_1, s_2	Variance of batch 1 and 2
σ_1, σ_2	Standard deviation of batch 1 and 2
δ	Axial displacement of inclined tuft
P	Axial load of inclined tuft
$d\varphi$	Infinitesimal change in tuft inclination
φ	Tuft inclination
l	Horizontal tuft length of inclined tuft
C	Compliance
r	Radius for polar coordinate
θ	Angle for polar coordinate
K_{Ic}	Critical stress intensity factor in mode I
σ_{YS}	Yield strength
ν	Poisson's ratio

Electrical:

I	Current
Q	Charge
E	Action integral
t	Time
t_l	Laminate thickness
R	Resistance
S	Surface area

LIST OF ABBREVIATIONS

CAI	Compression after impact
RTM	Resin transfer moulding
ADFP	Automated dry fibre placement
PTFE	Polytetrafluoroethylene
VARTM	Vacuum assisted resin transfer moulding
TTR	Through-the-thickness reinforcement
ACT	Advanced Composite Technology
BMI	Bismaleimide
UD	Uni-directional
OSS®	One-sided stitching
ITA	Institut für Textiltechnik
UAZ®	Ultrasonically assisted Z-Fibre®
PVC	Polyvinylchloride
ILSS	Interlaminar shear strength
DLR	Deutsches Zentrum für Luft- und Raumfahrt – German Aerospace Centre
DCB	Double cantilever beam
SEM	Scanning electron microscope
CBT	Corrected beam theory
GPIB	General purpose interface bus
LWD	Long way diamond
SWD	Short way diamond
FEM	Fenite element method

1 General introduction

1.1 Background and motivation

Advanced composite structures have been developed over the last decades in the aerospace, automotive, naval and energy industries with the aim of using the weight benefits of these materials compared to standard metallic solutions [1]. These applications make use of the high specific stiffness and strength of composites in the in-plane directions. Advanced aerostructures as well as structural automotive components require the integration of numerous composite and metallic parts. Aircrafts, such as the Boeing 787 Dreamliner or the Airbus A350 incorporate 50% and 53%, respectively, of carbon composite by weight [2, 3]. Fuselages in these large aircrafts are made of carbon composites and are reinforced by stiffeners of different geometries. Figure 1-1 shows a section of a fuselage made of composites produced for the Airbus A350 which comprises an assembly of the skin with numerous reinforcing elements. Composite wings of single-aisle aircrafts need to be joined to metal structures, such as the wing box. Such joints might have adverse effects on the weight which is saved by using composites.

The greatest weakness of composite structures is the susceptibility to delamination as the relatively weak resin matrix is the main carrying medium of out-of-plane loads due to the absence of fibres orientated in the thickness direction. In addition, the potential of composite structures is often not exploited fully as these might be designed as a direct replacement for metal parts. The issue with this is that holes are drilled through some composite structures for the insertion of bolts and rivets and consequently the structures are weakened and their integrity is compromised by introducing stress concentration sites deteriorating the in-plane properties. Composites in aerostructures, such as fuselages or wings made of composites, are accompanied by the requirement of additional lightning strike protection as composites are electrically inert. Currently, composite aerostructures are protected against lightning strike using bonded aluminium and copper foils or meshes, placed on the outer skin of the structures. The role of the protection is to dissipate the electrical current generated by the strike along the surface of the structures preventing structural

damage of the composite and failure of electric devices in the aircraft. This is disadvantageous since it increases the weight and manufacturing cost. Composite structures often involve complex shapes challenging automated through-thickness reinforcement processes, thereby, limiting their application. Although, some of these processes are performed using multi-axis robots to enable the reinforcement of complex shaped structures, the automation of the reinforcement process of such shapes is still unexplored.

Figure 1-1 Composite fuselage section of the Airbus A350, adapted from [4]

Addressing the weaknesses and unexplored areas by conducting further research could lead to significant improvements in the practical use of composites. The introduction of fibres in the thickness direction has the potential of improving the out-of-plane properties of composites. This can be addressed by different through-the-thickness reinforcement (TTR) methods, such as stitching, Z-pinning and tufting. In addition, the implementation of an automated tufting process in the manufacture of composite structures may provide a combination of joining dissimilar materials avoiding a degradation of the manufactured structures by drilling holes and insertion of metal fasteners and, at the same time, reinforcing composite structures by increasing their delamination toughness. Another element is the insertion of a tufting thread which has the potential of reducing manufacture and maintenance costs and weight and thus also reducing in-service costs compared to metal fasteners.

The tuft material is of paramount importance. Typical thread materials are aramid, glass or carbon. Metal tufts, combining characteristics typical for metals, such as high strength and ductility and low electrical resistivity, with the potential to be used for the manufacture of hybrid joints have not been considered for the through-thickness reinforcement of composites. Their use would potentially allow the composite to be working as a protection against lightning strike, and, at the same time, improve the properties with regards to weight, cost and delamination toughness. Furthermore, the successful incorporation of metal tufts might generate a natural opportunity for joining tufted composites to metallic sub-structures.

A very important element is the automated insertion process of multi-functional tufts improving the mechanical and electrical properties of composite structures. This is enabled by the use and right choice of the tuft material and adaption of tuft parameters and process to the complexity of structures of industrial scale. Usually, such structures contain complex shapes, such as double curvatures, and require reinforcements and joining in a time efficient way.

This thesis focuses on the challenges involved in tufting complex shapes using multi-material configurations. This is addressed by investigating the influence of tufting parameters, such as tufting depth and inclination as well as different materials suitable to reinforce composite structures on delamination performance. In addition, the influence of tufting on the lightning strike response of composites is evaluated.

1.2 Aim and objectives

The aim of this work is the use of automated tufting process as a route to integrate multi-material tuft threads into complex shaped composite structures to improve their mechanical and electrical behaviour. This is carried out by pursuing several activities addressing the manufacturing, mechanical behaviour and electrical response of tufted laminates. These can be summarised in the following objectives:

- Upgrade of the tufting process to allow automated tufting of complex shapes;

- Evaluation of the mechanical properties of tuft materials;
- Investigation on the effect of the tuft material on the delamination performance using metal and non-metal tufts;
- Investigation on the effect of the base composite material on the delamination performance of tufted materials;
- Investigation on the effect of the tufting depth on the delamination resistance using different thread materials;
- Investigation on the effect of the tuft inclination on the delamination resistance using different thread materials;
- Development of a simplified analytical model for the prediction of delamination toughness;
- Evaluation of the lightning strike response of tufted composites.

1.3 Thesis overview

Chapter 2 presents an exhaustive literature survey on the state of the art on through-the-thickness reinforcement methods and their effect on the delamination performance and in-plane properties of reinforced composites. The tufting and preform materials used throughout this study are presented in Chapter 3 alongside the tufting parameters, specimen manufacture and testing methods.

Chapter 4 deals with a case study of automated tufting of a tail cone, including the upgrade of the tufting process to enable tufting of complex shapes.

Chapter 5 focuses on the influence of tuft and base composite material on the mechanical behaviour, with the results of single thread testing combined with those of delamination tests. Results from the investigation of the influence of tufting depth on the mechanical response are reported in Chapter 6 and from the investigation of the influence of tuft angle in Chapter 7. Chapter 8 reports the results of the evaluation of the lightning strike performance of tufted composites and links these to the through-thickness electrical conductivity of the materials. Chapter 9 presents an overall discussion of the main outcomes of this study. The conclusions of the work are summarised in Chapter 10 alongside suggestions for further research.

2 Literature review on through-the-thickness reinforcement of composites

This chapter presents an exhaustive overview of through-the-thickness reinforcement methods, including research findings from their development and applications until today. The review focuses on experimental quasi-static interlaminar delamination performance and the effect on laminate mechanical properties, such as tensile, compression and interlaminar shear strength.

Composites show high performance when loaded in-plane. Depending on the lay-up, the advanced in-plane properties can be distributed to several directions within the plane. However, this performance is not matched in the out-of-plane direction, as through-thickness behaviour is governed by the properties of the resin matrix. Hence, composite structures suffer from low resistance to loading in the thickness direction which in the case of impact and bending leads to delamination. Several reinforcement methods have been developed in order to counteract the susceptibility to delamination. Some methods include the modification of the fibre architecture by creating a 3D fabric material such as knitting, 3D braiding and 3D weaving, whilst others are based on the development of high toughness matrices which are mostly compatible with a prepreg processing route. Other possibilities to reinforce structures prior to infusion/consolidation are stitching, Z-pinning and tufting which are reviewed in the following sections. In general, the choice of reinforcement depends on the design philosophy and the area to be reinforced. Stitches, Z-pins or tufts require a certain crack length to be active preventing delamination. However, if small areas need to be reinforced the TTR methods may not be suitable and matrices of high toughness may be considered in order to increase the overall delamination toughness of a structure. Depending on the design philosophy crack initiation in a structure should not occur or structures can have a long in service life containing cracks but prevented to propagate due to TTR. For structures with no tolerance in terms of crack initiation TTR may not be suitable as the load at crack initiation may be reduced due to the insertion of TTR. 3D braided or woven material may overcome such limitations.

2.1 Z-pinning

Z-pinning has been developed to reinforce prepreg laminates and is the only method to do that in large commercial quantities. The first use of pins was in the 1970s in the form of metal rods inserted manually which is too costly and labour intensive for large production [5]. In the 1980s a system for an automated insertion of thin fibres was developed by Tomashevkii et al. [6-8]. Simultaneously, Foster-Miller Inc. (later Aztex Inc. and now Albany International) developed an automated method to insert metal and fibrous pins at high speed using the patented ultrasonically assisted Z-Fibre® (UAZ®) technology. This is nowadays the most widely used way of pin insertion. These pins are usually made of titanium, steel or carbon fibre composite with a high stiffness and strength [9, 10]. Carbon fibre pins are usually made of pultruded T300 carbon fibre tows impregnated with bismaleimide (BMI) resin, with a pin diameter of 0.2 – 1 mm used at a volume fraction of 0.5 – 4%, corresponding to 8 – 70 pins/cm^2 [11]. Figure 2-1 shows a schematic of pin insertion steps. Pins are delivered in the form of a periodic pattern incorporated in carrier foam which is placed directly on prepreg stack (Figure 2-1a). This foam ensures the distance between pins and the pin orientation are maintained during the insertion. With the UAZ® method an ultrasonic tool, hand-held or automated, generates high frequency vibration and pressure which facilitate the pin insertion and lead to crushing of the foam (Figure 2-1b, c). Naturally, this automated process offers higher quality control in terms of pin inclination and consistent pressure. The propagation of vibration through the highly viscous uncured matrix generates heat. Consequently, the viscosity of the resin in the prepreg decreases and insertion becomes easier. The pins have a 45° chamfered tip to facilitate the insertion. After the pins are inserted, the compressed foam is removed and the excess of pins protruding the laminates is trimmed using a blade (Figure 2-1d, e).

Standard use of Z-pins is in prepregs, as they are held in position by the impregnated material before and during consolidation. In dry fabric the pins may fall out or rotate due to the movement of fabric layers and tows. However, Z-

pins have been successfully inserted in dry fabric in investigations of the bridging laws of single pins in miniature specimens [13].

The pinned material is consolidated and cured using vacuum bagging and autoclaving. An alternative route for Z-pinning using the pressure in the autoclave to crush the carrier foam and insert the pins has been proposed [14]. Nevertheless, the process of pin insertion is only a single step within the process chain of composite manufacture.

Z-pinning requires access only to one side of the laminate which allows the operation to take place in situ on the mould tool. This, alongside the portability of Z-pinning equipment, has significant efficiency benefits combined with minimal modification of the manufacturing procedure in order to incorporate this technology into a conventional process chain.

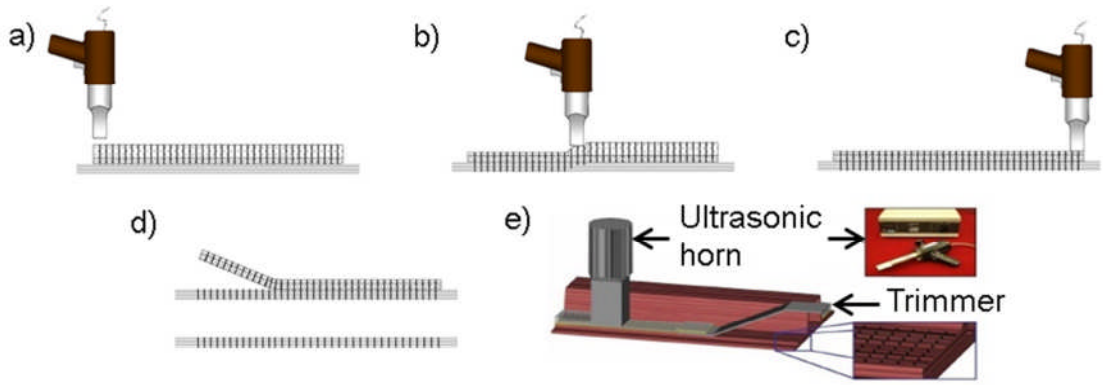

Figure 2-1 Z-pin insertions steps, adapted from [11, 12]: a) Carrier foam placed on prepreg, b), c) pin insertion with hand-held tool and d), e) removing of foam and trimming of pins.

Investigations on the tensile [15-23], compression [24], bending [24, 25], fatigue [16, 18, 22, 23, 26], impact [19] and pull-off strength [21, 26-39] of Z-pinned joints, such as single-lap, T-, I- and L-shaped joints as well as Ω-stiffeners, have been carried out showing an improved behaviour compared to equivalent unpinned joints. Z-pinning increases the load carrying ability of joints and stabilises the crack propagation along the joint line by developing a bridging zone. Z-pins have the potential to replace metal fasteners and eliminate the need to drill holes into composite structures. Cost savings in the order of $17,000 and a weight reduction of approximately 4.5 kg can be accomplished by replacing 1,000 titanium fasteners with Z-pins [40]. This fact has motivated

Boeing and McDonnell Douglas manufacturing the military fighter F-18 E/F Super Hornet to replace 4,600 titanium fasteners with 5 m^2 of manually inserted Z-pins (Figure 2-2a) [41]. This has resulted in cost and weight saving of $83,000 and 17 kg per aircraft, respectively. Jaguar Racing have used Z-pinning to reinforce the roll hoop of the R1 F1 car (Figure 2-2b) [12].

Z-pinning results in a significant increase in delamination toughness in mode I (up to 25 times [42]), mode II (up to 10 times [43]) and mixed mode (up to 18 times [44]) compared to unpinned structures [9, 19, 27, 42-53]. Z-pins have the ability to arrest long cracks (2 – 5 mm or larger), whilst they do not affect directly crack initiation [43, 47, 51, 54, 55].

Figure 2-2 a) Hat stiffener reinforcement of F-18 E/F Super Hornet, adapted from [41, 56] and b) Jaguar R1 F1 roll hoop reinforcement, adapted from [57].

Delamination toughness depends linearly on the pin volume content [55]. This effect is less prominent in mode II due to lower effectiveness in suppressing sliding displacements. Apart from improving the toughness, Z-pinning makes the crack propagation stable, compared to possible unstable and fast

propagation in unpinned structures. The mechanism of a pin action in mode I can be explained in three steps: (1) elastic pin stretching in the axial direction, (2) pin debonding from the surrounding composite and (3) frictional pull-out of the pin [55]. In some cases the second step occurs during the cure of the composite structure due to development of process stresses [55]. Process stresses develop mainly during the cool down stage of the cure. The higher thermal expansion coefficient of the composite in the through-thickness direction, in comparison to that of the pin, generates a strain mismatch, with the resin rich zone in the vicinity of the pin being under tension and the pin being under compression. Due to the difference in stiffness the resin undergoes significant tensile deformation accompanied by tensile stresses that can be higher than the failure stresses of the matrix system leading to debonding [58]. Frictional pull-out creates a bridging zone that can be tens of millimetres long behind the crack tip [55]. If the frictional forces are higher than the tensile strength of the pins, tensile failure occurs instead of pull-out. During pull-out a large amount of energy is required to overcome frictional forces, creating a traction force in the bridging zone. These traction forces decrease the strain energy at the crack tip, arresting the crack and improving the delamination toughness [55].

The failure mechanism of the pins in mode II is governed by a more complex process: (1) elastic shear deformation of the pin, (2) debonding of the pin, if this is not introduced during cure, (3) snubbing of the pin, and (4) shear-induced pull-out of the pin [55]. The snubbing effect contributes significantly to the delamination toughness. If the level of sliding displacements is high enough, the pins deform near the delamination plane and plough into the laminate, increasing the friction between the pins and the surrounding laminates and leading to a higher resistance against shear induced pull-out [55]. Figure 2-3 shows an example of a pin ploughing into the resin matrix. This mechanism can be exploited by inclined pin insertion, increasing the snubbing effect [55, 59].

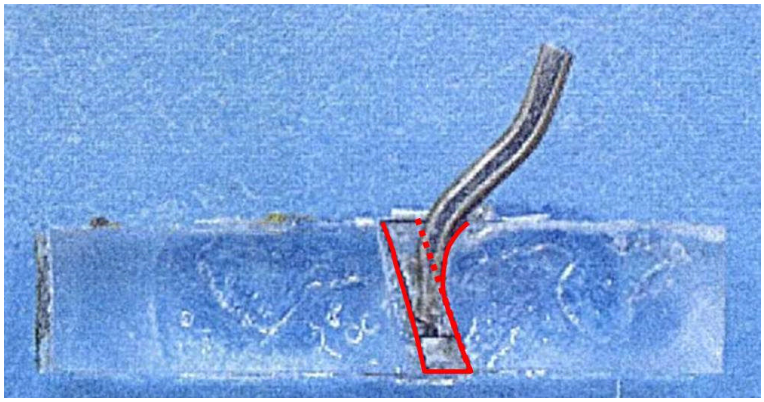

Figure 2-3 Example of pin ploughing into resin, adapted from [60].

2.1.1 In-plane tensile properties

Z-pinning causes defects in the composite laminate. The in-plane properties, such as tensile, compression and interlaminar shear strength can be negatively affected by pin insertion.

The elastic modulus decreases linearly by up to 13% [61] in Z-pinned structures compared to unpinned laminates [9, 14, 27, 61-68]. The modulus decreases with increasing pin volume fraction and diameter at equivalent pin volume fraction [27, 61-64, 66-68]. The composite lay-up affects the effect of Z-pinning on the elastic modulus, with uni-directional (UD) lay-ups showing the highest reduction, followed by cross-ply [0/90], quasi-isotropic [0/45/-45/90] and bias [+45/-45] laminates [27, 62, 65, 66]. The reduction in modulus is attributed to fibre crimping through-the-thickness, fibre waviness in the in-plane direction and swelling [55]. Swelling occurs due to the expansion of the laminate to accommodate the pins and the lower levels of compaction during consolidation and cure in the vicinity of the pins as a result of their higher stiffness compared to the uncured laminate in the through-the-thickness direction [69]. This leads to an unfavourable reduction in fibre volume fraction.

Similarly to the modulus, the tensile strength also decreases linearly by up to 30% [64] with increasing pin volume content and diameter at equivalent pin volume fraction [61-66, 68, 71]. The main reasons for the reduction in strength are the clustering of broken fibres due to pin insertion and the presence of resin rich regions around the pins. Forcing the pins into the laminate during insertion fractures some of the fibres. These areas enhance crack initiation leading to

failure in tensile. The size of the clusters increases with pin size and volume content [55]. Similarly to tensile modulus, the tensile strength reduces with decreasing fibre volume fraction due to swelling. Resin rich regions are created by pushing the laminate fibres apart during pin insertion, leading to diamond shaped voids which are filled with resin during consolidation [72, 73]. The size of such resin rich regions increases with increasing pin diameter, whilst their number increases with increasing pin volume content. In extreme cases, when the pins are inserted too close to each other, the resin rich regions overlap creating a resin channel in the fibre direction as shown in Figure 2-4 [55]. These areas are susceptible to crack initiation and propagation when the material is loaded transversely to the fibre direction.

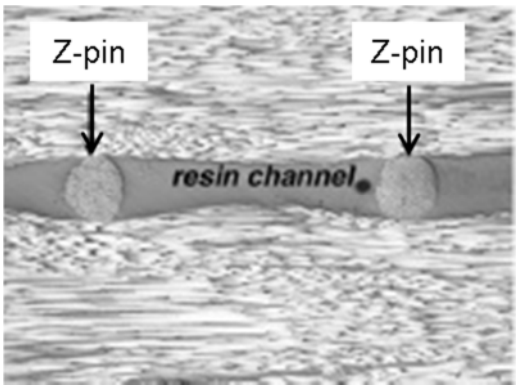

Figure 2-4 Resin channel created by too close Z-pins, adapted from [70].

2.1.2 In-plane compression properties

Z-pinned laminates are associated with reduction in compression modulus and strength by up to 20% [55, 70]. The main reasons for the reduction are the fibre crimping through-the-thickness and fibre waviness in the in-plane direction causing microbuckling and kinking [63, 70, 74-76]. A linear relation exists between the reduction in compression modulus and strength with increasing volume content and pin diameter at equivalent pin volume fraction [55]. The main reasons for the decreasing modulus are the fibre waviness around the pins and the swelling and associated decrease in fibre volume fraction. The reduction in modulus due to pinning is higher when more plies are orientated in the loading direction [70]. The compression modulus is sensitive to misalignment of 0° fibres and, therefore, the knock-down of the modulus

depends on the percentage of the 0° fibres in the laminate. The main cause of strength reduction is the fibre crimping leading to microbuckling. During pin insertion fibres are broken or crimped in the thickness direction. Figure 2-5 shows an example of fibre crimping with the dashed and solid line representing the theoretical and the actual direction of the fibres, respectively.

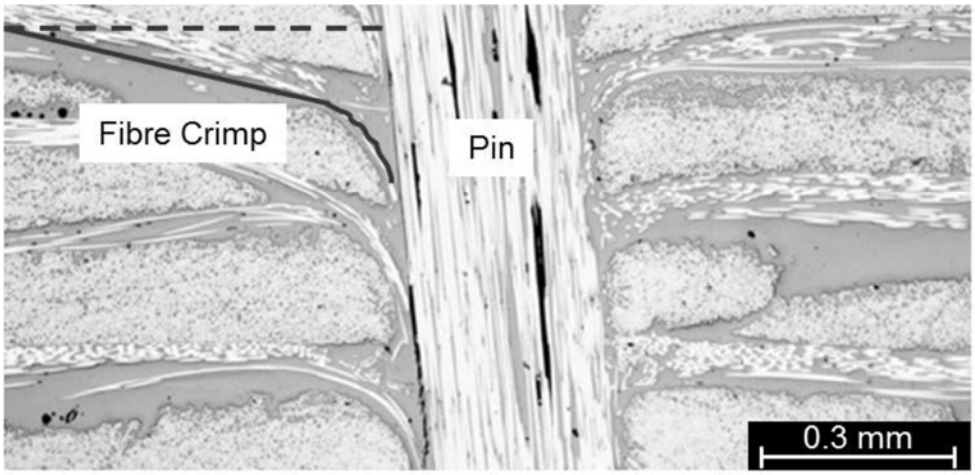

Figure 2-5 Fibre crimp, adapted from [55].

Compared to tensile loading, where the unbroken misaligned fibres can partially realign during loading and contribute to the tensile strength, in compression such fibres kink and buckle deteriorating the load bearing capability of the material. In open-hole specimens kinking starts at the location of maximum stress concentration. In unpinned specimens the kink band propagates in an unstable manner through the load bearing sections causing catastrophic failure. In pinned specimens the kink band propagates along the row of pins, closest to the hole, transversely to the compression load [70]. The reason for this behaviour, also confirmed by [73], is that the fibre misalignment around the pins causes shear stresses, reducing the required compressive stresses to initiate or propagate a kink band. Increasing the pin diameter reduces the kink stress around the pins leading to a reduction in strength by around 15% [70]. Increasing the diameter has the same effect as increasing the pin volume content with constant pin diameter: due to the reduced distance between the pins leading to shorter sections of straight fibres, the kink band can propagate with less resistance [70]. The laminate lay-up affects the compressive strength equivalently to the modulus, with the exception of bias lay-ups which show an

increase of 13% in strength for pinned laminates [70]. The effect of misalignment of ±45° fibres on the kinking stress and, hence, compression strength is marginal and cannot lead to reduction in strength [70].

2.1.3 Interlaminar shear strength

The effect of Z-pinning on the interlaminar shear strength (ILSS) is contradictory: ILSS appears to decrease by up to 20% as a result of Z-pinning following a negative trend as a function of pin volume content [71, 77]. However, increasing the pin volume content can also lead to an increase of the interlaminar shear strength [78]. The failure mechanism changes in short beam shear specimens with the presence of pins. The addition of pins in laminates that normally fail by interlaminar shear along the mid-plane changes the failure mode to rupture induced by bending [77]. Interlaminar crack propagation is suppressed by the Z-pins due to crack bridging in mode II delamination [77]. The large increase in ILSS can only be considered as a minimum threshold given the difference in failure mode between standard and pinned laminates [78]. A significant increase is obtained in notched specimens. In general, notches create stress concentration sites. Z-pins enhance the uniformity of the stress distribution along the specimens leading to higher load bearing capabilities and higher interlaminar shear strength compared to unpinned specimens [78].

2.2 Stitching

Stitching is a technology developed relatively early to improve the delamination resistance of composites. In the late 1980s Boeing Corporation and NASA Langley Research Centre for Aerospace developed a stitching machine for an automated stitching process joining dry fabric stringers to wing skin preforms as part of the Advanced Composite Technology (ACT) programme (Figure 2-6) [79, 80]. The role of stitching in this early development was two-fold: (i) to improve the robustness of the dry fabric assembly during processing for handling purposes and; (ii) to improve the mechanical performance of the component.

Figure 2-6 Stitching machine for ACT programme, adapted from [19].

Several variations of stitching have been developed during the last decades, such as chain stitching, standard lock stitching and modified lock stitching. These are shown in Figure 2-7. Chain stitching requires access to both sides of the preform using two needles and one or more threads. The interlocking occurs on the bottom side of the preform. Hereby, the tension of sewing threads is relatively low leading to reduced fibre spreading. However, the amount of thread on the seam and loop sides can cause crimping and increased fibre distortion [81]. Lock stitching uses one needle and one bobbin thread accessing the preform from the upper and lower surface sides, offering the use of two different thread materials. A bobbin following the stitching direction supplies the bobbin thread which is interlocked with the needle thread. A drawback is that the two threads are interlocked in the centre of the stack of plies creating stress concentration points [82]. Modified lock stitching is performed in a similar way; however, the threads are interlocked on the lower side of the preform by varying the tension of the needle and the bobbin thread. This reduces the defects generated with a standard lock stitch [81]. However, the thread knot on the outer surface can increase fibre crimping of outer plies [83].

In general, the potential to increase the damage tolerance and strength of composite structures and joints has led to a large interest to investigate the

adoption of stitching as a common reinforcement method. Stitching of different types of joints, such as single-lap, T-, J- and Omega-stiffener, single-blade stiffener and wing-to-spar joints resulted in improved mechanical performance in tensile [85-98], compression [87, 99], fatigue life [85, 88, 91-94], bending [87, 98, 100-102] and pull-off delamination [98, 102-105]. Furthermore, stitches are lighter and distribute stresses in joints more uniformly than metal fasteners commonly used, such as bolts and rivets [106]. Stitching has been applied to the reinforcement of bumper beams, floor panels and door members for the Avanti Sedan and the Consulier automobiles [107].

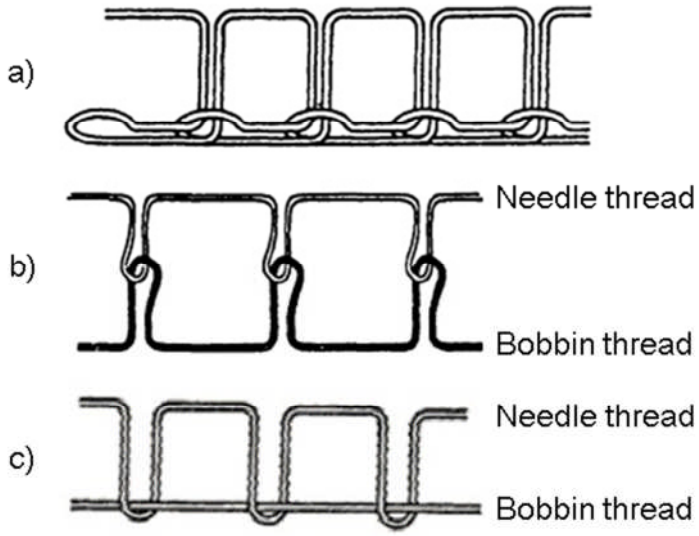

Figure 2-7 Schematic of the stitching types: a) chain stitch, b) lock stitch, adapted from [84] and c) modified lock stitch, adapted from [82].

The crack propagation resistance of stitched composites increases compared to unreinforced laminates by up to 45 times [108] in mode I [82, 108-148]. A significant increase in delamination toughness is reported with increasing stitch density [109, 113-117, 119, 121, 122, 125, 128, 131, 133, 134, 137, 138, 140, 141, 145-148], caused by the increased amount of stitches bridging the delamination crack and arresting its propagation, as well as with increasing thread diameter maintaining the areal stitch density or stitch pitch [116, 134, 135, 140, 141, 147], due to increased thread ultimate tensile strength and stiffness. Studies using different thread materials reveal that carbon is superior to Kevlar®, followed by glass, nylon and polyester [109, 123, 130, 134, 149]. The effect of the materials is explained based on the thread mechanical

properties and the quality of bonding to the resin system. The stitching direction also affects the delamination performance: stitching in the specimen longitudinal direction results in higher delamination toughness compared to stitching in the transverse direction [109, 117, 121]. However, the phenomenon is not entirely clear as there are reports of the opposite effect [141]. The crack energy release rate depends on the fibre orientation with an increasing delamination resistance with increasing fibre angle up to ±45° and the 0° having the lowest delamination toughness [137, 143]. Exceeding ±45° leads to a decrease of delamination performance. For angles up to ±45° the crack at the delamination plane propagates along the fibres resulting in the longest path per unit length of the specimen for specimens with a ±45° lay-up compared to smaller angles. The crack is subject to higher resistance with an increasing path due to the counter aligned fibres of opposing plies leading to an overall higher delamination resistance [137]. The delamination toughness for materials with a lay-up of ±60° or higher is reduced for two reasons: (i) cracks jump across the fibres, rather than following them reducing the crack path per unit length of the specimen and consequently the resistance to propagate and; (ii) cracks jump to adjacent plies during testing instead of propagating through the mid-plane [137]. This mechanism is less prominent in stitched specimens, since stitching is the dominating factor for affecting the delamination toughness suppressing the effect of fibre orientation.

The delamination toughness in mode II increases [112, 116-118, 125, 147, 150-156] by up to 15 times [151]. However, drops in delamination toughness by about 5% [117] have also been reported [117, 125]. Similarly to mode I, the delamination resistance in mode II increases with increasing stitch density and thread diameter at equivalent stitch pitch [116, 117, 125, 147, 150-152, 155, 156]. The effect of stitching is not as significant in mode II as in mode I; the shear strength of threads, which is of importance in mode II, is much lower than their tensile strength leading to less energy required to rupture the threads and hence lower delamination performance in mode II.

Stitching generates several defects, such as resin rich pockets between strands, fibre breakage caused by needle penetration and abrasion by the

thread, fibre misalignment generated during thread insertion [83, 127], porosity [157] and microcracking near the stitches due to process-induced strains [158]. Porosity can be caused by stitch distortion occurring upon preform compaction [116] creating voids at the thread/fibre interface which are not filled with resin. Furthermore, the stitching thread can be damaged during the stitching process by twisting, bending and sliding, reducing the in-plane and out-of-plane strength of the composite [82, 83].

A variety of fabric and prepreg materials with different fibre orientation have been reinforced by stitching. Stitching is commonly used with dry fabrics, since prepregs may blunt the needle due to the resistance of uncured resin. The contact of the needle with the uncured resin may also lead to needle fouling [83].

Generally, the laminate properties of stitched composites depend on several parameters, such as thread tension, fabric compaction by stitching tools and thread, type of needles (size and shape), thread type (size, stiffness and strength), preform fabric material, fibre orientation, stitching process speed, preform thickness, stitching density and stitching pattern [159]. The fibre volume fraction of stitching yarn within a structure is between 0.5% and 5%, corresponding to 1 to 25 stiches/cm^2, considering a thread diameter of 0.02 cm to 0.25 cm. A higher stitch density may lead to more fabric fibre damage, whereas a lower density may not reinforce sufficiently the structure [127]. These parameters also affect the permeability of the preform during infusion and the in-plane properties of the structure [160-162].

The influence of stitching on in-plane properties has not been clarified fully. In contrast to Z-pinning, identification of a clear trend on the dependence of in-plane behaviour on stitch density and thread properties is difficult. A number of works report a decrease in tensile modulus of stitched structures of up to 30% [163] in comparison to unstitched composites [64, 107, 109, 116, 124, 148, 150, 157, 163-175], whilst other studies confirm an increase of up to 20% [163] or no change in modulus [115, 116, 124, 148, 163, 171, 174, 176-180]. Stitching usually increases the fibre volume fraction leading to an increase in modulus caused by the compaction due to stitching thread tension. A decrease in

modulus can be explained by a reduction of the fibre volume fraction caused by spreading fabric fibres during the stitching process, fibre crimping and misalignment around the stitches [83].

2.2.1 In-plane tensile strength

The effect of stitching on in-plane tensile strength has been subject to some controversy. Some works report an increase [135, 141, 163, 175, 176, 178, 181-191] by up to 25% [181] attributed to compaction of the preform during the stitching process, leading to a higher fibre volume fraction [83], and to a uniform stress distribution due to stitching [163]. More commonly a degradation of the tensile strength of up to 45% [163] is observed, caused by the creation of clusters of broken fibres and fibre misalignment, produced during needle and thread insertion [64, 109, 115, 116, 124, 126, 141, 147, 148, 150, 163, 164, 168, 170, 172-174, 180-182, 186, 189-199], and by resin rich regions around the stitches generating crack initiation sites [64, 116, 141, 147, 150, 164, 170, 178, 190, 191, 197-199]. Plastic strains transmitted by internal matrix damage under high tension lead to damage of misaligned fibre bundles and reduction in strength [83]. Studies using uni-directional fabric lay-ups report a degradation of the tensile strength [115, 116, 126, 150, 163, 192, 197], whilst in quasi-isotropic [141, 170, 176, 181, 185, 186, 194-196, 198] and bi-axial [64, 124, 135, 147, 173, 174, 178, 180, 182-184, 188-190, 193] lay-ups stitching can lead to an increase or decrease in strength. The drop in strength increases with an increase of the fraction of plies orientated in 0°. The amount of 0° and 90° plies in bi-axial and quasi-isotropic is equivalent, leading to either a decrease or increase in strength depending on the fibre volume fraction and stitch density. Stitching creates stress concentration sites degrading the tensile strength [116, 148, 163, 189]. Stitching in the transverse direction [141, 164, 168, 174, 178, 189, 190, 196, 198, 200, 201], increasing the thread thickness at equivalent stitch pitch and distance [116, 126, 141, 147, 150, 186, 189, 194, 200, 202] or stitch density [64, 116, 126, 141, 147, 148, 163, 174, 183, 186, 190, 194, 202] have a detrimental effect on the tensile strength. Since the stitching thread in the transverse direction is not loaded in its axial direction, it cannot contribute to an increase in the tensile strength. The detrimental effect of increased thread

diameter and stitch density to fibre breakage and misalignment leads to further decrease of the tensile strength. However, stitching transversely to the loading direction increases the strength compared to stitches orientated in the loading direction [183, 188]. Also, converse results with respect to the thread diameter [135, 202] and stitch density [109, 115, 116, 126, 163, 164, 175, 191, 193, 194] effect have been found, depending on the stitch density and material. In some cases stitching appears not to have an effect on the tensile strength [115, 126, 176, 181, 183, 188]. These results have been obtained using different preform lay-up sequences, stitching thread materials and stitch directions. Hence, the only plausible explanation is the counteraction of the increased fibre volume fraction, improving the tensile strength, and the damage of the preform materials, reducing the strength.

2.2.2 In-plane compression strength

Similarly to tensile strength, the compression strength of stitched composite structures increases [141, 172, 192, 196, 198, 203-207] by up to 15% [205], degrades [100, 109, 116, 141, 157, 165, 166, 170, 176, 185, 192, 194, 197, 198, 202, 204, 208-227] by up to 54% [210] or is not affected [176, 196, 198, 204, 207] compared to unstitched composites. A decrease in strength occurs with bi-axial or uni-directional fabric lay-up with some exceptions for multi-axial preforms [100, 109, 141, 165, 170, 185, 192, 196, 202, 204, 227], whilst an increase in strength occurs if a multi-axial lay-up is used with exceptions of using a bi-axial preform [205] and eight harness woven materials [224]. However, multi-axial lay-ups containing more plies in the loading direction than the transverse direction show a decrease [141, 204, 217]. Hence, the reduction is mainly attributed to the fabric fibre direction as confirmed by [228]. As in the case of Z-pinning, the more plies are orientated in the loading direction the higher is the influence of waviness and crimp to the compression strength. Stitching does not have an effect on the compression strength if increased fibre volume fraction and fibre misalignment are cancelling each other out, as described for tensile strength. Despite the drop in strength of stitched composites compared to unstitched, the stitch orientation and density also affect the strength. Stitching quasi-isotropic prepreg with one row of

reinforcement leads to an increase in compression strength, whilst adding a second row causes a decrease in strength compared to unstitched prepreg [192]. In general, increasing the stitch density leads to a decrease in compression strength [116, 141, 194, 202]. Also, increasing the stich diameter at constant stitch distance and pitch is equivalent to an increased density, enhancing fibre misalignment and decreasing the compression strength [116, 141, 194, 202, 227]. However, some results contradict these general trends: the strength can increase with rising density [141, 170, 202, 221, 223, 227] and diameter [202]. These results indicate that stitching is effective if the distance and pitch lie between 3 mm and 10 mm approximately. Exceeding that range, i.e. reducing the density, might not be effective in reinforcing a structure as stitches are too far apart but is beneficial to the compression strength. If the stitches are closer, i.e. increasing the density, high fibre misalignment or resin channels occur, weakening the structure in compression. Nevertheless, stitching in the loading direction improves the compression strength compared to transverse stitching [141, 176, 196, 198, 203, 207]. The causes are not fully clarified; however, the tension of the needle and bobbin thread may lead to further fibre misalignment of the outer plies when the threads are orientated across the fibres, whilst when orientated parallel to the fibres the threads may shift fibres apart and occupy places between the fibres of the outer plies preventing misalignment and leading to an increase in strength.

In contrast to a reduced compression strength obtained with the short-block compressive method, the compression strength appears unchanged due to failure with a different failure mechanism when a large gauge length is used [217]. Unstitched specimens tend to fail by sudden delamination cracking between the plies leading to global buckling. Stitching suppresses the delamination, causing local in-plane fibre misalignment and leading to gradual failure by kink band formation and matrix cracking [109, 166, 210, 211, 228-230]. Furthermore, the misaligned fibre bundles are subjected to axial shear stresses, which cause microcracking in the matrix, resulting in a rotational movement of the fibre bundles and enhance damage [83]. A change in the failure mechanism from buckling to shear failure can also lead to higher

compression strength [205]. Although stitching suppresses delamination, the presence of the stitch seams and knots leads to out-of-plane fibre kinking of the outer plies, as fibre crimping is most severe at these locations [210, 211, 230]. The thread tension affects the fibre volume fraction of the structure which may influence the compressive strength equivalently to the tensile strength [59]. Minimising thread tension during stitching reduces kinking and increases the compressive strength [83, 84]. However, an increase in thread tension also leads to higher fibre volume fraction increasing the strength [206]. The compressive strength increases by up to 35% by removing the surface stitching loops eliminating crimping of outer plies. This is in agreement with the assumption that the compressive properties of composites are degraded by the crimped plies due to stitching [211, 216, 230].

In contrast to the tensile strength, the compressive strength of stitched specimens comprising of an open hole with a diameter between 5 mm and 13 mm increases [170, 185, 196, 198, 209, 231] by up to 37% [198], remains unchanged [87, 231, 232] or decreases [87, 232, 233] by up to 18% [233] compared to unstitched specimens. The stitching direction affects the compressive strength; specimens with stitches orientated in 45° relative to the loading direction obtain higher strength than 0° and 90° [196, 198]. Furthermore, a decrease in strength occurs in specimens with stitches in 0° [233] and circular shape around the hole [87, 232]. The failure mechanisms in unstitched and stitched open-hole specimens are not reported. However, kink bands may arise at the edge of the hole where stress concentration occurs [83]. The kink band grows away from the hole, followed by decreasing stresses. Indeed, as the highest stresses are located at the hole, the kink band has still a supporting effect on the compressive strength. Stitching, in this case, may be responsible for stable kink growth which might not occur in unstitched specimens.

2.2.3 Interlaminar shear strength

Stitching leads to an improvement in shear strength [116, 135, 192, 223, 229, 234-239] by up to 127% [239]. However, there are reports of no beneficial effect of stitching [116, 226, 236] or a deterioration of the shear strength due to

stitching [117, 141, 170, 194, 197, 226, 234, 236, 240] by up to 31% [170]. The shear strength is mainly dependent on the stitch density and thread diameter. The strength increases with increasing stitch density [116, 135, 229, 235, 239] and decreasing thread diameter at equivalent stitch pitch and distance [116, 141, 194]. However, contradicting results have been found: the strength decreases with increasing density [141, 236] and decreasing thread diameter [135]. The effect of stitch direction has not been investigated thoroughly; however, the shear strength tends to increase if stitches are orientated in the specimen's longitudinal direction, rather than transverse to it [192, 238, 239], whereas the opposite effect has also been reported [141]. The increase may be caused by the threads on the surfaces being loaded in axial direction contributing with their tensile strength when the specimen is bent.

In interlaminar shear loading one or more cracks are initiated in stitched and unstitched specimens, propagating simultaneously; however, one delamination crack dominates over all small cracks. This crack has the characteristics of a mode II delamination crack with microcracking and plastic yielding in the crack tip zone. The microcracks unite and produce layers of debris between the plies which cause friction [83]. These frictional zones can be up to two millimetres long [153, 241]. High energy is required to overcome the friction and to rupture the stitches. The amount of friction depends on the ratio between normal stress and shear stress acting on the delamination plane and its shape; a waved plane increases the friction stress compared to a smooth plane. This effect is governed by the fabric material and the stitching parameters [83]. Fibre deformation, caused by stitching, may increase the friction and, thus, the interlaminar shear strength. If the friction stresses are higher than the stresses required to break the stitches, the stitches will not affect the shear strength and fail abruptly once the friction stresses are reached. However, it may be possible that the stresses required to break the stitches are higher than the friction stresses. Thus, stitching improves the interlaminar shear strength by carrying some of the applied shear stresses by bridging the delamination cracks. A reduction in shear strength can be attributed to severely distorted fibres caused by stitching, considered as damage before the crack even reaches them [83]. It

is expected that stitched specimens fail by delamination along the mid-plane [83]. However, it has been observed that stitching causes cracking around misaligned fibres surrounding the stitches near the surface. With increasing load the cracks propagate delaminating the surface plies from the composite beneath and, thus, invalidating the tests. The overall shear strength is lower compared to the unstitched specimens [83], confirmed by [117], which reports the same trend and identifies stitches as stress concentration sites lowering shear strength.

2.3 Single-sided stitching

Single-sided stitching methods, comprising of one-sided stitching (OSS®), blind stitching and a stitching method developed by the Institut für Textiltechnik (ITA) at the RWTH Aachen [159], aim to overcome the limitations of the standard stitching process requiring access to both sides of the preform. These relatively new methods use stitching heads mounted on multi-axial robot arms, in order to ensure precision, versatility, speed and simple implementation into the automated manufacturing processes of composite structures at low costs [242].

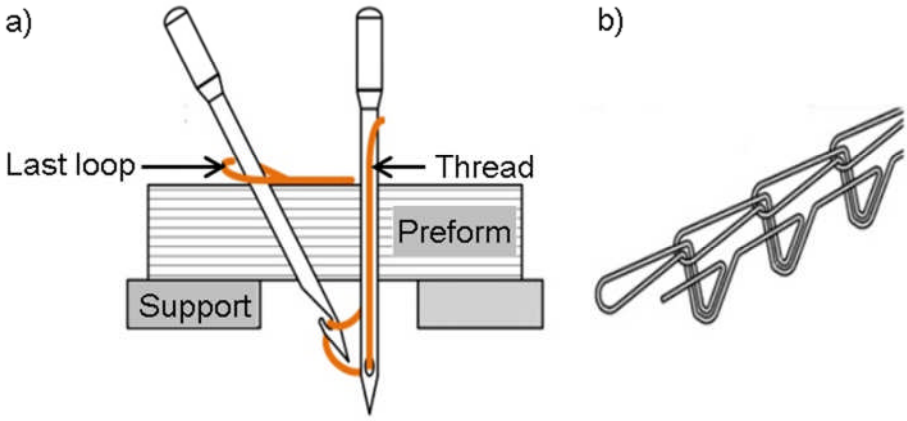

Figure 2-8 OSS® technique: a) needle configuration and b) stitch pattern, adapted from [13].

The OSS® technique was developed by Altin-Nähtechnik GmbH and is based on chain stitching as shown in Figure 2-8b [81]. It uses one thread and two needles, one of which is orientated vertically and the other one is inclined by 45°. The vertical needle penetrates the preform with the thread creating a loop on the lower side of the preform with a thickness of up to 20 mm. The inclined

needle catches the loop with a hook and retracts it to the top side of the preform interlocking the loop with the previous stitching loop (Figure 2-8a) [243].

The stitching technique developed by ITA uses two threads and two needles inclined by 45°, as shown in Figure 2-9a. Each of the two needles penetrates the preform with a thread, creating a stitching loop on the lower side of the preform and catching the loop of the other needle in fabrics of up to 8 mm thick. After interlocking the loops the needles retract again, creating a chain stitch pattern (Figure 2-9b).

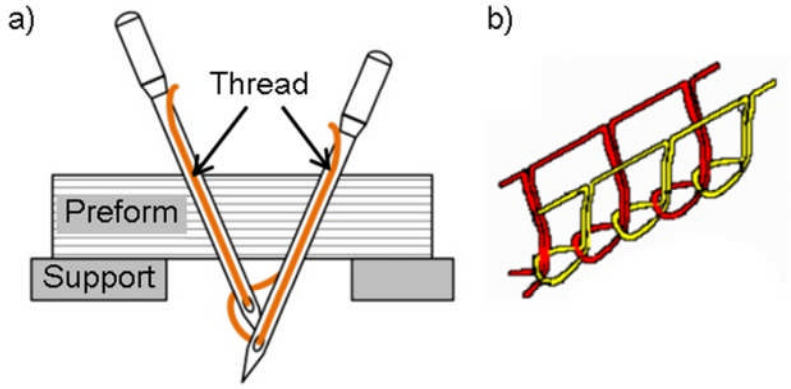

Figure 2-9 ITA stitching technique: a) needle configuration and b) stitch pattern, adapted from [13].

Both the OSS® and the stitching technique developed by ITA have only been used for research purposes [159, 172, 244-251]. The delamination toughness in mode I and mixed mode is improved by up to about four times compared to unstitched preforms using OSS® [247]. The in-plane compression and compression after impact (CAI) strength of quasi-isotropic preforms stitched with carbon threads decrease by approximately 20% and 10%, respectively [172]. This result is not universal as there has been a report of a small increase in compression after impact strength compared to unstitched specimens [250]. In general, the open-hole compression strength increases with decreasing density compared to unstitched composites, whilst the compression after impact strength increases with increasing density and transverse stitching. The open-hole compression strength increases by up to 7%, if stitched transversely with a low areal stitch density, and decreases by up to 10%, if stitched transversely with a high density. Similarly, the compression strength increases by up to 5%,

if stitched with a low areal stitch density, and decreases by up to 2%, if stitched with a high density [250].

The delamination toughness in mode I increases with increasing linear density of the stitching thread [248]. In mode II the effect of the linear density of the thread is negligible as the shear strength of the threads, which is crucial in mode II, is relatively low for both threads [248].

Overall, the OSS® and the ITA technique result in an improvement in mechanical properties of stitched composites. However, the results are in the same range as obtained with conventional stitching. Nevertheless, the access to only one side of the preform leads to higher versatility and speed of the reinforcement process.

The blind stitching technology was developed by KSL Keilmann Sondermaschinenbau GmbH [81]. A pressure foot compresses the preform while a curved needle, with a radius of 50 mm, penetrates the preform with a thread, creating a loop on the same preform side and retracting through the same path (Figure 2-10a). A hook mechanism catches the stitching loop and interlocks it with the previously created thread loop. The stitching pattern is based on chain stitching (Figure 2-10b) [81]. The maximum stitching depths is 10 mm. The advantage of blind stitching, compared to the other single-sided stitching techniques, is the potential to be applied to the preform after it is placed on the tool, as the needle is not required to penetrate fully the preform. In contrast, the other two single-sided stitching techniques need a support with a certain amount of space under the preform for the needles to be able to penetrate fully the preform [252].

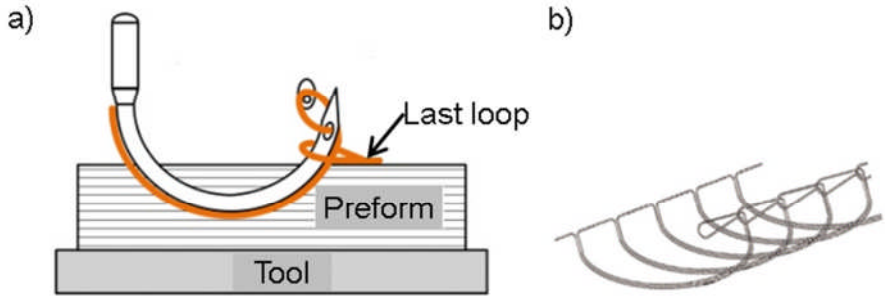

Figure 2-10 Blind stitching: a) schematic of curved needle and b) stitch pattern, adapted from [13].

Blind stitching has been successfully applied to the manufacture of the rear pressure bulkhead of the Airbus A380, joining stiffeners to the bulkhead (Figure 2-11) [253]. In addition, investigations have been done to implement the technology to manufacture an automotive roof structure [254].

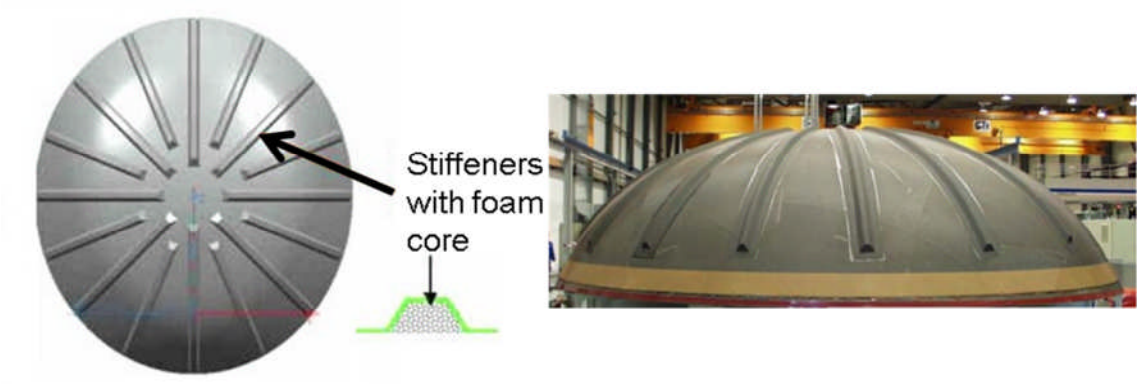

Figure 2-11 Pressure bulkhead of Airbus A380, adapted from [255, 256].

2.4 Tufting

In contrast to conventional stitching methods, tufting is a relatively new reinforcement method. A tufting head, which can be mounted onto a standard multi-axis robot arm, was developed by the German Aerospace Centre (DLR), EADS and KSL Keilmann Sondermaschinenbau. Figure 2-12a shows one of the first developed tufting heads. The tufting procedure can be explained in three steps as shown in Figure 2-12b: (i) a rounded pressure foot compresses the preform before the vertical orientated tufting needle penetrates at a chosen location; (ii) the needle penetrates the preform with a continuous thread up to a designated depth; (iii) the needle creates a thread loop and retracts through the same path it penetrated the preform.

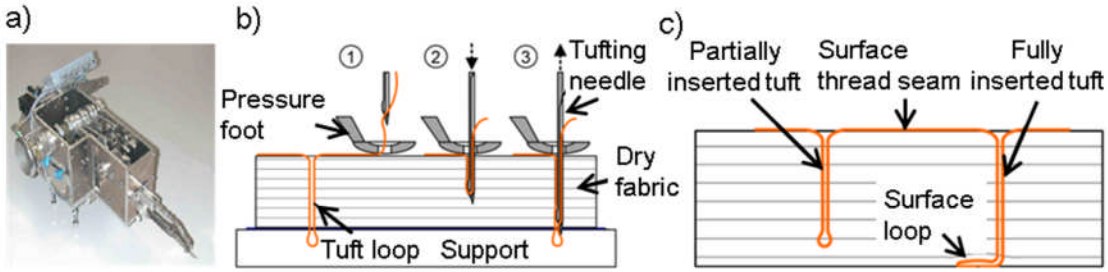

Figure 2-12 a) Tufting head, b) tufting procedure steps and c) schematic of partial and full tuft, adapted from [13, 257].

The role of the rounded pressure foot is to compress the preform with a pre-set pressure to near-net shape to ensure a uniform tuft loop creation and to hold the tufting thread seam in place, preventing pull-out of the previous tuft while the needle inserts a new tuft. This ensures that the thread material, which is required to create a tuft, is taken from the spool, rather than from already inserted tufts. The needle insertion depth is variable and is set by the user. Preforms with a thickness of up to 40 mm can be tufted fully through-the-thickness [243]. Partial tufting can be carried out with tuft loops inside the preform with a specially designed inclined needle eye [13]. In the case of full through-the-thickness tufting, space under the preform is required as the needle protrudes from the bottom surface, creating the tuft loops outside the preform. Placing the preform into the mould, after full through-thickness tufting, results in bending of the tuft loops onto the surface as shown in Figure 2-12c. The needle retracts while the thread is held in place by natural friction between the thread and the surrounding fabric layers [258]. Hence, the advantages of tufting, compared to conventional stitching, are the absence of interlocking and thread tension and of the associated defects. Furthermore, tufting offers maximum variability in stitch spacing, seam radius and insertion angle (45° – 135°) due to its simple mechanism, the requirement for access to one side of the preform only, the compactness of the tufting head and ability to tuft a preform thickness of up to 40 mm. The loops have to be kept as short as possible to prevent overlapping each other after compaction and creating a resin rich layer which may have an effect on the bending behaviour of the structure [259]. In addition, since there is no thread tension the preform has to be handled carefully after the tufting process to avoid pulling out the short loops.

The delamination toughness of tufted composites is up to 25 times [260] higher in mode I [12, 13, 260-263] and three times [262] higher in mode II [13, 261, 262, 264] compared to untufted composites. In general, the thread mechanical properties affect the delamination results; due to the strength of the carbon thread the delamination properties in mode I are better by about 10% compared to glass tufted composites [12]. Single and multi-thermoplastic filaments have been used in tufting resulting in an increase in mode I delamination toughness

of about 150% and 15%, respectively, compared to the untufted material [12]. Apart from improving the delamination resistance the crack propagation becomes stable, rather than unstable as occasionally observed in untufted specimens [262]. The crack propagates between the tufts, which are inserted at regular intervals, before being arrested due to tuft bridging. A typical characteristic of R-curves in mode II is the steady increase with the absence of a plateau region indicating a fully developed bridging zone [13, 264]. Often the maximum crack energy release rates are reported, which depend on the length of the specimen, making a comparison between different materials difficult [13, 262, 264].

Fibre spreading and openings caused by tufting, which fill with resin during infusion providing crack initiation sites after cure, affect the in-plane properties [265]. The tuft pattern is crucial as tufts placed close to each other may result in resin channels. However, test results on the accuracy of the tuft pattern reveal that the standard deviation of a repeated tuft pattern is 67% and 85% lower than that of OSS® and blind stitching, respectively, indicating a higher accuracy in tuft insertion (maintaining tuft pitch and distance) along tuft rows [265].

2.4.1 In-plane tensile properties

Improvements in delamination by tufting are accompanied with controversial findings for in-plane properties. Tufting can have a negative effect [12, 13, 260, 262, 266] of up to 18% [13] or a positive effect [13, 262, 266, 267] of up to 41% [13] on tensile strength and modulus. Generally, tufts create stress concentration sites, as recorded strain fields reveal during testing, introducing fibre misalignment leading to fibre rupture close to tufts [13, 267]. As identified for conventional stitching, the fabric fibre orientation affects significantly the tensile properties with the largest degradations in fabrics with uni-directional lay-up [13], followed by 0/90 woven and NCF and ±45 woven [12, 13, 260, 262, 266, 267]. The higher the proportion of 0° plies the greater decrease in strength is observed due to fibre misalignment and crimp [12, 13, 262]. An increase in in-plane properties (±45 woven) can be explained by an increasing fibre volume fraction with tufting leading to higher strength and preventing a drop in modulus for the tufted material. A further reason for the increase in strength may be the

suppression of local delamination by the tufts which can be caused by out-of-plane and interlaminar shear stresses due to fibre waviness [267]. The areal tuft density has a negligible effect on the strength and modulus; however, crack initiation and propagation are different for low density and high density tufted materials [12, 13, 262]. In untufted and low density tufted NCF material microcracks initiate in resin rich pockets and propagate along the 90° plies at low strains [13, 262]. At high strains these cracks continue propagating through 0° and 90° plies causing delamination. In addition, the straightening of misaligned fibres causes splitting cracks due to debonding of the fibre-matrix interface [13]. The delamination is suppressed in specimens with high tuft density and cracks are initiated in resin rich pockets by thermal stresses, propagating in the 0° (tuft seam) direction leading [12, 13]. The failure mechanism in densely tufted ±45 material is identified to be thermal cracks developing to shear macrocracks inside resin rich pockets [13]. At high strains debonding of the tuft loops and corresponding resin rich layers is observed. In general, the in-plane properties are different depending on the loading direction. The strength and modulus in the longitudinal direction for uni-directional preforms are reduced compared to the transverse direction if the tuft seams are orientated in transverse direction increasing the stiffness and strength in transverse direction [13, 266].

2.4.2 In-plane compression properties

Similarly to the tensile properties the compression properties are reported to increase [13, 172, 262, 268], by up to 14% [262], or decrease [13, 172, 206, 262], by up to 28% [13], depending on the fabric fibre orientation. Results show mainly a sensitivity of 0° fibres to compressive strength if tufts are inserted leading to the largest degradation in UD fabrics, followed by fabrics with fibres orientated in 0/90 and ±45, and quasi-isotropic fabrics. In bi-axial materials, local microbuckling occurs, increasing non-uniformly with higher loads [262]. Untufted materials fail due to local delamination and subsequent buckling. In tufted materials the tufts cause fibre undulation and kinked bands creating an inclined fracture plane at which shear failure develops, reducing the strength [13].

In materials with fibres orientated in ±45° the reinforcement causes crack closure and localised friction around the tufts due to fibre shearing [262]. The strength of material with quasi-isotropic lay-up decreases or increases [172, 206]. It is assumed that the strength of tufted materials is reduced due to fibre waviness caused by the tufts, whilst an increase in strength is caused by the suppression of delamination and buckling generated by the tufts. Overall, tufting may prevent global buckling improving the compression strength. In contrast, tufting increases the natural waviness and crimp which may reduce the compression properties. Furthermore, recorded strain fields reveal a doubling in strain along the tuft seams compared to areas between tuft rows causing kink bands and shear failure and deteriorating the mechanical properties [262].
Tufting also improves the edgewise compression strength of bi-axial woven sandwich structures containing a core: the strength increases, with increasing tuft density, by up to 25% [268]. Tufting leads to a change in failure mechanism: untufted sandwich structures fail with delamination of the skin from the core prior to outward buckling, whilst tufted structures delaminate and fail with outward or inward buckling without delamination.

2.4.3 Impact performance

The resistance of tufted structures to impact has been reported to increase, by up to 44% [12], or decrease, by up to 14% [269], compared to untufted material [12, 172, 206, 269, 270]. The amount of absorbed energy depends on the fabric material, tufting thread material and tuft density. In general, materials tufted with carbon show a higher compression after impact strength than structures tufted with glass thread which is attributed to the differences in the mechanical properties of the threads [12]. Tufting reduces the amount of damaged planes in the structure compared to untufted materials, whilst the size of the damaged area is similar. The damage in untufted composites develops progressively at constant load levels, with crack propagation along the fabric fibres forming a cross-shaped or diamond shaped damage area with the corners in the fibre direction. The damage areas in tufted composites are circular or cross-shaped [12]. In contrast to untufted material, tufting prevents crack propagation leading to higher load bearing capabilities and overall higher CAI strength by improving

the delamination toughness [12]. In general, the absorbed energy increases with increasing tuft density compared to untufted material [269]. In the untufted material the crack propagates along the fibres of the fabric, jumping between fabric plies. Tufting prevents delamination which leads to a reduction of overall damage compared to the untufted material. In densely tufted materials the tufts lead to a high amount of resin rich pockets, where cracks are initiated. Equivalently, using a thicker carbon thread leads to the same trend and a decrease in absorbed energy compared to a thinner thread at constant density [269]. Similarly to the absorbed energy, the CAI strength increases with increasing tuft density [172]. Tufting leads to slightly smaller damage areas, arresting crack propagation and fabric fibre buckling.

2.4.4 Bending properties

In general, tufting does not directly affect the bending stiffness of composite structures. However, an increase in laminate thickness due to tufting may result in a higher stiffness, depending on the tuft seam direction. Carbon tufted materials with a quasi-isotropic lay-up and tufts orientated in the specimen transverse direction are more compliant in bending than the untufted material [267]. The bending stiffness increases in the longitudinal direction compared to the untufted material. This is due to the thickness of the 0° ply and the fact that the tuft seams loaded in tension, both increasing the stiffness. The failure mechanism in the untufted material is delamination of plies and fibre damage by kinking at the compressed side and tensile failure at the side under tension. The tufted material also fails by kinking and tensile failure of fibres at the corresponding sides, whereas delamination is suppressed by the tufts.

Sandwich structures made of carbon fabric skin with a polyurethane core carry up to 107% or higher bending loads than untufted structures [268]. Equivalently to the bending load, the flexural stiffness increases by up to 900% compared to the untufted structure. Tufting leads to a change in failure mechanism; the untufted structure shows indentations, local yielding and deformation of the skin into the core during bending. Tufted structures fail due to coupled deformation of skins and core, caused by the bridging of the tufts, up to shear failure of the core [268].

2.4.5 Fatigue life

Tufting has the potential to increase the energy absorption by up to 30% [262] and the tensile-fatigue life by up to 200% [271], compared to untufted materials, depending on the loading direction. The tensile-fatigue life of tufted multi-axial material loaded in tuft seam direction, i.e. transverse to the non-structural stitches is higher compared to the transverse direction, whilst the untufted material shows the opposite behaviour [271]. Improvements when loaded in the seam direction are due to the contribution of the tuft thread to tensile strength. The tufts may have a detrimental effect on the fatigue life in the transverse to the seam direction due to fibre misalignment and openings in the fabric.

2.4.6 Joint strength

Tufting increases the load bearing capability of joints tested in pull-off by up to two times [272], the fatigue life up to 13 times [272] and the energy absorption by up to about 300% [273], depending on the type of joint and tuft material. Commonly, in untufted joints crack initiation occurs near the noodle, propagating along the skin-flange interface leading to complete delamination and failure. In tufted joints the crack propagates along the web, initiating multiple cracks in the web until joint failure by flexure, preventing crack propagation along the skin-flange interface due to the tufts [272, 273]. This failure mechanism is also active in fatigue of tufted and untufted T-joints which is increased for tufted joints compared to untufted [272]. The maximum load bearing capability and energy absorption also depend on the tufting material: carbon tufted joints are able to carry higher loads and absorb more energy than the glass tufted joints changing the failure mechanism. The propagation along the flange-skin interface is arrested by the tufts leading to progressive failure for carbon tufted joints and abrupt failure glass tufted joints [273]. The difference in failure may be caused by the lower tensile strength of the glass thread leading to crack propagation through the entire tuft rows without being arrested. A reinforcement at the skin-flange interface transition leads to an increased initial peak load during bending compared to untufted joints [275]. Close to the peak load, the untufted joint starts delaminating from the outer ends of the skin-flange

interfaces towards the web in the form of peeling. Although, the tufts prevent peeling, cracks are initiated along the interface. Final failure occurs as splitting of the web which is reduced with additional tufts. In general, the benefit of tufting lies in the prevention of crack propagation increasing the load bearing capabilities and damage tolerance of a tufted composite structure. However, the crack initiation load may be reduced due to fabric fibre misalignment, crimp and breakage. Joints, such as T-joints or I-beams typically start cracking at the noodle. Tufting the flanges of the joints increases the crack propagation toughness but may reduce the crack initiation load at the noodle leading to an earlier failure of the structure.

Apart from improving the mechanical properties of joints, tufting has the potential to reduce the costs per part by 27% for dry fabric tufted joints compared to unreinforced prepreg joints, assuming a production of 1,000 parts and not considering the required equipment [276].

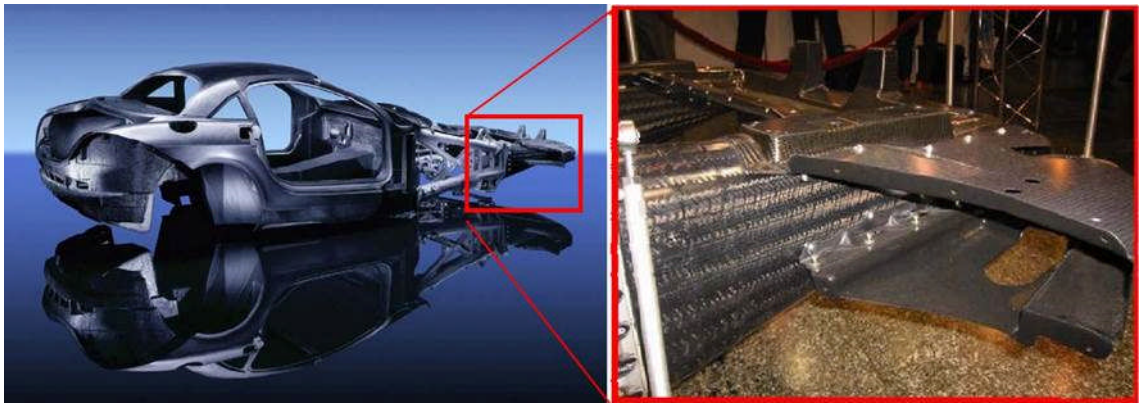

Figure 2-13 Reinforced crash box, adapted from [256].

Tufting has been successfully applied at industrial level: the crash box of the Mercedes SLR has been reinforced by tufting to join I-stiffeners to braided bridges connected to the skin as shown in Figure 2-13 [256]. Cranfield University was involved in the reinforcement of a 1.2 m long landing gear brace prototype using a carbon thread. The reinforced braces are now into production and applied to the Boeing 787 Dreamliner (Figure 2-14) [277].

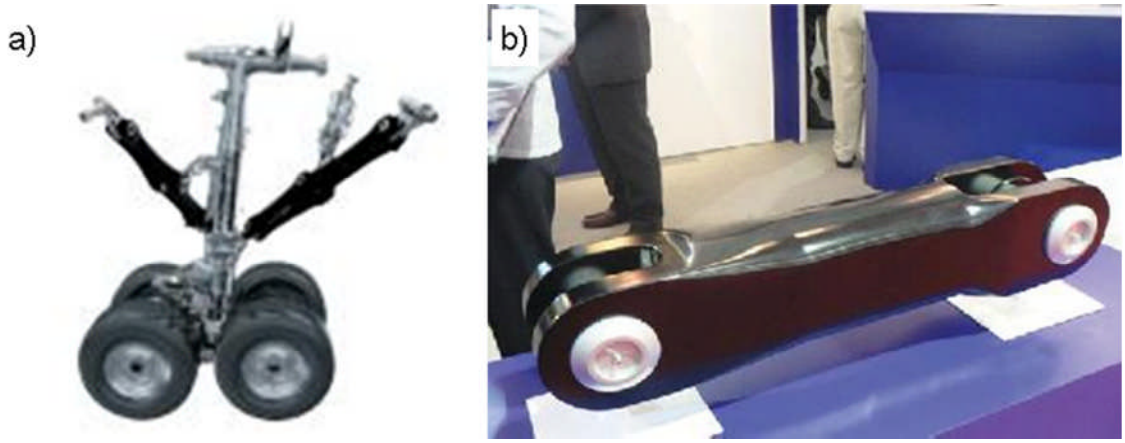

Figure 2-14 Landing gear braces: a) black coloured parts and b) real size at an exhibition, adapted from [277].

2.5 Comparison of TTR methods

Based on the exhaustive literature review Z-pinning may lead to the largest improvement in delamination toughness accompanied with lower reductions in in-plane properties compared to the other TTR methods. However, the fact that it can be applied to prepregs only limits its range of application. In addition, Z-pins are more expensive than threads used for stitching and tufting. Nevertheless, the pin insertion process is considered as robust and leads to efficiently reinforced composites.

The stitching and single-sided stitching processes are less robust; the presence of a second needle or thread adds a further source of error and decreases the probability of first-time successful manufacture. The correct synchronisation and alignment of the needles can be disturbed by the fabric preventing hooking of the thread and the creation of the knots. The knots have a detrimental effect on the in-plane properties due to generation of fibre kinking, misalignment and resin rich areas. This can be counteracted by increasing the thread tension and the resulting fibre volume fraction of the structure and improving its in-plane and out-of-plane properties. Compared to Z-pinning stitching is compatible to a larger range of materials and can be applied to both prepregs and dry fabrics. However, in the case of blind stitching the in-plane and out-of-plane properties of reinforced composites are not well known and it can be assumed that the complete insertion of a curved needle may lead to significant damage to the fabric decreasing the in-plane properties.

The tufting process proves to have a higher robustness than stitching, being comparable to Z-pinning, due to the use of only one thread and one needle and relying on the natural friction between the thread and the surrounding composite. In addition, the manufacturing costs are lower than for Z-pinning and conventional stitching as common dry threads, supplied by a large quantity of manufacturers, are cheaper than Z-pins and the tufting robot occupies less space than a stitching machine. However, tufting is usually used for dry fabrics as prepregs require high motor power for needle insertion and the uncured resin may damage the needle and the thread. The in-plane and out-of-plane properties of tufted composites are comparable to those of stitched composites. Indeed, if a low thread tension for the stitching process is used, which is comparable to the tension of a tufting thread, the in-plane properties of stitched composites may be lower than for tufted structures due to the knot further crimping the fabric fibres.

In general, a comparison between tufting and other TTR methods is limited as tufting is a relatively new reinforcement method and is not fully explored. Currently, major research gaps are the effect of a large variety of tufting parameters, such as the tufting depth, angle and density, on the in-plane and out-of-plane properties of tufted composites. Furthermore, the tufting thread materials used for testing of tufted composites and being published in the literature are minimised to glass, carbon and aramid and offer great space for research of new materials. In addition, the overall efficiency of tufting and costs of the entire process have to be explored to make tufting a reinforcement method to be used in industrial applications.

3 Materials, specimen manufacturing and methods

This chapter introduces the materials, manufacturing procedures and testing methods used in this study. The materials include the tufting threads, resin and preforms. The manufacture of specimens involves both tufting and resin transfer moulding as well as the preparation of impregnated threads. Testing methods refer to mechanical tests including the investigation on the effect of the tuft and preform material, tufting depth and tufting angle on the mode I delamination performance of tufted DCB specimens. Furthermore, electrical conductivity and lightning strike tests were carried out on tufted specimens to evaluate the effect of different tuft materials on the electrical properties of composite structures. Microscopically analyses were carried out on mechanically and electrically tested specimens to characterise the failure mechanisms.

3.1 Materials

3.1.1 Tufting threads

In this study tufting was carried out using aramid, carbon, glass and stainless steel threads as well as a copper wire. They are shown in Figure 3-1. The high strength aramid thread or a variation of it was already used in previous studies and proved to be suitable for the tufting process and able to reinforce composites [13, 258, 259]. There is no published information about the use of a stainless steel thread or a copper wire in a through-the-thickness reinforcement method. All DCB specimens tested in mode I were tufted with aramid, stainless steel and copper, whilst the electrical properties were characterised on carbon, glass, stainless steel and copper tufted specimens as shown in Table 3-1.

Table 3-1 Overview of tuft material applied on manufactured specimens.

Material	Aramid	Steel	Copper	Glass	Carbon
Mechanical tests	X	X	X		
Electrical tests		X	X	X	X

The type of the aramid thread is Kevlar® 29 (DuPont®) and is made of three yarns twisted together, each containing 220 filaments. The stainless steel

thread, Thermotech N-30, is manufactured by Tibtech and is made of AISI 316L steel. The thread is structured out of two yarns each containing 180 filaments. The copper wire supplied by Goodfellow Cambridge Ltd. is made of standard annealed copper and is a single wire with a cross sectional area of 0.05 mm^2. The linear weight was measured on a precision scale (Mettler AT 460 Delta-Range). The E-glass thread is manufactured by Saint Gobain Vetrotex and is specified as EC9 68×3 S260. The thread consists of three yarns twisted together, each comprising of 411 filaments. The carbon fibre thread is manufactured by Schappe Techniques® and is a twisted thread made of two yarns, each comprising 1000 filaments. Table 3-2 summarises the properties of the threads.

Figure 3-1 Tufting thread materials.

The twisting of threads is an important feature as it reduces their bending stiffness, which is beneficial for the tuft loop creation, and abrasion of the yarns and compacts the yarns forming a cross section which can be considered as circular. This reduces the risk of rupture in the thread feeding mechanism and the needle eye during the reinforcement process [82]. Currently, the needles used for the tufting process have a needle eye diameter of 0.7 to 1.0 mm. This limits the choice of available threads. In addition, criteria, such as permeability during infusion and compatibility to the preform materials and resin systems, have to be taken into account for the selection of threads [278]. In a previous study the aramid, carbon and glass thread, also used in this study, proved to

have good bonding properties to the surrounding resin (Advanced Composite Group Ltd., MVR 444) [13]. Furthermore, these threads, including the stainless steel thread and the copper wire comprise of a relatively small diameter leading to reduced fabric fibre misalignment and crimp affecting the permeability.

Table 3-2 Tufting thread material properties.

Material		**Aramid**	**Steel**	**Copper**	**Glass**	**Carbon**
Manufacturer	[-]	DuPont®	Tibtech	Goodfellow	Saint Gobain Vetrotex	Schappe Techniques®
Type	[-]	Kevlar® 29, Tkt 40	Thermotech N-30, AISI 316L	Annealed copper	EC9 68x3 S260	Tenax® Carbon HTA40
Filament count	[-]	3 x 220	2 x 180	1	3 x 411	2 x 1000
Linear weight	[g/km]	74	240	438	204	140
Fibre density	[g/cm^3]	1.4	7.9	8.9	2.6	1.8
Cross sectional area	[mm^2]	0.05	0.03	0.05	0.08	0.08

3.1.2 Preform materials

For this study a dry pseudo-unidirectional fabric (HexForce® G1157 D 1300) made of carbon tow (TENAX E HTA40 E13 6K) with a small amount of non-structural glass weft yarns (EC9 34 Z40 1383) was used for delamination specimens. In order to investigate the effect of the laminate material on the delamination performance of tufted specimens, this fabric was compared to the equivalent fabric containing 7 g/m^2 of an epoxy binder powder applied to each side of the fabric layers (HexForce® G1157 D 1300 INJ AIRBUS E01 2F). Furthermore, a highly bindered uni-directional carbon fabric made of 6.35 mm wide tapes of fibres (HexTow® AS7 J12K) containing a thermoplastic veil (V800) on both sides (HiTape®) (produced within the European project ADVITAC [279]) was utilised as a case of very high delamination toughness. The type and amount of binder material is not published. These highly bindered tapes are considered as dry fibres and can be placed in any direction by automated dry fibre placement (ADFP). This process uses a 6-axis robot arm

mounted on a 2-axis rail system and equipped with a fibre feeding system and a deposition head. The reinforcement is led through flexible pipes protecting the fibres on the way from the spools of the creels and fed to the deposition head by the feeding system. The deposition head preheats the surface in order to activate the binder. The heat is generated by a heating lamp, hot air torches if higher temperatures are required or a laser with a higher ramp than the other heat sources leading to faster fibre deposition [258].

Table 3-3 Preform fabric material properties.

Name		**HexForce® G1157 D 1300**	**HexForce® G1157 D 1300 INJ AIRBUS E01 2F**	**HiTape®**	**C-BX440**
Manufacturer	[-]	Hexcel®	Hexcel®	Hexcel®	OCV™ Technical Fabrics
Warp fibre	[-]	TENAX E HTA40 E13 6K	TENAX E HTA40 E13 6K	HexTow® AS7 J12K	Toray T700 12k
Weft fibre	[-]	EC9 34 Z40 1383	EC9 34 Z40 1383	-	Polyester
Areal weight	[g/m^2]	277	277	252	440
Weight ratio (warp/weft)	[%]	97/3	97/3	100/0	98.6/1.4
Nominal fabric thickness	[mm]	0.26	0.26	0.26	0.45
Binder	[-]	-	E01 2F epoxy	-	-
Binder weight	[g/m^2]	-	14	-	-

Electrical tests were carried out on carbon composite panels made of non-crimp bi-axial [±45] fabric plies (C-BX440), (Toray T700 12k). Each pair of plies, with fibres orientated perpendicularly to each other, was non-structurally stitched together with a texturised polyester yarn. The main properties of the four dry fabric types are summarised in Table 3-3. Table 3-4 summarises the applications the fabrics are used for in this study, whilst Figure 3-2 shows the different fabrics.

Table 3-4 Overview of preform material application.

Material	HexForce® G1157 D 1300	HexForce® G1157 D 1300 INJ AIRBUS E01 2F	HiTape®	C-BX440
Mechanical tests	X	X	X	
Electrical tests				X

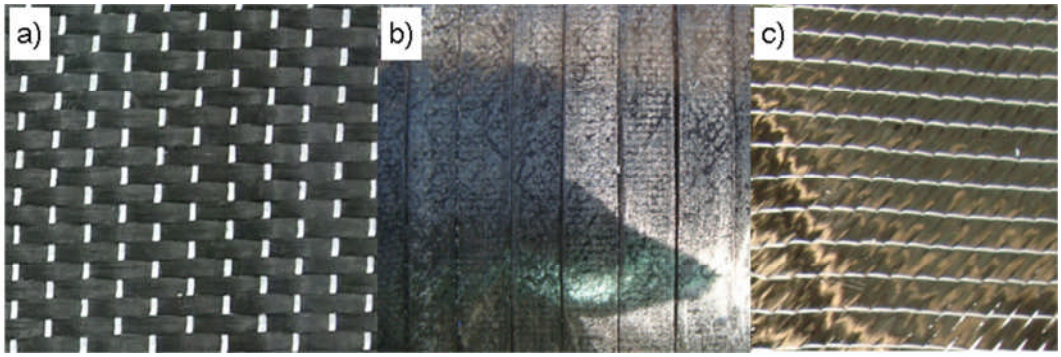

Figure 3-2 Sections of the fabric materials: a) pseudo-UD, b) UD tape and c) bi-axial [±45].

3.1.3 Resin and adhesives

The resin used throughout in this study is a single component epoxy resin (HexFlow® RTM6) specifically designed for aerospace applications manufactured using liquid composite moulding [280]. This resin was chosen due to its low infusion temperature (minimum of 80 °C) with a corresponding low viscosity of approximately 180 mPas.

Metal loading blocks were used to introduce the load applied by the test machine for DCB specimen opening. These blocks were attached using a two component epoxy adhesive (Huntsman Araldite® 420 A/B). Resin component A was mixed with a hardener component B with a ratio by weight of 100:40 [281]. The adhesive has a shear strength of 35 MPa after cure which is sufficient to delaminate fully all types of specimens in this study without debonding of the metal blocks.

3.2 Specimen manufacturing

3.2.1 Thread preparation

Aramid, stainless steel and copper tuft materials were tested in tension in order to obtain their tensile properties, such as strength, Young's modulus and ultimate strain. Twisting threads leads to a reduction in their strength [82]. Therefore, properties of untwisted yarns or bulk materials cannot be used. The thread materials were characterised in a dry and impregnated state. Before impregnating the threads the HexFlow® RTM6 epoxy resin was degassed in a vacuum chamber for 45 minutes. Thread pieces of 750 mm length were laid on a table and the central region with a length of 300 mm was impregnated with resin using a brush (Figure 3-3a). The dry ends were used to wind the threads around the oven rack. In addition, the dry ends allowed fixing of the threads around the test clamps. Resin cure was carried out in a fan oven (Binder GmbH, Klasse 2.0) following a standard cure cycle of 75 minutes at 160 °C followed by 120 minutes at 180 °C. During cure, metal weights were attached to the thread to add pretension and to ensure straightness of the tested thread sections (Figure 3-3b). Figure 3-4 shows the dry and the impregnated threads.

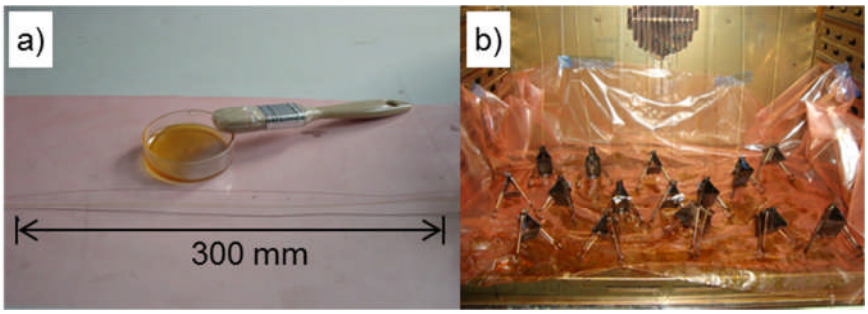

Figure 3-3 a) Impregnation of threads and b) oven cure with metal weights.

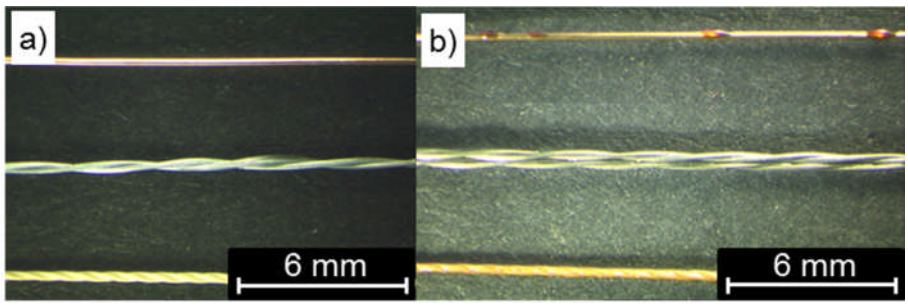

Figure 3-4 Cooper wire, stainless steel thread and aramid thread (from top to bottom) in: a) dry state and b) impregnated state.

3.2.2 Preform lay-up

The pseudo-unidirectional fabric preforms for the DCB specimens were made of 24 layers of unbindered and bindered uni-weave fabrics with dimensions of 200 × 200 mm. The stacks of fabric were laid up in uni-directional orientation with the non-structural glass stitches being orthogonal to the fibre direction. A 10 µm thick polytetrafluoroethylene (PTFE) film (L5337629 SDS, supplied by Goodfellow Cambridge Ltd.) with dimensions of 200 × 71 mm was placed in the mid-plane of the stack of fabric layers to act as a crack starter during testing. Bi-axial preforms for the highly bindered DCB specimens were made of UD tapes placed following a $[0/90]_{2s}$ lay-up sequence with 16 and 32 layers of tapes corresponding to a nominal thickness of 4 mm and 8 mm, respectively, and dimensions of 500 × 250 mm. A 13 µm thick PTFE film with the dimensions of 500 × 100 mm was placed in the mid-plane, between two layers orientated in 0°. Ten panels, each made of 8 layers of the [±45] NCF, were laid up and cut to dimensions of 350 × 350 mm for electrical testing. The final thickness of the panels was approximately 4 mm.

Table 3-5 Theoretical fibre volume fraction of each laminate.

Material		**HexForce® G1157 D 1300**	**HexForce® G1157 D 1300 INJ AIRBUS E01 2F**	**HiTape®**	**C-BX440**
Fibre volume fraction	[%]	63	66	57	50

The nominal fibre volume ratio v_f for each laminate was determined as follows:

$$v_f = \frac{N \cdot W_A}{2h \cdot \rho_f} \quad \textbf{3-1}$$

where N is the number of plies, W_A the areal weight of the fabric, h half the laminate thickness after cure and ρ_t the fibre density. The results of the calculation are presented in Table 3-5.

3.2.3 Tufting

Before tufting, the preforms were laid on a foam (Airex® R63.50) to support the tuft loop formation during tufting. In this arrangement the loops are held in place

by the friction between the thread and the foam. Tufting was carried out using a tufting head (KSL KL 150) mounted on a 6-axis robot (Kawasaki FS 20N), as shown in Figure 3-5.

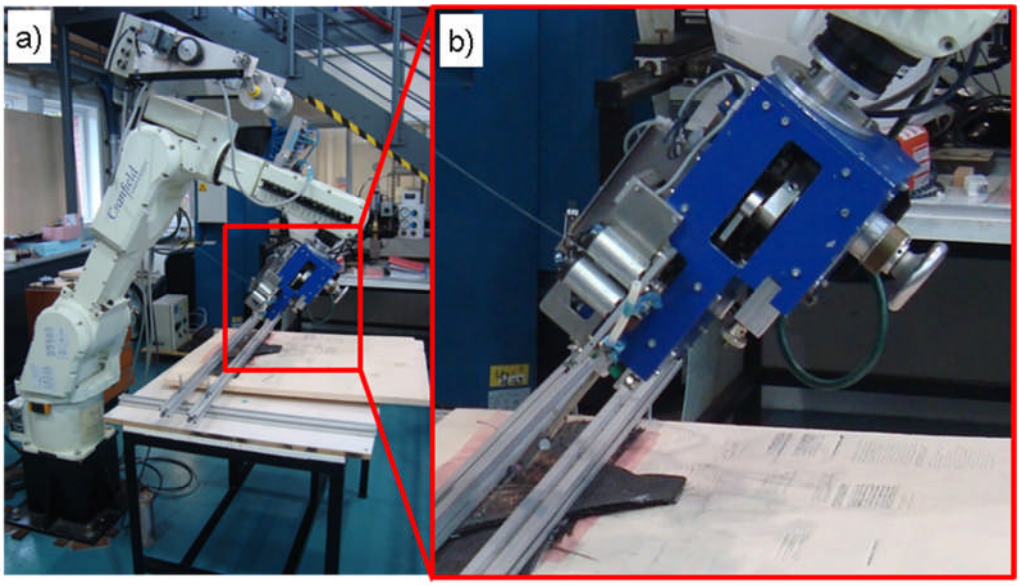

Figure 3-5 a) Kawasaki FS 20N robot arm and b) KSL KL150 tufting head.

The tufting process is controlled using a desktop PC and the software KCWin written in the simple AS programming language. The program offers four options as tufting arrangements: tufting single rows in x- and y- direction, a rectangular area and angled tufting in x-direction. The tufting coordinate system is the same as the robot coordinate system. Figure 3-6 shows the possible tuft arrangements.

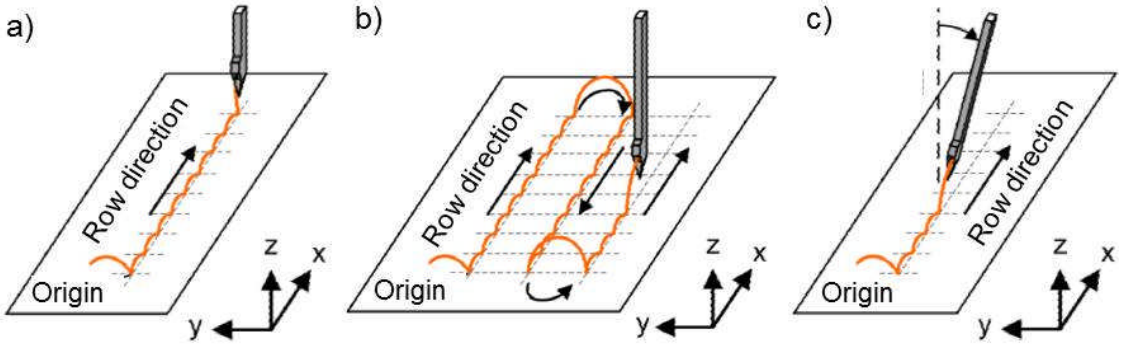

Figure 3-6 Tuft arrangements: a) single row in x-direction, b) rectangular area and c) angled tufting, adapted from [13].

Each tuft arrangement is defined by the total length of a tuft row, tuft pitch within the row s_x, distance between two adjacent tuft rows s_y and tuft speed being

measured as percentage of the maximum speed of 500 tufts per minute. In the case of tufting a rectangular area, a square and a triangular pattern can be chosen. The difference between these cases is the alignment of tufts of the adjacent tuft rows as shown in Figure 3-7.

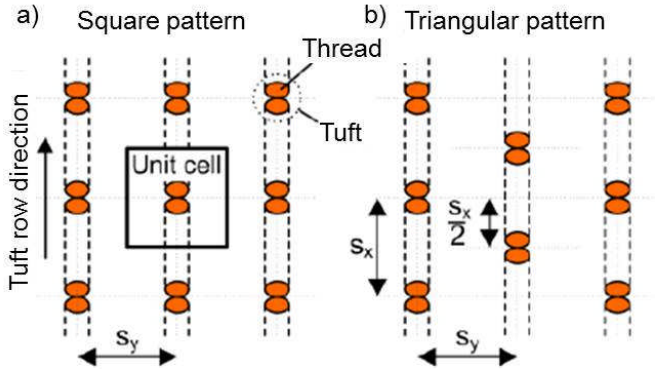

Figure 3-7 Unit cell definition, adapted from [13].

The tuft pitch and the distance between rows are of importance for the calculation of the areal tuft density which has a significant effect on the mechanical performance of tufted composite structures. The tuft density ρ_t describes the ratio between the cross sectional area of a tuft A_t and the preform area within a specified unit cell calculated as follows:

$$\rho_t = \frac{A_t}{s_x \cdot s_y} \qquad \textbf{3-2}$$

The cross sectional area of a tuft is considered as twice the cross sectional area of the thread, determined by the linear weight W_L and the fibre density ρ_f as follows:

$$A_t = 2\frac{W_L}{\rho_f} \qquad \textbf{3-3}$$

Panels manufactured for the investigation of the effect of tufting depth on the delamination performance were tufted with an angle of 90° to the preform surface and the tuft seam was orientated perpendicularly to the fabric fibre direction (parallel to the glass weft). A square pattern with an areal tuft density of 0.5% was used corresponding to a tuft pitch of 4.5 mm for the aramid thread, 3.5 mm for the stainless steel thread and 4.4 mm for the copper wire. The first tuft row was inserted at a nominal distance of 15 mm from the crack starter film. In order to test the effect of tufting depth on the delamination resistance four,

ten and twenty central plies, corresponding to a nominal tuft depth of 1.0 mm, 2.6 mm and 5.2 mm, respectively, were tufted and then incorporated in a stuck of 24 layers of the fabric as shown in Figure 3-8. This arrangement achieves identical flexural response of specimens with different tufted thicknesses, facilitating comparison of delamination performance. The tuft loops were kept as short as possible in order to minimise the resin layer between the adjacent plies. The average loop length was approximately 4 mm.

The highly bindered material was tufted with aramid thread with a tuft density of 0.5% and a square pattern. The first tuft row was placed at a nominal distance of 15 mm from the crack starter film. The tufts were inserted fully leading to tuft lengths of 4 mm and 8 mm.

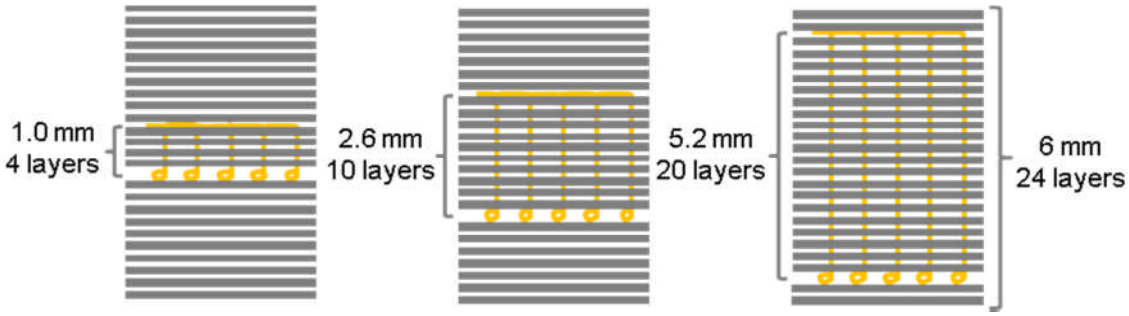

Figure 3-8 Schematic of the tufting arrangement for different depths.

Based on simple commands, such as entering the numbers at the beginning of the options, the user is led through the entire menu to set the parameters before starting the tufting process. In the case of angled tufting a positive or negative angle can be chosen relative to the vertical position of tufting needle. For angled tufting an especially designed pressure foot is available consisting of a smaller contact surface compared to the standard foot (Figure 3-9).

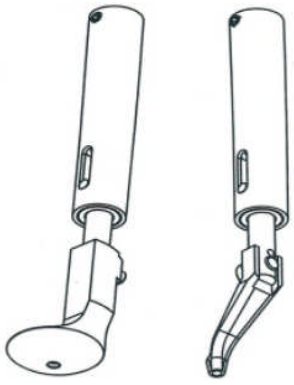

Figure 3-9 Pressure foot: left - vertical tufting, right - angled tufting.

Aramid, stainless steel and copper were used to prepare DCB specimens with inclined tufts. For the tufting procedure the pressure foot of the tufting head, as described in section 2.4, had to be taken off. The shape of the pressure foot used for vertical tufting is not suitable for inclined tufting and would lead to bending of the shaft. This resulted in a less compressed preform. The inclination was chosen to be 45°, maintaining a square pattern with an areal tuft density of 0.5% (Figure 3-10). The vertical tufting depth was 2.6 mm. The first tuft row was inserted at a distance of 16.3 mm from the crack starter film, so that the tufting thread bridges the preform mid-plane at a distance of 15 mm from the crack starter film.

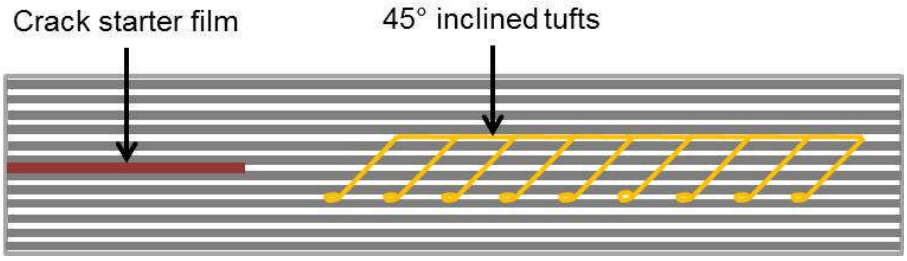

Figure 3-10 Schematic of inclined tufts in DCB specimen.

For the lightning strike test eight preforms were tufted with carbon, glass, stainless steel thread and the copper wire. Six panels were fully tufted (Figure 3-11a), one with each tuft material, whilst two panels were tufted with carbon and stainless steel thread only in a central area with dimensions of 100 × 100 mm (Figure 3-11b). The distance between tufts and rows was 3 mm and the tuft seam was orientated in 90° direction, orthogonal to the non-structural stitching seam.

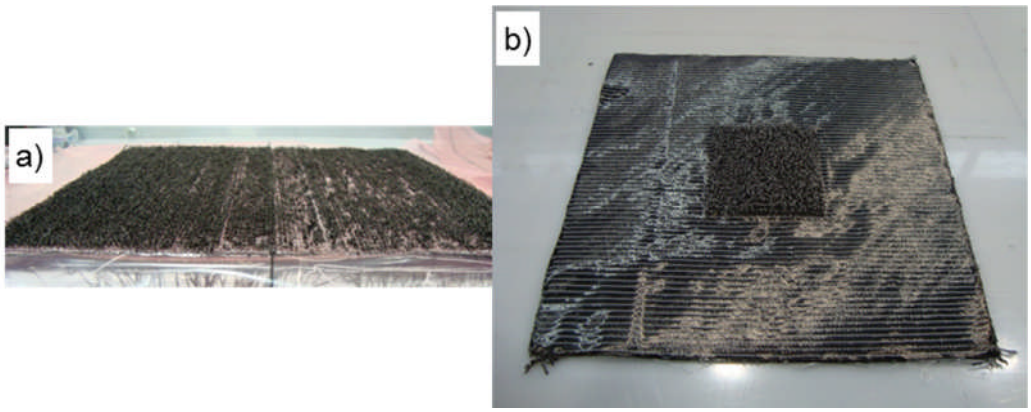

Figure 3-11 a) Fully tufted panel with carbon thread and b) central square tufted with stainless steel.

In addition, an untufted panel and two fully tufted panels with carbon and glass thread were covered with a copper mesh applied currently for lightning strike protection in aircrafts. One panel was tested for each configuration. Table 3-6 summarises the configurations of the lightning strike panels.

Table 3-6 Types of panels tested for lightning strike protection.

Material	Untufted	Carbon	Copper	Glass	Steel
Whole panel	X	X	X	X	X
Square		X			X
Copper mesh	X	X		X	

3.2.4 Liquid moulding

The preforms used for delamination testing were impregnated with HexFlow® RTM6 epoxy resin using resin transfer moulding (RTM) to ensure a consistent nominal thickness of 6 mm across all specimens. The moulding was carried out in a heated square cavity with dimensions of 200 × 200 × 6 mm (Figure 3-12b) using an Isojet RTM injection piston as shown in Figure 3-12a. The piston inside the heated barrel, with a volume of 3 litres, pressurises the resin through a heated pressure cell and a pipe inside the mould cavity. The temperature of the barrel, pressure cell and the pipe are adjustable and were adapted to the data sheet recommended injection temperature of 80 °C for the RTM6 resin.

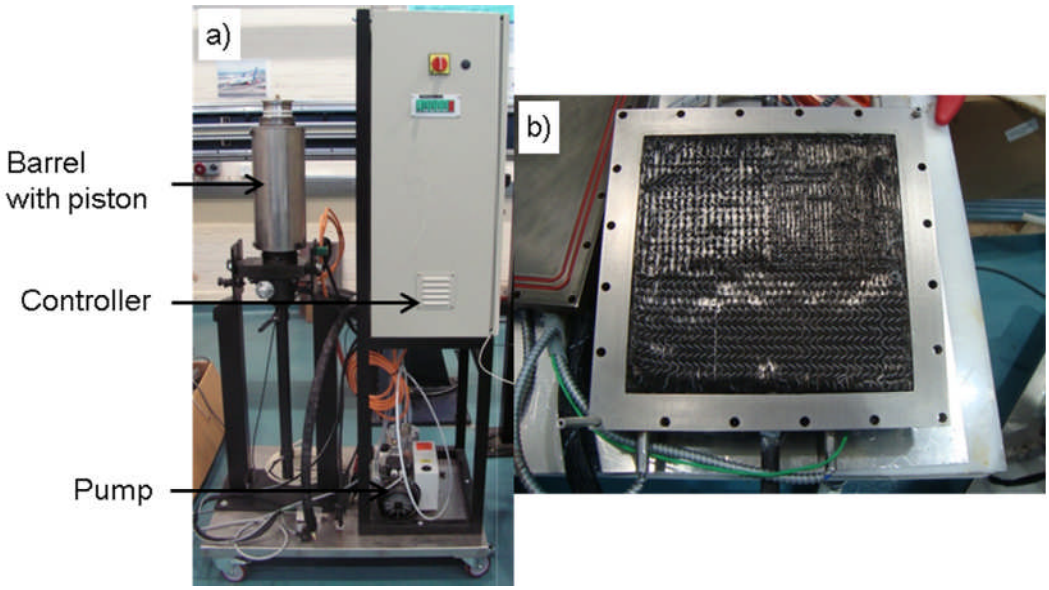

Figure 3-12 a) Isojet RTM piston and b) RTM mould with 6 mm thick metal frame.

The injection and cure cycle followed the resin system data sheet. After application of vacuum with the pump (Leybold Sogevac SV-10 16B) (Figure 3-12a), the injection started with a relatively slow flow of 500 cm^3/min in order to remove trapped air in the mould until a pressure of 2 bar was reached. This pressure was then utilised during the injection and the temperature was kept at 80 °C in the piston and 120 °C in the mould. Before the plates were cured at 160 °C for 75 min upon completion of impregnation the outlet valve of the mould was closed and the pressure was increased to 4 bar. The temperature of the upper and lower mould halves is controlled by an extra controller, independently of the piston controller. Finally, the plates were de-moulded and cured at 180 °C for 120 min freestanding in a fan oven (Binder GmbH, Klasse 2.0). Figure 3-13 shows the interface used for the RTM injection. The software allows setting the temperatures for the barrel, pressure cell and pipe independently and also shows the actual temperatures. Similarly, the pressure and the flow rate for the injection can be set and are displayed on the panel, changing the speed the piston moves. By choosing the auto transition function the software starts injecting the resin according to a pre-set flow rate up to a pressure limit. Once the pressure limit is reached it is maintained and the injection is pressure controlled. Simultaneously, the vacuum applied by the pump, connected to the RTM controller, is measured consistently giving an indication of the vacuum level.

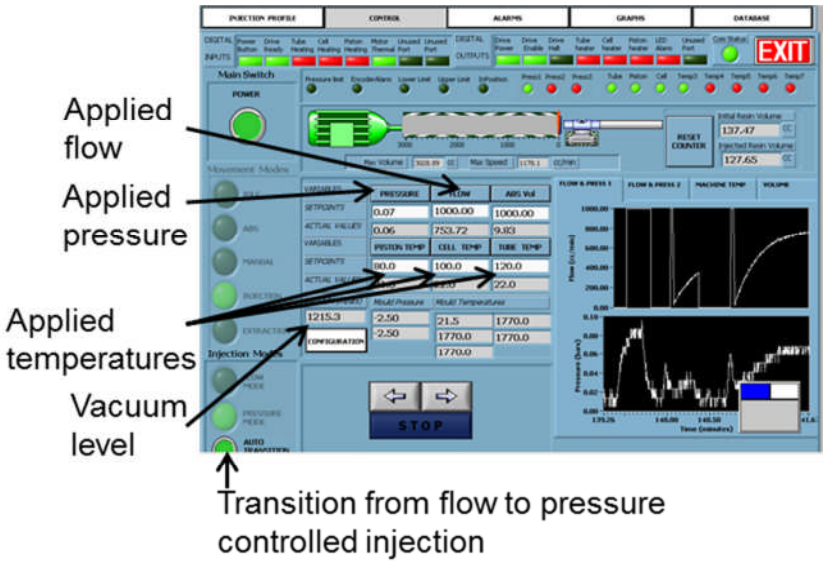

Figure 3-13 User interface for RTM injection.

The highly bindered preforms and the electrical testing preforms were infused in a fan oven (Caltherm Ltd.) via vacuum assisted resin transfer moulding (VARTM) with RTM6. The preforms were laid between two layers of peel ply (VAC Innovation Ltd., N85PS-x) to facilitate the separation of the panel and the mould plate on the bottom and a flow media on top. The flow media was made of PTFE and is suitable for high temperature infusions. Another layer of peel ply was laid between the flow media and the vacuum bag to prevent piercing of the bag by the flow media. Figure 3-14 shows two panels, for electrical testing, being infused simultaneously. The mould plate was heated to 120 °C, whilst the resin was heated to 80 °C and degassed for 45 minutes. The inlet pipe for the infusion was laid along the edge of the each panel, whilst through the outlet pipe at the other end of the mould plate a negative pressure of 1 mbar was applied using a pump (Leybold Sogevac SV40). The cure cycle followed the resin data sheet.

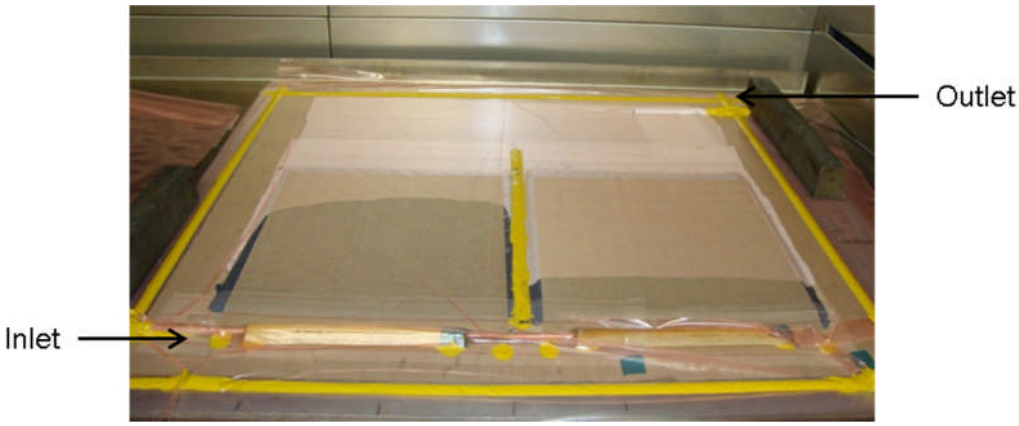

Figure 3-14 Simultaneous VARTM of two panels used for electrical testing.

3.2.5 Cutting and introduction of loading blocks

The plates were cut to the appropriate double cantilever beam (DCB) specimen dimensions (170 × 20 × 6 mm), using a diamond impregnated saw blade (Crandon 60/85), with the specimen longitudinally aligned to the fibre direction. The specimen ends with the crack starter film were trimmed off in order to reduce the film length to 61 mm leading to an initial crack length of about 50 mm considering the load line of the loading blocks. Before bonding the loading blocks to the specimens, the corresponding specimen surfaces were roughened with abrasive paper and, subsequently, cleaned with acetone. The aluminium

loading blocks (15.5 × 20 × 8 mm) were adhesively bonded to the specimens using the two component epoxy adhesive Huntsman Araldite® 420 A/B. The specimens were placed in a fan oven at 50 °C for 4 hours to cure the adhesive as stated in the data sheet [281].

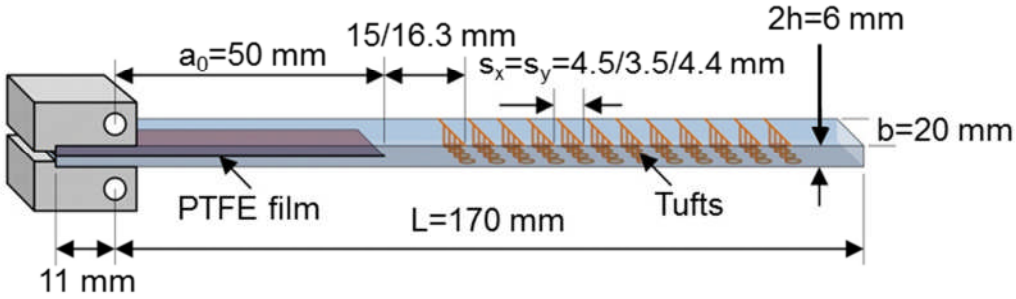

Figure 3-15 Schematic of the manufactured DCB specimens.

The geometry of the DCB specimens produced is shown schematically in Figure 3-15. The total length, width and thickness of the specimens were approximately 170 mm, 20 mm and 6 mm, respectively. The distance from the end of the crack starter film to the first tuft row was 15 mm for vertical and 16.3 mm for inclined tufts (at specimen's top surface).

The panels manufactured for lightning strike tests were trimmed along the edges in order to obtain a final size of 320 × 320 × 4 mm. Electrical conductivity tests were carried out on small coupons (20 × 20 mm) cut out of undamaged sections of lightning strike panels after testing. The electrically insulating resin rich layers on top and bottom surfaces were removed using 2400 grit paper without damaging the tuft seams and loops and the copper mesh in order to establish good electrical contact with the electrodes in conductivity measurements (Figure 3-16).

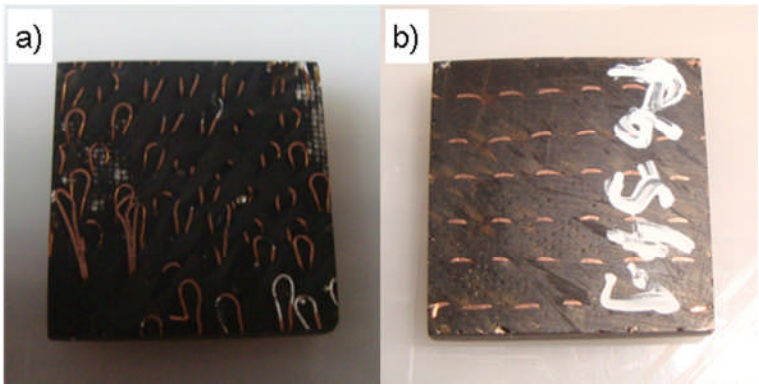

Figure 3-16 Copper tufted specimen: a) loop side and b) seam side.

3.2.6 Preparation of microscopy specimens

3.2.6.1 Delamination test specimens

Sections of the tested delamination testing half beams were analysed under optical and scanning electron microscopy (SEM) to identify the failure mechanism of tufted specimens. For SEM (Philips, XL 30 SFEG) delaminated half beams were cut in squares of 10 × 15 mm and coated by sputter deposition (Polaron Equipment Ltd., E5100) of a thin layer of conductive gold alloy. The optical microscopy (Nikon stereo microscope, Nikon Eclipse ME600) was carried out on entire half beams without any treatment in order to obtain a broader impression of the fracture surface compared to the SEM.

3.2.6.2 Lightning strike specimens

After the lightning strike tests areas with high surface damage were covered with a two component epoxy resin in order to maintain the damage after these sections were cut out (Figure 3-17). Such damaged sections and undamaged areas were cut out at a size of 10 × 10 mm and fully embedded in Struers Ltd. EpoFix resin and hardener (ratio of 100:12 by weight). After cure for 24 hours at room temperature the surfaces of the coupons were ground off up to the surface of interest using 1200 and 2400 grit silicon carbide paper and polished with 9 µm diamond spray.

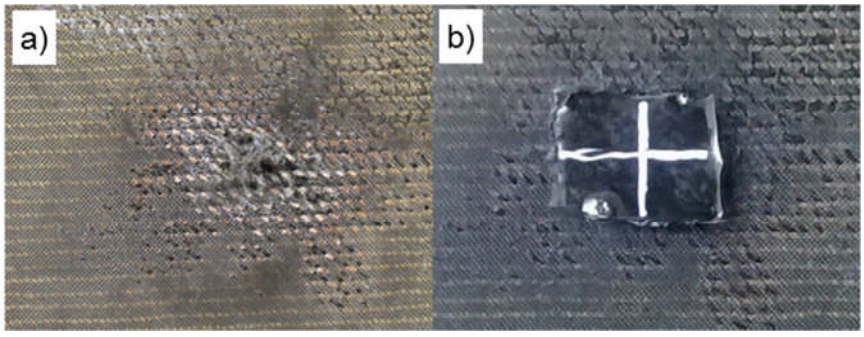

Figure 3-17 a) Damage after lightning strike and b) same damage embedded in resin.

3.3 Testing methods

3.3.1 Tufting thread tensile tests

Thread tensile tests were carried out using a screw driven electro-mechanical Zwick Z010 testing machine equipped with a 2 kN load cell. Five specimens of

each material and each impregnation state were tested. The thread ends were wound around two radiussed steel clamps with a radius of 25 mm in order to reduce the stress concentration at the clamps as shown in Figure 3-18.

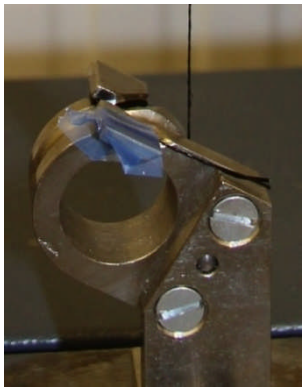

Figure 3-18 Radiussed clamp for thread tensile test.

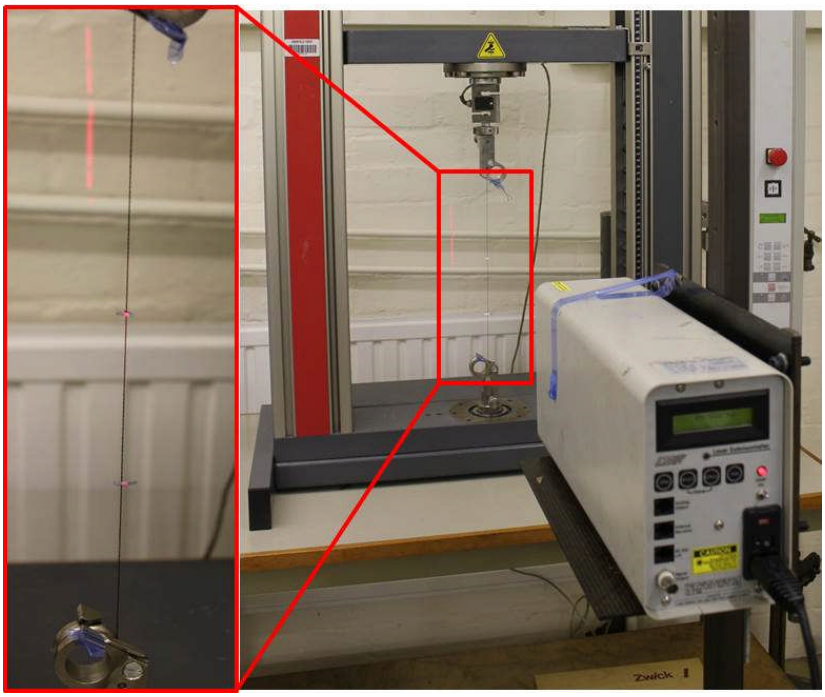

Figure 3-19 Testing setup for thread tensile test.

The tensile tests were based on the British Standard BS ISO 3341:2000 using a displacement controlled crosshead displacement of 1 mm/min, simulating the test speed of standard mode I delamination tests. The threads were wound only one time around the clamps to avoid slippage during the tests which could lead to fluctuating load-displacement curves. The initial gauge length between the clamps was 300 mm. During testing the load was recorded by the testing machine, while the displacement was measured by a laser extensometer (EIR

LE-05). Therefore, two strips of reflecting tape were attached to the threads with an initial gauge length of approximately 90 mm. Figure 3-19 shows the testing setup.

The axial thread stress was calculated by dividing the recorded loads F by the nominal cross sectional area A_{th} which was determined by means of the linear weight of the thread and its fibre density. The strain was calculated by dividing the recorded displacement by the initial gauge length between the reflective tape strips.

3.3.2 Delamination testing

The DCB specimens were painted white and marked every millimetre on one side in order to record the crack length. The mode I tests were carried out on an electro-mechanical Zwick Z010 test machine with the same load cell as the thread testing using a crosshead displacement of 1 mm/min. The test procedure followed the British Standard BS ISO 15024:2001. During the tests the applied loads and crosshead displacements were recorded automatically and the crack length was determined visually by means of a magnifying glass and recorded regularly alongside the corresponding load and displacement. The specimen thickness of 6 mm for most specimens and 4 and 8 mm for highly bindered specimens was chosen in order to avoid the fracture of a half beam by bending due to the reinforcement by the tufts, whereas the recommended thickness (3 mm) in the standard refers to unreinforced specimens.

The initiation fracture toughness was determined using the 5%/max point, considering the initial compliance C_0 and the compliance equal to $1.05 \cdot C_0$ in the load-displacement curve. The corrected beam theory (CBT) was used for the data reduction. According to BS ISO 15024:2001 the critical energy release rate G_{Ic} can be calculated by:

$$G_{Ic} = \frac{3Fd}{2b(a + |\Delta|)} \frac{B}{Q_c} \qquad \textbf{3-4}$$

where F is the applied load, d the displacement at load line, b the specimen width, a the total crack length, Δ the linear fit intercept, B the correction factor for the reduction of the lever arm at large displacements due to rotation at the

end of the specimen and Q_c the correction factor compensating the rotation at the delamination front due to asymmetrical specimen clamping and stiffening and rotation of the specimen due to the loading blocks. By plotting $\sqrt{\frac{C}{Q_c}}$, where C is the compliance, versus crack length a, a linear fit through the data can be drawn to estimate Δ. If the value of Δ is positive, it can be considered to be zero. Both B and Q_c correction factors depend on d, a, l_1 and l_2, where l_1 is the distance from the centre of the loading pin to the mid-plane of the specimen and l_2 the distance from the load line to the end of the loading block facing the specimen centre. It is important to note that the load line in this study was eccentric to the loading block

3.3.3 Lightning strike testing

In general, lightning strike tests aim to reproduce the effects of natural lightning strikes considering the high current, voltage and duration of strikes. The lightning strike tests were carried out at Cobham Antenna Systems, Lightning Testing Services, Abingdon, UK. Figure 3-20a shows the testing setup and the current path of a typical lightning strike test.

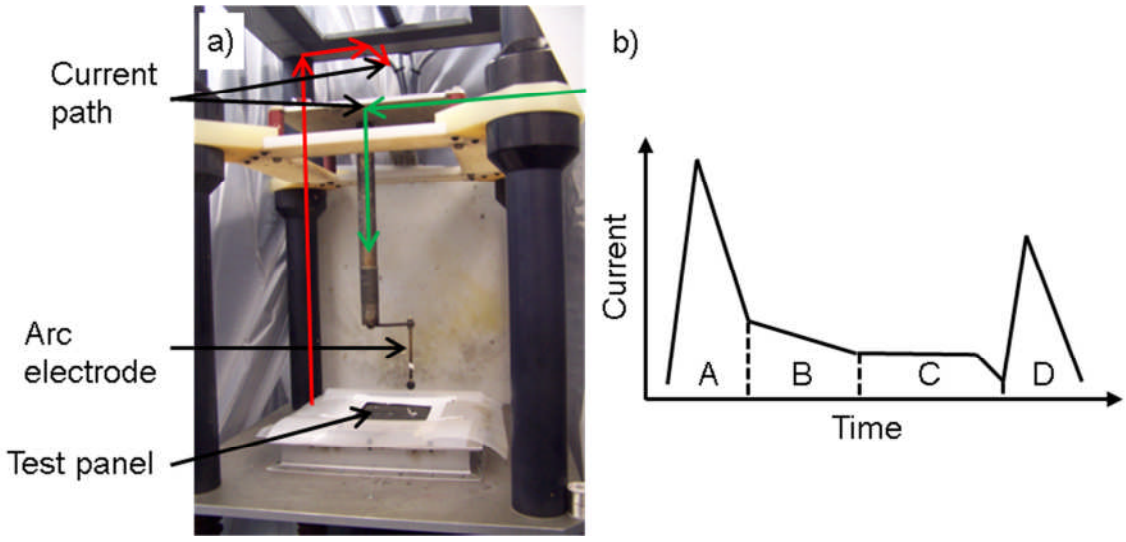

Figure 3-20 a) Lightning strike test rig and b) components of current waveform, adapted from [282].

All ten specimens were subjected to simulated Zone 2A lightning strikes, comprising three current components: the slow waveforms B and C and the fast

waveform D (Figure 3-20b). Component B has an average current amplitude of 2 kA with a maximum duration of 5 ms. This is followed by component C with a current amplitude of 200 – 800 A and a duration of 0.25 – 1 s. Component D is considered as the restrike current reaching approximately 100 kA with a duration of maximum 500 µs [282].

The test results include the maximum applied current I, the charge Q and the action integral E which represents the ability of the current to deliver energy dependent on the duration t. The action integral is calculated as follows:

$$E = \int_0^T I\,(t)^2 dt \qquad \textbf{3-5}$$

The action integral is of importance since the energy delivered by the current includes both high currents occurred for short time and low currents occurred for long time, both leading to damage of the composite structure.

3.3.4 Ultrasound scanning

After the lightning strike tests the panels were analysed for internal and surface damage using ultrasound C-scanning (Structural Diagnostics Inc., Model 3510). Each panel was immersed in a water bath. The entire panel was scanned with a probe (2 – 10 MHz) inside the water, facing normally to the damaged surface (Figure 3-21).

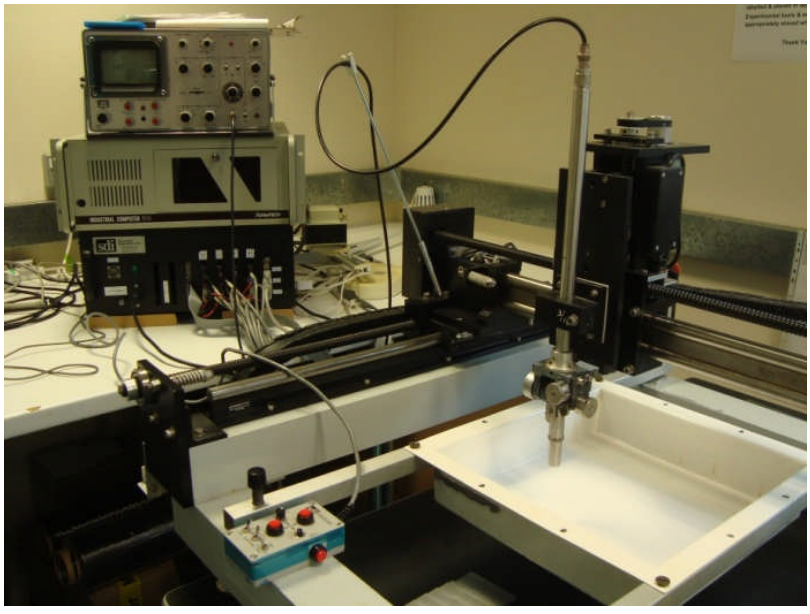

Figure 3-21 Ultrasound scanning equipment.

The resolution was 0.25 × 0.25 mm. The general settings had to be adjusted to every tufting thread material and panels with only a tufted square section in the centre had to be scanned twice: the entire panel to scan the untufted region and the tufted central section with different settings.

3.3.5 Electrical conductivity

The electrical conductivity tests were performed using an in-house built testing rig. The specimens were clamped between two sheets of copper foil with dimensions of 50 × 50 × 0.01 mm. The low thickness of the foil allowed adapting it to the waviness of the specimen surfaces increasing the contact area and improving the iso-potential condition of the specimen face. The foils were placed between two wooden squares and copper cylinders and were connected to the current source (Keithley 6220) and the nanovoltmeter (Keithley 2182A) as shown in Figure 3-22. The two copper cylinders were electrically insulated by the rest of the assembly using Kapton film, whilst the arrangement allowed fixing the cylinders at an adjustable distance.

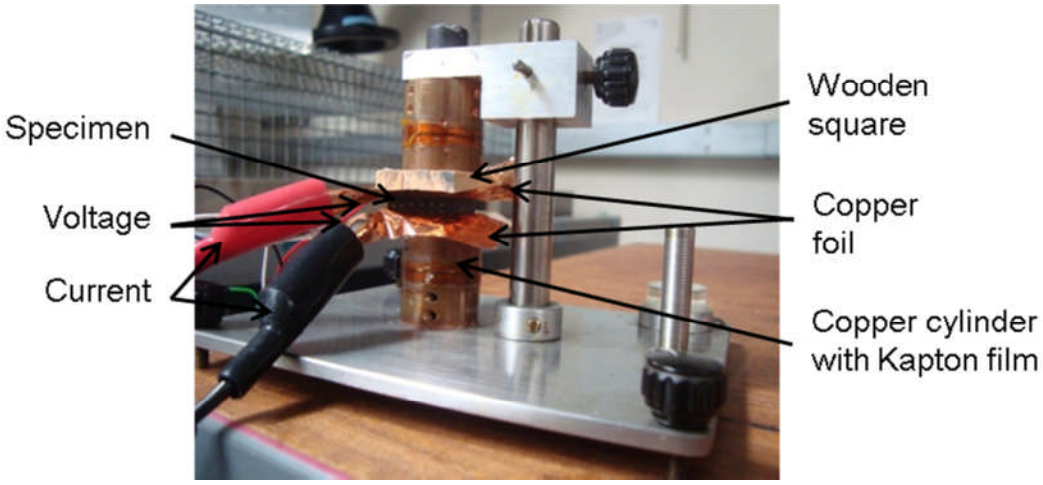

Figure 3-22 Testing setup for electrical conductivity measurement.

The electrical test data were collected using an in-house software interface implemented in LabVIEW. The current source is connected to a PC using a general purpose interface bus (GPIB) interface, whilst the nanovoltmeter and current source are also connected and operate together in Delta mode. This allows application of a sequence of currents of opposing polarities to eliminate any thermoelectrical contributions at contact points. The source current is set by

the user and the LabView software calculates the resistance using the current level and measured voltage. In these tests, the current was initially set at the minimum value (0.001 μA) and then increased gradually until the resistance measurement was stabilised. The stabilisation occurred at a current level that was typically 1,000 – 10,000 μA. The conductivity σ was calculated using the measured resistance R, the specimen surface area S and the thickness t_l as follows:

$$\sigma = \frac{t_l}{RS} \qquad \textbf{3-6}$$

Measurement of the thread conductivities was also carried out. This was performed by connecting two ends of a 2 m long piece of thread to the setup and measuring the resistance. In this case the thread cross sectional area was used as the surface area and the specimen length as the thickness in Eq. 3-6.

4 Manufacturing of a complex structure using tufting

4.1 Introduction

The applications of tufting have so far been limited to flat panels for research purposes as well as for industrial application to reinforce the crash box of the Mercedes SLR [256] and the landing gear braces of the Boeing 787 Dreamliner [277]. Work within the European project ADVITAC [279] has addressed the use of this technology in a complex aerospace structure for joining stiffeners to a curved composite skin. This project dealt with the design and manufacture of a composite tail cone for a business aircraft aiming to produce a lightweight tail cone by reducing the weight of the structure using composite materials and by avoiding the use of metal fasteners, leading to lower CO_2 emissions. In addition, the goal was to reduce the overall costs by decreasing the weight and integrating an automated manufacturing process. A consortium comprising several organisations (Daher Aerospace, Coriolis Composites, Embraer, Honeywell, Recomet – Impex, NLR, Free Field Technologies, Inasmet - Tecnalia) worked together to carry out the design, manufacture and testing of the tail cone which included ten Ω–stiffeners joined to the skin.

The skin was manufactured, using bindered carbon tapes and automated dry fibre placement (Figure 4-1a), by Coriolis Composites. The ADFP technique uses sets of narrow slit tapes to produce the preform by means of robotic deposition. The deposition process is combined with consolidation due to the action of heat and pressure on binder pre-dispersed in the fibre tows as shown in Figure 4-1b. The incorporation of tufting in this structure gave the opportunity to adapt current tufting technologies for addressing composite structures involving large size, curvature and a certain level of manufacturing and functionality complexity. The outcome of this activity was a set of refined objectives leading to an overall aim of exploiting tufting in advanced aerospace structures. This chapter describes the developments of the manufacturing process necessary for implementation of tufting in such a complex case as the tail cone, reports the results of the manufacturing activity and identifies the

knowledge gaps that need to be addressed to allow design of integrated components that use this technology.

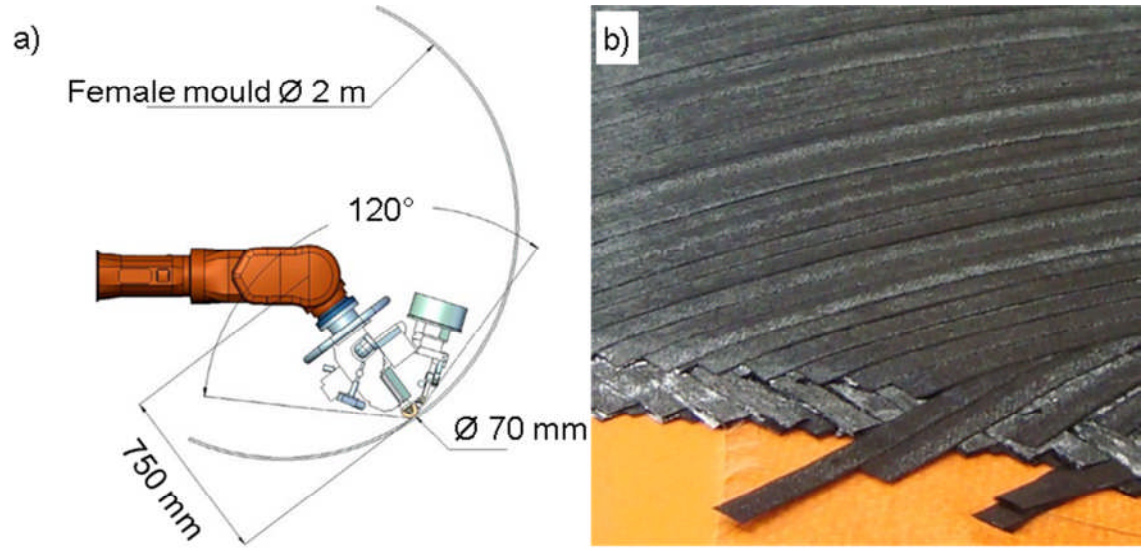

Figure 4-1 a) Schematic of the ADFP deposition head, adapted from [258] and b) skin on tool of the tail cone.

4.2 Task description and challenges

The task of the Enhanced Composites and Structures Centre at Cranfield University was to use the process of tufting in order to reinforce all stiffener-skin joints along the stiffener flanges and increase the performance of the skin-to-stiffener interface to a sufficient level to replace traditional mechanical fasteners. The tail cone, which is shown in Figure 4-2, had a length of 2.5 m, a maximum height of 1.9 m and a width of 1.4 m. Including the support with the axes to rotate the tail cone, the total length was 4.2 m. The shape of the tail cone changed from an almost circular cross section with a diameter of 1.5 m at the rear to an elliptical cross section with a major axis of 0.65 m and a minor axis of 0.3 m at the front, with irregular curvatures along the length. The tail cone incorporates ten carbon composite Ω-stiffeners which are attached to the skin inside the tail cone with different distances to each other. Each stiffener has two flanges (marked in red in Figure 4-2) of different length; the maximum length is 2 m, whilst the shortest flange is 1.2 m long, following the curvatures of the tail cone skin in each direction. Each flange needed to be tufted with two tuft rows from rear to front following the shape and curvatures of the flanges and

skin. However, due to the size and shape of the tail cone the robot was able to reinforce three stiffeners, before a manual rotation of the tail cone was needed to reach the other stiffeners (Figure 4-3a, b). The rotational system with the front and rear axis was designed by Recomet – Impex to facilitate ADFP and tufting. To reach the three stiffeners the robot was placed on a plinth with a height of 1.5 m (Figure 4-3c), designed to withstand the loads of the robot with the relatively high lever arm due to the height of the structure.

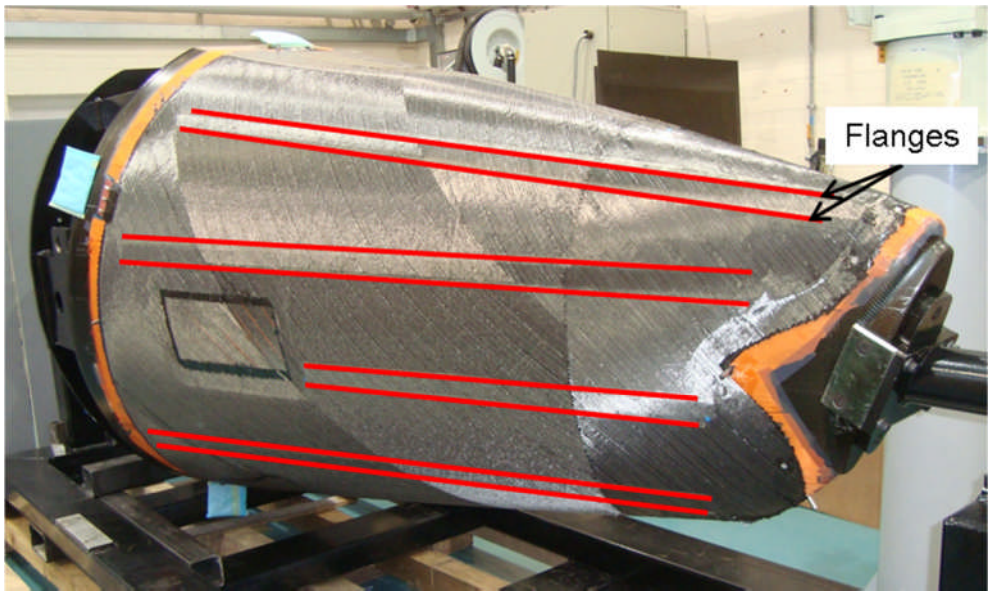

Figure 4-2 Composite tail cone with reinforced Ω-stiffeners marked in red.

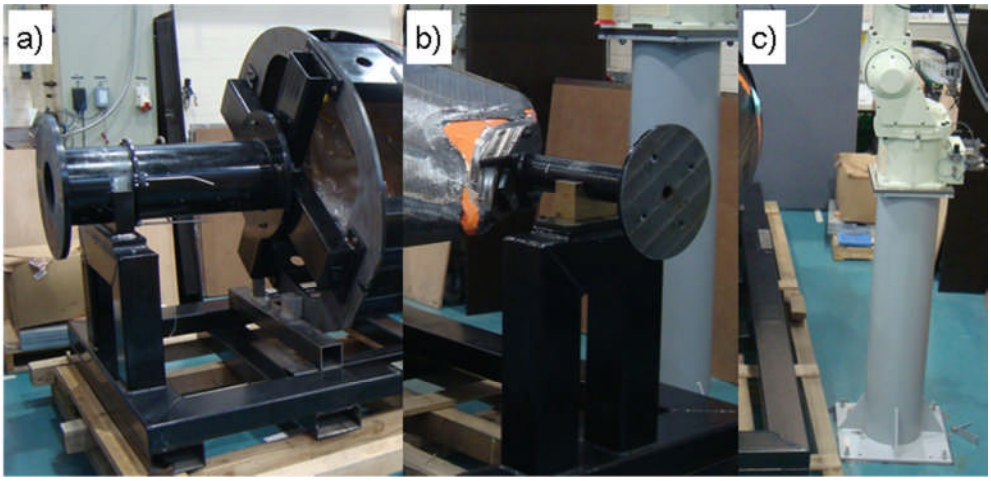

Figure 4-3 a) Rear rotational axis, b) front rotational axis and c) plinth for elevated position.

In order to reinforce the stiffener flanges, the following main challenges needed to be addressed:

- Selection of backing and tuft material:
  Early stages of this activity dealt with tufting trials to source the tufting support material, such as silicon or thermoplastic foam which is placed inside the flanges, and the tuft thread, such as aramid, carbon or glass. The trials led to the conclusion that the thermoplastic foam and aramid thread are the most suitable materials for tufting in conjunction with the preform material for this application.
- Implementation of blind tufting:
  The stiffeners are attached to the skin inside the tail cone making them invisible on the outside surface. Tuft insertion points were generated using a CAD-file of the tail cone with the exact position of the stiffeners, their coordinates and vectors exported and transformed into the robot coordinate system. The robot was able to move to the corresponding tuft locations for tuft insertion.
- Application of tufting on a doubly curved surface:
  The tufting end effector changed its inclination for every tuft to be inserted according to the imported vector coordinates, following the double curvature of the tail cone, to tuft parallel to the groove walls of the flanges preventing damage to the needle and the tool.
- Application of tufting to a structure with variable thickness:
  The tuft length had to be adapted to the skin and flange thickness in order to obtain a uniform loop length preventing tuft pull-out due to a too short loop length. The variable thickness led to irregular curvatures along the tuft rows affecting the coordinates of the tuft insertion points.
- Use of tufting with a bindered material:
  The large amount of binder in the preform exacerbated the insertion of the tufting needle and thread leading to damage to the preform, needle and thread. Heating up the preform before tufting softened the binder material and facilitated the tuft insertion.
- Implementation for a large axisymmetric structure, exceeding 2.5 ×1.4 × 1.9 m in dimension:

Due to the size of the tail cone the robot had to be moved on a plinth of 1.5 m height in order to enlarge the envelope of the robot. All ten stiffeners were tufted in several stages by manually rotating the tail cone.

- Process automation:
  A software routine was developed to address the automated reinforcement of the complex shaped flanges. The code controlled the robot movement for tuft insertion points and setting of the corresponding inclination of the tufting needle to insert the tufts and dealt with the necessary coordinate transformations allowing translation of CAD based point and vector coordinates to the current position of the tail cone in the manufacturing setup.

4.3 Process development

To overcome the obstacle of the large size of the tail cone a CAD-file (CATProduct in CATIA V5) of the entire tail cone was utilised to design a plinth to ensure a larger envelope of the robot arm (Figure 4-4). This was carried out by simulating the robot used for tufting according to the real robot dimensions, degree of movements and range of each joint and placing it next to the tail cone. The plinth was designed to a particular height, to ensure that the robot was able to tuft a maximum amount of stiffeners, maintaining a high tuft quality in terms of inclination, depths and following the curvatures of the flanges and skin, without rotating the tail cone. The new plinth with a height of 1.5 m had a circular cross section with a diameter of 330 mm, corresponding to that of the robot, and was welded to a square plate with dimensions of 600 × 600 × 15 mm. The welded joint was reinforced by four triangular webs with an angle of 60°. The robot was mounted with four M16 bolts on a top square plate with dimensions of 400 × 400 × 15 mm, welded to the main body of the plinth. The entire plinth was made of S275 steel and fastened to the floor with eight M16 resin anchored bolts in order to withstand the high moment generated by the robot in fully outstretched position. Appendix A shows the detailed drawing of the plinth.

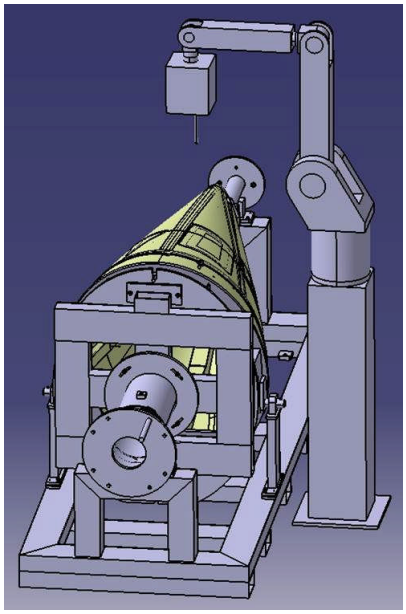

Figure 4-4 CAD-file of tail cone and robot on the new plinth.

Each flange had to be reinforced by two tufting rows using the aramid tufting thread introduced in section 3.1.1. Consolidated ADFP preforms are not as easy to tuft as standard, unbindered materials as the limited mobility of the fibres hinders the insertion of the tufting needle. This limits the grades of suitable thread to the strongest, as brittle filaments tend to break upon insertion [258]. Each flange groove was filled with thermoplastic polyvinylchloride (PVC) foam (Airex® R63), presented in section 3.2.3, which was determined to be a suitable support material for the tufting loop [258]. In general, foams for the tufting loop creation are removed after the tufting process and prior to resin infusion as they can soak the resin and add significantly to the weight of the entire structure without affecting its mechanical properties.

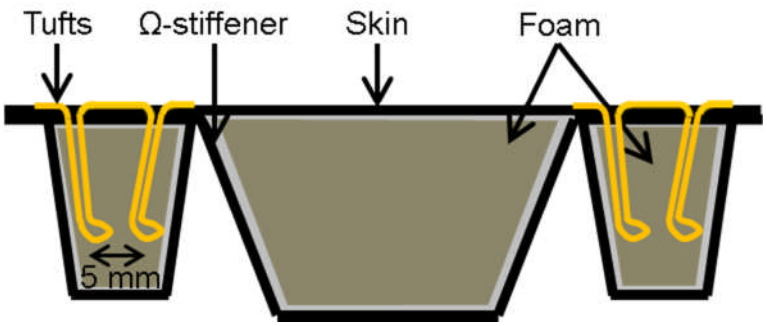

Figure 4-5 Schematic of the cross section of Ω-stiffener.

The cross section of a flange and its groove correspond to a trapezium with the bottom surface being smaller than the top surface (skin). The tuft pitch was 5 mm and each tuft row was placed 2.5 mm away from the centre line of the bottom surface, as shown in Figure 4-5. Due to the double curvature of the stiffeners the inclination of the tufting needle in two directions is crucial. The tufts have to be inserted parallel to the walls of the stiffener grooves (y-z-plane) and normal to the skin surface (x-z-plane) in order to avoid contact with the walls of the tool which could lead to potential damage of the needle and the tool. An incorrect inclination may also lead to the pull-out of previously inserted tufts, since the pressure foot would not be holding the tuft seam in place.

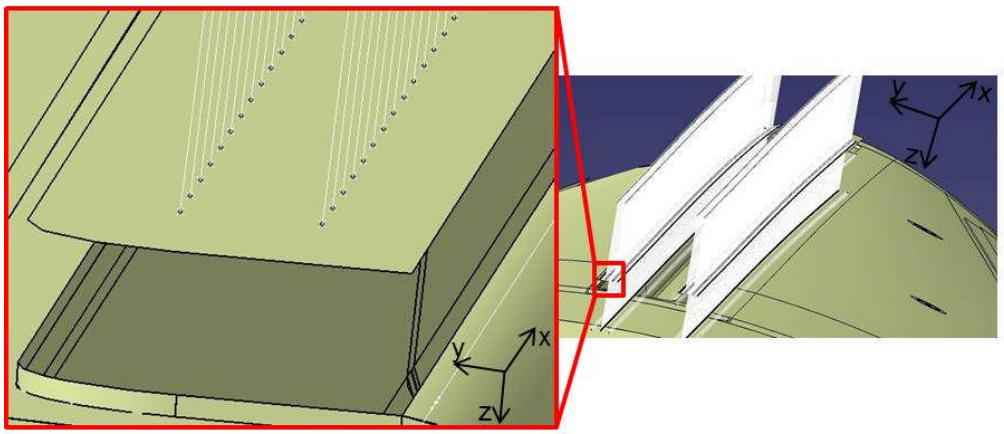

Figure 4-6 Tuft insertion points with vectors.

A CAD drawing of the tail cone including the stiffeners and their exact locations was used to overcome the obstacle of invisible stiffeners and inclined tufting and to ensure a regular tuft insertion with uniform tuft depth and angle. Therefore, the location of every single tuft had to be known before starting the tufting process. The CAD software used for this activity was CATIA V5. The stiffener surface was projected to a distance of 5 mm, mimicking the skin with a thickness of approximately 5 mm and curvatures equivalent to the stiffener surface. Using a macro (Appendix B) points and vectors were generated on the skin at every tuft insertion location with the vectors intersecting the points parallel to the walls of the stiffener grooves and normal to the skin surface (Figure 4-6).

The tail cone had several marked locations on the outer surface of the skin, with known coordinates in the CAD-file. These points, such as those are shown in

Figure 4-7, were utilised as reference locations for the necessary coordinate transformations. The tufting needle was driven to at least four known reference points after each rotation or relocation of the tooling assembly. The coordinates in the robot coordinate system were read and calibrated with those of the CAD coordinate system. By means of the virtual and real coordinates a coordinate transformation was carried out, using an in-house code developed via VBA (Appendix C) which calculated the rotational matrix and the angles in x, y and z-direction.

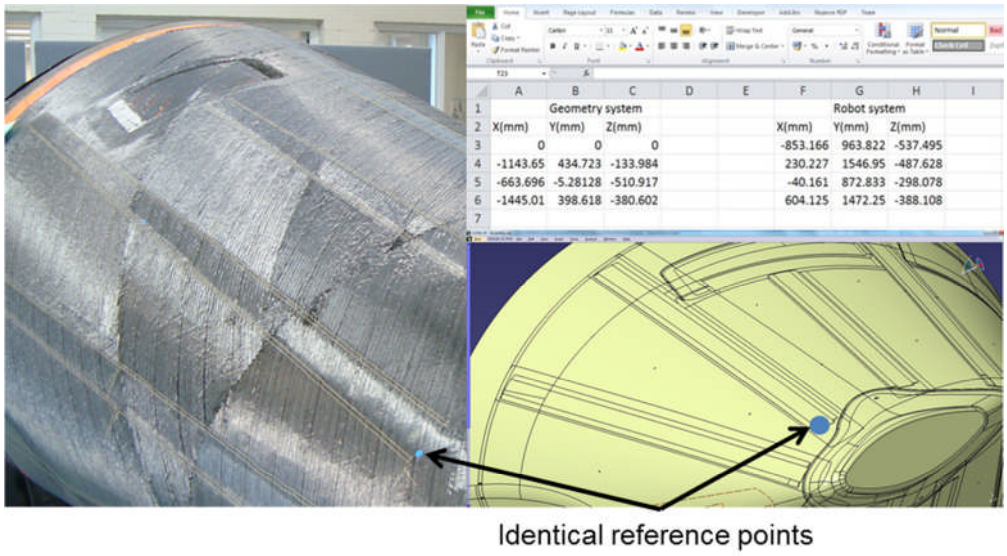

Figure 4-7 Identical reference points on real and virtual structure with corresponding coordinates in MS Excel.

The entire set of coordinates of the tuft insertion points, vectors and reference points (Figure 4-6) were extracted and imported into MS Excel. Using the in-house developed VBA routine and the computed rotational matrix and angles all exported coordinates of the tuft insertion points and vectors were translated into the robot coordinate system. The robot subroutines and commands were upgraded (Appendix D) for tracking the spatial movement of the robot on the basis of the coordinates generated by the CAD-file (Figure 4-8). The VBA routine calls the robot user interface “KCWin” and writes the corresponding commands to drive the robot. A calibration of the virtual and real reference points had to be carried out after each rotation of the tail cone. This increased the time and effort required for the process and also increased the probability of errors in the coordinate transformation process.

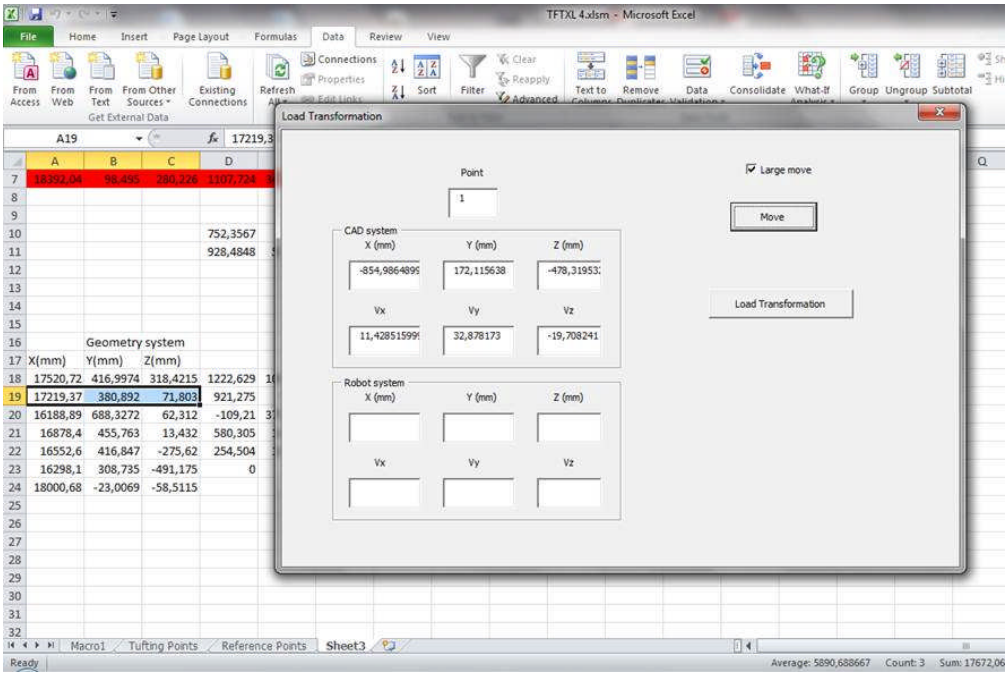

Figure 4-8 Coordinate transformation and interface for automated tuft insertion.

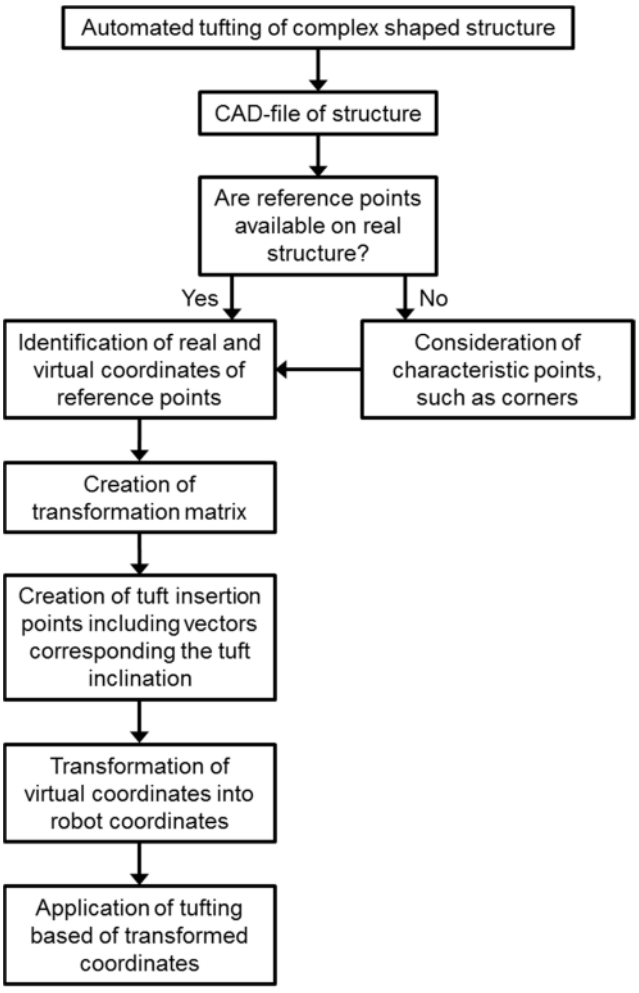

Figure 4-9 Flow diagram for tufting procedure of complex shapes.

The construction of the tufting head and the motor power to drive the needle shaft did not facilitate insertion through the highly bindered material. Repeated insertion led to blunting of the needle tip which further hindered the process. Thick areas were more difficult to tuft requiring manual facilitation of the needle insertion process by placing an infrared heating bulb. The heat partially activated the binder softening the preform facilitating the needle insertion. The heating source was moved manually according to the tufting head location.
The procedures described here were necessary to overcome the challenges described in section 4.2. The flow diagram in Figure 4-9 illustrates these required steps in order to enable the automated tufting of complex shapes.

4.4 Results and discussion

The routine developed (Appendix B to Appendix D) enabled automated blind tufting of complex shapes to be carried out; the robot moved to the tuft insertion locations given by the routine and adapted its inclination according to the walls of the grooves. Furthermore, curvatures present in the virtual structure were followed on the real structure. However, the low motor power did not allow fully automated tuft insertion controlled by the developed routine which was facilitated by manual operation.
On average each tufting row had approximately 550 tufts, leading to 2,200 tufts per stiffener, or 22,000 tufts in total. After every single tuft insertion point was read by the subroutine, the robot moved automatically by 5 mm to the next tuft location and corrected its inclination according to the curvature. The stiffeners were placed in carbon composite moulds in order to stabilise and maintain them firmly before and during the tufting process. These moulds showed slight distortions at some locations caused during cure, leading to waviness in the stiffeners. These affected the tuft insertion since the needle could be damaged touching the mould. Therefore, pins were inserted into the flanges along the walls to identify the local depth of the tail cone and allow corrections to the tuft insertion points maintaining a certain distance to the walls as shown in Figure 4-10.

Figure 4-10 Insertion of pins to maintain distance to the walls.

The maximum length of approximately 2 m of the stiffeners was larger than the envelope of the robot; once the robot reached its maximum range the tail cone had to be moved in its longitudinal direction bringing the untufted sections within the envelope of the robot. Furthermore, after reinforcing three stiffeners the tail cone was rotated manually. After both the longitudinal movement and the rotation a coordinate calibration had to be carried out in order to find the new coordinates of already used or new reference points.

Softening the large amount of binder by partially activating it by means of a heating bulb required attention to avoid exceeding a certain temperature activating the binder material. This could have led to detachment of the carbon tows and deterioration of the integrity of the structure and tuft performance. Generally, loose tows may lead to misalignment of the tufts inside the structure and affect the tuft depth and loop length. The final outcome is shown in Figures 4-11 – 4-13 presenting the entire tail cone with tufted Ω–stiffeners. The inset in Figure 4-11 shows a reinforced stiffener incorporating a complex shape by changing the curvature at the centre. Figure 4-14 presents the tail cone after infusion and curing carried out at Daher Aerospace.

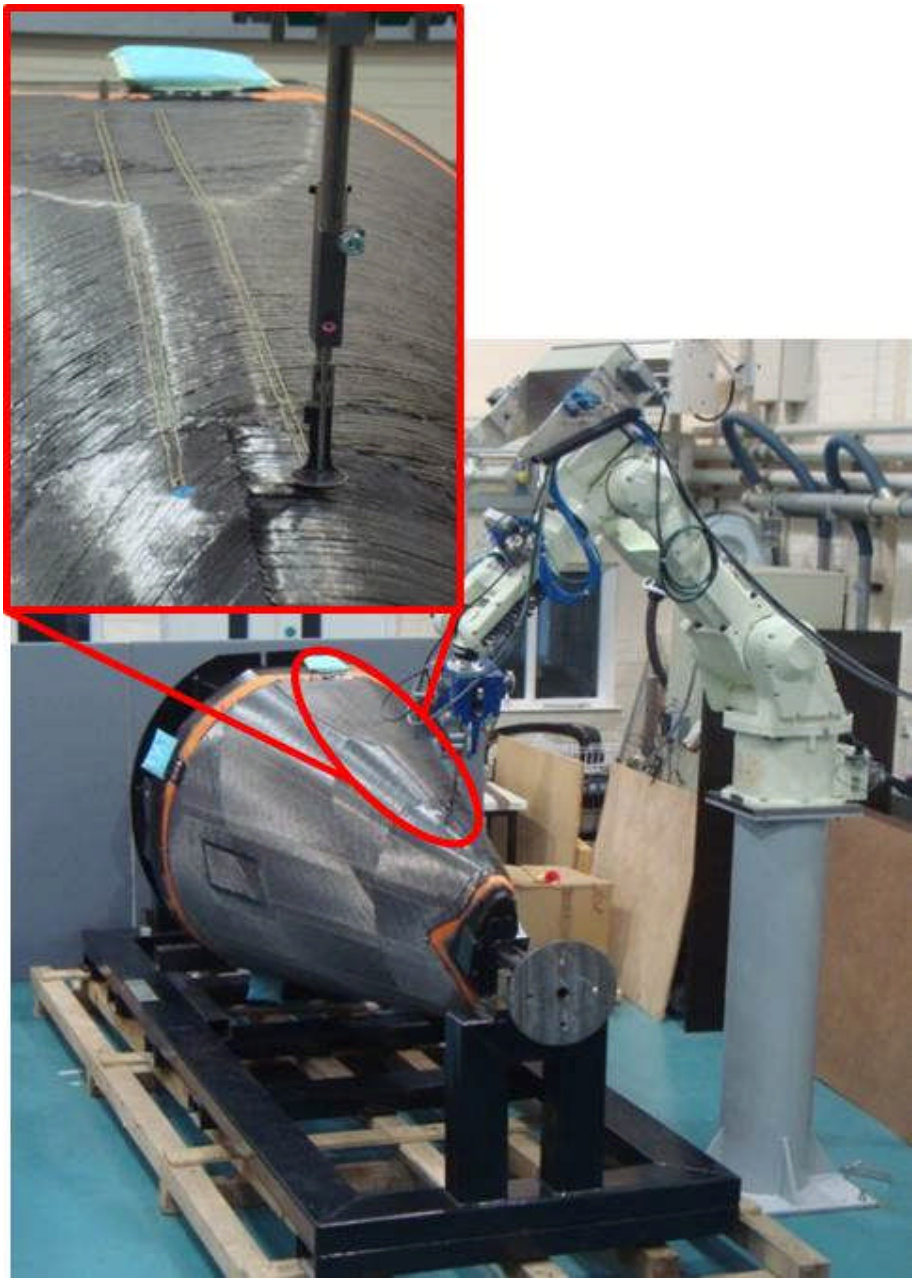

Figure 4-11 Tail cone with inset: reinforced skin-to-stiffener joint.

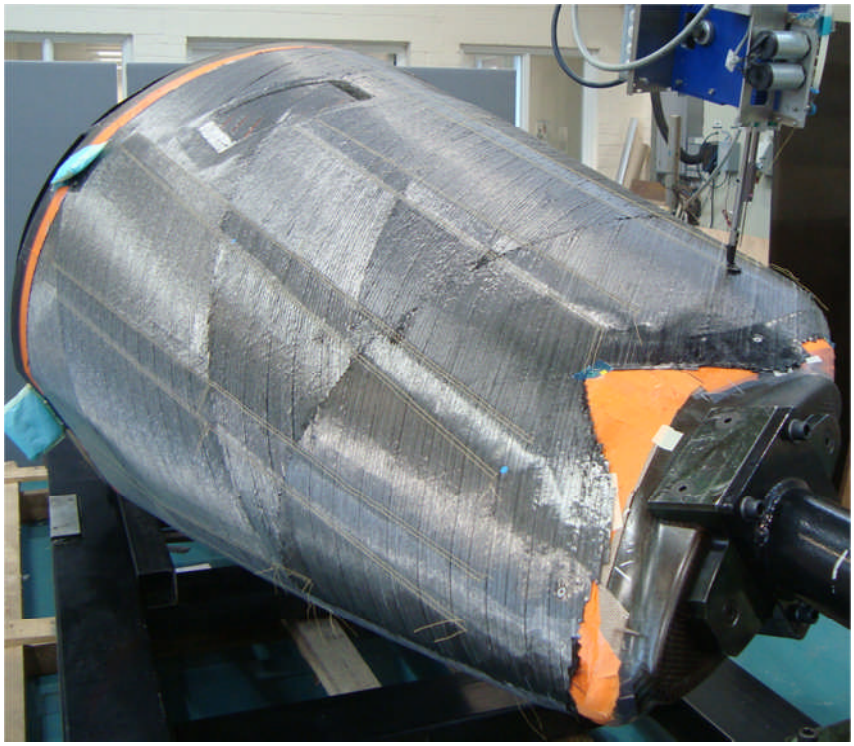

Figure 4-12 Side of tail cone with reinforced stiffeners.

Figure 4-13 Front view of tail cone with reinforced stiffeners.

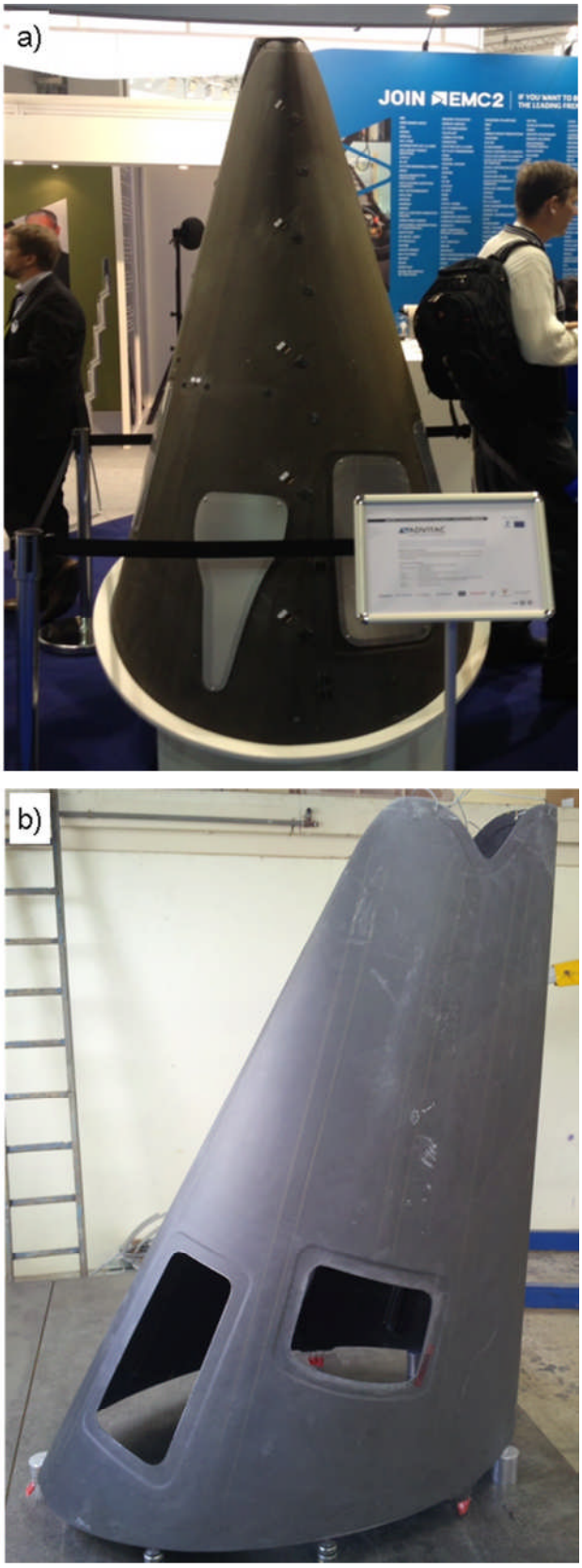

Figure 4-14 Cured tail cone: a) exposed at an exhibition and b) visible tuft rows on the skin. Courtesy of Daher Aerospace.

The cost involved in the tufting process of large composite structures and the additional weight must be considered alongside mechanical performance improvement. An average amount of 2,200 tufts per stiffener requires around 100 m of thread, assuming that 45 mm are used per tuft leading to 1 km of thread for the entire tail cone. This results in an increase in weight of 74 g and costs of £30 caused by the aramid thread only. Considering an automated tuft insertion with a tufting speed of 250 tufts per minute the time to insert all tufts is approximately 1.5 hours. The setting up of the structure and initial tool installation requires around 3 hours, whilst taking the relocations into account, due to the envelope of the robot, and the corresponding calibrations a duration of 7.5 hours can be assumed leading to a total operation time of approximately 12 hours. Assuming capital costs of £150,000 and a depreciation period of 10 years the costs will be around £100. For the entire operation two technical officers are required leading to further costs. However, the time for the CAD preparation has to be taken into account, which is assumed to be 2.5 hours per stiffener, i.e. 25 hours for the entire tail cone and additional costs for a CAD engineer and for software license and computing equipment.

4.5 Conclusions and research questions

The use of a CAD-file is essential in order to enable blind tufting of complex geometries to be carried out within the envelope of the robot. With the upgraded routines and commands it was possible to reinforce ten Ω–stiffeners using an automated tufting process, following the curvatures and known thickness variations. The high amount of binder limits the choice of tufting thread materials to the aramid thread which was able to withstand the resistance by the binder. In order to facilitate the thread insertion and reduce the resistance by the bindered fabric a heat source can be used activating the binder and softening the fabric. The low estimated costs and increase in weight show that tufting could be a good alternative to metal fasteners. As described in section 2.1 replacing 4,600 titanium fasteners with Z-pins resulted in weight and cost savings. Given that tufts have a similar weight to Z-pins and lower costs than metal fasteners the aramid thread may reduce the weight and costs of composite structures in contrast to metal fasteners. Furthermore, drilling holes

through the skin and flanges before attaching metal fasteners compromises the integrity of composite structures and deteriorate their mechanical properties. However, the mechanical properties of the stiffener flange-to-skin joint of the tail cone including metal fasteners have not been tested and cannot be compared to tufted joints.

Nevertheless, features, such as the high amount of binder in the preform, the double curvature of the structure and the associated tuft inclination and the varying thickness of the skin, lead to a number of research questions related to the effect of various parameters on the mechanical properties of tufted composites. A double curvature including constraints by the inclined walls leads to, partially, angled tufting. The effect of inclined tufts, with respect to the surface plane, has not been investigated in the literature. Usually, stiffeners are tested in pull-off to determine the strength of the skin-to-stiffener joint. The effect of inclined tufts on the delamination toughness can be determined by testing DCB specimens in mode I consisting of inclined tufts with different thread material. Knowing the effect of inclined tufts can optimise the reinforcement of structures by adapting to the direction of applied loads. The varying thickness is crucial to the tuft length. In addition, the effect of partially inserted tufts on the delamination toughness is not well investigated; fully inserted tufts are preferred in general since it is possible to control their length more accurately. Furthermore, fully inserted tufts and the surface loops assist progressive failure of the structure since the increased influence of snubbing may lead to thread ploughing into the composite prior to fracture during pull-out. However, if the loads applied to a structure are known the way in which the structure can delaminate can be determined. The tuft depth can be limited to reinforce the delaminating plies only; hence, the overall thickness of the structure can be reduced and the delamination toughness increased leading to savings of materials and costs.

The high likelihood of an aircraft being subjected to lightning strike leads to the requirement of improved protection for composite aerostructures. Apart from improving the mechanical properties of a composite tail cone, such a structure has to be protected against lightning strikes. In general, the electrical

conductivity of composites has to be enhanced by metal attachments, such as copper or bronze meshes. The incorporation of tufts for mechanical integrity purposes generates an opportunity for potential replacement of protection meshes or foils by tufting threads. Electrically conductive materials, such as carbon or metallic tufting threads can be inserted, to protect the composite structure in combination with the improved mechanical properties. This requires evaluation of the electrical behaviour and lightning strike response of tufted composites.

In subsequent chapters, a number of these research questions are addressed. These are as follows:

- Effect of laminate material on the tuft performance:
  The delamination behaviour in mode I using different preform materials, containing different amount of binder, and tufted with aramid thread is investigated.
- Influence of tuft material on tuft performance:
  The mode I response of laminates containing different tuft materials is evaluated.
- Influence of tuft depth on tuft performance:
  The mode I response of a laminate incorporating different tuft depths is evaluated.
- Investigation on the effect of tuft inclination on the tuft performance:
  Different tuft materials are used for inclined tufting and the behaviour in mode I delamination is investigated.
- Investigation on the effect of tuft material on the lightning strike performance of tufted structures:
  Panels tufted with a variety of tuft materials are tested against lightning strike protection and compared with actual lightning strike protection systems.

5 Influence of material on delamination behaviour

This chapter focuses on the effects of the tufting thread and composite material, introduced in Chapter 3, on the mode I interlaminar fracture toughness. The behaviour of the threads under tension is correlated with the influence of tufting on the delamination behaviour. Furthermore, the influence of tufting for different laminate systems is investigated as a function of the baseline toughness of the unreinforced material.

5.1 Effect of tufting thread material

5.1.1 Thread behaviour

Figure 5-1 illustrates the average stress-strain curves of the dry aramid and stainless steel threads as well as of the copper wire, using the cross sectional areas of the threads calculated by the ratio of linear weight and fibre density (section 3.2.3) and the gauge lengths, considering global displacements, presented in section 3.3.1. The average stresses were determined at specific strain increments using linear interpolation of the experimental datasets. The last point of each curve represents the average failure stress and strain at failure, including the error bars which show the spread in values for both stress and strain at failure for the five specimens. The stainless steel thread is stiffer than aramid, but has lower load carrying capability. Both the aramid and stainless steel threads have a relatively high strength compared to the copper wire. However, the copper wire shows a typical ductile behaviour with a high strain at failure. Table 5-1 summarises the key properties of the thread materials. The elastic moduli for aramid, stainless steel and copper are calculated by the stress to strain ratio between a tensile strain of 0.0155 and 0.023 for the aramid thread, 0.0022 and 0.0044 for the stainless steel thread and 0 and 0.00024 for the copper wire. The modulus of the aramid thread and the copper wire is in line with the modulus of an aramid yarn with 70.5 GPa [283] and that of the copper bulk material with 124 GPa [284], whilst that of the stainless steel thread is lower than the modulus of the bulk material with 200 GPa [285]. The drop in stiffness of the stainless steel thread may be caused by the twisting of the yarns leading to misaligned fibres, reducing the stiffness of

the material. Although, during testing the fibres straighten due to the axial tension a certain degree of misalignment is always present due to the constraints imposed on a filament by its neighbouring filaments.

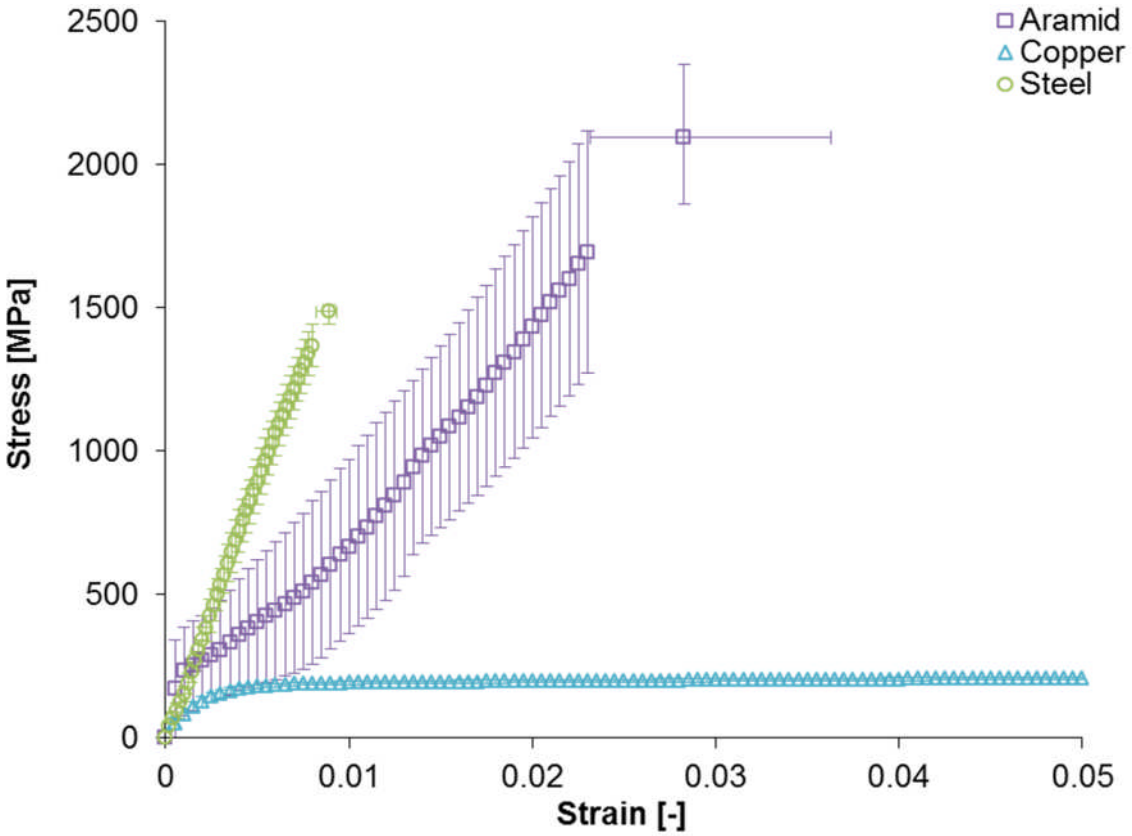

Figure 5-1 Stress-strain curves of dry tufting thread materials presented as the average response of five specimens. Error bars represent the spread of values of failure stress and strain obtained in the experiments. The average strain of the copper wire reaches 0.19.

The ultimate tensile strength of the aramid thread is in line with the strength of 2018 MPa reported in the literature [13]. The tensile strength of the copper wire corresponds to that of the bulk material with 220 MPa [286] since the single wire is not twisted or misaligned. However, the ultimate strength of the stainless steel thread is significantly higher than that of the bulk material with 538 MPa [287]. The increase in strength of the stainless steel thread, compared to the bulk material, can be attributed to the manufacturing process of drawing used to obtain fibres which is accompanied with increasing tensile strength due to work hardening [288]. Figure 5-1 shows that the stainless steel thread is relatively brittle indicated by a low ultimate strain, whereas the aramid thread is more

ductile, followed by the significantly more ductile copper wire showing a high ultimate strain. The variability in ultimate strain for the steel is about ten times lower than that of aramid and 20 times than that of the copper wire as reported in Table 5-1. Thus, the variability in ultimate strain decreases with increasing brittleness of the material reducing the range of the ultimate strain of the threads and the wire. The variability in strength is very low for the copper wire, has a high value for the aramid and an intermediate value for the steel as observed in Figure 5-1 and reported in Table 5-1. Thus, the variability increases with increasing ultimate strength. The variability of the moduli for aramid, stainless steel and copper, respectively, is relatively low and lies within the range of standard experimental error.

Table 5-1 Tensile properties of dry and impregnated threads. Standard deviations are reported in brackets.

Thread material	**Aramid**		**Copper**		**Steel**	
	Dry	Wet	Dry	Wet	Dry	Wet
Tensile modulus [GPa]	71 (±1)	77 (±1)	120 (±2)	132 (±6)	179 (±2)	212 (±6)
Tensile strength [MPa]	2095 (±163)	1755 (±107)	224 (±3)	219 (±9)	1487 (±26)	1380 (±67)
Strain at failure [%]	2.8 (±0.5)	2.4 (±0.4)	19.4 (±0.9)	15.3 (±2.4)	0.9 (±0.04)	0.7 (±0.1)

A comparison of the tensile test results in Figures 5-1 and 5-2 show that the performance of the impregnated threads is in the same order in terms of stiffness, strength and strain as in the dry state. However, the impregnation of threads affect the tensile properties compared to the dry state as reported in Table 5-1. The moduli increase by 9% and 18% for the aramid and stainless steel thread, respectively, whilst that of the copper wire increases by 7%. The moduli are calculated within a tensile strain of 0.0155 and 0.019 for aramid, 0.0022 and 0.0044 for stainless steel and 0.00022 and 0.00032 for the copper wire. The change in modulus for the steel and aramid threads can be explained by the presence of cured resin in the twisted and impregnated threads. The resin in the thread is crushed during testing as the yarns are realigned in

transverse direction generating friction between the yarns and the crushing resin. During the tests of dry threads a significant rotational movement of up to 270° was observed caused by the twist of the threads. This rotation is suppressed mainly by the resin coat leading to constraints of movement and, hence, to an increased number of twists, compared to dry threads, leading to an increased stiffness. The copper wire is not affected by the resin to such an extent since it is impregnated by resin and is not twisted as shown in Figure 3-3. It should be noted that the case of the wet copper wire involves the highest coefficient of variation in modulus observed.

The tensile strength is calculated using the cross sectional area of the dry threads since the applied load is borne by the fibres or the wire. The strength decreases by 19.4%, 7.8% and 2.3% for the aramid and stainless steel thread and the copper wire, respectively, in comparison to the dry threads. In contrast to the stiffness, the higher amount of twists, compared to the dry threads, due to the suppression of thread rotation, and therefore increased misalignment, leads to a lower tensile strength and ultimate strain as also reported in the literature [82]. The strain at failure is reduced for all of the tuft materials: a drop of 17%, 27% and 29% is observed for aramid, stainless steel and copper, respectively (Table 5-1). The variability of tensile modulus, strength and strain for the stainless steel thread increases by 200%, 158% and 150% in the impregnated state compared to the dry state. Equivalently, the variability of the modulus, strength and strain of the copper wire increases by 50%, 200% and 167%, respectively. The resin in the thread leads to irregularities in testing behaviour, depending on the amount of resin between the filaments. The amount of resin is affected by the use of a brush and the changing viscosity of the resin during impregnation, due to natural cooling, leading to irregular resin content in the threads. However, the variability of the aramid thread remains constant for the modulus (±1 GPa) and decreases by 34% and 20% for the strength and strain, respectively. This can be attributed to better compatibility of the thread with resin and the suppression of thread rotation resulting in a consistent or reduced variability compared to the dry threads. Overall, the difference in standard deviation between the impregnated tuft materials is dependent on the tensile

properties of the material, as it is the case for dry threads, and, in addition, on the resin content in the threads and the uniformity of its distribution.

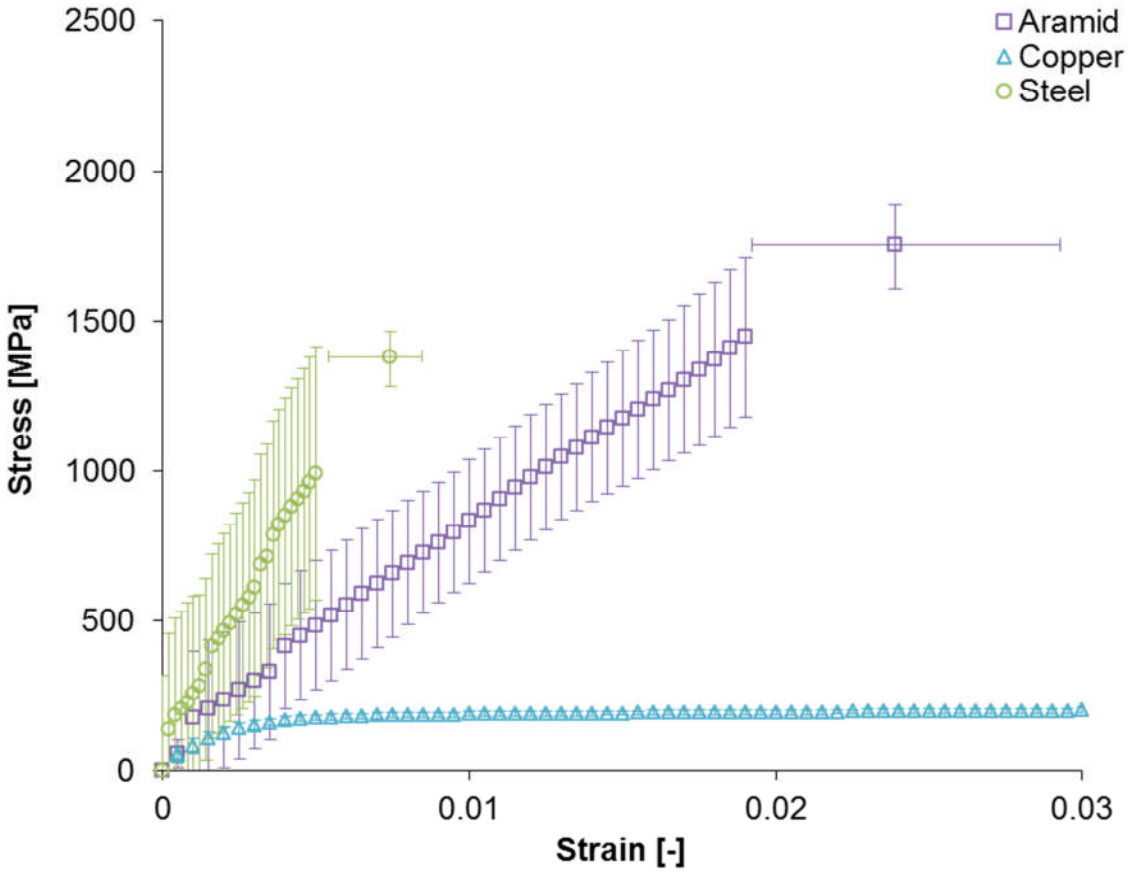

Figure 5-2 Stress-strain curves of impregnated tufting thread materials. Error bars represent the spread of values of failure stress and strain obtained in the experiments. The average strain of the copper wire reaches 0.15.

5.1.2 Delamination response of bindered material for different threads

Typical force-displacement curves obtained during mode I DCB testing of the bindered control laminate and the three tufted materials are shown in Figure 5-3. The general shape and qualitative characteristics of the control laminate curve are typical of mode I testing: the load starts increasing nearly linearly, due to fibre bridging and undulation, once the crack is initiated in the section after the crack starter film and continues propagating.

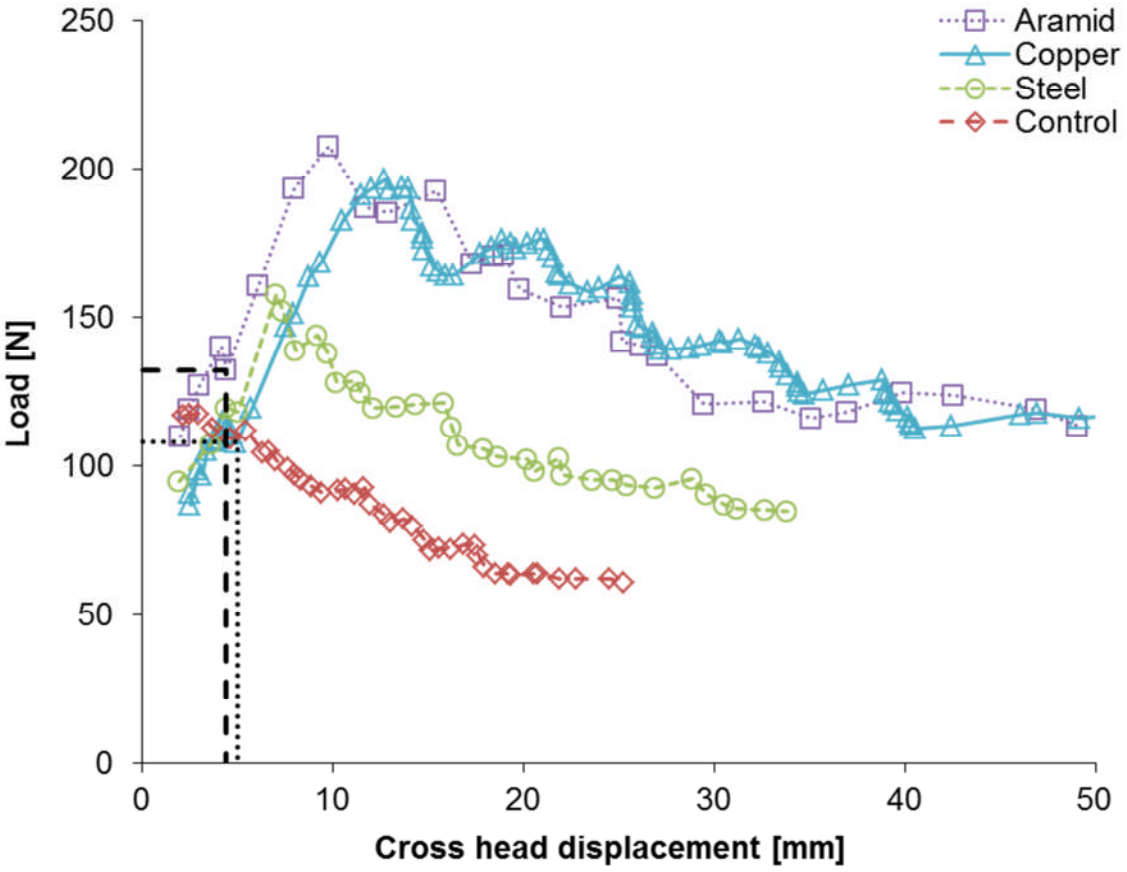

Figure 5-3 Representative load-displacement curves in delamination tests of bindered material tufted using different threads. The tufting depth is 5.2 mm.

The load decreases at a load of approximately 118 N due to an increasing lever arm caused by the delaminating beam with occasional minor increases in load generated by fibre bridging and undulation. Bridging is caused by fibre bundles being attached to both delaminated beam halves and holding them together leading to higher loads to overcome the resistance and propagating the crack. Fibre undulation is caused by the non-structural stitches and natural waviness of the fibres and is enhanced by the insertion of the tufting needle and thread leading to a wavy delamination plane. Once the bundles detach or rupture the load decreases. In the case of tufted materials the load starts increasing almost linearly and drops shortly before the crack reaches the first tuft row (dotted line for copper and steel, dashed line for aramid). The drop is attributed to a propagating crack shortly before reaching the tuft row. The load of tufted materials starts increasing shortly after, once the crack propagates to the first tuft row. While the crack keeps propagating, activating more than one tuft row,

the load reaches its maximum, increasing by approximately 89% for aramid, 116% for copper and 66% for stainless steel compared to the initial load, and drops once the first tuft row ruptures and the crack propagates. From this point on the load decreases continuously with the load varying between propagation and arrest values periodically, caused by regular tuft bridging and rupture at large scale and irregular fibre bridging and undulation at low scale. This can be described by means of the aramid tufted specimen reaching local maxima in load at cross head displacements of 5 – 7 mm caused by tuft bridging, whilst fibre bridging and undulation increases locally the load for cross head displacements of 2 – 3 mm.

Table 5-2 Average crack initiation and propagation energy release rate of bindered composites tufted with different thread material. The tufting depth is 5.2 mm. Standard deviations are reported in brackets.

Thread material		Control	Aramid	Copper	Steel
$G_{Ic,\ ini}$	[J/m^2]	331 (±15)	306 (±46)	272 (±18)	245 (±32)
G_{Ic}	[J/m^2]	579 (±110)	2286 (±247)	2262 (±217)	1230 (±93)

Figure 5-4 illustrates crack resistance curves for mode I tests of the bindered material with a tufting depth of 5.2 mm and the control laminate. The strain energy release rate is interpolated and averaged over four tested specimens for specific increments of crack length. Table 5-2 shows that the differences between the crack initiation toughness of the materials are higher than the variability in results, pointing to an indirect influence of tufting on the initiation toughness. This can potentially be attributed to a decrease in the resin layer thickness in tufted materials during the compression in the RTM mould leading to a reduced initiation toughness. The energy release rate increases until the crack propagates around 15 mm reaching the first tuft row (dotted line). At this point the delamination toughness increases rapidly due to the bridging of the tufts within the first tuft row until their rupture. A bridging zone, involving more than one row of tufts, is developed once the plateau is reached starting from a crack length of approximately 75 mm. The average delamination toughness values for crack propagation are summarised in Table 5-2. The crack energy

release rate increases by about 300%, 290% and 110% for aramid, copper and stainless steel, respectively, compared to the untufted material. The standard deviation in Table 5-2 and the corresponding error bars in Figure 5-4 show that the variability increases with increasing delamination toughness for tufted materials. Since this behaviour was also observed in the tensile behaviour of dry threads and wire (section 5.1.1), where the variability of the tensile strength increases with increasing average tensile strength, this can be attributed to the behaviour of the tufts.

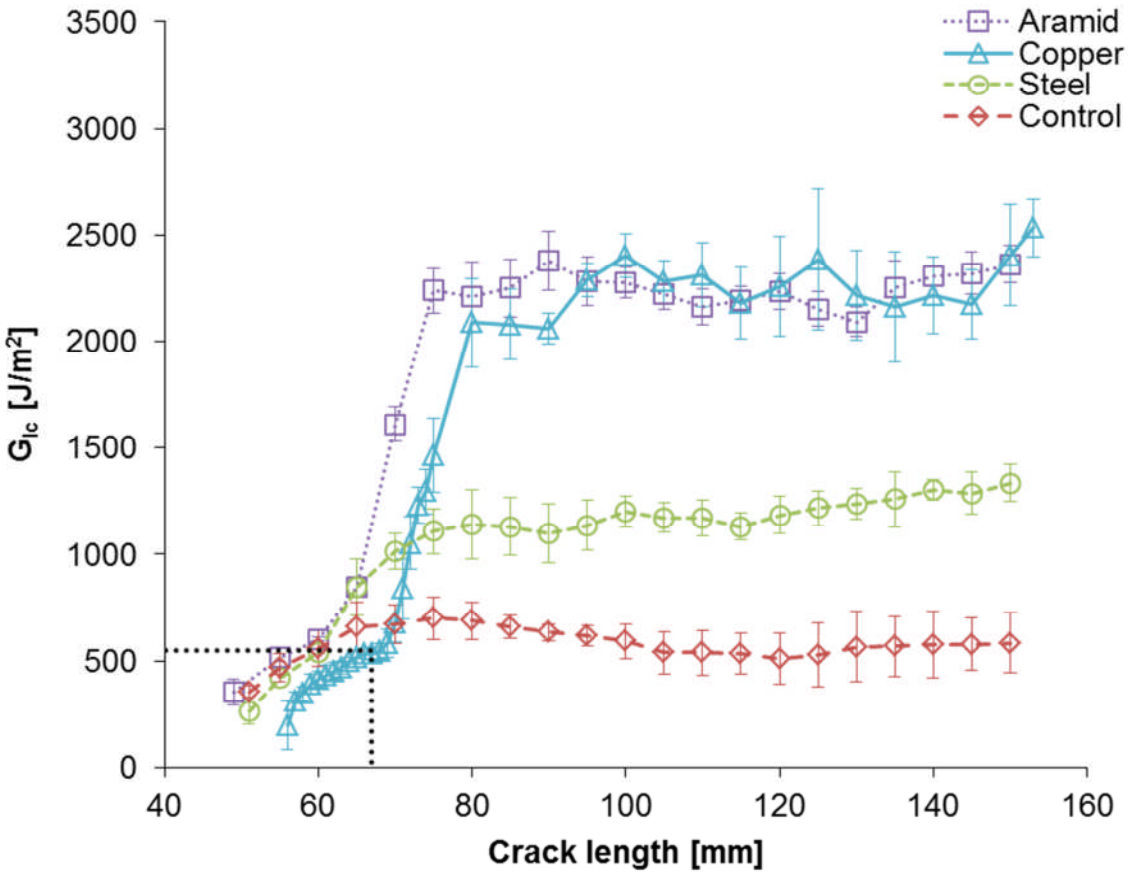

Figure 5-4 Delamination fracture toughness vs crack length of bindered composites tufted with different thread material. The tufting depth is 5.2 mm. Error bars represent one standard deviation.

The general role of tufts during mode I delamination is to increase the closure traction within the bridging zone. This results in crack arrest and higher load bearing capabilities. The performance of the tufts in composite structures loaded in mode I is highly dependent on the tuft material and its tensile properties as well as on the preform material. The failure strength and the

ultimate strain of the aramid and stainless steel thread (Figures 5-1 and 5-2) are in line with the delamination performance shown in Figure 5-4: the aramid thread, with a tensile strength and strain of 40% and 200% higher than stainless steel, respectively, improves the delamination toughness by 90%.

During testing, the crack reaches a tuft row and the tufts start stretching. For aramid and stainless steel tufted materials, usually, two to three tuft rows are active. This is governed mainly by the ultimate strain of the thread material which controls the point at which tufts rupture and the accumulated energy is released. The crack propagates in an unstable manner through, at most, two tuft rows until it is arrested again. This stick-slip behaviour has been also observed in mode I tests of tufted [13, 263], stitched [119] and pinned [42] DCB specimens, affecting the R-curves with variations in energy release rate in the plateau region. Furthermore, occasional fibre bridging and undulation cause local increases in energy release rate which is observed to be common in mode I delamination tests of reinforced composites [13, 68, 116, 119]. Despite the low failure strength of the copper wire, the delamination toughness of copper tufted material is significantly higher than that of the stainless steel tufted material. This is due to the ductility and the high ultimate strain of copper, leading to a great amount of tuft stretching. In contrast to aramid and stainless steel, the crack in copper tufted material is arrested by bridging of four to six tufts simultaneously. This increases the fracture toughness, compared to two to three active stainless steel tufts, and leads to a progressive failure as the crack propagates slowly through single tuft rows, being arrested continuously.

5.1.3 Failure mechanisms during mode I delamination of tufted composites using different thread materials

In general, during delamination in mode I the thread or wire debonds from the surrounding matrix starting at the specimen delamination plane and progressing in the direction of the tufting loop and seam. This is followed by axial elongation of the thread or wire, dictating the delamination performance, and a subsequent tuft failure at the delamination plane. Figure 5-5 shows a part of the cross section of a stainless steel tufted specimen with the thread debonded from the surrounding composite.

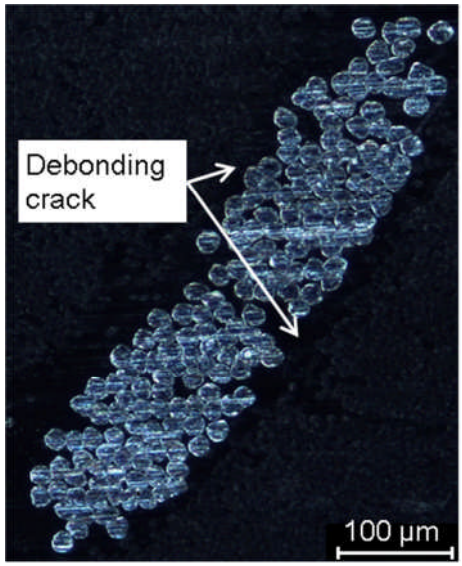

Figure 5-5 Section of a stainless steel thread debonded in delamination testing from the surrounding composite.

Figure 5-6 shows the fracture surfaces of aramid (Figure 5-6a), stainless steel (Figure 5-6b) and copper (Figure 5-6c) tufted specimens with visible tufts. The opposite beam halves show the same tuft fracture indicating that the tufts ruptured at the delamination surface, rather than inside the composite with subsequent pull-out.

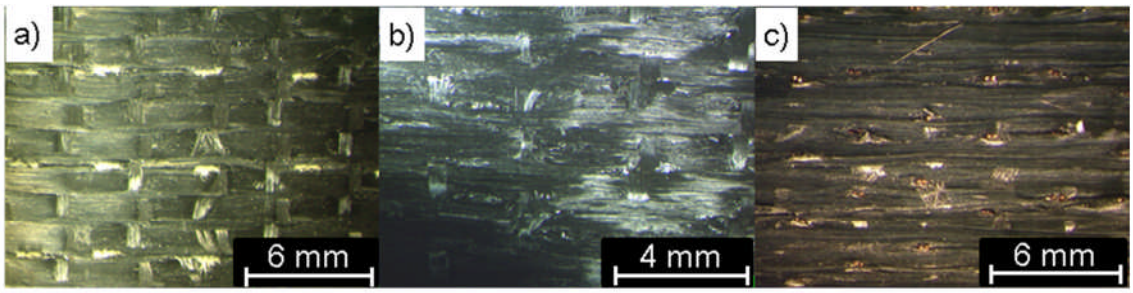

Figure 5-6 Delamination fracture surfaces of a) aramid, b) stainless steel and c) copper tufted bindered composite with tuft rupture at the delamination plane, for tufting depth of 5.2 mm

In addition to the mechanisms of tuft stretching and debonding, which are expected to be active during delamination of through-thickness reinforced composites [13, 260], the presence of tufts induces fibre bridging and undulation at the interface. The carbon fibres being attached to the tufting thread are elevated during thread stretching and break the non-structural glass stitches, as shown in Figure 5-7. The bridging itself and the resistance by the

glass stitches lead to an increase in delamination resistance, whereas in the case of the untufted material the glass stitches are intact (Figure 5-8a). Figure 5-8b shows the mid-plane of an aramid tufted specimen with broken stitches close to tufts. Fibre bridging occurs more frequently in aramid tufted material than in stainless steel tufted material due to the greater aramid thread elongation.

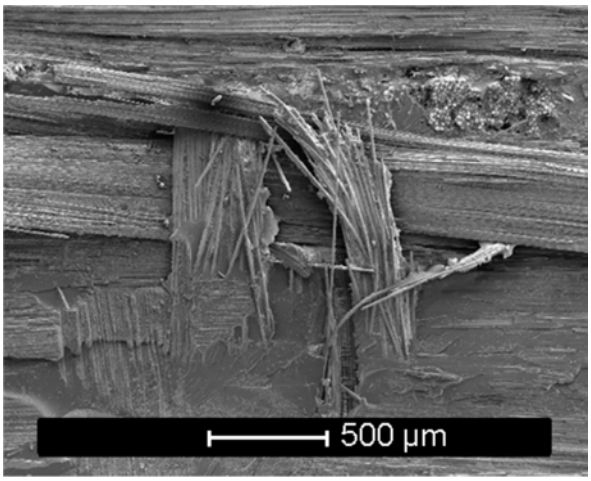

Figure 5-7 Broken glass stitch of stainless steel tufted bindered composite. The tufting depth is 5.2 mm.

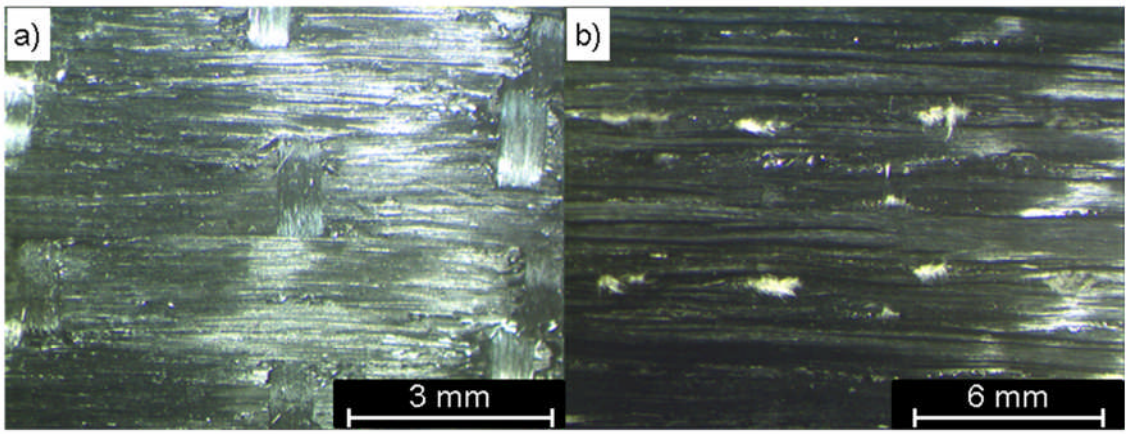

Figure 5-8 Fibre bridging at delamination surface: a) control bindered composite with intact glass stitches and b) aramid tufted bindered composite with broken glass stitches. The tufting depth is 5.2 mm.

5.1.4 Bridging law of tufted composites using different thread materials

The delamination test results, reported in section 5.1.2, are used to determine the bridging law of the tufted composites. Bridging laws have been usually determined by miniature singe-tuft specimens tested in mode I in order to analyse the tuft behaviour during testing and to obtain the tuft bridging stresses [12, 13]. Experimental R-curves from standardised delamination tests can replace single-tuft specimens, which are not standardised, facilitating the manufacturing and testing process. The bridging law derived from delamination tests reveals the contribution of the resin/fibre interface stresses and the tuft bridging stresses to the delamination resistance which can be used for any model predicting the delamination toughness of tufted materials. The bridging law corresponding to the delamination R-curves can be determined by calculating the fracture surface stress σ by differentiating the crack energy release rate G_{Ic} with respect to beam opening displacement δ^* at the initial crack position as follows [289]:

$$\frac{\partial G_{Ic}}{\partial \delta^*} = \sigma(\delta^*) \qquad \textbf{5-1}$$

The opening displacement δ^* can be calculated, according to linear beam theory, by the following expression:

$$\delta^* = \frac{F x^2}{6EI}(3L - x) \qquad \textbf{5-2}$$

with

$$x = a - a_0 \qquad \textbf{5-3}$$

where F is the applied load, L the beam length starting at the load line and equivalent to crack length a, x the position at which the opening displacement δ^* is calculated, a_0 the length of the crack starter film, i.e. the initial crack length, E the Young's modulus and I the second moment of area. Combining Eqs. 5-2 and 5-3 yields:

$$\delta^* = F(a - a_0)^2 \frac{(2a + a_0)}{6EI} \qquad \textbf{5-4}$$

The results of this calculation are illustrated in Figure 5-9, showing the average fracture stresses and opening displacements interpolated at the equivalent increments of crack length as the average delamination toughness in Figure 5-4. Figure 5-9 also shows the stress-strain curves of the tuft threads as tuft load per unit area versus tuft elongation, based on the beam opening displacement of the DCB specimens. The figures compare only the stresses of the bridging law of tufted materials and those of the tufts and do not allow comparisons of delamination toughness due to different beam opening displacements applied for the calculations. As the tuft load is distributed evenly across the unit area, but in the experiments the tuft load is concentrated in the centre of the unit area, the location of the tuft load per unit area for the bridging law is shifted by half the length of the unit area. This leads to concentric unit areas in the experiments and bridging law. The tuft load per unit area is determined by calculating the beam opening displacement δ', i.e. tuft elongation, at the position of the first tuft row using following equation:

$$\delta' = \frac{\delta^* \left(a - a_0 - \left(t - \frac{\sqrt{A_u}}{2} \right) \right)^2 \left(2a + a_0 + \left(t - \frac{\sqrt{A_u}}{2} \right) \right)}{(a - a_0)^2 \, (2a + a_0)} \qquad \textbf{5-5}$$

where t is the distance between the end of the crack starter film and the first tuft row and A_u the size of the unit cell corresponding to a fracture surface area each tuft bridges. Dividing the tuft elongation by the initial tuft length (5.2 mm) results in the thread or wire strain which can be used to interpolate the corresponding thread or wire stress obtained by the tensile tests. The tuft load per unit area σ_t is then calculated, by normalising the thread or wire stress with respect to the unit area covered by a tuft, as follows:

$$\sigma_t = \frac{\sigma_{th} \cdot 2 \cdot A_{th}}{A_u} \qquad \textbf{5-6}$$

where σ_{th} is the thread or wire stress and A_{th} the cross sectional area of the thread or wire, i.e. half of that of the corresponding tuft. The size of the unit cell is 19.98 mm^2, 11.97 mm^2 and 19.63 mm^2 for aramid, stainless steel and copper, respectively.

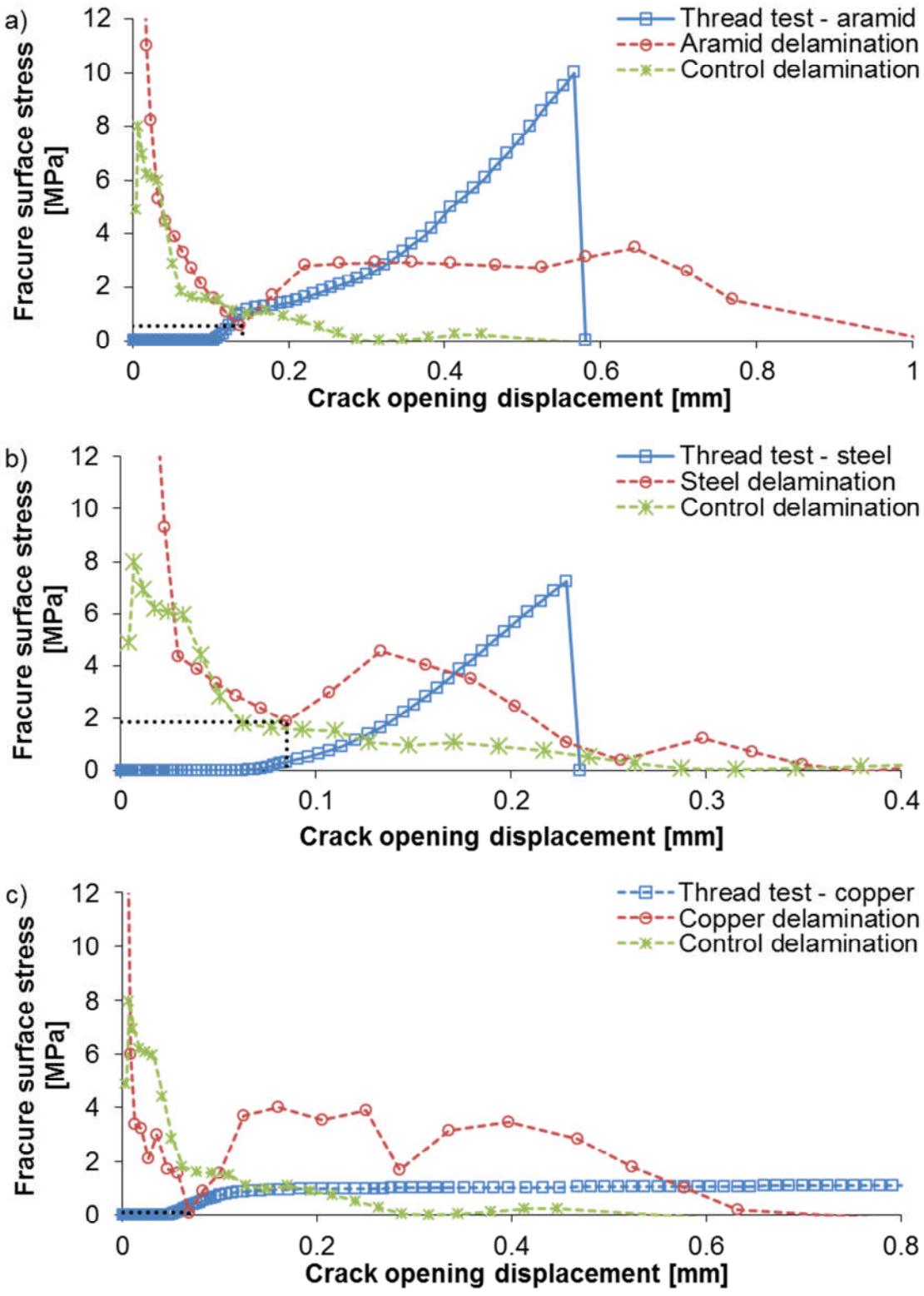

Figure 5-9 Fracture stress – crack opening curves: a) aramid tufts, b) copper tufts and c) stainless steel tufts for the bindered composite at a tufting depth of 5.2 mm. The dotted lines show the point the crack reaches the first tuft row in the tufted delamination curve.

The initial rise in fracture stresses at very low opening displacements is caused by the typical high stresses around the crack tip during crack initiation in the untufted region. Once the crack propagates and the slope of the delamination toughness decreases, the fracture stresses drop. In the case of the untufted control material the fracture stress decreases at relatively low openings. At that point the fracture stress is negligible (Table 5-3). The corresponding R-curve is considered to have reached a plateau with a consistent energy release rate. For the aramid tufted material (Figure 5-9a) the fracture stress increases again at 0.14 mm opening. This is due to the crack reaching the first tuft row (dotted line) leading to tuft bridging accompanied by fabric fibre bridging. The bridging fibre bundles transfer the applied loads to the fractures surfaces, whilst the material is delaminating, increasing the stress. The bridging stress then starts decreasing, with minor increases and decreases due to fibre bridging and undulation, and diminishes once the bridging zone is fully developed. Stainless steel specimens (Figure 5-9b) show an equivalent behaviour characterised by lower openings (Table 5-3). The smaller openings, in contrast to aramid, can be related to the lower failure strains of the stainless steel thread as shown in Figure 5-1. The stress for the copper tufted material (Figure 5-9c) rises at a beam opening of 0.07 mm and becomes negligible at 0.72 mm.

The solid lines show the stress-strain curves of the tuft threads or wire as tuft load per unit area versus tuft elongation. The stress of the aramid (Figure 5-9a) and stainless steel (Figure 5-9b) tuft start rising at a beam opening of 0.1 mm and 0.08 mm, respectively, i.e. once the crack reaches that tuft row. The high initial slope of the aramid tuft stress curve is a result of the thread tensile test. The subsequent low slopes of the aramid and stainless steel tuft stress curves can be attributed to the fact that more than one tuft are active in the delaminating material. The subsequent slopes between an opening of 0.3 mm and 0.55 mm for the aramid and 0.15 mm and 0.22 mm for the stainless steel curve correspond to that of the rise in fracture surface stress, confirming that this rise is attributed to the activation of the first tuft row in the material. The compactness of the composite around the tufts partially prevents the rotational movement, observed during the thread tensile tests, and axial elongation of the

threads is required to fully exploit the thread properties. This results in tuft failure below the maximum thread tensile strength and strain leading to lower fracture surface stresses and crack opening compared to the maximum stresses and elongation of the tuft curve. The tuft stress of the copper wire (Figure 5-9c) starts rising once the crack reaches the first tuft row at a beam opening of 0.05 mm. With the crack propagating slowly to the third tuft row and further, the slope of the fracture stress curve increases at a beam opening of 0.07 mm indicating a stiffer response of the specimen due to bridging of four to six tuft rows and leading to higher stresses compared to a single wire tested in tensile. Furthermore, constraints in movement due to the composite may increase the stiffness compared to the wire tensile test.

Table 5-3 Crack opening displacements at first tuft position and at fully developed bridging zone for untufted and aramid, copper and stainless steel tufted material.

Thread material		Control	Aramid	Copper	Steel
First tuft	[mm]	-	0.14	0.07	0.08
Plateau	[mm]	0.30	1.04	0.72	0.40

5.2 Effect of laminate material

5.2.1 Delamination response of different laminate materials tufted using aramid

In order to determine the influence of the preform material on the delamination toughness, two different uni-directional fabrics and a bi-axial [0/90] preform were tufted with aramid thread as described in 3.2.3. The unbindered and intermediately bindered material without tufting and with a tufting depth of 5.2 mm are compared with the highly bindered material with a thickness of 4 mm. In general, the representative load-displacement curves in Figure 5-10 show the same characteristics as described for the curves in Figure 5-3: the load starts increasing almost linearly, whilst the crack is propagating. In untufted specimens the load reaches a peak of 86 N, 127 N and 106 N for the unbindered, bindered and highly bindered materials, respectively. The increased load at crack initiation and maximum load of the intermediately

bindered material, compared to the unbindered material, is a result of the toughening of the resin combined due to the epoxy binder increasing the load bearing capability of the material and leading to higher initiation loads at equivalent cross head displacement. The highly bindered material shows a higher load bearing capability than the unbindered material due to a similar toughening mechanism, however, the initiation load is reduced compared to the intermediately bindered material due to the lower specimen thickness and the lay-up with the fibres orientated in 90° not contributing to the stiffness. After reaching the peak, the load decreases continuously until specimen failure of the untufted specimens. During delamination and the corresponding decrease in load, the highly bindered untufted material shows more variations in load than the other control material. This is due to the large amount of binder enhancing fibre bridging as observed during delamination tests. The binder increases the bonding strength of the matrix/fibre interface leading to fibre bundles being locally attached to the resin, whilst adjacent bundles delaminate from the matrix. In the unbindered material the matrix/fibre interface is weaker preventing fibre bridging and leading to an almost straight decrease in load. The final beam opening of the highly bindered specimen has more than tripled compared to the unbindered specimen due to the reduced specimen stiffness and increased resin toughness.

In general, tufted materials reach higher maximum loads than untufted materials due to the tuft bridging leading to high loads to rupture the tufts. The maximum load of the intermediately bindered material is 18% and 50% higher than that of the unbindered and highly bindered material, respectively. The reasons are similar to the case of the control material: the epoxy binder causes toughening leading to higher loads required to delaminate the intermediately bindered material compared to the unbindered. Furthermore, the binder enhances fibre bridging by improving the fibre/matrix interface and by the fibres being attached to the tufts, elevating during tuft elongation and leading to higher loads. The reduced maximum load of the highly bindered material, compared to the other tufted specimens, is caused by the lower specimen thickness and the bi-axial lay-up reducing the specimen stiffness. However, these characteristics and the

tough matrix system lead to the potential of high bending during delamination testing without breaking in flexure. The difference in load between the unbindered untufted specimen and the highly bindered untufted specimen is larger than the corresponding tufted specimens due to the suppression of the binder toughening mechanism by the tufts. In the tufted specimens the tufts are the load bearing factor, whereas in the untufted specimens the binder contributes mainly to the load bearing capability leading to a larger difference in load if no binder is present.

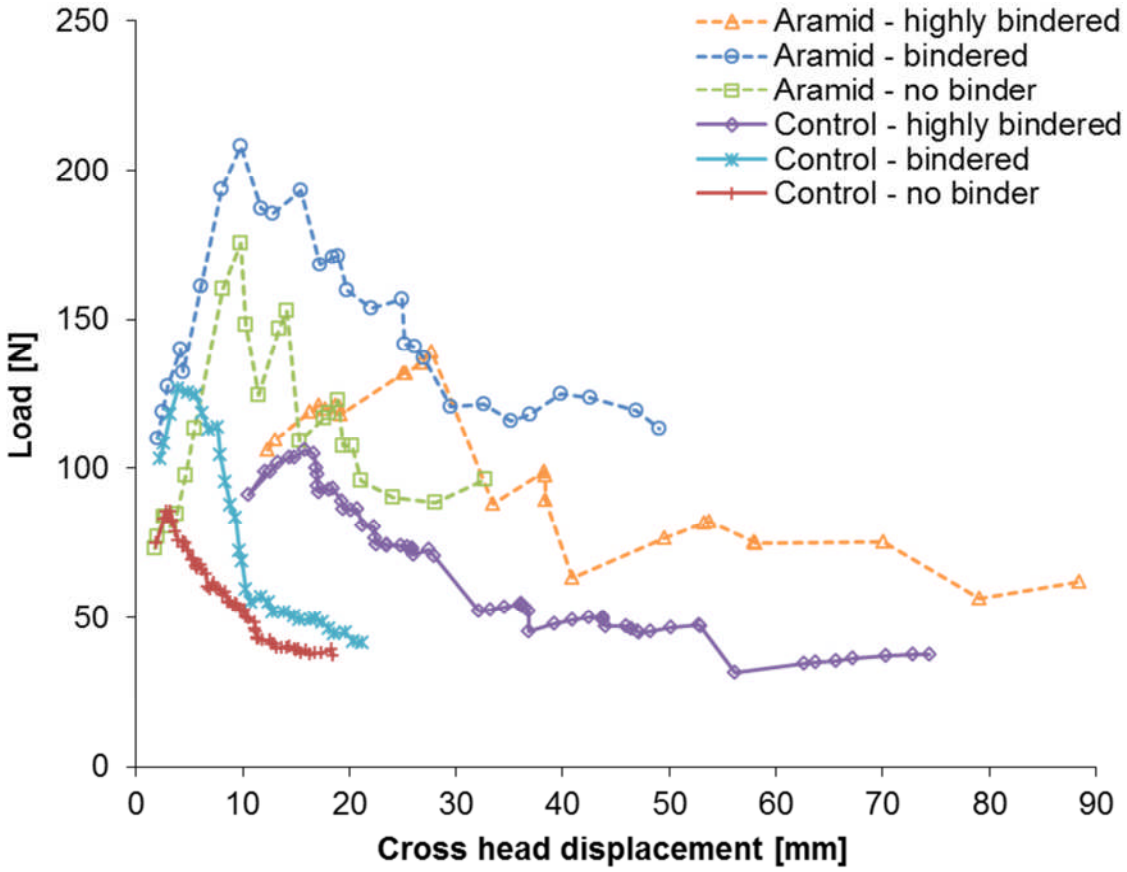

Figure 5-10 Representative load-displacement curves of delamination tests of untufted and tufted specimens with different amount of binder.

Figure 5-11 illustrates the averaged R-curves for the different binder states and the corresponding results for the tufted material. Each mark represents the interpolated and average energy release rate, out of four specimens, at specific increments of crack length. Table 5-4 summarises the crack energy release rates showing a significant effect of the amount of binder on the delamination toughness.

Table 5-4 Average crack energy release rate for crack initiation and propagation of unbindered and bindered material tufted with aramid. Standard deviations are reported in brackets.

Thread material	Control			Aramid		
	unbindered	bindered	highly bindered	unbindered	bindered	highly bindered
$G_{Ic,\ ini}$ [J/m²]	179 (±8)	331 (±15)	1591 (±156)	169 (±26)	306 (±46)	1513 (±145)
G_{Ic} [J/m²]	303 (±22)	579 (±110)	1264 (±160)	1457 (±172)	2286 (±247)	2444 (±308)

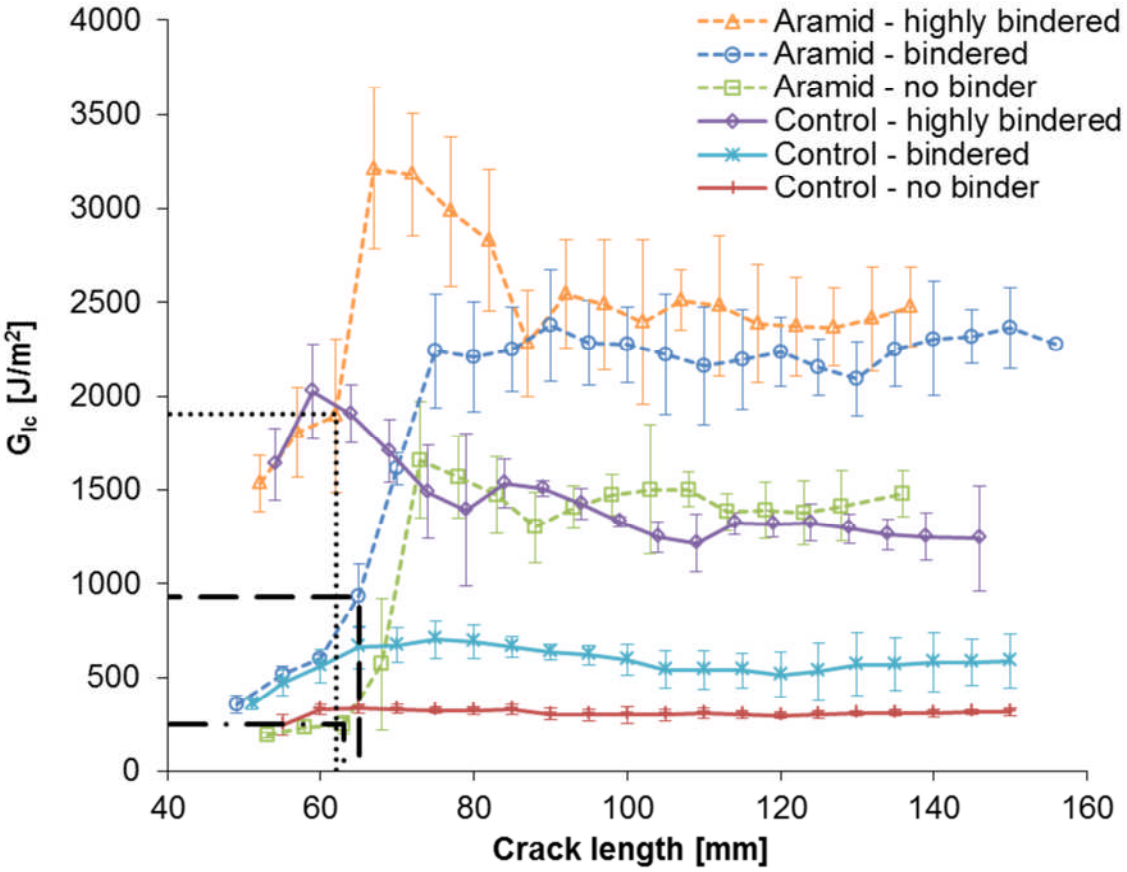

Figure 5-11 R-curves for different aramid tufted preforms. Error bars represent one standard deviation.

The values of crack initiation toughness show a dependence on the amount of binder. The crack initiation toughness for untufted preforms increases with increasing amount of binder. This is attributed to the toughening mechanism of

the epoxy binder. The increase is about 90% between the unbindered and the intermediately bindered untufted preform, and further 380% for the highly bindered untufted preform. The main reason for the increase in delamination resistance of the highly bindered material is the greater matrix toughness and stronger matrix/fibre interface caused by the epoxy binder, leading to higher energies required for crack propagation. The amount of binder also increases the amount of fibre bridging leading to an improvement of the delamination performance. The R-curve of the intermediately bindered material shows variations in crack energy release rate caused by fibre bridging and undulation, whilst the curve of the unbindered material is relatively flat due to the absence of fibre bridging as observed during testing. The bridging of fibre bundles leads to crack tip closure increasing the energy release rate. The highly bindered material shows more fibre bridging due to the higher amount of binder leading to greater variations in energy release rate, compared to the other control materials. The variations in energy release rate can be attributed to the irregular contribution of fibre bridging and undulation to the delamination toughness dependent on the length of the bridging fibre bundles and the bonding strength between the bundles and the resin.

The crack initiation toughness of tufted materials increases with rising amount of binder material due to the improved fracture toughness of the matrix system. The values for crack initiation toughness in Table 5-4 show a slight difference compared to the corresponding untufted specimens. This can potentially be attributed to changes in resin rich layer thicknesses due to tufting. The crack propagation toughness of the tufted specimens increases rapidly at a crack length between 62 mm and 74 mm, depending on the preform and reinforcement, eventually reaching a plateau for a developed bridging zone. Tufting improves the toughness following the same order as the corresponding untufted material: the fracture toughness of the tufted material with intermediately amount of binder is higher than the unbindered tufted material by about 60%. The increase in toughness between the highly bindered and the intermediately tufted material is marginal (about 5%) and within the limits of experimental spread of values. As observed in Figure 5-11, tufting with aramid

increases the toughness significantly. The relative effect is influenced by the toughness of the control material. The improvements in fracture toughness are around 380%, 290% and 90% for the unbindered, intermediately bindered and highly bindered materials, respectively. These results indicate a diminishing relative effect of the tufting as the toughness of the control delamination interface increases. The improvement of the delamination performance is mainly a synergistic effect of the resin toughening mechanism, caused by the binder material, and tuft bridging. However, an increasing amount of binder material suppresses the tuft performance if the strength of the interface is higher than that of the tufts, becoming the main resistance to crack propagation. In general, tufting also enhances fibre bridging and undulation. It is assumed that crimped and broken fabric fibres, caused by the tufting process, around the tufts stick to the thread, especially in the presence of binder material, causing bridging once the tufts stretch behind the crack tip. This reinforces the stick-slip behaviour and also increases the delamination toughness. The difference in fracture toughness between the unbindered and intermediately bindered tufted preform is attributed to the binder, as the tufting configuration is the same for both specimens and hence the binder is the only difference between them. A similar relation is present between the intermediately bindered and highly bindered tufted specimens. The improvement in delamination toughness is mainly caused by the difference in the amount of binder material. However, the reason for the relatively small increase in toughness may be a lower difference in the amount of binder material, compared to the intermediately bindered material, and the lower stiffness of the highly bindered specimens. A lower stiffness may lead to a reduced crack length at equivalent beam opening activating fewer tuft rows leading to a smaller improvement of the delamination resistance than stiffer specimens.

Variability increases with the amount of binder and with the presence of tufts. The variability of the untufted specimens changes by 400% and 630% between the unbindered and intermediately bindered and highly bindered materials, respectively, caused by the different degree of delamination toughness improvement. This can be related to the enhancement of fibre bridging with

increasing amount of binder material. The variability of the tufted specimens is affected for the same reason as well as the inherent variability in thread response, with tufting increasing the variability by 680%, 130% and 90% for the unbindered, intermediately bindered and highly bindered materials, respectively. Furthermore, fibre bridging and undulation is also enhanced by the tufts which may vary within a type of specimens depending on the fracture surface and factors, such as fibre misalignment, crimping and breakage caused by tufting.

5.2.2 Failure mechanisms in different laminate materials tufted using aramid

All three types of tufted materials fail in the same way: in addition to the main delamination crack smaller cracks debond the tufts from the surrounding composite, followed by rotation and axial elongation of the tufts until final rupture. The intermediately bindered untufted and tufted materials correspond to those used in section 5.1.2 and their failure mechanism is described in section 5.1.3. The unbindered untufted and tufted specimens show a similar failure mechanism; however, the presence of fibre bridging is reduced due to the absence of epoxy binder as shown in the micrographs in Figure 5-12. In bindered material the binder increases the fibre/resin and fibre/tuft interface, enhancing fibre bridging as the strength of the interfaces is larger than without binder material. Compared to the intermediately bindered material, shown in Figure 5-7, the non-structural glass stitches in the unbindered material are fully intact indicating an absence of fibre bridging.

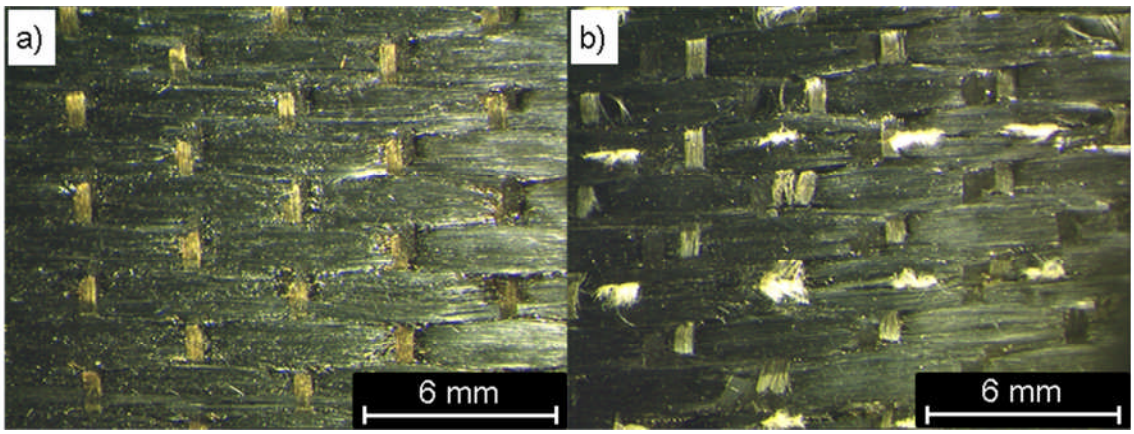

Figure 5-12 Fracture surface of unbindered specimens: a) untufted control and b) aramid tufted for tufting depth of 5.2 mm.

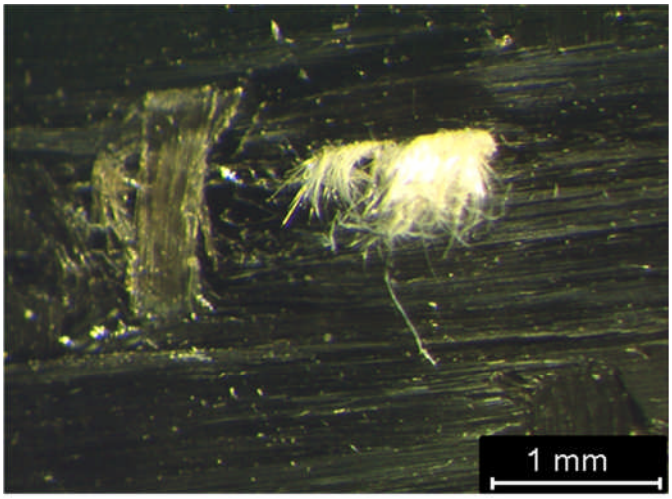

Figure 5-13 Ruptured aramid tuft at delamination surface of unbindered material for tufting depth of 5.2 mm.

During delamination the aramid tufts in the unbindered material debond from the surrounding composite, elongate, rotate and rupture at the delamination plane as shown in Figure 5-13. The opposite beam half also shows visibly ruptured aramid tufts confirming a tuft fracture at the delamination plane.

The highly bindered material shows a more uneven delamination surface (Figure 5-14a) compared to the unbindered material as a result of fibre bridging during the testing. The high amount of binder enhances fibre bridging leading to higher delamination resistance. Resin rich channels are generated between the regularly placed tufts by shifting entire fibre bands aside during tufting (Figure 5-14b). These channels can act as crack initiation sites, raising the susceptibility of the material to crack propagation and preventing an increase in delamination toughness.

The highly bindered material is fractured at the delamination plane after axial elongation as shown in Figure 5-15. However, comparing the fractured tuft of the highly bindered material with that of the unbindered material (Figure 5-13), it can be observed that tufts in the highly bindered appear to have a shorter tuft section outside the composite indicating a smaller elongation during delamination. This confirms the assumption that the large amount of binder increases the constraints in tuft movement, preventing greater elongations and suppressing the effect of tufting.

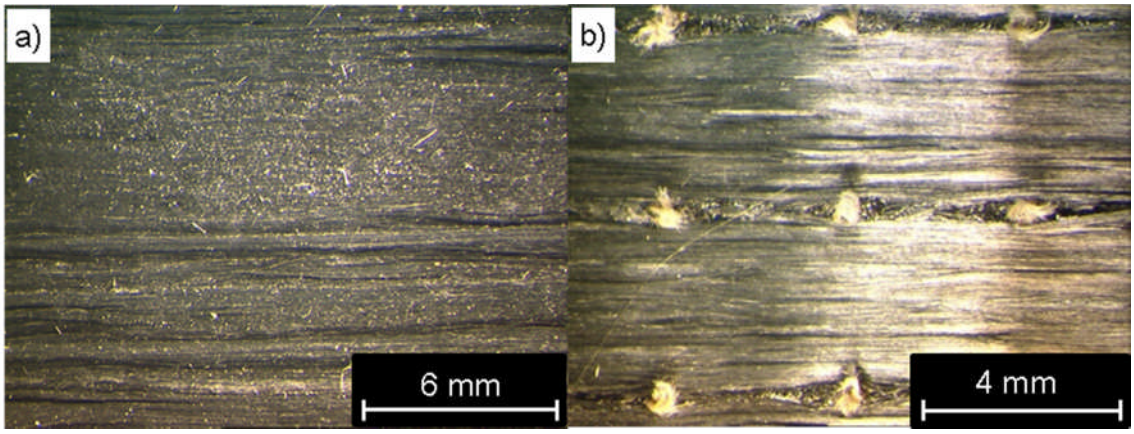

Figure 5-14 Fracture surface of highly bindered specimens: a) untufted control and b) aramid tufted for a tufting depth of 4 mm.

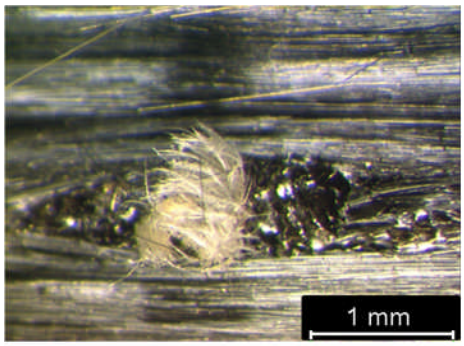

Figure 5-15 Ruptured aramid tuft at fracture surface of highly bindered specimen for tufting depth of 4 mm.

5.2.3 Bridging laws in different laminate materials tufted using aramid

Figure 5-16 illustrates the surface fracture stress versus the crack opening displacement for the different control laminates using aramid tufting. These are calculated as described in section 5.1.4. The initial high surface stresses at crack initiation are attributed to the stresses at the crack tip during crack initiation. The subsequent drop in stresses is caused by the propagation of the crack in the untufted section.

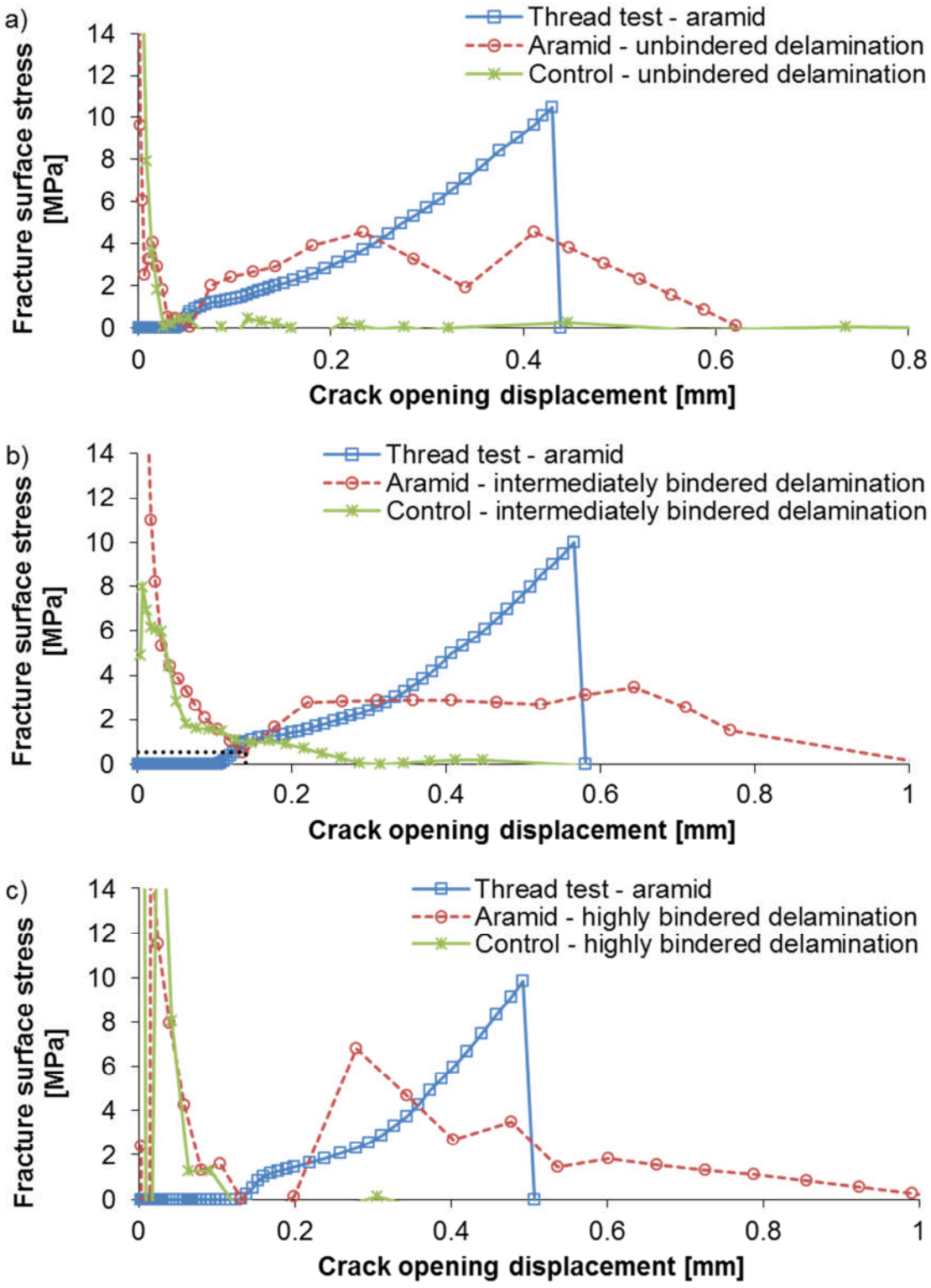

Figure 5-16 Average surface fracture stress - opening displacement curves for: a) unbindered, b) intermediately bindered and c) highly bindered material tufted with aramid. The dotted lines show the point the crack reaches the first tuft row in the tufted delamination curve.

The stress of the unbindered control material (Figure 5-16a) drops continuously until it becomes negligible (Table 5-5) corresponding to a steady state crack propagation after the initial high peak at the end of the crack starter film. The unbindered tufted material shows an oscillating stress due to the continuous tuft bridging and subsequent rupture. The tuft stress resulting from thread testing starts increasing once the crack propagation in the tufted specimen reaches the first tuft row. The slope of the tuft curve corresponds to that of the delamination tests indicating the activation of more than one tuft row in the delamination specimen. The higher ultimate stress in the tuft curve is due to the constraints in movements of the tufts imposed by the surrounding composite leading to a tuft failure before reaching the thread tensile strength.

The surface stress of the intermediately bindered control material (Figure 5-16b) decreases after the initial peak with a reducing rate caused by fibre bridging and undulations maintaining a low stress level until it becomes negligible. The surface stress of the intermediately bindered tufted material starts increasing at an opening of 0.14 mm with a slope corresponding to that of the thread test curve, indicating that the increase in stresses is attributed to the activation of the first tuft row (dotted line) arresting the crack propagation. In contrast to the stress curve of the unbindered tufted material, the stress of the intermediately bindered tufted material remains constant after the initial peak, indicating a contribution of the binder to the bridging with occasional fibre bridging and undulations leading to high surface stress once the first tuft row ruptures. Similarly to the results presented in Figure 5-16a, the tensile strength and strain of the thread test are higher than that of the tuft in the composite due to fewer constraints.

The fracture surface stress of the highly bindered untufted material (Figure 5-16c) drops after the initial high peak until it becomes negligible (Table 5-5). The stress of the tufted material drops at the same rate as the untufted specimens but starts increasing again at an opening of 0.19 mm with a higher rate than the thread test curve indicating that the crack reached the first tuft row and the tufts start to bridge the crack opening with a high amount of binder which is not considered in the thread test. The stress reaches a high level

probably caused by the synergistic effect of tufts and fibre bridging, the latter being caused by the binder and the aramid tuft, or by the toughening due to the binder. The stress decreases with local peaks caused by tuft bridging and/or fibre bridging and undulations until the stress is negligible. Similarly to the unbindered and intermediately bindered materials, the thread test curve of the highly bindered material reaches a higher tensile strength and strain due to fewer constrains in movement compared to the tufts in the composite.

Table 5-5 Crack opening displacements at first tuft position and at fully developed bridging zone for untufted and aramid tufted material with different amount of binder.

Thread material		**Control**			**Aramid**		
		unbindered	**bindered**	**highly bindered**	**unbindered**	**bindered**	**highly bindered**
First tuft	[mm]	-	-	-	0.04	0.14	0.19
Plateau	[mm]	0.06	0.60	0.13	0.62	1.03	1.03

5.3 Comparison of superposition of direct material response with experimental behaviour

The thread tensile behaviour can be used alongside the response of the reinforced laminate to obtain a trend for the mode I delamination performance incorporating tufts of aramid, copper and stainless steel. This is carried out by an analytical approach of superimposing the incremental crack energy release rates contributed by the fracture surface stresses σ_R of the control material, as used for the bridging law, and the tufts σ_t. The surface stresses caused by the resin/fibre interface start at the end of the crack starter film (a_0 in Figure 5-17) and continue throughout the specimen corresponding to the bridging law introduced in section 5.1.4. The required energy to overcome the stresses accumulates to the energy required to elongate the tufts starting at a larger crack length considering another bridging law for a uniformly tufted area. The sections with pure resin bridging stress σ_R and superimposed bridging stresses σ_{t+R} are defined, from the specimen loading point, as follows:

$$\sigma_R\colon\ a_0 < x > a_0 + t - \frac{\sqrt{A_u}}{2} \qquad \textbf{5-7}$$

$$\sigma_{t+R}\colon a_0 + t - \frac{\sqrt{A_u}}{2} < x > a \qquad \textbf{5-8}$$

where x is the current location in crack propagation direction.

The pure resin bridging stresses and superimposed bridging stresses are integrated over the beam opening displacement at the corresponding location (δ^* and δ', respectively) in order to calculate the total crack energy release rate. The opening displacement δ' at the tuft location is calculated using the beam opening δ^* at the crack starter (Figure 5-17) according to Eq. 5-5. The fracture surface stress σ_R is determined by interpolating the calculated beam openings and surface stress of the control material (section 5.1.4) for a predefined beam opening δ^*, whilst the tuft stress per unit cell area σ_t is determined according to Eq. 5-6. In general, the delamination toughness G_{Ic} for uniform bridging stresses is defined as follows [289]:

$$G_{Ic} = \int_0^{\delta^*} \sigma \, d\delta \qquad \textbf{5-9}$$

Assuming that the stress σ is composed of the resin bridging stresses and superimposed bridging stresses Eq. 5-9 yields:

$$G_{Ic} = \int_0^{\delta'} \sigma_{t+R} \, d\delta + \int_{\delta'}^{\delta^*} \sigma_R \, d\delta \qquad \textbf{5-10}$$

Substituting the term for σ_R with terms containing limits starting from zero results in:

$$G_{Ic} = \int_0^{\delta'} \sigma_{t+R} \, d\delta + \int_0^{\delta^*} \sigma_R(\delta) \, d\delta - \int_0^{\delta'} \sigma_R(\delta) \, d\delta \qquad \textbf{5-11}$$

The second term on the right hand side in Eq. 5-11 is substituted, so that the limits correspond to the limits of the other integrals. Subsequent differentiation of Eq. 5-11 with respect to $d\delta^*$ and substituted limits yields:

$$\frac{dG_{Ic}}{d\delta^*} = \sigma_R(\delta^*) + \left(\sigma_{t+R}(\delta') - \sigma_R(\delta')\right) \frac{d\delta'}{d\delta^*} \qquad \textbf{5-12}$$

The second term on the right hand side describes tuft bridging stresses. Eq. 5-12 becomes:

$$dG_{Ic} = \sigma_R(\delta^*)\, d\delta^* + \sigma_t(\delta')\, d\delta' \qquad \textbf{5-13}$$

Integrating the fracture surface stresses and tuft bridging stresses over the beam openings δ^* and δ' of the control specimens, respectively, yields in discretised form:

$$G_{Ic,j} = \sigma_{R,j-1}\left(\delta_j^* - \delta_{j-1}^*\right) + \sigma_{t,j-1}\left(\delta_j' - \delta_{j-1}'\right) + G_{Ic,j-1} \qquad \textbf{5-14}$$

where j is the current number of increment.

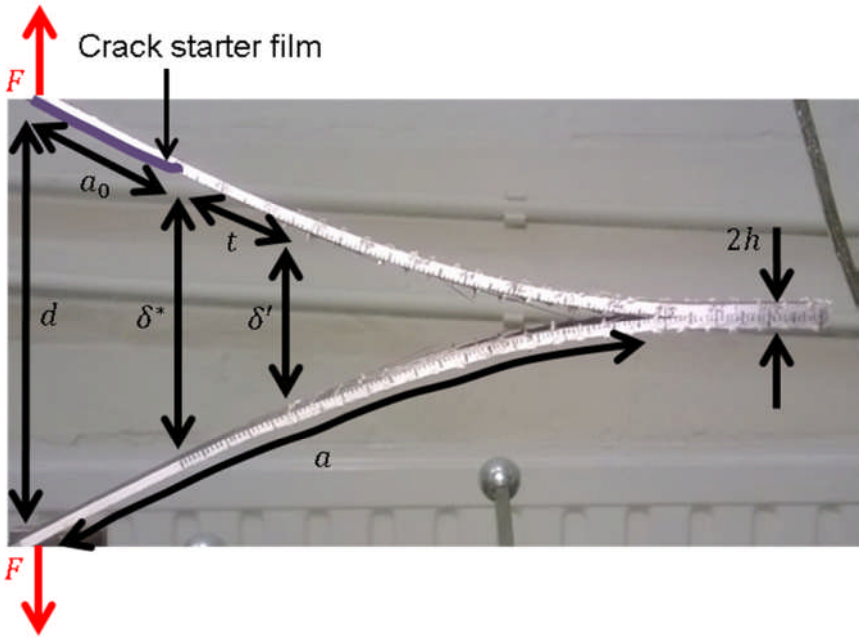

Figure 5-17 Schematic of specimen with dimensions used for the calculation of the delamination toughness.

In order to plot the R-curves the crack length a corresponding to delamination toughness G_{Ic}, has to be calculated. Standard beam theory for a cantilever beam leads to:

$$d = \frac{2Fa^3}{3EI} \qquad \textbf{5-15}$$

where F is the load required to open the specimens, a the crack length and also the total length of the beam, E the Young's modulus and I the moment of

inertia. The factor doubling the load is required since the displacement d refers to the entire opening of the double cantilever beam. The load F can be expressed as follows:

$$F = \frac{2G_{Ic}ba}{3d} \quad \textbf{5-16}$$

where G_{Ic} is the critical energy release rate in mode I, b the width of the specimen and a the crack length. Substituting F in Eq. 5-15 with Eq. 5-16 and the moment of inertia with $\frac{bh^3}{12}$ results in:

$$d = \frac{4}{3}a^2\sqrt{\frac{3G_{Ic}}{Eh^3}} \quad \textbf{5-17}$$

In order to minimise the dependence on geometrical data of the specimen Eqs. 5-16 and 5-17 are substituted into Eq. 5-4 yielding:

$$\delta^* = \sqrt{\frac{G_{Ic}}{3Eh^3}}\frac{(a-a_0)(2a+a_0)}{a} \quad \textbf{5-18}$$

Figure 5-17 shows the dimensions used for Eqs. 5-15 – 5-18. Eq. 5-18 results in a third order polynomial as a function of the crack length a which is solved using the Newton-Raphson method. The solution involves several iterations to determine the crack length a according to a particular beam opening δ^*. Eq. 5-18 is simplified with the introduction of the factors a_1 to a_3:

$$a_1 = -\frac{3}{2}a_0 \quad \textbf{5-19}$$

$$a_2 = -\delta^*\sqrt{\frac{3Eh^3}{4G_{Ic}}} \quad \textbf{5-20}$$

$$a_3 = \frac{1}{2}a_0^3 \quad \textbf{5-21}$$

The solution of Eq. 5-18 is equivalent to solving:

$$f(x) = x^3 - x^2\frac{3}{2}a_0 - x\,\delta^*\sqrt{\frac{3Eh^3}{4G_{Ic}}} + \frac{1}{2}a_0^3 \quad \textbf{5-22}$$

In discretised form this is expressed as:

$$f(x_{ij}) = x_{ij}^3 - x_{ij}^2 \frac{3}{2} a_0 - x_{ij}\, \delta^* \sqrt{\frac{3Eh^3}{4G_{Ic,j}}} + \frac{1}{2} a_0^3 \qquad \textbf{5-23}$$

with the index i standing for number of iteration and j the number of increment. The first derivative of $f(x_{ij})$ is:

$$f'(x_{ij}) = 3x_{ij}^2 - 2x_{ij} \frac{3}{2} a_0 - \delta^* \sqrt{\frac{3Eh^3}{4G_{Ic,j}}} \qquad \textbf{5-24}$$

In the iterative Newton-Raphson method the solution is approximated using an initial value x_{ij} as a close to a real value of a_0 obtained by tested specimens to reduce the number of iterations. The discrepancy of the solution at iteration i is computed using Eq. 5-23 and a new approximation at iteration $i+1$ is obtained using:

$$x_{i+1j} = x_{ij} - \frac{f(x_{ij})}{f'(x_{ij})} \qquad \textbf{5-25}$$

This iteration is carried out until the discrepancy of the last two solutions is below 0.001 mm. For the next increment of δ^* the starting value x_{ij+1} is increased by 0.1 mm compared to x_{i+nj}. The simplicity of this analytical approach allows the implementation of the model in MS Excel enabling fast calculations.

5.3.1 Superposition for different tufting material

The results of the calculation are presented in Figure 5-18 for different tufting materials for the case intermediately bindered reinforcement and a tufting depth of 5.2 mm. The superimposed crack energy release rates (Eq. 5-14) are plotted against the calculated crack length (Eq. 5-25) leading to a predicted delamination toughness by representing the contribution of the resin and tuft elongation, based on tensile behaviour (section 5.1.1), to the delamination toughness. The delamination toughness of the aramid tufted material based on the superposition increases almost linearly and follows closely the experimental

R-curve in the initial part corresponding to the untufted section. However, the delamination toughness of the experimental curve in the untufted section increases with a lower slope than the superimposed toughness. This may be caused by a thinner resin layer at the delamination plane, due to tufting, decreasing the delamination toughness. At a crack length of approximately 63 mm the crack tip reaches the first tuft row and the delamination toughness increases. The superimposed R-curve of the tufted material increases with an initially lower slope than the experimental curve which then changes to a similar slope. The shape of the curve is caused by the non-linear dependence of the crack length on the beam opening displacement at the crack starter film. Furthermore, the stiffness of the tufts in the delamination specimen is higher due to shear stresses at the tuft caused by beam bending, also reducing the tuft strain which increases the apparent stiffness. The plateau region of the superimposed curve occurs at a lower crack energy release rate compared to the experimental curve. This is due to the fact that the model only considers tuft elongation and energy absorption mechanisms like shear and friction at the tuft/resin interface and fibre bridging are not considered in this calculation.

The behaviour of the stainless steel thread in Figure 5-18 is comparable to that of the aramid: the initial untufted region of the modelled tufted material increases equivalently to that of experimental response. At a crack length of 63 mm the crack tip reaches the first tuft row and the slope of the R-curves rises with the slope of the superimposed curve corresponding to that of the experimental one. The smaller difference in crack propagation resistance of the modelled and experimental R-curves, compared to the aramid tufted material, is attributed to the brittleness of the stainless steel thread leading to a relatively larger contribution of thread stretching in this case.

The delamination resistance of the initial untufted region of the superimposed copper tufted material (Figure 5-18) increases following the experimental R-curve corresponding to a crack propagation of up to 67 mm. The subsequent rise of the predicted R-curve differs from that of the experimental curve as a result of the higher ductility (large strain) of the copper wire during the tensile tests compared to the tuft in the delamination specimen and due to the non-

linear relation between the beam opening displacement and crack length. The copper tufts are constrained by the surrounding composite increasing the apparent stiffness. The final slope of the increase in delamination performance is comparable to that of the experimental curve corresponding to almost fully stretched tufts in both cases. As for aramid and stainless steel the plateau region of the modelled R-curve is below the experimental due to consideration of only tuft stretching. However, the difference in plateau values is smaller as a result of the major role of copper tuft ductility.

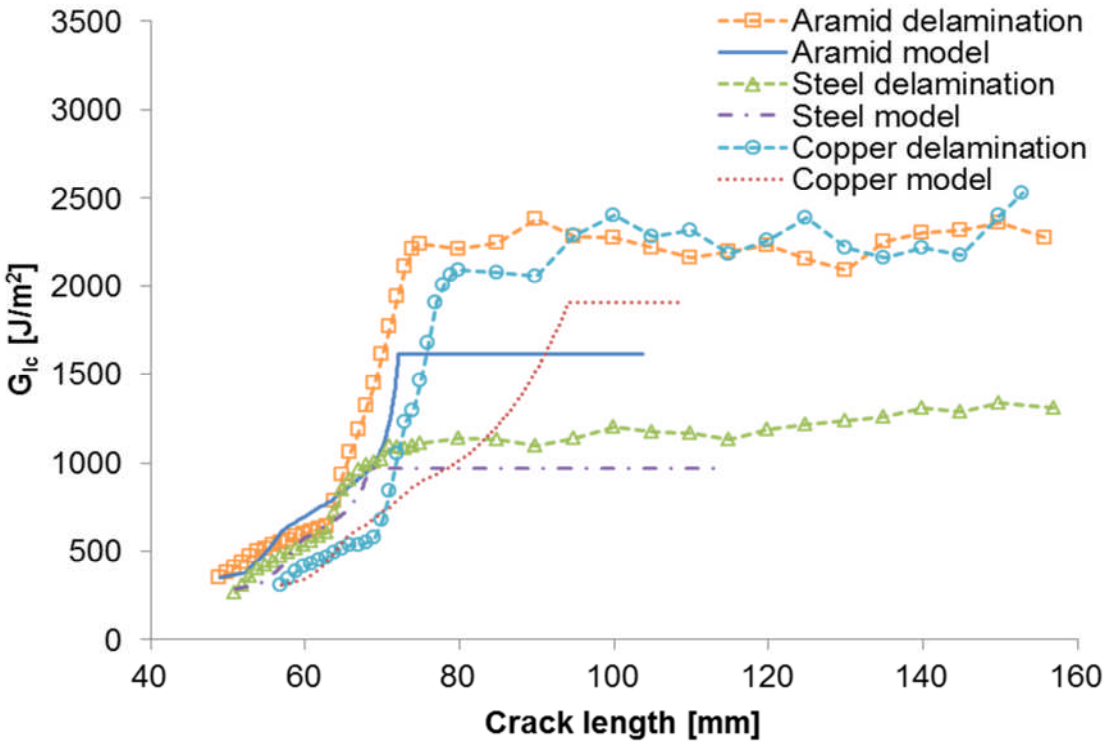

Figure 5-18 R-curves of superimposed control/tuft delamination performance of intermediately bindered material tufted with aramid, stainless steel and copper with a tufting depth of 5.2 mm.

5.3.2 Superposition for different preform materials

Figure 5-19 presents the predicted delamination toughness for laminates with different amount of binder tufted with aramid thread. In all three cases the experimental behaviour in the untufted region is reproduced well by the model. In the undinbered material the first tuft row arrests the crack tip at a crack length of 64 mm; the same phenomenon is observed in the intermediately bindered and the highly bindered materials at the corresponding first tuft location (63 and

61 mm, respectively). The propagation to the third row of tufts occurs at lower slope for the model curves as a result of the non-linear dependence of the beam opening on the crack length. Higher fracture surface stresses increase the delamination toughness for a given crack length leading to an increase in the slope of the superimposed R-curve. At the latest stages of propagation to the third row the model slopes reach values similar to those observed in experiments. Similarly to the results presented in section 5.3.1, the difference in the predicted and experimental plateau region is caused by the consideration of tuft elongation as the only contributing mechanism in tufted materials.

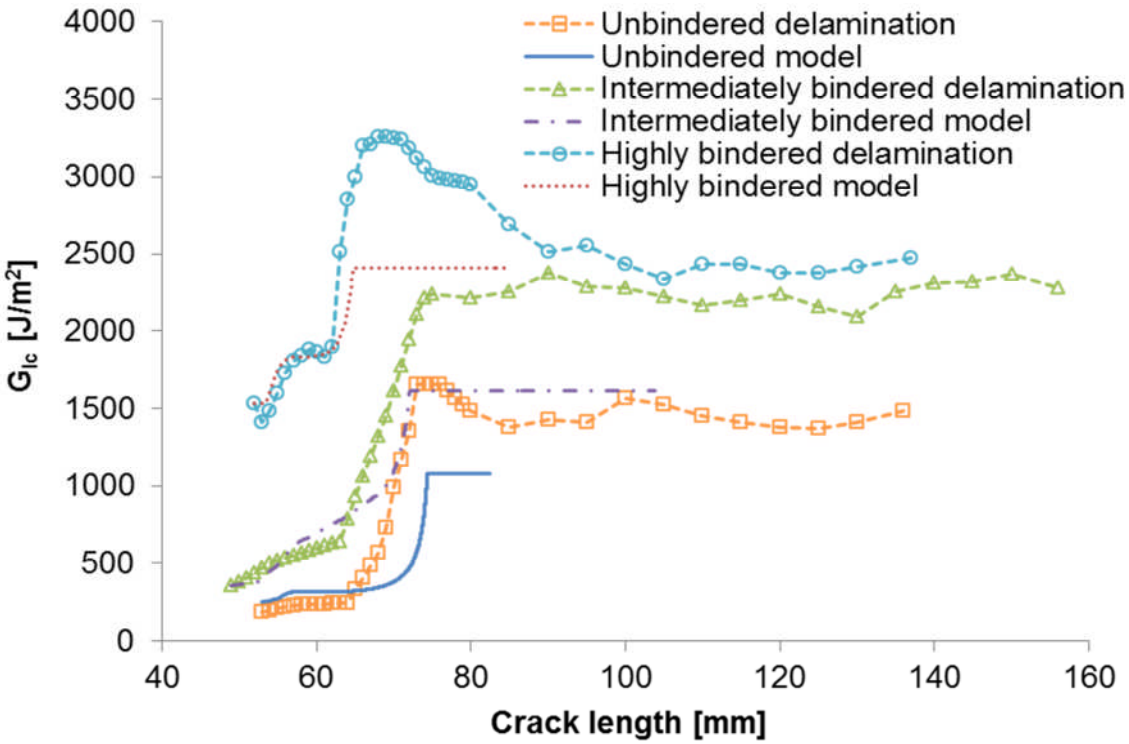

Figure 5-19 R-curves of superimposed control/tuft delamination performance of unbindered, intermediately bindered and highly bindered aramid tufted material. The tufting depth is 5.2 mm for the unbindered and intermediately bindered materials and 4 mm for the highly bindered material.

The superposition reproduces successfully most qualitative characteristics of the behaviour of tufted laminates. The slope in the tufted region increases with increasing toughness of the unreinforced material. This behaviour is followed by the superposition predictions in Figure 5-19. Similarly, the plateau toughness follows the order of toughness of the unreinforced material; this behaviour is also followed by the model results. The decreased superimposed delamination

toughness plotted versus the equivalent calculated crack length causes a lower slope until the tufts are fully stretched.

5.4 Conclusions

The tensile properties of tufting threads are affected by the presence of cured resin, with a drop in properties due to additional constrains in inter-thread movement. Tensile properties are affected by the state of the tuft. The copper wire shows features typical for metals, such as the ductility, whereas the twisted stainless steel thread is brittle. Both metal threads have a lower tensile strength than the aramid thread. The stainless steel thread and the copper wire are capable of reinforcing composite structures by improving their through-the-thickness properties. The thread material and its tensile properties have a high impact on the delamination toughness of composite structures. A thread with high tensile strength is not always preferable as this may be linked to brittleness and may lead to catastrophic failure. Using the copper wire, with its low tensile strength, may not result in a fracture toughness as high as with the aramid thread but due to its significant high ultimate strain several tuft rows bridge the crack opening simultaneously, leading to progressive failure. In general, the insertion of tufts in a highly bindered preform can lead to an improvement of the crack energy release rate of up to 700% compared to an unbindered and untufted preform. The amount of binder alters the delamination properties of composite structures, with and without tufts. Fibre bridging and fracture of non-structural stitching increases with tufting and contributes to an increase in delamination toughness.

An analytical approach of superimposing the crack energy release rates contributed by tuft elongation and the fracture surface stress of the control material was utilised to explain and predict trends in delamination resistance. Generally, it is possible to predict the trends by knowing the delamination resistance of the untufted material and the tensile properties of the tuft material. However, the predictions underestimate the delamination toughness compared to the experimental R-curve as fibre bridging and friction between tuft and the surrounding composite are not considered leading to lower delamination toughness estimates.

6 Influence of tuft depth on delamination behaviour

This chapter investigates the effect of tufting depth on the delamination behaviour using different tufting thread materials. This is carried out using mode I delamination testing of partial tufted specimens at different depths across the delamination interface as described in section 3.2.3. The results of delamination are combined with microscopy observations to explain how changes in tuft length affect failure mechanisms at the delamination interface.

6.1 Delamination performance for different tufting depths

6.1.1 Dependence of delamination response of tufting depths for intermediately bindered material

Representative load-displacement curves of the DCB mode I delamination tests are illustrated in Figure 6-1. All curves show the same characteristics in the initial part: crack initiation occurs at a load between 75 N and 80 N. From that point on the crack propagates through the initial untufted region followed by a linear increase in load up to approximately 125 N. At 125 N the load of the control specimens starts decreasing continuously until specimen fracture, whilst in tufted specimens the crack is shortly arrested by the first tuft row (dotted line) followed by slow propagation to the second or third tuft row in aramid and stainless steel tufted specimens, and fifth or sixth row in copper tufted specimens, leading to a linear increase in load up to the peaks of 208 N and 176 N for aramid tufted (Figure 6-1a) and stainless steel (Figure 6-1b) tufted specimens with a tufting depth of 5.2 mm, respectively, and 190 N for copper (Figure 6-1c) tufted specimens with a depth of 1.0 mm. The maximum load of aramid tufted specimens reduces marginally with decreasing tufting depth: the maximum load of the specimens with a tufting depth of 2.6 mm and 1.0 mm is reduced by 2% and 17%, respectively. Similar behaviour is found with copper tufted specimens: the maximum load of the 1.0 mm and 2.6 mm deep tufted specimens is reduced by 6% compared to the 5.2 mm deep tufted specimens.

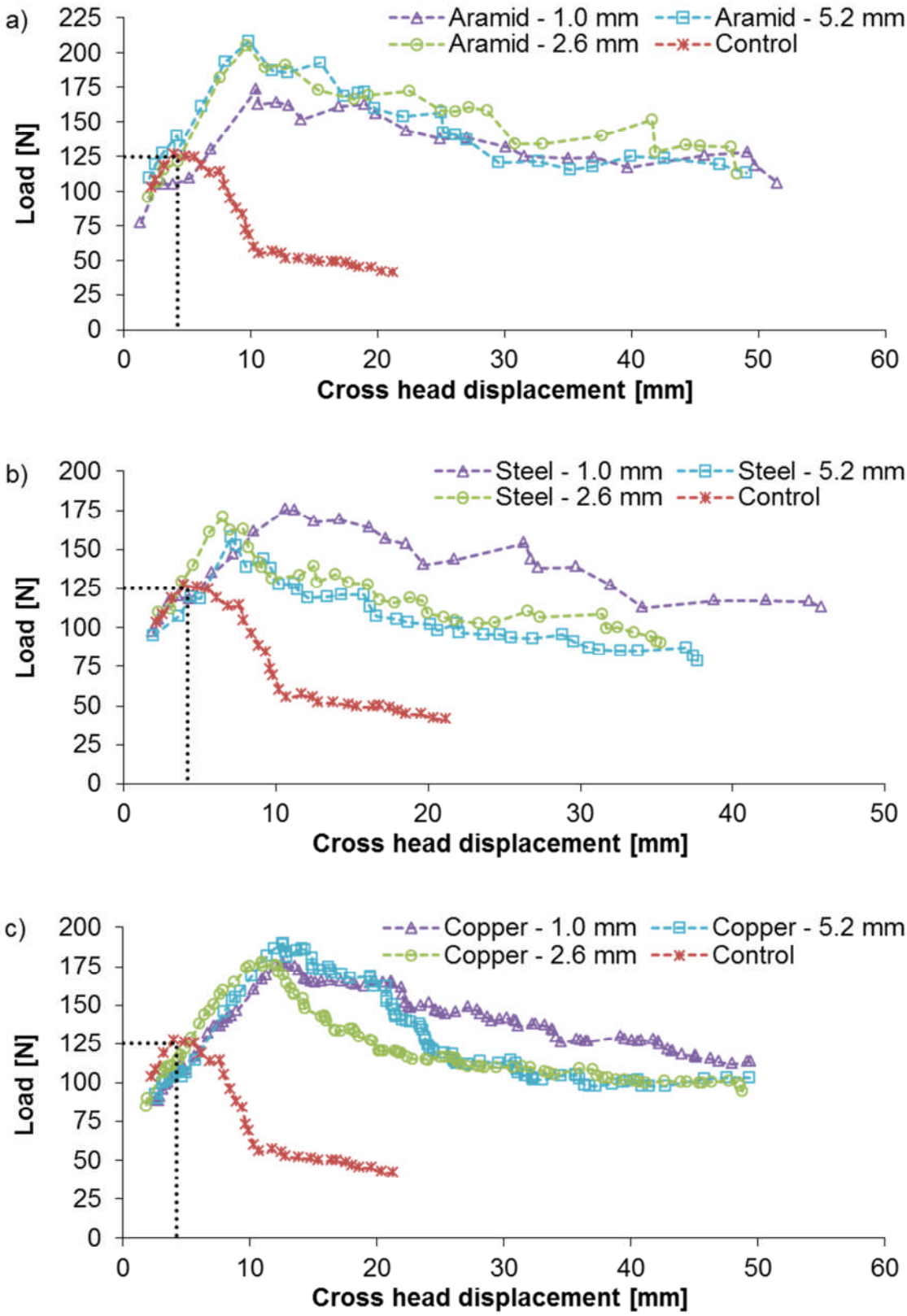

Figure 6-1 Representative load-displacement curves of: a) aramid, b) stainless steel and c) copper tufted intermediately bindered materials with tufting depths of 1.0 mm, 2.6 mm and 5.2 mm. Dotted lines represent the first tuft row.

The opposite effect occurs with stainless steel tufts: the 2.6 mm deep tufted specimens have a maximum load 3% lower than that of the 1.0 mm deep tufted specimens, whilst the maximum load of the specimens with a tufting depth of 5.2 mm is reduced by 10% compared to that of 1.0 mm deep tufted specimens. Once the first tuft row ruptures the high amount of energy accumulated is partially released so that the crack propagates abruptly, breaking up to two more tuft rows before being arrested by tufts leading to a decrease in load. This behaviour continues until final fracture of the specimen with relatively low variations in load during the entire delamination process, caused by periodic crack arrests and fibre bridging and undulation, both leading to an increase in load.

The crack resistance curves for all tested materials are presented in Figure 6-2. Every series point represents the average value out of four specimens for each type of specimen. Although the load-displacement curves are very similar, the R-curves in Figure 6-2 show a significant effect of the tufting depth on the delamination resistance between the materials with a tufting depth of 1.0 mm, 2.6 mm and 5.2 mm. Crack initiation of tufted materials occurs at a relatively close range of toughness values (Table 6-1). The crack propagates with an increasing crack energy release rate up to approximately 600 J/m^2 corresponding to a crack propagation of 15 mm, i.e. reaching the first tuft row in tufted specimens, marked as a dotted line in Figure 6-2. From this point on the delamination behaviour of untufted and tufted specimens differs: in untufted control specimens the crack propagates in a stable manner until final specimen fracture, occasionally arrested by fibre bridging and undulation leading to slight increases in delamination toughness. In tufted specimens, the crack continues propagating slowly reaching the second or third tuft row (solid lines) in aramid (Figure 6-2a) and stainless steel (Figure 6-2b) tufted materials and fifth or sixth tuft row in copper (Figure 6-2c) tufted materials. Once the first tuft row ruptures, the crack propagates until being arrested by subsequent tuft rows leading to slip-stick behaviour and a plateau in the R-curves.

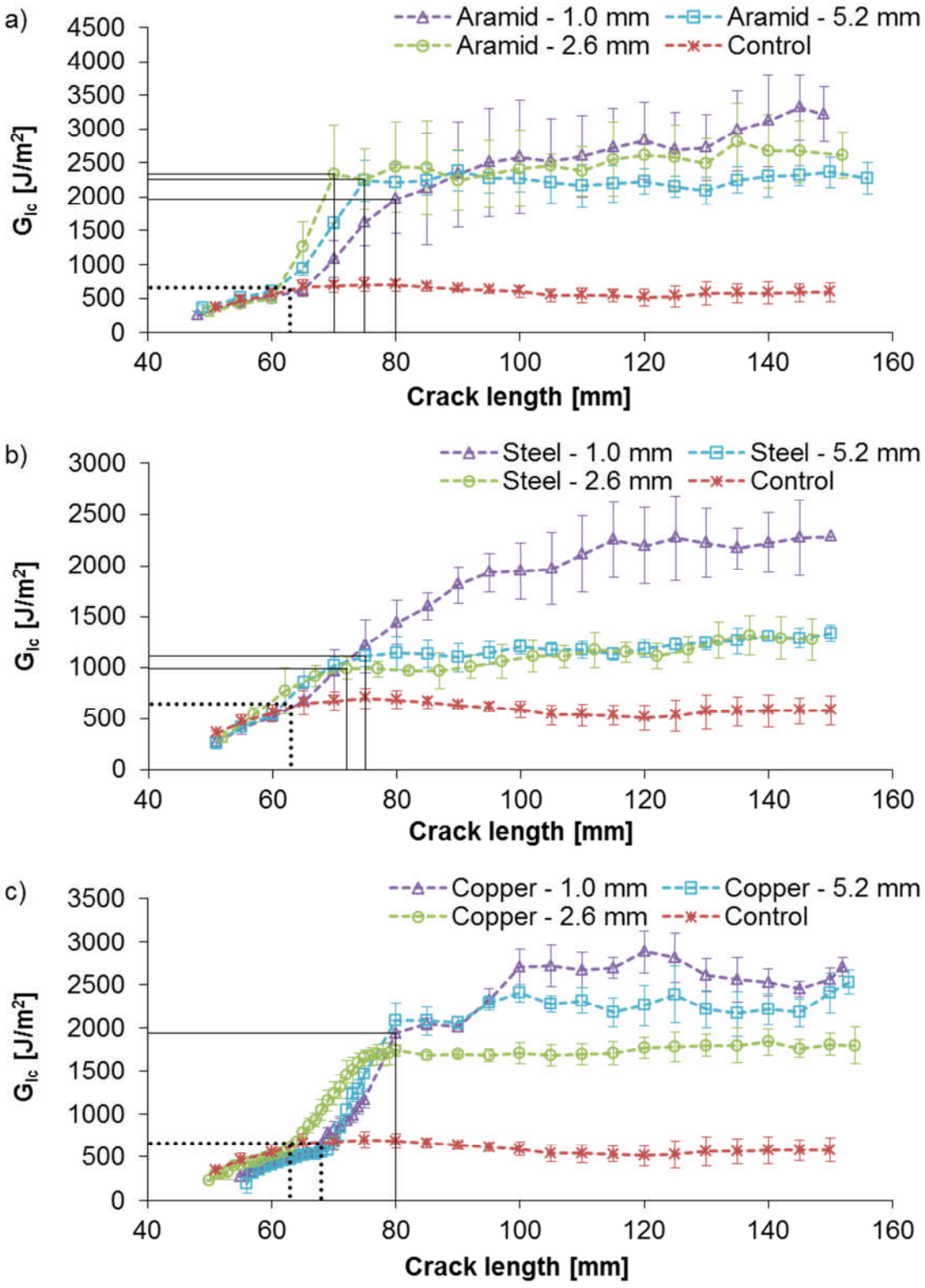

Figure 6-2 Average crack resistance curves of: a) aramid, b) stainless steel and c) copper tufted intermediately bindered materials with tufting depths of 1.0 mm, 2.6 mm and 5.2 mm. Dotted and solid lines represent first tuft and third or sixth row, respectively. Error bars represent one standard deviation.

The results show an increase in crack propagation resistance for all tufted materials with aramid performing better than copper, followed by stainless steel. A tufting depth of 1.0 mm, 2.6 mm and 5.2 mm using stainless steel improves the delamination resistance by around 270%, 105% and 110%, respectively, in comparison to the untufted control material. The improvement by tufting 1.0 mm, 2.6 mm and 5.2 mm deep using aramid is around 410%, 350% and 295%, respectively. Tufting with copper wire improves the delamination toughness by up to 360%, 200% and 290% using a tufting depth of 1.0 mm, 2.6 mm and 5.2 mm, respectively. The average values of the strain energy release rate and the standard deviation for each type of material are summarised in Table 6-1. The results emphasise the effect of tufting depth on the delamination resistance: for the twisted aramid and stainless steel thread the constraints in rotation and elongation caused by the surrounding composite, as discussed in section 5.1.2, rise with increasing tuft depth leading to reduced tuft elongation and delamination toughness. However, the stainless steel tufted material with a tuft depth of 2.6 mm and 5.2 mm show similar delamination toughness. This may be caused by the brittleness of the stainless steel thread resulting in comparable elongations for both tuft depths and being affected less by the compression of the surrounding composite. The copper wire is not subject to the same constraints due to its untwisted structure, leading to larger elongations with increasing tuft depth. This results in longer crack bridging, improving the delamination performance with increasing tuft depth. For aramid and stainless steel, the larger tuft elongation at lower tuft depth enhances fibre bridging, increasing further the delamination resistance, whilst for the copper wire this occurs at a high tuft depth.

Figure 6-2 and Table 6-1 also show that the variability increases with decreasing tufting depth for aramid and stainless steel tufted material: from a tuft depth of 1.0 mm to 2.6 mm the variability of the aramid tufted material decreases by 26% and from 2.6 mm to 5.2 mm by 38%, whilst for stainless steel it reduces by 46% and 44%, respectively. This is a result of the ductility of the thread material and the increasing constraint in thread mobility with increasing tuft depth. The difference in variability between the stainless steel

tufted materials is lower than that between the aramid tufted materials due to the brittleness of the steel thread creating a smaller range the thread may break in. This range is further decreased with increasing tuft depth; the constraints in thread mobility caused by the surrounding matrix leads to lower delamination toughness resulting in a lower range for different delamination performances. The variability of the copper tufted material does not follow this trend, with 2.6 mm deep tufted material showing the lowest variability, followed by 5.2 mm and 1.0 mm deep tufted material. Since the copper wire is a homogeneous single strand and untwisted wire it is less affected by the surrounding composite leading to small differences in variability between the copper tufted material and to the independence of tuft depth.

Table 6-1 Average crack energy release rates for crack initiation and propagation of intermediately bindered untufted and aramid, copper and stainless steel tufted material with tuft depths of 1.0 mm, 2.6 mm and 5.2 mm (standard deviations are reported in brackets).

Thread material		Control	Aramid	Copper	Steel
$G_{Ic,\,ini}$ (1.0 mm)	[J/m^2]	331 (±15)	202 (±63)	282 (±21)	237 (±10)
$G_{Ic,\,ini}$ (2.6 mm)	[J/m^2]	331 (±15)	227 (±9)	229 (±15)	262 (±31)
$G_{Ic,\,ini}$ (5.2 mm)	[J/m^2]	331 (±15)	306 (±46)	272 (±18)	246 (±32)
G_{Ic} (1.0 mm)	[J/m^2]	579 (±110)	2950 (±537)	2674 (±239)	2157 (±309)
G_{Ic} (2.6 mm)	[J/m^2]	579 (±110)	2599 (±399)	1741 (±138)	1189 (±167)
G_{Ic} (5.2 mm)	[J/m^2]	579 (±110)	2286 (±247)	2262 (±217)	1230 (±93)

6.1.2 Dependence of delamination response of tufting depth for highly bindered material

The highly bindered material, tufted fully with aramid thread, was tested in mode I for thicknesses of 4 mm and 8 mm. The representative load-displacement curves, shown in Figure 6-3, indicate a much higher crack initiation load for the tufted 8 mm thick specimen compared to the 4 mm thick and untufted control specimens. This is caused by the greater stiffness of 8 mm thick specimens. The maximum load of 338 N for the thicker specimen is reached after the crack initiation at an opening displacement of 12 mm; due to the high stiffness the half

beams do no bend as much as of thinner specimens leading to less peeling and faster crack propagation. This results in the crack reaching the first tuft row (dotted line) at lower openings. The crack continues propagating slowly to the second or third tuft row (solid line), whilst the load reaches its maximum. After rupture of the first tuft row the crack propagates and load decreases continuously but at changing rates as the crack is periodically arrested by tufts. In addition, the high amount of binder enhances fibre bridging as the fibres stick to the aramid thread also leading to small variations in load. The 4 mm thick specimen reaches a maximum load of 139 N at a beam opening of 28 mm, once the crack reaches the second or third tuft row (solid line). The rate of load increase from initiation to the peak is lower compared to the thicker specimen as the bending of the beam halves is greater due to the reduced stiffness leading to slower crack propagation and higher opening displacement at maximum load. The load of the thinner material decreases continuously, also showing small variations in load due to tuft and fibre bridging and undulation occurring periodically. The untufted control specimen with a thickness of 4 mm reaches a maximum load of 106 N. The increase in load is caused by fibre bridging and undulation, which also occurs throughout the specimen delamination, leading to light increases in load until final failure of the specimen. The reduced stiffness for the 4 mm tufted specimen and control specimen compared to the 8 mm tufted specimen leads to a final opening displacement around double of that of the thicker specimen.

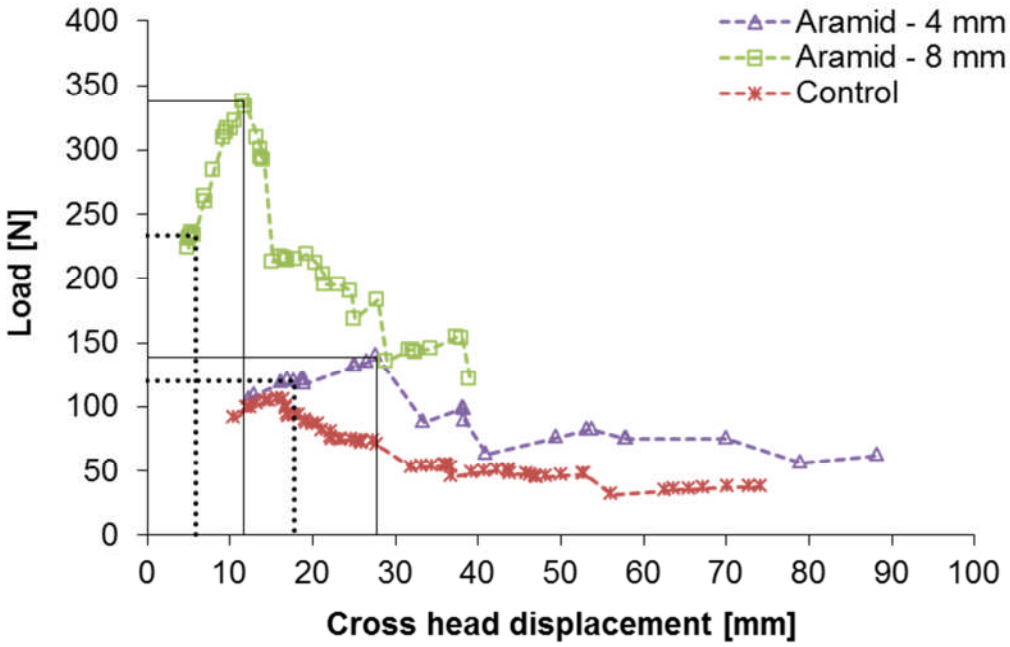

Figure 6-3 Representative load-displacement curves of highly bindered untufted and aramid tufted specimens with a thickness of 4 mm and 8 mm. Dotted and solid lines represent first and third tuft row, respectively.

The corresponding average R-curves are presented in Figure 6-4. These are evaluated by interpolation of the crack energy release rate at specific increments of crack length and averaging of five specimens. The crack initiation toughness values (Table 6-2) are within the range of standard spread of results but could also be indicating a slightly lower initiation toughness of the tufted materials. For the control material the crack energy release rate increases linearly up to a crack length of 59 mm caused by matrix toughening and initial fibre bridging due to the high amount of binder. From that point on the delamination toughness decreases reaching a plateau with an averaged value of 1264 J/m^2 until final failure of the specimens with slight variations in energy release rate due to fibre bridging and undulation. The crack in the tufted materials propagates up to 62 mm and 64 mm for the 4 mm and 8 mm thick specimens, respectively, reaching the first tuft row (dotted lines) and leading to an increase of the delamination toughness. Once the crack propagates to the second or third tuft row (solid lines), the first row ruptures and the crack continues propagating accompanied by a decrease in crack energy release rate. The high peak before the drop is probably caused by extensive fibre

bridging generated by the elongating tufts. The average delamination toughness values of the 4 mm and 8 mm thick specimens are presented in Table 6-2. These results show a negligible effect of the tufting depth on the delamination toughness of highly bindered material. The energy required to debond the tuft/composite interface and pull-out the tuft is too high due to the high amount of binder. In addition, the high amount of binder improves the tuft/composite interface, constraining the movements of the tufts close to the specimen fracture surface and suppressing the effect of the tuft depth. The average delamination toughness of the different cases is summarised in Table 6-2. As shown by the error bars in Figure 6-4 and the values in Table 6-2, variability is higher for the thinner tufted material compared to the thicker one. The reason may be the larger elongation of the tufts in the thinner composite, due to the lower specimen stiffness and reduced constraints in tuft movement caused by the surrounding composite, leading to different delamination performance. The control material has the lowest variability as the specimens do not depend on the performance of tufts leading to similar delamination performance of the single specimens.

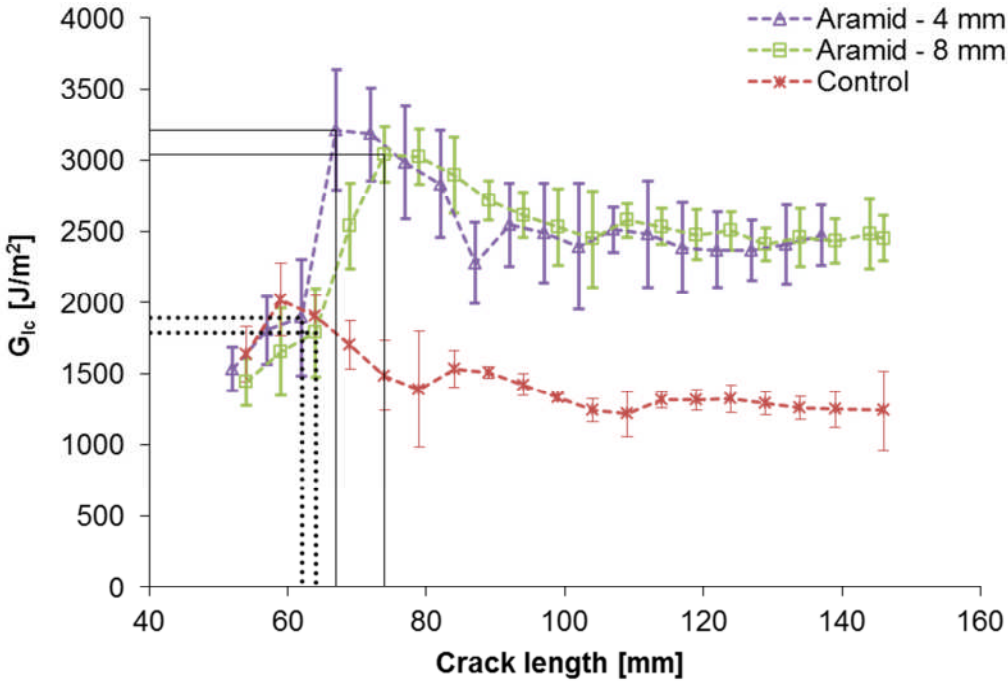

Figure 6-4 Averaged R-curves of highly bindered untufted and aramid tufted DCB specimens with thicknesses of 4 mm and 8 mm. Dotted and solid lines represent first and third tuft row, respectively. Error bars represent one standard deviation.

Table 6-2 Average crack energy release rates for crack initiation and propagation of highly bindered untufted and aramid tufted specimens of 4 mm and 8 mm thickness (standard deviations are reported in brackets).

Thread material		Control	Aramid
$G_{Ic,\ ini}$ (4 mm)	[J/m^2]	1591 (±156)	1513 (±145)
$G_{Ic,\ ini}$ (8 mm)	[J/m^2]	-	1440 (±168)
G_{Ic} (4 mm)	[J/m^2]	1264 (±160)	2444 (±308)
G_{Ic} (8 mm)	[J/m^2]	-	2460 (±221)

6.1.3 Statistical significance of differences in delamination behaviour between different tufting depths

As reported in Tables 6-1 and 6-2 delamination resistance results and standard deviations are similar for the 2.6 mm and 5.2 mm deep stainless steel tufted materials and the 4 mm and 8 mm thick aramid tufted specimens. In order to evaluate the statistical significance of the results two different tests were carried out: the two-tailed Welsh's t-test, for testing the hypothesis that the averaged crack delamination resistances are statistically different and the one-sided f-test to test if the standard deviations are statistically different. For both tests the materials with the same thread type are compared. The null hypothesis is that there is no difference in the obtained average delamination resistance and the standard deviation.

The Welsh's t-test uses to statistical value t_T, and the degrees of freedom df, calculated using the following equations, to test the null hypothesis:

$$t_T = \frac{\bar{X}_1 - \bar{X}_2}{\sqrt{\frac{s_1^2}{N_1} + \frac{s_2^2}{N_2}}} \qquad \textbf{6-1}$$

$$df = \frac{\left(\frac{s_1^2}{N_1} + \frac{s_2^2}{N_2}\right)^2}{\frac{s_1^4}{N_1^2 \nu_1} + \frac{s_2^4}{N_2^2 \nu_2}} \qquad \textbf{6-2}$$

with $\nu_{1/2} = N_{1/2} - 1$.

Here $\bar{X}_1$, $\bar{X}_2$ are the mean values, s_1 and s_2 the variance, N_1 and N_2 the number of values and ν_1 and ν_2 the degree of freedom associated with the variances, respectively. The f-test is carried out by calculating the ratio f of the squared standard deviations as follows:

$$f = \frac{\sigma_1^2}{\sigma_2^2} \qquad \textbf{6-3}$$

Table 6-3 t-test results for intermediately bindered aramid, copper and stainless steel tufted specimens with tuft depths of 1.0 mm, 2.6 mm and 5.2 mm and highly bindered aramid tufted specimens with 4 mm and 8 mm thickness.

Compared specimen types	t	df	Conclusion
Aramid – 1.0 mm – 2.6 mm	3.56	76.62	*Null hypothesis is rejected*
Aramid – 1.0 mm – 5.2 mm	7.56	48.38	*Null hypothesis is rejected*
Aramid – 2.6 mm – 5.2 mm	5.37	92.05	*Null hypothesis is rejected*
Copper – 1.0 mm – 2.6 mm	51.69	<1	*Null hypothesis is rejected*
Copper – 1.0 mm – 5.2 mm	19.65	<1	*Null hypothesis is rejected*
Copper – 2.6 mm – 5.2 mm	32.68	<1	*Null hypothesis is rejected*
Steel – 1.0 mm – 2.6 mm	17.53	50.37	*Null hypothesis is rejected*
Steel – 1.0 mm – 5.2 mm	17.83	39.68	*Null hypothesis is rejected*
Steel – 2.6 mm – 5.2 mm	1.64	1437	*Failed to reject null hypothesis*
Aramid – 4 mm – 8 mm	0.40	1910	*Failed to reject null hypothesis*

Tables 6-3 and 6-4 show the results for the t-values and f-values, degrees of freedom and the consequence. The null hypothesis is rejected if the results are statistically different with a confidence level of more than 95%. The results in Table 6-3 reveal that there is no difference between the 2.6 mm and 5.2 mm deep stainless steel tufted and intermediately bindered materials and 4 mm and 8 mm thick highly bindered specimens in terms of crack delamination resistance, whilst all other comparisons prove a difference. The reason for the similar delamination toughness of the stainless steel tufted material may be the brittleness of the thread leading to the same tuft elongation independent of the tuft depth and the corresponding constraints in tuft movement by surrounding composite. Such constraints are increased by the large amount of binder in the

highly bindered material resulting in comparable tuft elongations and delamination performance in the 4 mm and 8 mm thick specimens. The results in Table 6-4 show that the null hypothesis is rejected for any standard deviation confirming that variability in delamination response is affected by tuft depth in all cases.

Table 6-4 f-test results for intermediately bindered aramid, copper and stainless steel tufted specimens with tuft depths of 1.0 mm, 2.6 mm and 5.2 mm and highly bindered aramid tufted specimens with 4 mm and 8 mm thickness.

Compared specimen types	f	N_1/N_2	Conclusion
Aramid – 1.0 mm – 2.6 mm	1.81	41/59	*Null hypothesis is rejected*
Aramid – 1.0 mm – 5.2 mm	4.72	41/87	*Null hypothesis is rejected*
Aramid – 2.6 mm – 5.2 mm	2.61	59/87	*Null hypothesis is rejected*
Copper – 1.0 mm – 2.6 mm	2.98	223/273	*Null hypothesis is rejected*
Copper – 1.0 mm – 5.2 mm	1.22	224/255	*Null hypothesis is rejected*
Copper – 2.6 mm – 5.2 mm	2.45	255/273	*Null hypothesis is rejected*
Steel – 1.0 mm – 2.6 mm	3.43	37/59	*Null hypothesis is rejected*
Steel – 1.0 mm – 5.2 mm	11.08	37/67	*Null hypothesis is rejected*
Steel – 2.6 mm – 5.2 mm	3.23	59/67	*Null hypothesis is rejected*
Aramid – 4 mm – 8 mm	1.94	83/125	*Null hypothesis is rejected*

6.2 Delamination fracture mechanisms for different tuft depths

As described in section 5.1.3 the thread debonds from the surrounding matrix starting at the specimen delamination plane followed by propagation in the direction of the tufting loop and seam. With an increased tufting depth the debonding crack requires more energy for full thread debonding leading to a thread rupture rather than a pull-out. Figures 6-5 and 6-6 show scanning electron micrographs of the fracture surfaces of the DCB specimens with aramid and stainless steel tufts, respectively. The 2.6 mm aramid tuft in Figure 6-5a shows a highly deformed fracture state compared to the thread fracture for 5.2 mm long tufts (Figure 6-5b). This can be attributed to greater constraining of

longer tufts by the surrounding composite. The expected deformation of tufts during mode I delamination includes rotation due to the thread twist and stretching in the axial direction. These modes of deformation are constrained by compression by the surrounding composite. The constraint becomes more severe with greater tufting depth. The energy consumed during delamination includes contributions from thread deformation and fracture as well as failure and friction at the thread/composite interface. The balance between the different contributions is governed by the relative energies required for each of them. The energy release rate corresponding to interfacial contributions scales up with increasing tufting depth due to the linear increase in tuft surface, whilst that corresponding to tuft fracture remains constant with increasing depth as the cross sectional area does not change. Therefore, as the tuft depth increases tuft fracture becomes the lower energy path and tufts fail early resulting in lower accumulated energy due to failure and friction at the interface. This results in lower toughness as the depth increases.

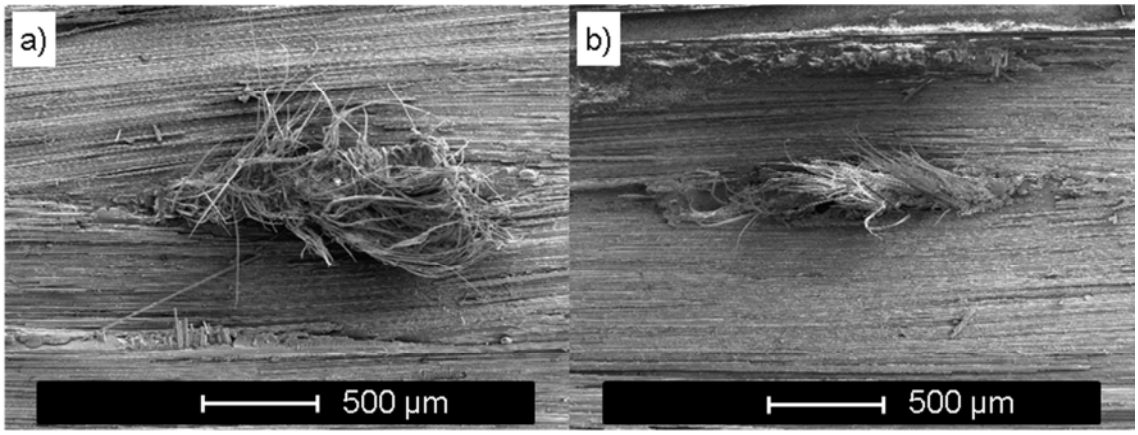

Figure 6-5 Micrograph of aramid thread at fracture surface of intermediately bindered material with a tuft depth of: a) 2.6 mm and b) 5.2 mm.

The micrographs illustrated in Figure 6-6 show similar fracture surfaces for stainless steel threads tufted at depths of 2.6 mm and 5.2 mm, respectively. This is in line with the delamination test results in Figure 6-2 and the statistical significance test results (Table 6-3), showing the same level of toughness. This difference compared to the behaviour to aramid tufting can be attributed to the more brittle nature of the stainless steel thread (Figure 5-1) which is not affected by the constraints in movement caused by the surrounding composite.

The interfacial contributions are governed by the structure of the thread, fibre architecture of the composite and the material of thread and composite. The latter can be related to the large amount of binder in the highly bindered material leading to significant amount of energy required to debond the tuft/composite interface resulting in rupture of the tufts as shown in Figure 5-14b for the 4 mm thick specimen and Figure 6-7 for the 8 mm thick specimen. In addition, the high amount of binder constraints the movements of the tufts close to the fracture surface and suppresses the effect of the tuft depth. This is confirmed by the results in Figures 5-15 and 6-7b, showing a fractured tuft at the delamination surface of a 4 mm and an 8 mm thick specimen, respectively, displaying the same fracture, indicating an equivalent amount of elongation. Furthermore, the resin rich channels between the tufts in the 4 mm thick specimen, as reported in section 5.2.2, are also present in the 8 mm thick specimen as shown in Figure 6-7a. These channels can create crack initiation sites, raising the susceptibility of the materials to crack propagation and preventing an increase in delamination toughness of the material.

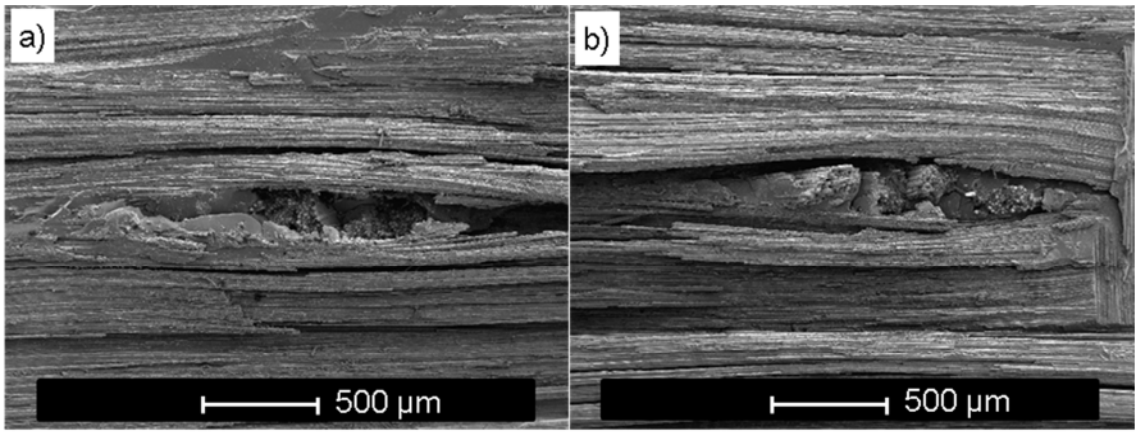

Figure 6-6 Micrograph of stainless steel thread at fracture surface of intermediately bindered material with a tuft depth of: a) 2.6 mm and b) 5.2 mm.

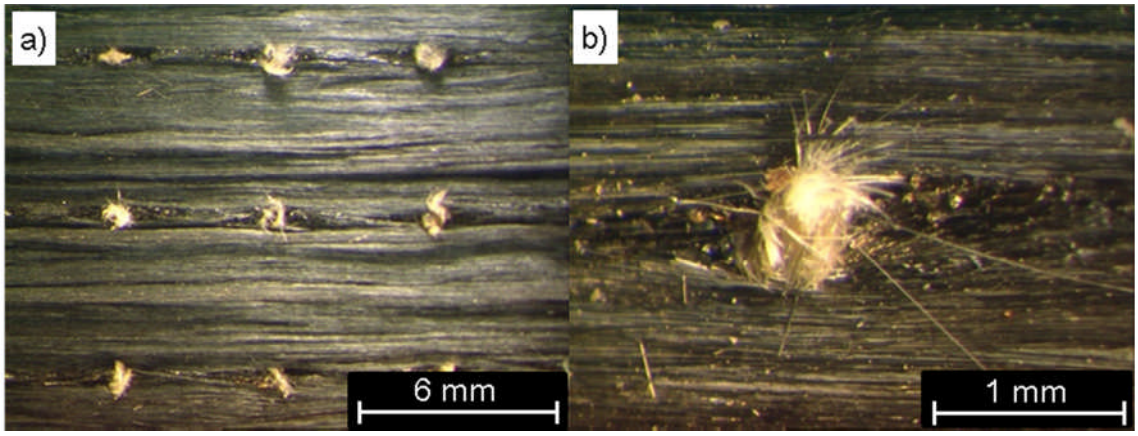

Figure 6-7 Micrograph of aramid thread in highly bindered material with a tuft depth of 8 mm: a) delamination fracture surface and b) ruptured tuft at delamination surface.

Specimens with a tufting depth of 1.0 mm fail by tufts being pulled-out of the substrate as shown in Figure 6-8. During this process high amount energy is required to debond the entire tuft including the loops. This energy is released slowly in the form of friction between the tufts and the surrounding composite. This and the rotational movement and axial elongation of the tufts before pull-out, due to reduced constraints in movement by the relatively thin surrounding composite, lead to high delamination toughness. Figure 6-8a shows copper tuft loops on the fracture surface pulled-out of the opposite beam half (Figure 6-8b) leaving imprints in the composite. This process also leads to fibre bridging, as shown in Figure 6-8b of fibres sticking to the tuft threads. Figure 6-8c shows pulled aramid tuft loops leading to fibre bridging (Figure 6-8d) covering most of the imprints of the tufts (Figure 6-8d). The amount of friction during the frictional pull-out depends on several factors, such as resin inside the tuft and the loop length. After resin infusion, resin cures inside the tufts in-between the threads and filaments. During delamination testing the threads and wire are straightened and stretched crushing the resin inside the threads. Depending on the amount of resin and the degree of thread twist within a tuft the frictional surface between the tuft and the surrounding composite can vary affecting the force of friction and the closure traction of the tufts. In addition, it is difficult to achieve a consistent loop length. Tufts with shorter loops can be pulled-out

faster leading to a lower delamination resistance increasing the variability of delamination test results of 1.0 mm short tufts compared to the longer tufts.

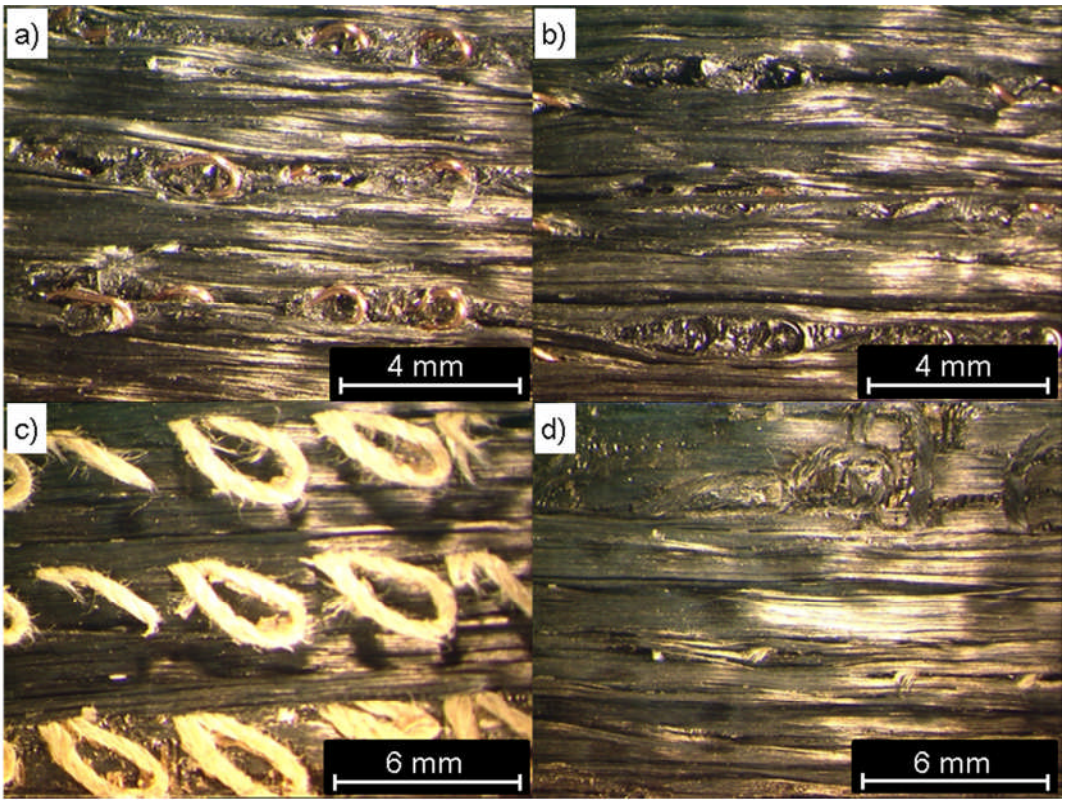

Figure 6-8 Tufting loops pulled-out of specimens with tuft depth of 1.0 mm: a) cooper tufts, b) imprints of copper loops, c) aramid loops and d) imprints of aramid loops.

6.3 Dependence of bridging law on tuft depth

The bridging laws corresponding to the delamination tests are calculated using Eqs. 5-1 – 5-4, whilst the thread and wire test curves are calculated according to Eqs. 5-5 and 5-6 adapting the thread/wire strain to the corresponding tuft depth and the elongation on the average fracture stress and crack opening displacement of the DCB specimens with the corresponding tuft depth.

6.3.1 Bridging law at different tufting depths for intermediately bindered material

Figure 6-9 illustrates the bridging laws in the case of the intermediately bindered material tufted at different depths and their comparison with thread behaviour. The slopes of the thread tests corresponding to 2.6 mm and 5.2 mm tuft depth match the slopes of the increase in stress for aramid and stainless steel tufted

laminates with a tuft depth of 2.6 mm and 5.2 mm, respectively, indicating that the increase in fracture stress is mostly attributed to tuft bridging (Figure 6-9a, b). The increase in stress is caused by the activation of the first tuft row once the crack reaches its position, marked with black dashed-dotted, dotted and large dashed lines for materials with a tufting depth of 1.0 mm, 2.6 mm and 5.2 mm, respectively, and summarised in Table 6-5. The slope of the stress curve of 1.0 mm aramid and stainless steel tufted material is reduced compared to the other tuft depths as a result of a change in failure mechanism. While the tufts at tuft depths of 2.6 mm and 5.2 mm rupture at the delamination plane, as shown in Figure 5-6b, the majority of the tufts in materials with a tuft depth of 1.0 mm are pulled-out during testing. Hence, the failure mechanism changes from axial elongation and rotational movement with subsequent rupture to frictional pull-out confirming the results in delamination performance (Figure 6-2). This behaviour results in decreased fracture surface stresses compared to a tuft elongation and rupture at the delamination plane.

The behaviour of copper tufts (Figure 6-9c) differs from that of aramid and stainless steel, mainly because the wire is ductile and not twisted (Figure 5-1). It has been observed that during testing four to six copper tuft rows bridge the delamination crack. This is attributed to the ductility of the copper wire leading to high elongation of the tuft rows further behind the crack tip, confirming the large opening displacement observed in Figure 6-9c. The bridging zone for 1.0 mm, 2.6 mm and 5.2 mm deep copper tufted material is fully developed at crack openings greater than for the stainless steel tufted materials (Table 6-5). However, the aramid tufted materials reach a relatively similar opening to copper. The increase in fracture stress of the copper tufted specimens occurs at the first tuft row, marked with black dashed-dotted, dotted and large dashed lines for materials with a tufting of 1.0 mm, 2.6 mm and 5.2 mm, respectively, and starting at a crack opening of around 0.07 mm for all tuft depths.

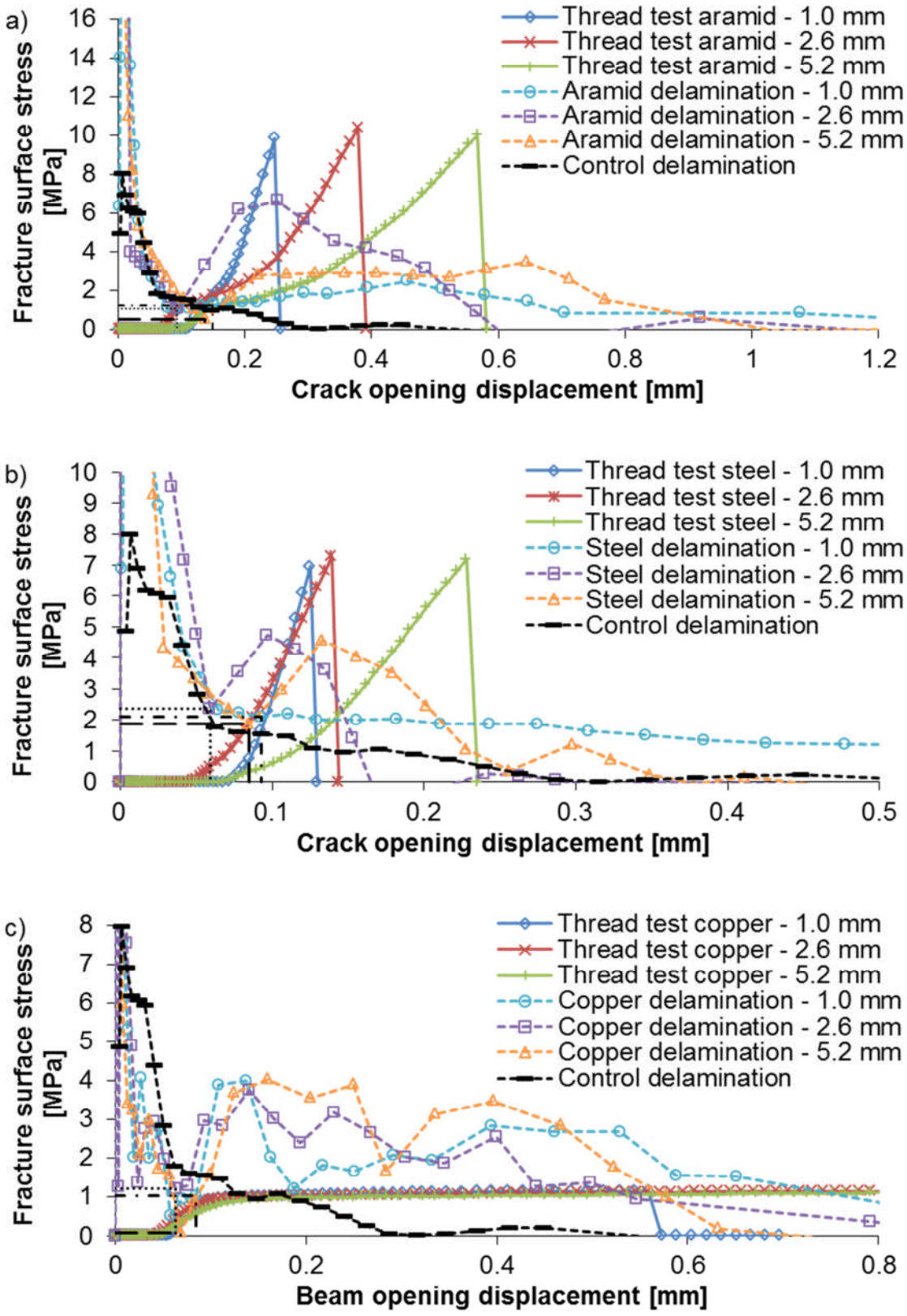

Figure 6-9 Fracture stress-beam opening and thread test curves corresponding to tuft depths of 1.0 mm, 2.6 mm and 5.2 mm of: a) aramid and b) stainless steel and c) copper tufted intermediately bindered material.

Due to the fact that the homogenous copper wire is untwisted, it elongates during delamination without rotational movements. Furthermore, it is expected that the bonding behaviour of copper and the resin system is weaker compared to that of fibrous tufting threads, requiring less energy to propagate the debonding crack along the tuft in specimen thickness direction and, therefore, less dependent on the tuft depth. A significant difference between the tuft depths is the drop in stress at a crack opening of approximately 0.2 mm which increases with decreasing tuft depth. This is attributed to the tuft elongation generating surface stresses; longer tufts elongate more than shorter, maintaining surface stresses for longer, whereas short tufts elongate less and rupture earlier, leading to an earlier drop in surface stresses. This is also the reason for the increased crack propagation resistance for 5.2 mm deep tufted copper material compared to a tuft depth of 2.6 mm: the high elongation of 5.2 mm long tufts leads to longer tuft bridging improving the delamination performance. However, the failure mechanism of specimens with a tuft depth of 1.0 mm changes to frictional pull-out of the tufts leading to high delamination toughness due to the high energy consumption caused by friction and tow bridging.

Table 6-5 Crack opening displacements at first tuft position and at fully developed bridging zone for untufted and aramid, copper and stainless steel tufted material with tufting depths of 1.0 mm, 2.6 mm and 5.2 mm.

Thread material		**Control**	**Aramid**	**Copper**	**Steel**
First tuft (1.0 mm)	[mm]	-	1.00	0.70	0.07
First tuft (2.6 mm)	[mm]	-	0.90	0.70	0.06
First tuft (5.2 mm)	[mm]	-	0.14	0.70	0.09
Plateau (1.0 mm)	[mm]	0.56	3.20	3.30	2.40
Plateau (2.6 mm)	[mm]	0.56	0.58	0.92	0.17
Plateau (5.2 mm)	[mm]	0.56	1.00	0.70	0.37

6.3.2 Bridging law at different tufting depths for highly bindered material

Figure 6-10 illustrates the bridging laws for the highly bindered material tufted at different depths and their comparison with thread behaviour. The fracture stress curves of the 4 mm and 8 mm thick highly bindered material show high variations in stress at very low crack opening, caused by matrix toughening and fibre bridging enhanced by the large amount of binder. Due to the high stiffness of the 8 mm thick specimen and the associated effect on the crack propagation the activation of the first tuft row (black dotted line) occurs at a lower beam opening than for the 4 mm thick specimen (Table 6-6). The subsequent increase in stress is generated by tuft bridging up to three tuft rows leading to peaks in stresses of 9.7 MPa and 6.8 MPa for the 8 mm and 4 mm thick laminates, respectively. Once the first tuft row ruptures the crack propagates and the stress decreases with several transient peaks and troughs due to bridging of subsequent tuft rows, fibre bridging and undulation. The stress becomes negligible indicating a fully developed bridging zone (Table 6-6). The stress of the corresponding thread test curves starts rising once the crack reaches the first tuft rows. The slopes of the increase in stress are lower than the delamination fracture surface stresses. This is caused by the deviation from ideal tuft elongation behaviour within the composite material. The maximum fracture surface stress of the delamination results are lower than the maximum thread tensile stresses due to the constraints in tuft movement caused by the surrounding composite. Compared to the intermediately bindered material the fracture stress of the highly bindered material is relatively high which is probably caused by the large amount of binder material improving the fibre/resin interface and increasing the surface stress.

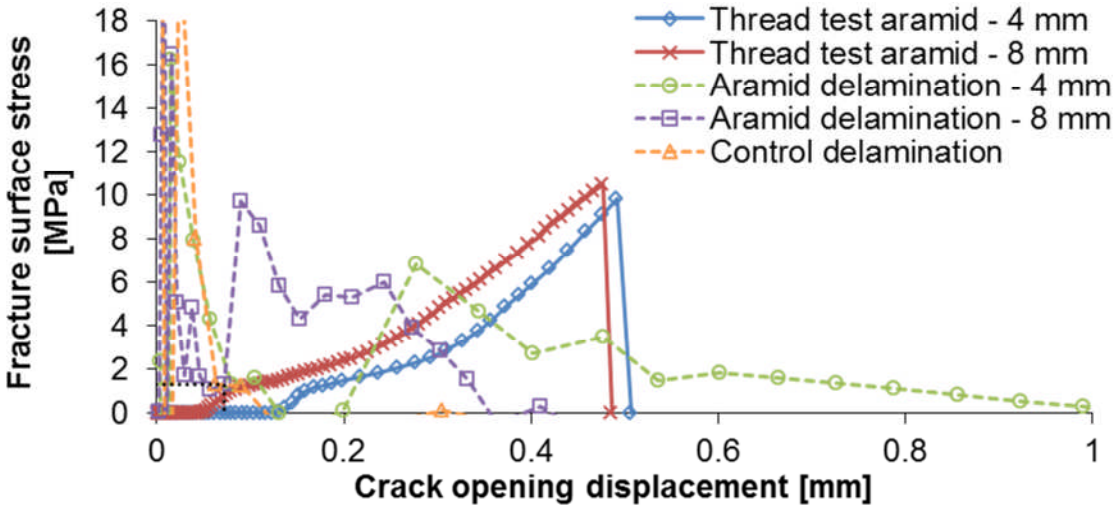

Figure 6-10 Averaged fracture stress-beam opening and thread test curves of highly bindered untufted and aramid tufted specimens with a thickness of 4 mm and 8 mm.

Table 6-6 Crack opening displacements at first tuft position and at fully developed bridging zone for untufted and aramid tufted highly bindered material with specimen thicknesses of 4 mm and 8 mm.

Thread material	Control	Aramid
First tuft (4 mm) [mm]	-	0.20
First tuft (8 mm) [mm]	-	0.07
Plateau (4 mm) [mm]	0.12	1.06
Plateau (8 mm) [mm]	0.12	0.36

6.4 Superposition of thread response and unreinforced material behaviour for different tufting depths

Equations 5-14 – 5-25 can be used for predicting the effect of depth on delamination. Figure 6-11 shows the predicted delamination resistance of the aramid tufted material with intermediate amount of binder. For all three tuft depths the predicted crack propagation in the initial untufted section corresponds to the experimental R-curve.

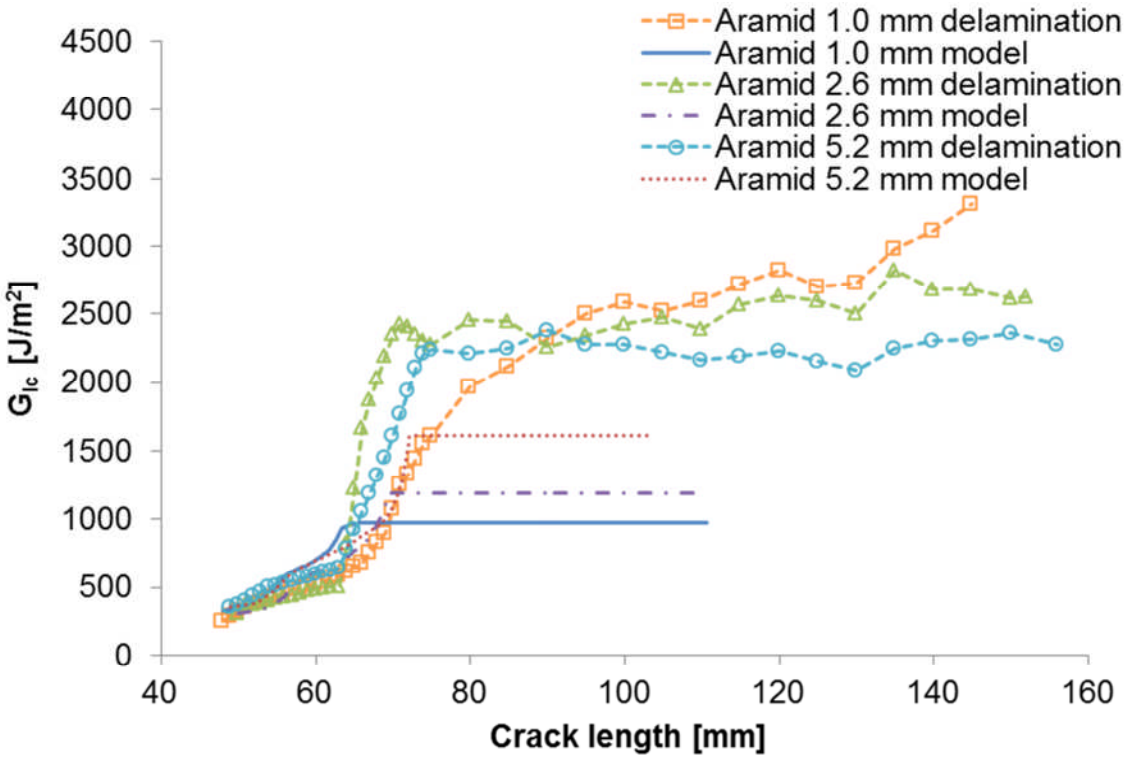

Figure 6-11 R-curves of superimposed control/tuft delamination performance of intermediately bindered material tufted with aramid and a tuft depth of 1.0 mm, 2.6 mm and 5.2 mm.

At a tuft depth of 1.0 mm the first tuft row prevents crack propagation at a crack length of approximately 60 mm. The crack continues propagating to the third tuft row, whilst the delamination resistance increases. Whilst the slope of the predicted R-curve corresponds to that of the experimental, the delamination toughness for the fully developed bridging zone differs from the experimental R-curve caused by the fact that tow bridging, which is the major toughness enhancement in this thickness, is not included in the model. The predicted behaviour of tufts includes only axial elongation of the three tuft rows with a reduced strain due to the small tuft length of 1.0 mm and subsequent rupture, leading to lower delamination toughness. This is also the reason for the higher predicted delamination toughness of the material with a tuft depth of 2.6 mm and 5.2 mm; the model assumes larger tuft elongations with increasing tuft depth, bridging the delamination cracks for longer resulting in higher delamination toughness for the 2.6 mm and 5.2 mm deep tufted material compared to the 1.0 mm. The predicted slope of the increase in delamination

resistance of 2.6 mm is in agreement with the experimental curve. However, the fully developed bridging zone is lower than the experimental as a result of the fact that fibre bridging and interactions of tufts and the resin are not considered in the model. The trends in slope and plateau level observed in experiments are followed by the prediction in the case of 2.6 and 5.2 mm deep tufting. However, in the case of 1.0 mm deep tufting, the experimental trends breakdown as a result of excessive tow bridging, whilst the model follows the expected behaviour of increasing slope and decreasing plateau toughness with decreasing tuft depth.

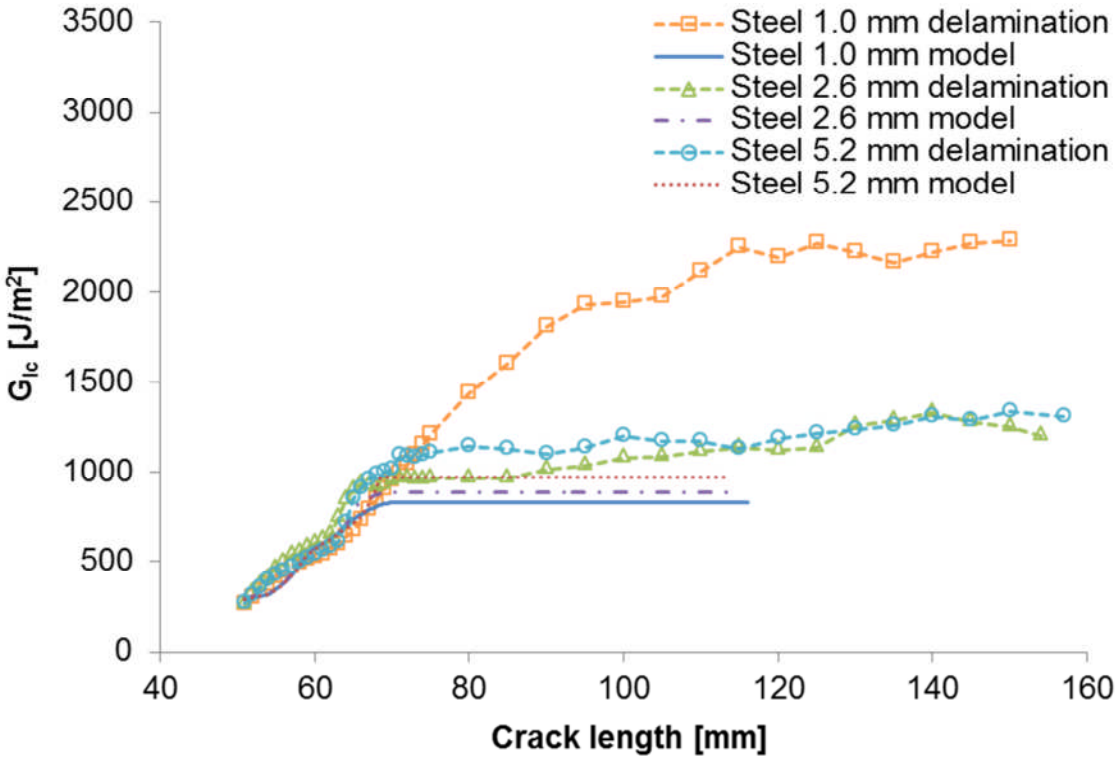

Figure 6-12 R-curves of superimposed control/tuft delamination performance of intermediately bindered material tufted with stainless steel and a tuft depth of 1.0 mm, 2.6 mm and 5.2 mm.

The behaviour of the predicted stainless steel tufted material (Figure 6-12) is comparable to that of the aramid tufted one: the delamination toughness of the material with a tuft depth of 1.0 mm is lower than the corresponding experimental response as the failure mechanism is assumed to be tuft rupture after a small tuft elongation, rather than pull-out and tow bridging. The model assumes that the elongation increases with greater tuft depth leading to higher

delamination toughness. However, the experiments show the opposite, as explained in section 6.2, due to the increasing constraints in tuft movement caused by the surrounding composite. Nevertheless, because of the similar tuft elongation of the 2.6 mm and 5.2 mm deep tufted material, due to the brittleness of the stainless steel thread, the delamination resistance of the 5.2 mm deep tufted predicted R-curve is similar to the experimental curve.

The assumption in terms of elongation has equivalent repercussions for the 1.0 mm deep copper tufted material in Figure 6-13 to the aramid and stainless steel cases leading to a lower predicted delamination toughness compared to the other tuft lengths and experimental curve as the main failure mechanism (pull-out and tow bridging) is not taken into account. The predicted delamination toughness of the 5.2 mm deep tufted material is higher than the 2.6 mm deep tufted material due to larger elongations assumed by the model. This agrees with the experimental results as the copper wire is not affected by the constraints caused by the surrounding composite leading to higher delamination toughness. In general, the high ductility of the copper wire leads to relatively low increase in predicted delamination toughness during crack arrest and, as described in section 5.3.1, the non-linear behaviour of the beam opening and crack length generates the initial low increase in stiffness with subsequent steep increase. Furthermore, as the model is controlled by increments of beam opening displacement δ^*, i.e. tuft elongation, the strain reduces with increasing tuft depth leading to lower stiffness.

The correlation between predictions and experimental results is better in the case of the highly bindered material (Figure 6-14). The 8 mm thick tufted material in Figure 6-14 has a higher predicted delamination toughness than the 4 mm thick material due to the increased tuft elongation. The constraints by the compactness of the thicker material and the large amount of binder suppressing the effect of tufts are not considered for the superposition of resin and tuft contribution. This leads also to the overestimation of the predicted delamination toughness of the 8 mm thick material compared to the experiment.

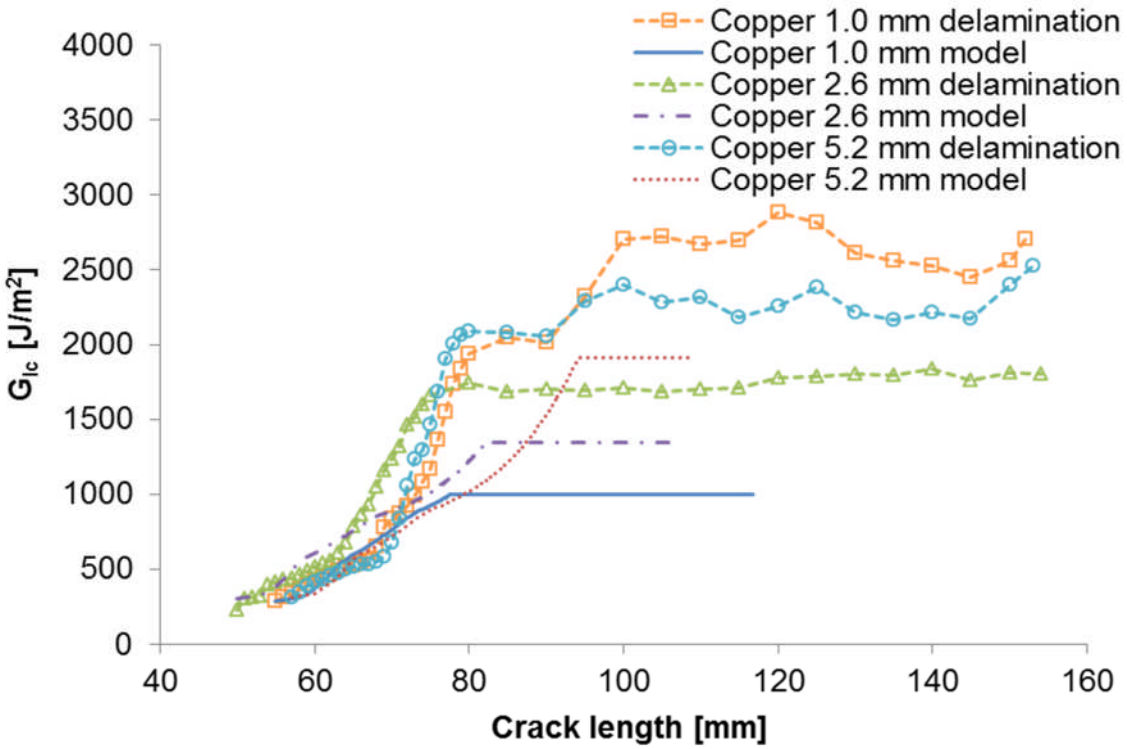

Figure 6-13 R-curves of superimposed control/tuft delamination performance of intermediately bindered material tufted with copper and a tuft depth of 1.0 mm, 2.6 mm and 5.2 mm.

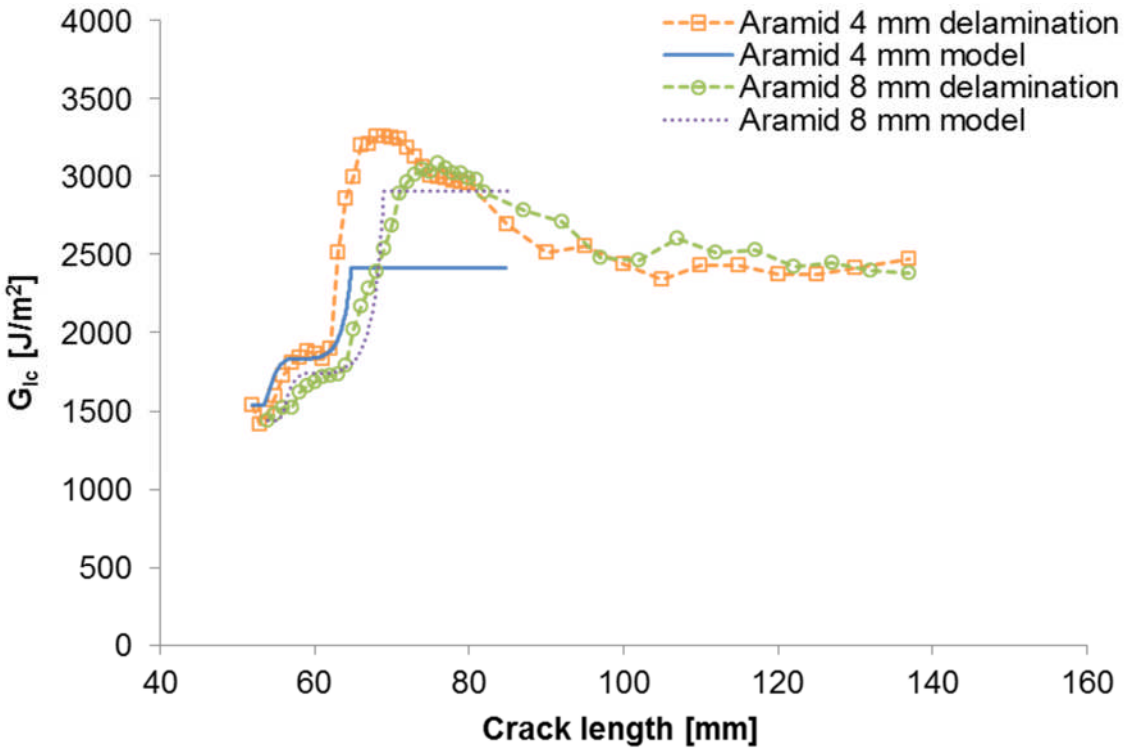

Figure 6-14 R-curves of superimposed control/tuft delamination performance of highly bindered material tufted with aramid and a thickness of 4 mm and 8 mm.

6.5 Conclusions

The main finding in this chapter is that the strain energy release rate decreases with increasing tufting depth. The magnitude depends, among others, on the tufting thread material. The aramid thread shows clear tufting depth dependence in contrast to the brittle stainless steel thread and ductile copper wire; the atypical brittleness of stainless steel eliminates the tufting depth effect for long tuft lengths, whilst the copper wire elongates more with increasing tuft depth. The mobility of the tufting thread, which is restricted in materials with the greatest tufting depth, is of importance for the full exploitation of tuft performance. Overall, increasing the tufting depth results in greater constraints in the deformation of the tufting thread and the delamination resistance decreases.

Although the copper wire has a lower tensile strength than the stainless steel thread, it leads to higher delamination toughness due to more extensive bridging. In tufted materials fibre bridging and the contribution of non-structural stitching are enhanced with increasing thread elongation leading to a further increase of strain energy release rate.

The superposition of unreinforced toughness response and thread behaviour leads to underestimation of the delamination toughness but is capable to reproduce a trend for the resin and tuft contribution to the delamination resistance with an indication at which crack length the tufts start to bridge the crack. The predicted results for the dependence of the delamination performance on the tufting depth are contradicting the experimental results. The main reason is the fact that some of the failure mechanisms, such as the constraints in tuft movement by the surrounding composite, are ignored. Instead, the model assumes a larger tuft deformation with increasing tuft length leading to higher delamination resistance for long tufts.

7 Influence of tuft angle on delamination behaviour

This chapter focuses on the effect of tufting angle on the delamination behaviour. This is carried out using mode I delamination testing on DCB specimens manufactured with partial tufting with a vertical depth of 2.6 mm across the delamination interface and a tuft angle of 45°. The test results are compared with those obtained by vertically inserted tufts containing a tuft depth of 2.6 mm.

7.1 Delamination performance

Representative load-displacement curves of the tufted DCB specimens, described in section 3.2.3 and tested in mode I delamination, are presented in Figure 7-1. The untufted control material and materials with conventional vertical tufts (90°) with a tufting depth of 2.6 mm in Figure 7-1 are equivalent to the materials presented in Figure 6-1. Figure 7-1 shows that an increased load is required for delamination of tufted specimens compared to the control specimen. However, the load during delamination of the initial untufted region increases with the same rate as for the control specimen. The maximum load of the control specimen is 127 N, whilst that of aramid, copper and stainless steel tufted specimens with 45° inclined tufts is 283 N, 171 N and 170 N, and of the materials with 90° tufts is 205 N, 178 N and 171 N, respectively. For 45° tufted specimens the maximum load occurs after a linear increase in load, starting at approximately 115 N when the crack tip reaches the first tuft row. During the increase the crack propagates slowly by a length corresponding to the distance of one or two tuft rows without load drops, due to bridging of the first two tuft rows. Once the first tuft row ruptures the load decreases until final failure with periodic slight increases in load due to arrest of the crack propagation by tuft rows and occasional fibre bridging and undulation. The load of the control specimen drops after reaching the maximum load until failure of the specimen with very low increases in load caused by fibre bridging and undulation. The significant difference in maximum loads reflects the thread tensile test results (Figure 5-1); the high tensile strength of the aramid thread leads to high loads required to delaminate the aramid tufted specimen. The loads required to

delaminate the 45° copper tufted specimen are equivalent to the loads of the 45° stainless steel specimen. Although the tensile strength of copper is lower, the bridging of four to six tuft rows increases the loads compared to two to three stainless steel tuft rows.

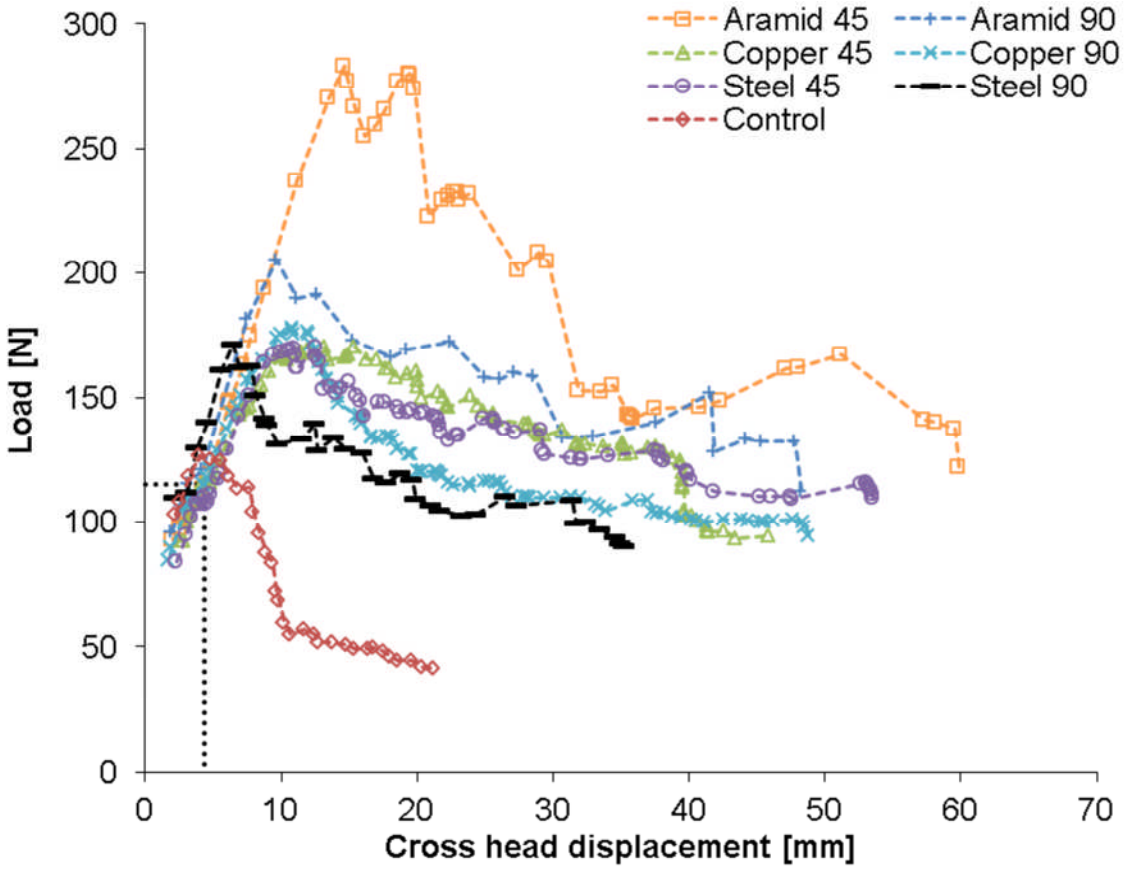

Figure 7-1 Representative mode I delamination load-displacement curves of intermediately bindered untufted and tufted with 2.6 mm long inclined tufts using aramid, copper and stainless steel tufts. Dotted line represents the first tuft row.

The corresponding crack resistance curves in Figure 7-2 are averaged out of four specimens for each tuft thread material interpolated at predefined increments of crack length. The crack initiation toughness is reduced for tufted materials compared to the control material (Table 7-1). This behaviour is due to the influence of tufting on the resin rich layer geometrical characteristics. The crack propagates through the region up to the first tuft row, whilst the energy release rate increases up to 550 J/m^2 in materials with tufts inclined by 45°. With two to three tuft rows arresting the crack propagation in aramid and stainless steel materials and four to six rows in copper tufted materials, the delamination

toughness reaches plateaus indicating a fully developed bridging zone. These plateaus show improvements in delamination toughness at steady state by up to 490% for 45° aramid tufted materials and 290% for 45° copper and 45° stainless steel tufted materials compared to the control material, corresponding to the trend of the load-displacement curves shown in Figure 7-1. The stainless steel tufted materials reach a delamination toughness comparable to copper tufted materials, whereas with vertical tufts and the same vertical tufting depth the copper results in about 45% higher delamination resistance compared to stainless steel. The delamination toughness of the aramid tufted material is improved by up to 30% compared to vertical inserted aramid tufts with a tuft depth of 2.6 mm. Similarly, the inclined copper tufts result in increased crack energy release rate by up to 30% compared to equivalent vertical tufts. The toughness of the inclined stainless steel tufted material is almost doubled compared to the conventional tufted material using the same thread. All curves contain minor variations generated by stick-slip behaviour of the crack propagation and fibre bridging and undulation. The control material has an average delamination toughness of 580 J/m^2, also containing minor increases due to fibre bridging and undulation. Table 7-1 summarises the delamination toughness for crack propagation.

Table 7-1 Average crack initiation and propagation toughness of untufted and tufted intermediately bindered material with inclined 2.6 mm long aramid, copper and stainless steel tufts (standard deviations are reported in brackets).

Thread material		Control	Aramid	Copper	Steel
$G_{Ic,\ ini}$ (45°)	[J/m^2]	331 (±15)	279 (±87)	255 (±21)	247 (±38)
$G_{Ic,\ ini}$ (90°)	[J/m^2]	331 (±15)	227 (±9)	229 (±15)	262 (±31)
G_{Ic} (45°)	[J/m^2]	579 (±110)	3438 (±475)	2280 (±234)	2225 (±104)
G_{Ic} (90°)	[J/m^2]	579 (±110)	2599 (±399)	1741 (±138)	1189 (±167)

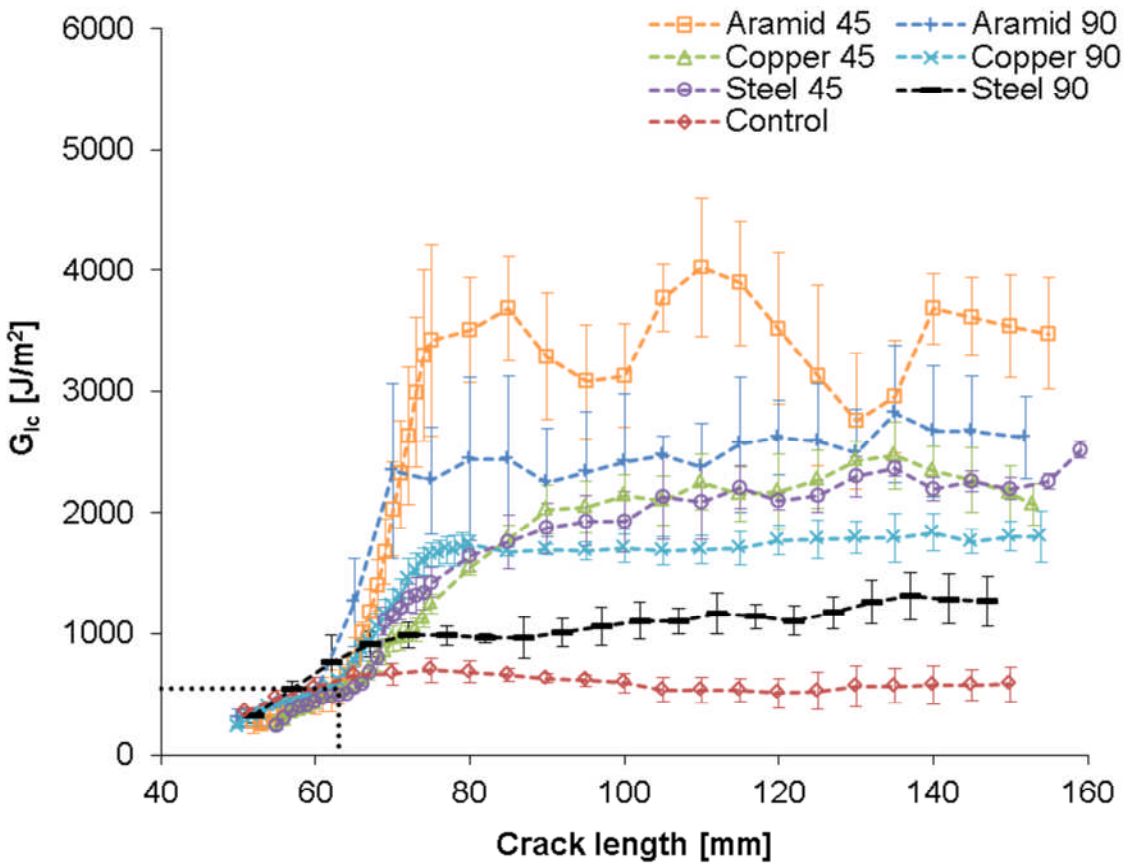

Figure 7-2 Average crack resistance curves of untufted and tufted intermediately bindered material with inclined 2.6 mm long tufts using aramid, copper, stainless steel thread. Dotted line represents first tuft row. Error bars represent one standard deviation.

7.2 Manufacturing defects in angled tufting

During tufting of the dry preform the pressure foot had to be dismounted to carry out the tufting with an angle of 45° as explained in section 3.2.3. The absence of the pressure foot results in limited preform compression causing movement of fabric plies and of inserted tufts inside the preform. As described in section 3.2.3 the role of the pressure foot is to induce compression of the preform leading to a relatively uniform preform thickness and tuft loop length. Without the pressure, the thickness of the preform is irregular and a larger loop length of 6 mm, rather than 2 – 3 mm, needs to be used to prevent tuft pull-out during the manufacturing process, as shown in Figure 7-3a. This excessive loop length leads to an increased resin rich layer around the loops which is susceptible to crack initiation. In addition, movement of inserted tufts can occur in the absence

of pressure. This in turn causes rotation of inserted tufts as the tufting needle moves to the next tuft insertion point due to the tension in the thread. Furthermore, entire tuft rows shift along the uni-directional fabric fibres approaching each other, as shown in Figure 7-3b. Some tuft rows are blocked by the non-structural glass stitches, whilst others shift the glass stitches in their movement.

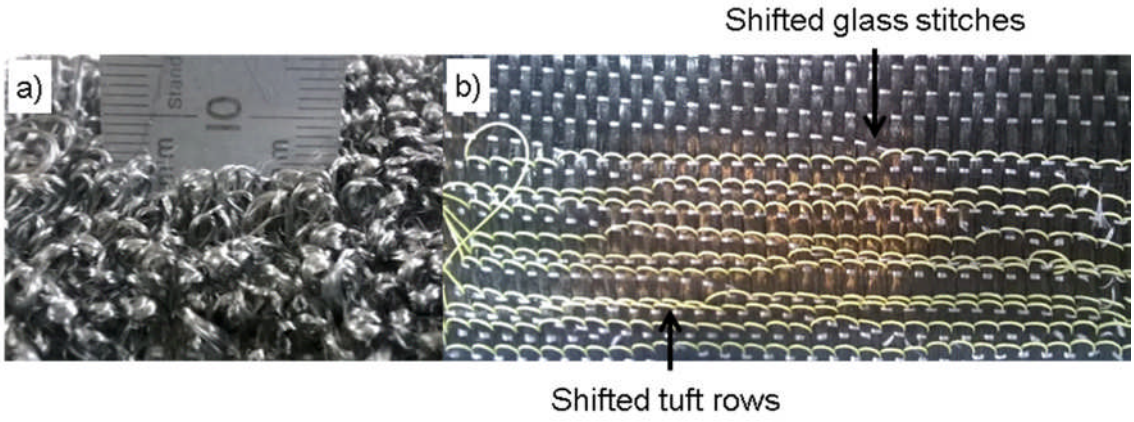

Figure 7-3 Manufacturing defects in angle tufting: a) excessive loop length of stainless steel tufted material and b) shifted glass stitches and aramid tuft seams.

The perforation of the support foam under the preform showed a regular tuft pattern and needle insertion. However, micrographs of delaminated fracture surfaces show an irregular tuft pattern as observed in Figure 7-4. Although the load-displacement curves reflect the delamination performance shown in Figure 7-2, the high oscillation in delamination toughness of the aramid tufted material may be caused by the irregular tuft pattern. The increase in crack energy release rate is caused by arrest of the crack propagation by tuft rows placed close together, with a subsequent drop in delamination toughness when the crack propagates through a large untufted area. The irregular tuft pattern (tufts are marked with red) is also observed in stainless steel (Figure 7-4a), and copper (Figure 7-4b) tufted materials. Such irregularities can affect the delamination performance if only single tufts of a tuft row are active, rather than the entire row further increasing the delamination toughness. Furthermore, Figure 7-4b shows a resin rich channel (marked with red) created by shifted

tufts placed too close, generating crack initiation sites, weakening the structure and decreasing the crack energy release rate.

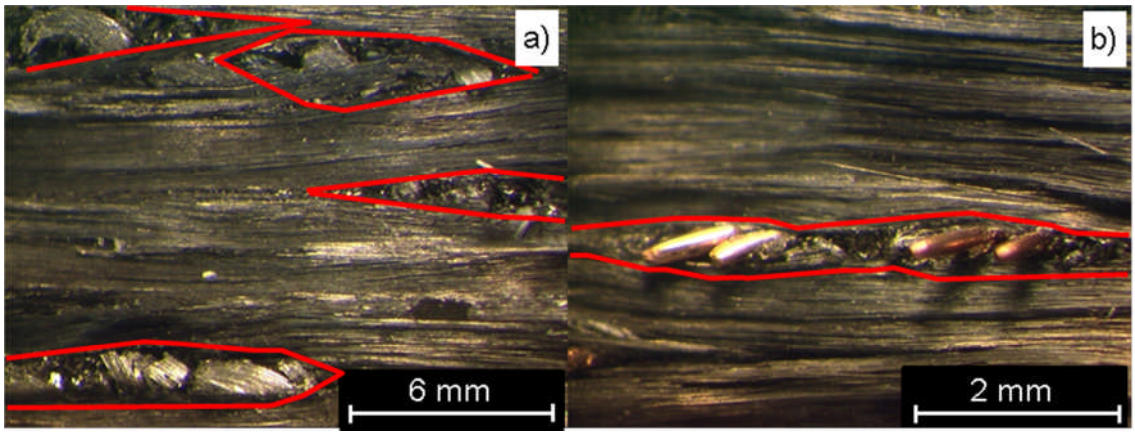

Figure 7-4 Irregular tuft pattern at delamination surface: a) stainless steel and b) copper 45° tufted material.

7.3 Failure mechanisms of 45° tufted materials

Analysis of the fracture surfaces of aramid and stainless steel tufted specimens reveals a new mechanism of toughening the interface which is active in inclined tufts. As shown in Figure 7-5 resin ploughing by the tufts occurs during delamination. The red circled areas represent the initial tuft position before ploughing. During mode I delamination, the threads straighten, plough into the resin resulting in increased delamination toughness. Hence, resin ploughing is a major contribution to the increase in delamination toughness, considering the improvements in delamination toughness of inclined aramid, and stainless steel tufted composites compared to vertically tufted material. A large amount of energy is required as the threads cut into the resin. This energy is accumulated during delamination raising the strain energy release rate. This failure mechanism was also identified to improve the delamination performance of composites reinforced with Z-pins [55, 59, 60]. The tufting threads are partially pulled-out due to ploughing leading to extensive tow bridging, increasing further the delamination toughness. Figure 7-6 shows elevated fibres covering stainless steel tufts. Although the delamination toughness of copper tufted composites is improved by 30% in comparison to material incorporating of vertical inserted copper tufts with a tuft depth of 2.6 mm, the fracture surfaces

with inclined tufts do not show evidence of any ploughing (Figure 7-7a). However, the copper tufts elongate significantly (Figure 7-7b) and rupture after necking of the wire (Figure 7-7c). This is due to the low tensile strength and the ductility of the copper wire leading to yielding, rather than ploughing into the resin. Instead, the wire elongates and undergoes shear deformation due to the inclination and absence of ploughing. Hence the strength and strain of the tufting material partially dictate the failure mechanism: high strength/low strain materials (aramid, stainless steel) plough into the resin and low strength/ductile materials (copper) yield, rather than plough. Nevertheless, the improvement compared to vertical copper tufts with same tuft depth is a result of the ability to shear due to the original inclination of the tufts. These results contradict the results of a similar study conducted on DCB specimens containing vertical inserted stitches and stitches orientated in 45° and 22.5°, resulting in a decrease in delamination toughness with decreasing insertion angle [139].

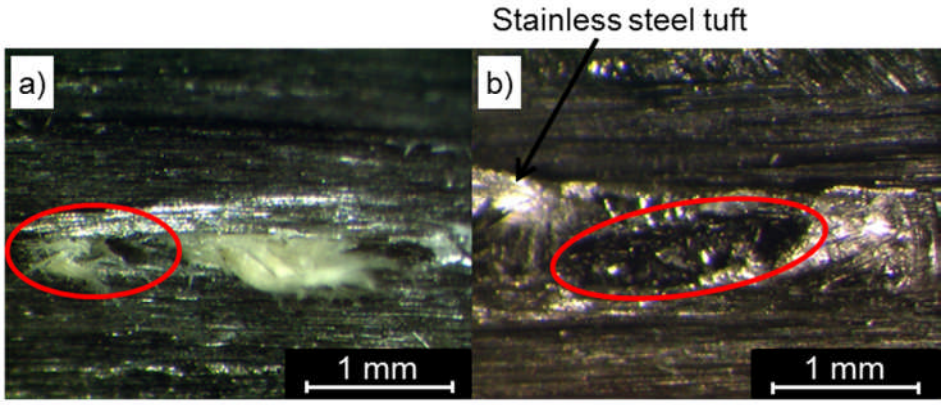

Figure 7-5 Resin ploughing at delamination surface: a) aramid and b) stainless steel inclined tuft with red marked initial tuft position.

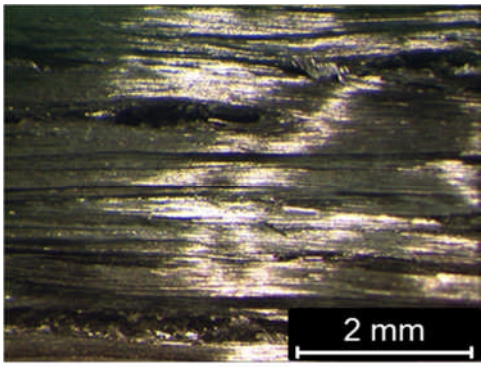

Figure 7-6 Fibre bridging at delamination surface covering inclined stainless steel tufts.

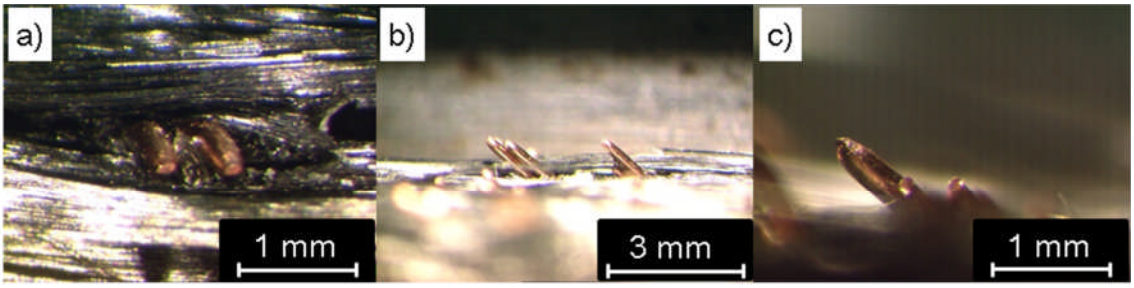

Figure 7-7 Angled copper tufts at delamination surface: a) no ploughing, b) elongation and c) necking.

The irregular tuft pattern, resin rich channels and the resin ploughing also affect the variance of the delamination behaviour of angled tufted materials. The large standard deviation of aramid tufted materials, as reported in Table 7-1 and shown in Figure 7-2, may be caused by the irregularity of the tuft pattern, fibre bridging and undulation and resin ploughing which can be different for every single tuft row. However, the standard deviation is also affected by the nature of the threads as suggested by the decreasing variance with decreasing delamination toughness. The brittleness of the stainless steel thread does not permit high variations in ultimate strain and strength leading to a low variance. Due to the absence of ploughing, the elongating copper wire bends at the delamination surface towards a vertical direction. The bend may lead to failure of single tufts affecting the delamination toughness and the variance. The control material shows the lowest variance, as only fibre bridging and undulation affect the variability of its delamination response.

7.4 Bridging law for inclined tufts

In order to determine how the stress-strain behaviour of threads affects the fracture stress and crack opening displacement curves during delamination of 45° tufted composites, the inclination of the tufts has to be considered. Figure 7-8 shows simplified assumptions of the tuft movement during delamination.

During mode I delamination, a load F is applied leading to a vertical tuft displacement δ' and an axial elongation δ. The tuft, experiencing an axial load P, rotates by an angle of $d\varphi$. The vertical distance $2h$ corresponds to the thickness of ten plies, i.e. 2.6 mm, whilst the horizontal distance l between the tuft loop and seam is 3.7 mm considering a nominal tuft inclination φ of 45°.

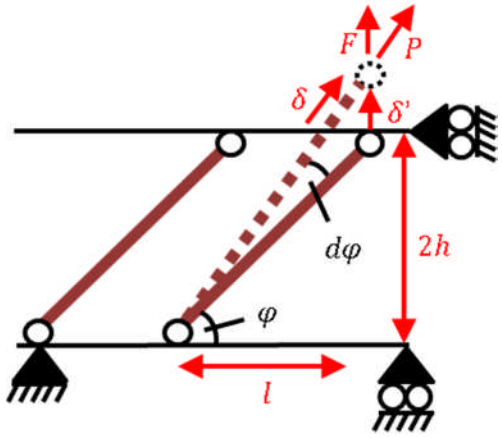

Figure 7-8 Schematic of tuft movement during testing.

The vertical opening δ' at the tuft location is determined as explained in section 5.1.4 and used to calculate $d\varphi$ as follows:

$$d\varphi = \operatorname{atan}\left(\frac{\delta' + l\ \sin(\varphi)}{l\cos\varphi}\right) - \varphi \qquad \textbf{7-1}$$

The axial tuft elongation $\boldsymbol{\delta}$ is calculated using:

$$\delta = \frac{l\cos(\varphi)}{\cos(\varphi + d\varphi)} - l \qquad \textbf{7-2}$$

The tuft elongation is used to determine the strain and the thread stress via interpolation of the thread tensile test results. The thread stress is translated to tuft load P considering twice the cross sectional area of the thread for a tuft. The vertical load F is calculated via the tuft load P and the geometry:

$$F = \frac{P}{\sin(\varphi) + \cos(\varphi)\dfrac{\cos(\varphi)}{\sin(\varphi)}} \qquad \textbf{7-3}$$

As described in section 5.1.4 the tuft stress is the load P referred to the unit cell area covered by one singe tuft.

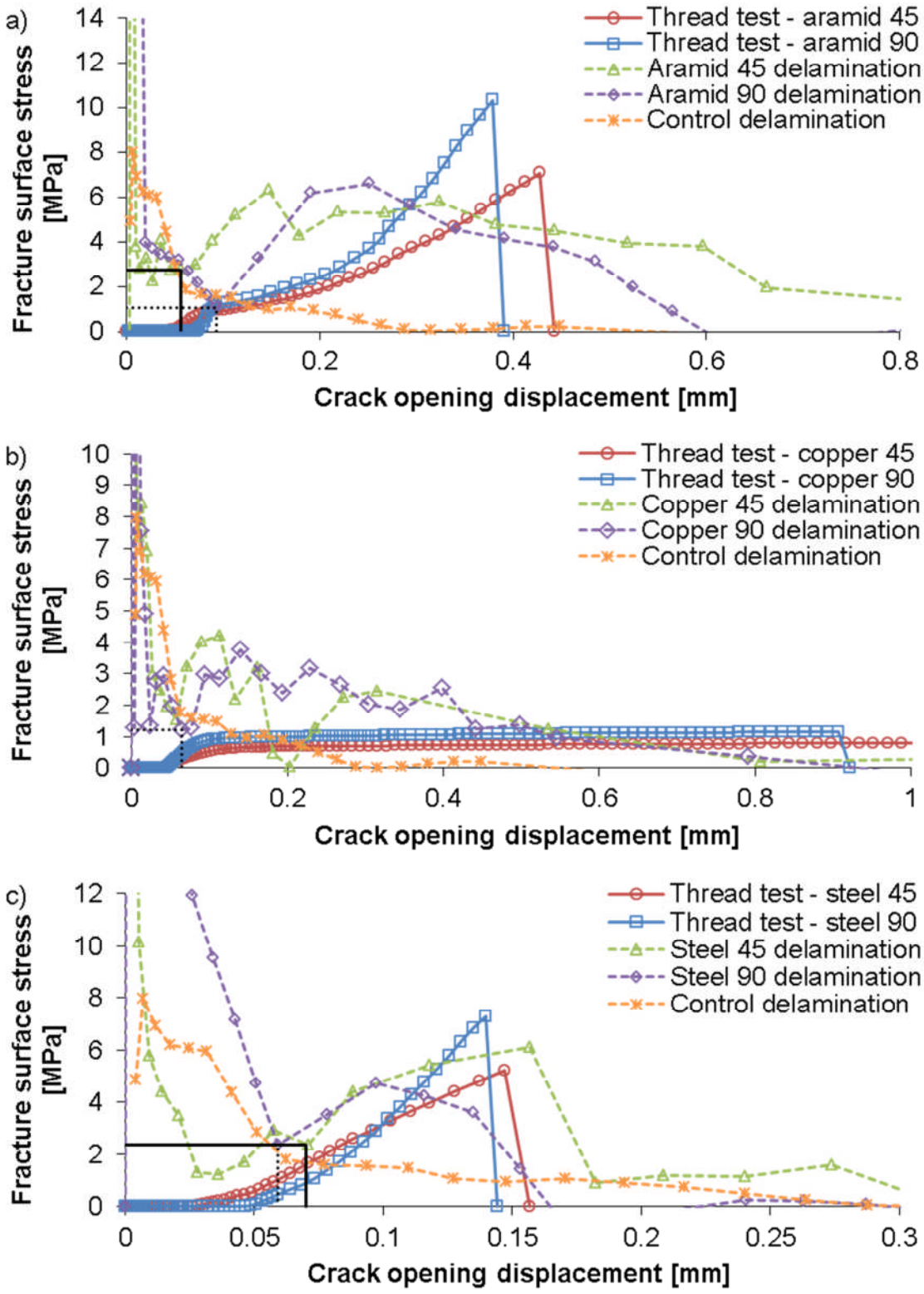

Figure 7-9 Fracture surface stress-crack opening displacement and thread behaviour of untufted, 45° and 90° tufted intermediately bindered materials: a) aramid, b) stainless steel and c) copper. Red dotted and green solid lines represent first tuft row.

Table 7-2 Crack opening displacements at first tuft position and at fully developed bridging zone for untufted and tufted intermediately bindered material with inclined 2.6 mm long aramid, copper and stainless steel tufts.

Thread material		Control	Aramid	Copper	Steel
First tuft (45°)	[mm]	-	0.07	0.06	0.04
First tuft (90°)	[mm]	0.90	0.70	0.06	0.90
Plateau (45°)	[mm]	0.56	1.50	1.30	0.70
Plateau (90°)	[mm]	0.56	0.58	0.92	0.17

Figure 7-9 shows the thread tensile test and fracture surface stress-crack opening displacement curves, including the 90° tufted specimens presented in Figure 6-9 for facilitating the comparison. The surface stress of 45° aramid, copper and stainless steel tufted specimens increases linearly corresponding to a crack tip position at the first tuft row (black solid lines) as presented in Table 7-2. The linear increase represents an axial elongation of the tufts, confirmed by the slopes of 90° tufted material and the slopes of the linear increase corresponding to the slopes of the thread test curves. At an opening of 0.09 mm the rate of increase in stress in 45° aramid (Figure 7-9a) and stainless steel specimens (Figure 7-9b) starts decreasing due to tuft ploughing into the resin. This is confirmed by comparing the stress curves of the corresponding 90° tufted material which only shows the linear increase due to axial elongation. This is also a reason for the fact that the fracture surface curve of the 45° stainless steel tufted materials exceeds the ultimate strength of the stainless steel thread. Hence, the tufts in the specimens are stretched initially and subsequently start ploughing into the resin. The 45° copper tufted materials (Figure 7-9c) show a lower surface stress than the aramid and stainless steel specimens due to the absence of ploughing. However, the slope of the 45° copper thread test does not correspond to that of the copper tufted specimen stress curve which is steeper due to interaction of copper tufts with the surrounding composite. The copper thread stress diminishes at a tuft elongation of 1.6 mm. The surface stress in the 45° aramid tufted materials decreases at a slower rate than in copper and stainless steel tufted specimens leading to a fully developed bridging zone, i.e. negligible stress curve at high crack openings (Table 7-2).

7.5 Superposition of material response and response of tufts with different inclination

Figure 7-10a illustrates the calculated delamination toughness of 45° inclined aramid tufts. The behaviour is similar to the experimental toughness in the initial untufted region of the propagation. Both, the toughness of the 45° experiment and of the 45° superposition increase at a crack length of 62 mm and 63 mm, respectively, due to bridging of the first tuft row. The plateau region of the 45° superposition is lower than that of the experimental 45° tufted material as ploughing of the tufts into the surrounding resin, which increases the delamination toughness of the materials, is not taken into account by the analytical prediction. In the model the tufts fail by rupture without resin ploughing. Similar results are obtained for the toughness calculation of 90° tufted material and the 90° tufted experimental results. Both show lower delamination toughness than the corresponding 45° tufts. The reason for a higher toughness of 45° superimposed tufts compared to 90° superimposed tufts is the assumption in Figure 7-8, that the vertical load F for inclined tufts is lower than the axial tuft load P, which is equal to the tuft load of vertical tufts, reducing the tuft stresses and leading to larger beam opening with the tuft still bridging the crack. The load-displacement curves (Figures 6-1 and 7-1) show the opposite effect, with inclined tufts leading to higher loads as resin ploughing is not considered by the model. Furthermore, the inclined tufts are slightly longer than vertical tufts leading to larger elongations and longer crack bridging leading to higher calculated delamination toughness. However, the crack propagation in the initial untufted area is equivalent for all four curves indicating the same resin contribution. The subsequent slope of the increase in toughness of the superimposed 90° and 45° tufts is lower compared to the experimental curves as the interactions of inclined tufts and the surrounding composite are not considered, whilst the predicted curves follow a non-linear crack length dependence on the beam opening displacement.

The delamination toughness in the initial untufted region is equivalent between the experimental 45° and predicted R-curve of the stainless steel tufted material as shown in Figure 7-10b. The crack propagates by 64 mm until reaching the

first tuft row. The subsequent crack propagation up to the third tuft row leads to similar slopes of the predicted and experimental curves. The 45° inclined stainless steel tufts in the experiments are affected less by the surrounding composite than the aramid thread due to their low ultimate strain. Therefore, the slope of the experimental 45° R-curve increases with a similar slope to that of the 45° superimposed R-curve. Similarly to Figure 7-10a, the plateau region of the predicted 45° R-curve is lower than that of the experiment due to neglecting resin ploughing as well as fibre bridging and friction between the tufts and the surrounding resin. The R-curve of the 90° prediction has the same delamination behaviour as the 90° experiment up to a crack length of 62 mm where the crack tip reaches the first tuft row. The experimental toughness of the 90° tufted material reaches a fully developed bridging zone at a similar toughness to the 90° superimposed curve due to the brittleness of the thread affected less by friction between tufts and the composite. The low strain also leads to similar toughness for the 45° and 90° superimposed R-curves; the 45° tuft is longer than the 90° tuft and hence elongates more, whilst the brittleness of the thread limits the effect on the delamination toughness. The results for inclined copper tufting (Figure 7-10c) show that the slopes of the increase in toughness in the untufted region of the experimental and superimposed 45° curves are equivalent, indicating the same delamination behaviour. At a crack length of 67 mm and 63 mm the first tuft row starts arresting the crack propagation in the experimental and predicted R-curve. The subsequent initial increase in predicted delamination toughness differs from the experimental curves due to non-linearity of the crack length. The predicted slope changes following the slope of the experimental curves. The plateau region of the 45° experimental R-curve is higher than that of the 45° superimposed curve due to the interactions of the tufts with the surrounding composite. The difference between the 45° copper superimposed and 45° copper experimental curves is lower compared to stainless steel and aramid due to weaker interactions between copper tufts and the surrounding composite. Equivalently to aramid and stainless steel, the 45° superimposed delamination toughness for the fully developed bridging zone is higher than that of the superimposed 90° curve due to lower vertical tuft stress

and longer inclined tufts, both leading to larger tuft bridging increasing the delamination toughness.

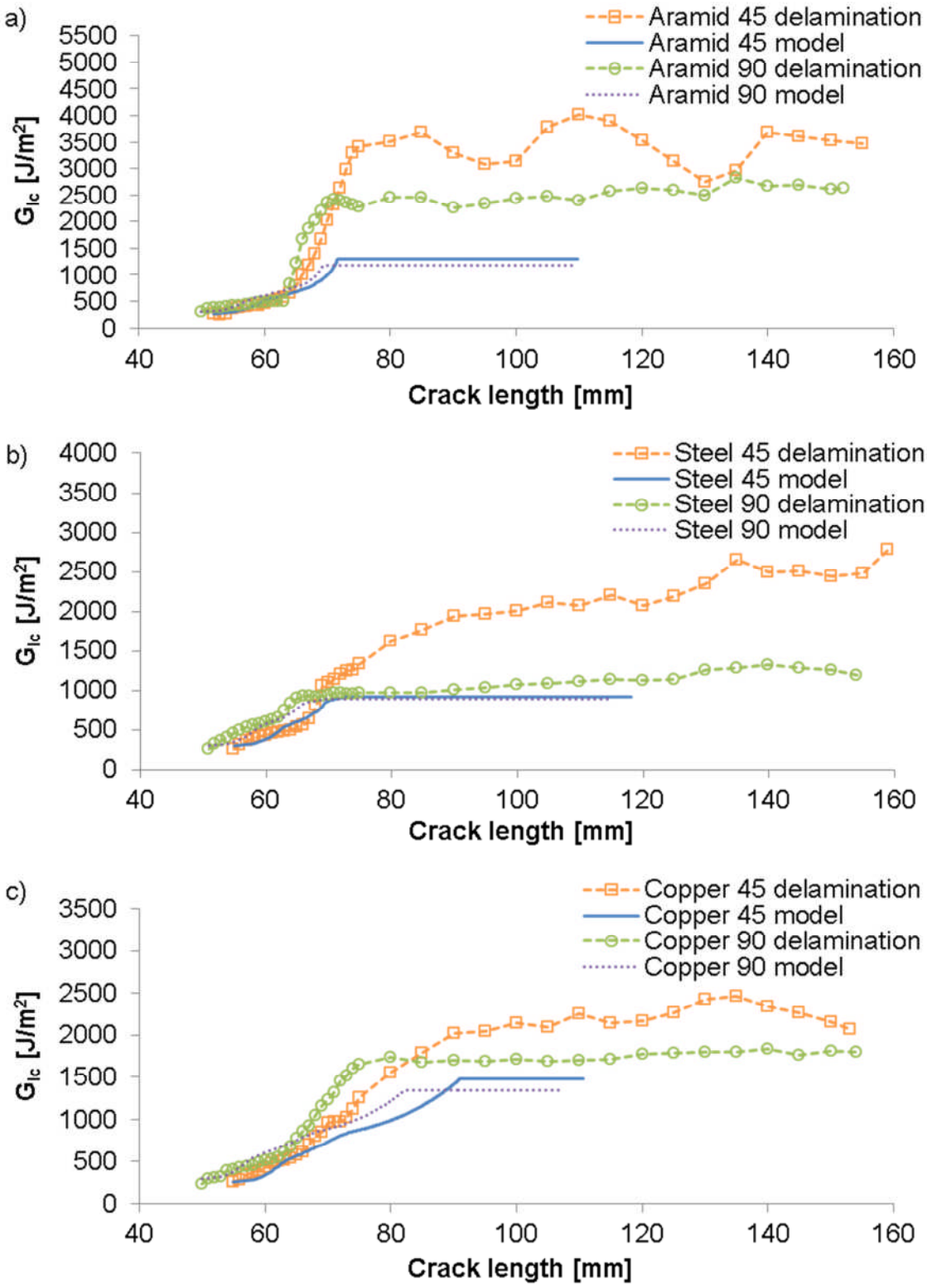

Figure 7-10 R-curves of superimposed control/tuft delamination performance with 45° and 90° inserted tufts: a) aramid, b) stainless steel and c) copper.

7.6 Conclusions

Tuft inclination has a significant effect on delamination performance. Delamination resistance increases with a tuft insertion angle of 45° compared to vertical tufts. Micrographs reveal resin ploughing in aramid and stainless steel tufted materials around the tufts before tuft rupture, leading to an additional toughening mechanism. The delamination toughness of copper tufted material is improved in comparison to materials with vertical tufts due to friction between the inclined tufts and the resin during elongation, reduced effect of constraints caused by the surrounding composite and greater tuft length which increases the elongation of the wire and, hence, energy absorption.

The analytical approach of superimposing the tuft stresses and the fracture surface stresses shows that the predicted delamination toughness is lower than the experimental R-curves, since the interaction of the tufts with the surrounding composite and resin ploughing is not taken into account. Although the model estimates correctly that the delamination toughness of inclined tufted material is higher than that of vertical tufted material, the reason is the larger tuft length and lower tuft stresses per unit area, both leading to larger tuft elongation. The actual reason responsible for the increase in delamination toughness (resin ploughing) is not considered.

8 Influence of tufting on the electrical properties of carbon composites

This chapter focuses on the electrical properties of composite structures tufted with a variety of threads, such as carbon, glass and stainless steel as well as the copper wire. An introduction, providing a short literature review on lightning strike performance of composites, is followed by the presentation of the results of lightning strike and electrical conductivity tests of tufted specimens.

8.1 Introduction

Each commercial aircraft is hit by lightning strike on average once a year [290]. This usually happens during take-off or landing or during the flight through clouds [291]. Typical locations of lightning strikes are the nose and the wing tips [292]. Entering at one point the lightning is led through the most conductive path and exits from another extremity of the aircraft. Due to the movement of the aircraft the lightning discharge moves along the aircraft, being swept for a certain distance. The locations with the highest lightning energy density are at the entry and exit points of the current surge. The electrical conductivity of the materials in the relevant areas of the aircraft controls the rate of energy dissipation and indirectly the damage caused by lightning [293]. Six different zones can be distinguished according to the likelihood of being struck by lightning currents and hang-on, as shown in Figure 8-1. Hang-on is the attachment of lightning at a particular point, where it remains for longer duration than at other locations increasing the dwell time and potential for damage [293, 294]. In general, Zone 1 has the highest probability to be stroke by a lightning and to have return strokes, with Zone 1A having low probability of hang-on, Zone 1B having high probability of hang-on and Zone 1C likely to be hit by the first return stroke of reduced amplitude and low probability of hang-on. A lightning strike consists of several strokes or return strokes of which the first one discharges the highest amplitude of current (200 kA) of the lightning on the aircraft, corresponding to component A in Figure 3-20b in section 3.3.3. The return strokes occur quickly and are usually repeated several times within milliseconds [295]. Zone 2 is defined by the likelihood of experiencing

subsequent swept strokes or re-strikes, with Zone 2A having low probability of hang-on and Zone 2B having high probability of hang-on. A swept stroke is the repeated attachment of a stroke along the aircraft caused by the fast movement of the aircraft, for example along the fuselage if lightning strikes at the nose. The highest amplitude of the current in Zone 2 corresponds to component D in Figure 3-20b in section 3.3.3. Zone 3 is the area between direct or swept stroke attachment points, supporting large lightning currents [296].

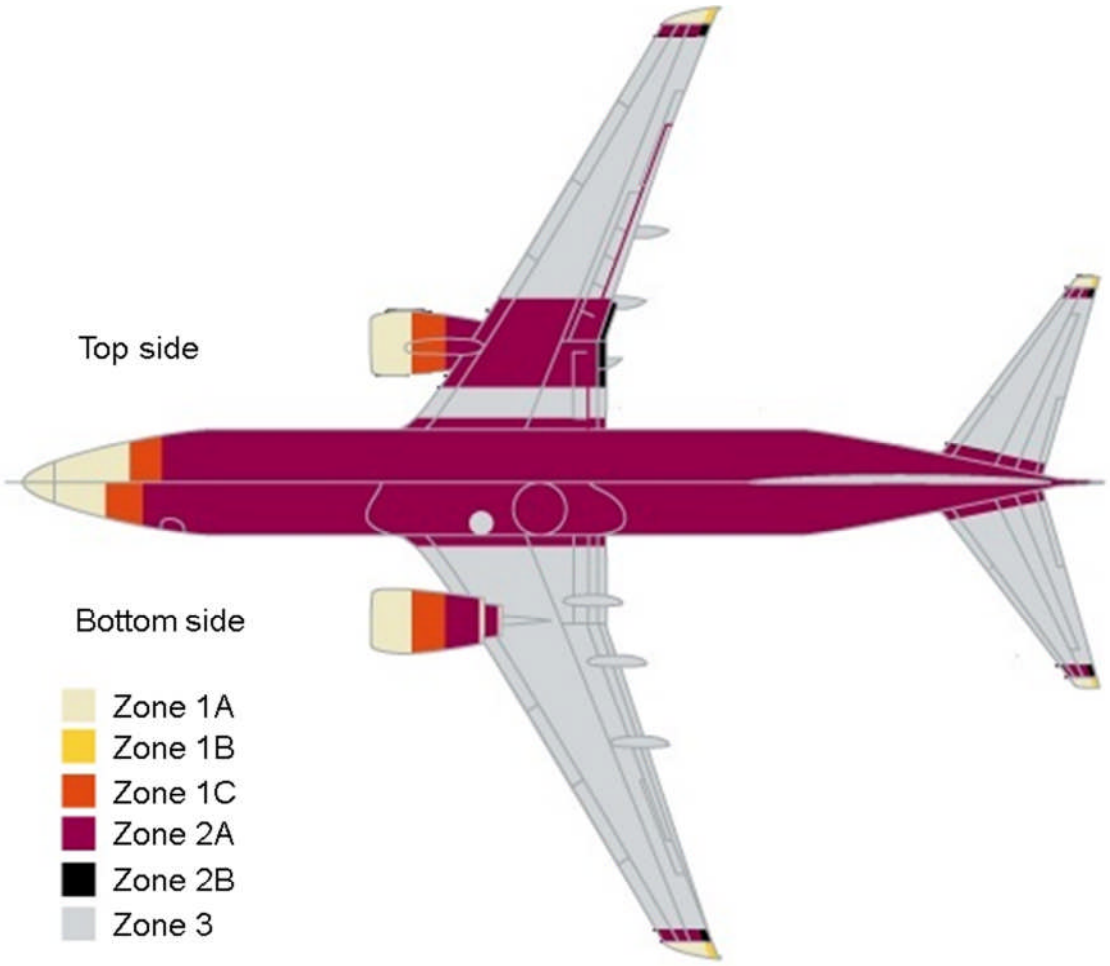

Figure 8-1 Lightning strike zones for a commercial aircraft, adapted from [297].

Lightning can cause direct and indirect damage [296]. Direct effects correspond to damage in the area near the stroke, such as fibre fracture, vaporisation of resin, delamination or burn-through of the laminate, whilst indirect effects include damage of electrical equipment by magnetic fields [293]. In metal aircrafts the lightning current is dissipated along the metal parts and the electromagnetic waves are prevented from entering and damaging electrical

devices. Aircrafts with large composite parts do not have the same capability of dissipating currents.

Composite parts are currently protected against direct and indirect effects by metal meshes, foils or interwoven fabrics made of copper, bronze or aluminium, as shown in Figure 8-2. These metals have a high specific electrical conductivity. Interwoven fabrics are made of glass, carbon or aramid fibres interwoven with metal fibres and used as the top layer of the structure. Woven meshes (Figure 8-2a) are made of metal strands in a particular pattern, connecting to each other when crossed in order to conduct electricity. At the cross points the meshes have increased conductance due to the double thickness. However, this also leads to an increase in weight. Non-woven meshes (Figure 8-2c) are manufactured by perforating a metal foil. This type of mesh can be flattened to decrease the thickness and requires less mechanical strength than woven meshes in which the wires are subjected to higher stresses during manufacture. The shape of the mesh can be varied changing the long and short unit cell diagonal dimension (LWD and SWD, respectively) affecting the resistance of each in-plane direction. Meshes are attached to composites using resins or adhesives. If embedded in resin, the mesh should be of low thickness to reduce the volume and weight of the resin needed to fill the area. Adhesives are applied between the mesh and the composite, covering the mesh and also protecting the structure against air and water during service [293]. In contrast to interwoven fibres, the disadvantages of the use of metal meshes are the increase in weight and, hence, in fuel consumption and the greater manufacturing cost due to the introduction of an additional processing step. The open areas of the mesh geometry have to be maximised and the thickness minimised in order to reduce the weight, subject to the constraint of introducing an amount of conductive material sufficient to dissipate the energy of the strike effectively.

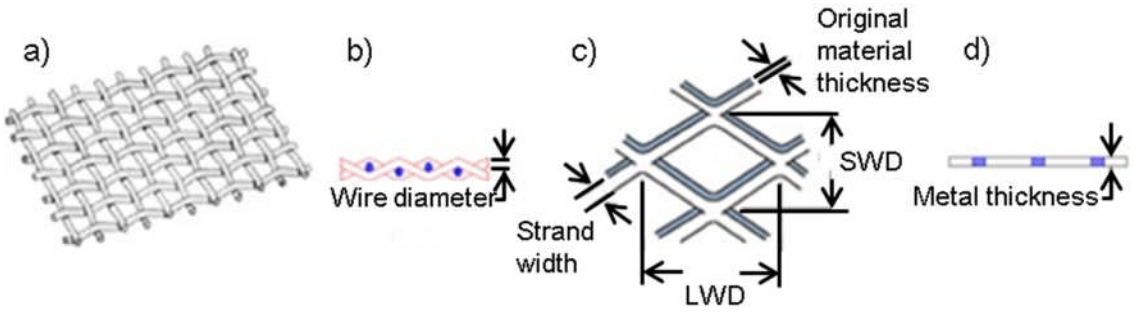

Figure 8-2 Metal meshes: a) woven mesh, b) side view of woven mesh, c) non-woven mesh and d) side view of non-woven flattened mesh, adapted from [293]

In general, the magnitude and type of damage in composites depends on the amplitude of the current of the lightning strike and the material, geometry and attachment of the protection. These factors affect the current density in the moment of lightning strike; the damage increases with increasing current density. Therefore, the purpose of the protective layers is the efficient spreading of the current in order to minimise the concentration of the current on one location.

Lightning strike tests have shown a decrease in damage by up to 80% when covering the composite with protective metal layers, such as meshes or fibres, compared to equivalent unprotected composite structures [298-301]. Tests are carried out according to Zone 1 with currents of up to 200 kA or Zone 2 with currents up to 80 kA using non-woven meshes made of aluminium or copper [299, 300], interwoven phosphorous-bronze mesh [299], nickel coated carbon fibres [298] and aluminium interwoven fabric [301], show reduced surface and internal damage with increasing conductivity of the metal. The least amount of damage has been reported to be degradation of the paint and metal protection for aluminium mesh, nickel coated carbon fibres and aluminium interwoven fabric [298, 299, 301], followed by burn-through of the composite with increasing diameter of the internal and surface damage using a copper mesh, phosphorous-bronze mesh and no protection [299]. However, an insulating material is placed between the composite and the aluminium mesh, such as glass fibres, to protect the composite against galvanic corrosion caused by the aluminium, reducing structural damage of the composite underneath. Burn-through of the composite includes degradation of the paint and metal protection,

fracture of the fabric fibres and vaporisation of the resin [299, 300]. The results mainly depend on the current level, composite thickness, conductivity of the metal and the form of the protection applied; interwoven fabric has the potential to use the conductivity of the metal and the carbon fibres to reduce the damage caused by lightning strike, whilst the insulating layer applied between carbon fabric and metal meshes deteriorates the performance [299, 302]. Furthermore, the damage increases with rising current level [303].

Generally, the paint layer covering the metal lightning strike protection and the composite structures of aircrafts is always damaged after a lightning strike since it is the outermost surface and it is non-conductive. Hence, the thickness of the paint layer has to be minimal in order to enable the metal protection to conduct the current [304] and to limit surface damage to sizes obtained in unpainted structures [305]. Furthermore, the thickness of the paint layer has to be appropriate for the thermal expansion mismatch with the metal mesh during service which can lead to cracking of the paint and increase the risk of corrosion of the metal layer [306]. This has motivated research aiming to increase the mechanical properties and conductivity of the paint by adding nanoparticles in order to conduct high currents through the paint and metal layer underneath [293, 307].

The type of lightning strike protection, which is applied on aircrafts, is different for every type of aircraft depended on a large variety of factors, such as cost, weight penalty, durability and corrosion of the protection and on the geometry of the aircraft [307, 308]. The Boeing 787 Dreamliner composite fuselage incorporates interwoven conductive wires on the outermost ply for lightning strike protection [309].

8.2 Electrical conductivity of tufted materials

8.2.1 Electrical conductivity of tufting materials

As described in section 3.3.5 the conductivity of tufts was determined by measuring the resistance of 2 m long carbon and stainless steel threads and copper wire. The glass thread is considered as non-conductive and not considered in this analysis. Table 8-1 summarises the results for the

conductivity for carbon, copper and stainless steel. The measured data is in line with published resistivity values of 5.0×10^{-4} Ωm for carbon fibres in a composite structure [310], 1.7×10^{-8} Ωm for copper [311] and 7.7×10^{-7} Ωm for stainless steel [312], both in form of bulk material at 20 °C.

Table 8-1 Electrical conductivity of tuft materials.

Material		Carbon	Copper	Steel
Conductivity	[S/m]	6.2×10^{4}	5.4×10^{7}	1.2×10^{6}

8.2.2 Through-thickness conductivity of tufted laminates

Three specimens, as introduced in section 3.2.5, were tested for electrical conductivity in the thickness direction out of each untufted and fully tufted panel without mesh, manufactured for the lightning strike tests. Table 8-2 summarises the average conductivity and its standard deviation for each type of specimen.

Table 8-2 Averaged through-the-thickness conductivity test results of untufted and fully carbon, copper, glass and stainless steel tufted materials with eight layers of ±45° carbon plies and infused with RTM6 (standard deviations are reported in brackets).

Material	Control	Carbon	Copper	Glass	Steel
Conductivity [S/m]	1.9×10^{1} (±1.6)	1.3×10^{2} (±14.6)	5.0×10^{3} (±535.7)	2.1×10^{1} (±5.0)	7.9×10^{2} (±81.5)

The test results reveal an increase in conductivity for tufted composites compared to the untufted material. The copper tufted material has the highest conductivity, about 250 times higher than that of the untufted composite. This is due to the high conductivity of the copper wire. The same effect is observed in stainless steel tufted composites and the carbon tufted material, with a 40 and 10-fold increase compared to the control. The conductivity of the glass tufted material is very close to that of the control as a result of the fact that the glass thread is electrically inert. The trend of the conductivities of the tufted materials corresponds to the conductivities reported for the pure tuft materials in section 8.2.1. The results also reveal a rising standard deviation with increasing conductivity; however, the coefficient of variation remains relatively constant,

implying similar mechanisms of variability generation and scaling according to the conductivity of the constituents.

8.2.3 In-plane conductivity of tufted materials

The specimens used for the through-the-thickness conductivity measurements were also utilised for measuring the conductivity in the 90° and 0° to the non-structural stitching direction. The results reported in Figure 8-3 show that tufting through-the-thickness does not change the conductivity in 90° and 0° direction. The conductivity in the 90° direction is 7100 S/m for the control, 5600 S/m for the carbon tufted laminate, 6800 S/m for the glass tufted material and 6400 S/m for the stainless steel tufted composite. The relatively high conductivity of the copper tufted material of 12000 S/m is caused by the conduction of the current through the overlapping tuft loops creating a high conductive surface. The results in the 0° direction show a similar trend due to the bi-axial fabric lay-up. The conductivities are 4700 S/m for the control, 5600 S/m for carbon tufted, 7700 S/m for copper tufted, 6400 S/m for glass tufted and 5100 S/m for stainless steel tufted materials. The copper tufted material has a higher conductivity than the untufted material, however, considering the high conductivity of the control in the 90° direction (7100 S/m) the conductivities in 0° can be considered to be in the same range. The variation between the materials may be caused by the quality of the contact between fibres and copper foil electrode. Although in 0° direction copper tufting improves the conductivity by 64% compared to the untufted material, its conductivity is 36% lower than that of copper tufted material in the 90° direction. This is attributed to the orientation of tuft seams in the 90° direction.

Overall, the results show that the conductivities in the thickness direction are lower than that of 90° and 0° directions. This is expected for the control material as conduction through-the-thickness is influenced significantly by the insulating resin. In tufted materials with conductive reinforcement the gap between in-plane and through-thickness conductivity is significantly lower, with the copper leading to values two orders of magnitude higher than that of the control.

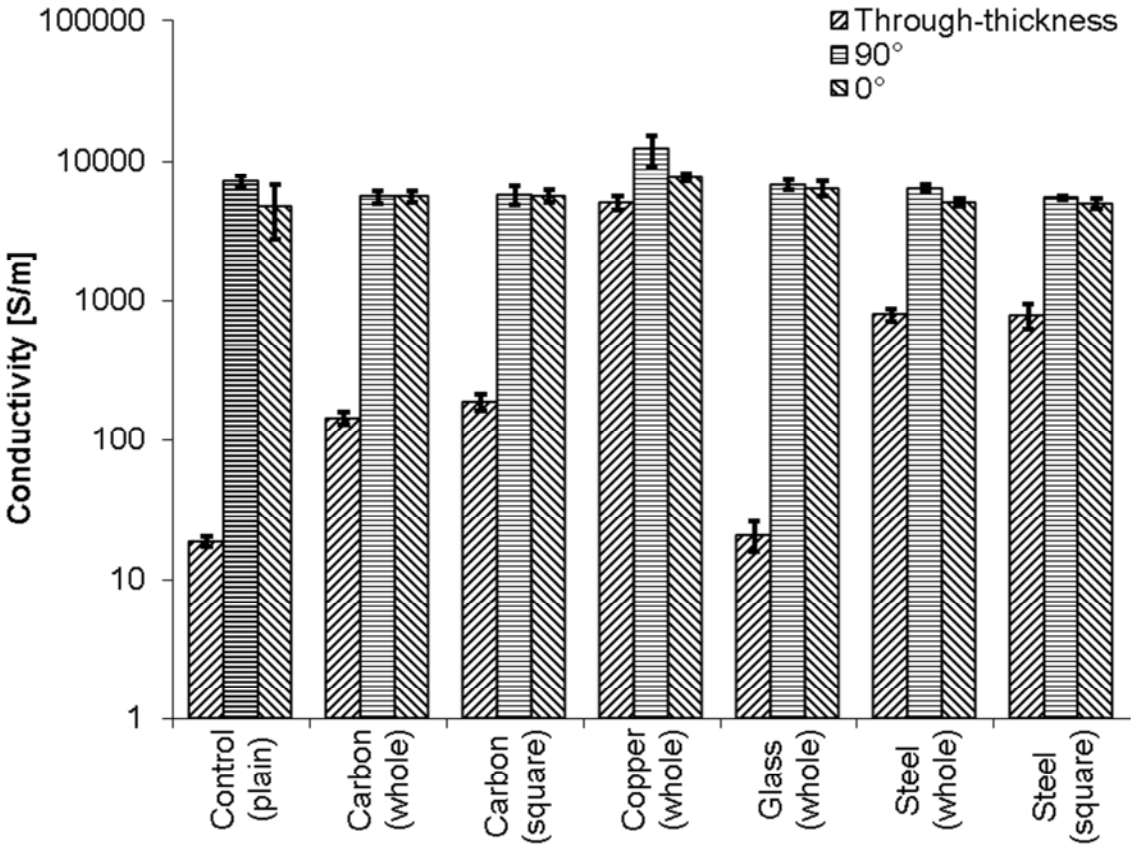

Figure 8-3 Conductivity in through-thickness, 90° and 0° direction of tufted composites.

8.3 Lightning strike performance of tufted carbon composites

All ten panels, described in 3.2.3, were subjected to lightning strike in order to establish the effect of tufting on the lightning strike performance of composite structures. The types of damage, such as resin burn off and fabric fibre tufting, and the magnitude was identified using visual inspection and C-scanning and used as criteria for performance. Figures 8-4 and 8-5 present the panels after lightning strike with visible surface damage, showing that the untufted materials (Figure 8-4a, b) display the largest damage. In the untufted material without copper mesh (Figure 8-4a) the lightning attachment causes a relatively large amount of resin vaporisation in the centre of the panel with fibre tufting (referring to damage of fibres) and resin cracking as shown by the micrograph in Figure 8-6. This type of damage can be considered as critical and would result to deterioration of structural integrity in operation. Small areas of damage can also be observed around the central damage; these are probably generated

by return strokes of lower current than the initial attachment. The control material with copper mesh protection (Figure 8-4b) shows very little fibre tufting damage and extensive resin and mesh vaporisation in the centre of the panel. This result demonstrates the benefits of the incorporation of the mesh protection, as the damage in this case becomes non-critical for structural integrity in the short term. The role of the copper mesh is to conduct the current and distribute it over the entire surface, thus reducing the energy density at the attachment location. When protection is not utilised a high current density penetrates the material locally leading to damage caused by high temperature.

The copper tufted panel (Figure 8-4c) is nearly undamaged; the high conductivity of the copper tufts leads to the conduction of the current through the panel along the tufts and along the surface via the tuft seams and overlapping tuft loops. The significantly higher conductivity of copper results in very limited resin burn off on the panel surface as shown in Figure 8-7a. The fully carbon tufted (Figure 8-4d) and central square carbon tufted (Figure 8-4e) display similar damage since the lightning attachment occurred on the tufted area of each panel. The conductive carbon tufts dissipate the current through the internal part of the panel, rather than concentrating it as in the control panel, leading to only surface damage in the form of resin burn off and a small spot of fibre tufting (Figure 8-8). Indeed, the conductive tufts are covered by insulating resin which is burned off at some locations before the current reaches the conductive tufts. In the case of the central square tufted panel, the current is conducted through the carbon tufts resulting in equivalent damage compared to the fully tufted panel (Figure 8-9). The conductivity of the carbon tufts is lower than that of the copper tufts resulting in slightly more surface damage and a small amount of fibre tufting. The carbon tufted panel containing a copper mesh (Figure 8-4f) shows a similar damage pattern as the other two carbon tufted panels. The resin degradation in the centre of the panel is caused during the initial lightning attachment burning off the resin surrounding the copper mesh. However, the high conductivity of the copper mesh eliminates fibre tufting. As observed in Figure 8-4f, the carbon tufted panel with mesh protection has some

surface dry spots as well some secondary surface damage probably caused by the return stroke.

The amount of surface dry spots is higher in the fully glass tufted material (Figure 8-5a); these are also present in the central area of the panel as shown in Figure 8-7b. This may be the reason for the relatively small damage of the panel, despite containing non-conductive glass tufts. The presence of dry spots leads to a direct conduction of the current through the conductive carbon fabric fibres accompanied with a small amount of fibre tufting (Figure 8-9). The damage of the glass tufted material covered with a copper mesh (Figure 8-5b) is similar to that of the glass tufted material without mesh. Dry spots are not present which may lead to increased damage due to the insulating resin; however, the copper mesh reduces the damage by conducting the current along the surface.

The surface damage of the fully stainless steel tufted material (Figure 8-5c) is comparable to those of the fully carbon tufted material without mesh (Figure 8-4d); the initial lightning attachment burns off the top resin layer in the centre and leads to a small amount of fibre tufting (Figure 8-9), whilst the current is conducted by the highly conductive stainless steel tufts inside the panel. Return strokes occur off centre and lead to small areas of resin burn off. The central square stainless steel tufted laminate (Figure 8-5d) displays internal damage in the form of resin burn off and fabric fibre tufting outside the tufted area. The large damage next to the tufted area is comparable to that of the untufted control material without mesh (Figure 8-4a). The tufted area shows only limited resin vaporisation due to the conductivity of the stainless steel tufts. Figure 8-10 shows the defects in the central square stainless steel tufted panel with fibre tufting starting in the untufted section, whilst the conductive tufts clearly reduce the damage to occasional resin burn on the surface.

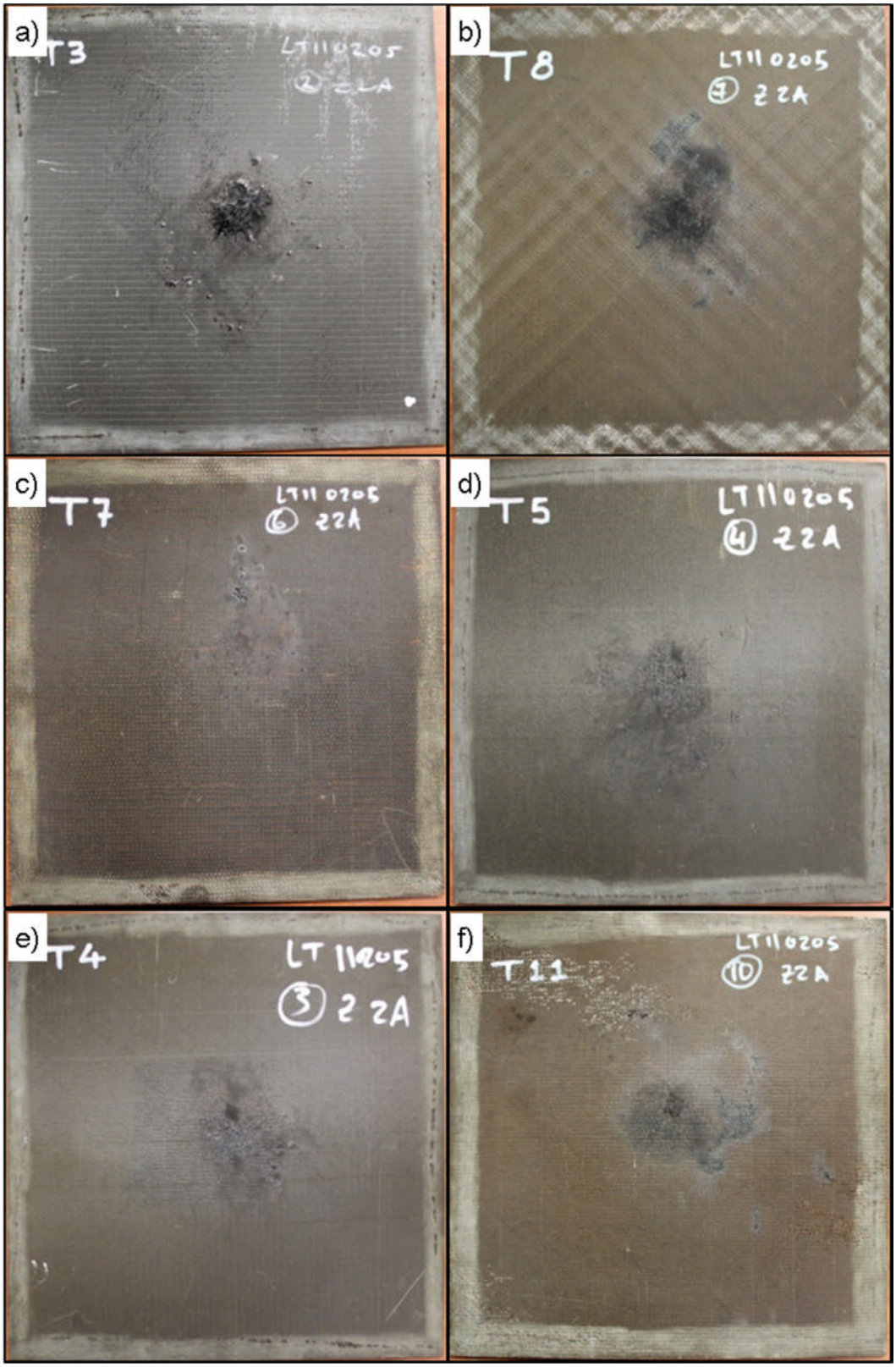

Figure 8-4 Panels after lightning strike: a) plain control, b) control with copper mesh, c) copper tufted, d) fully carbon tufted, e) central square carbon tufted and f) carbon tufted with copper mesh.

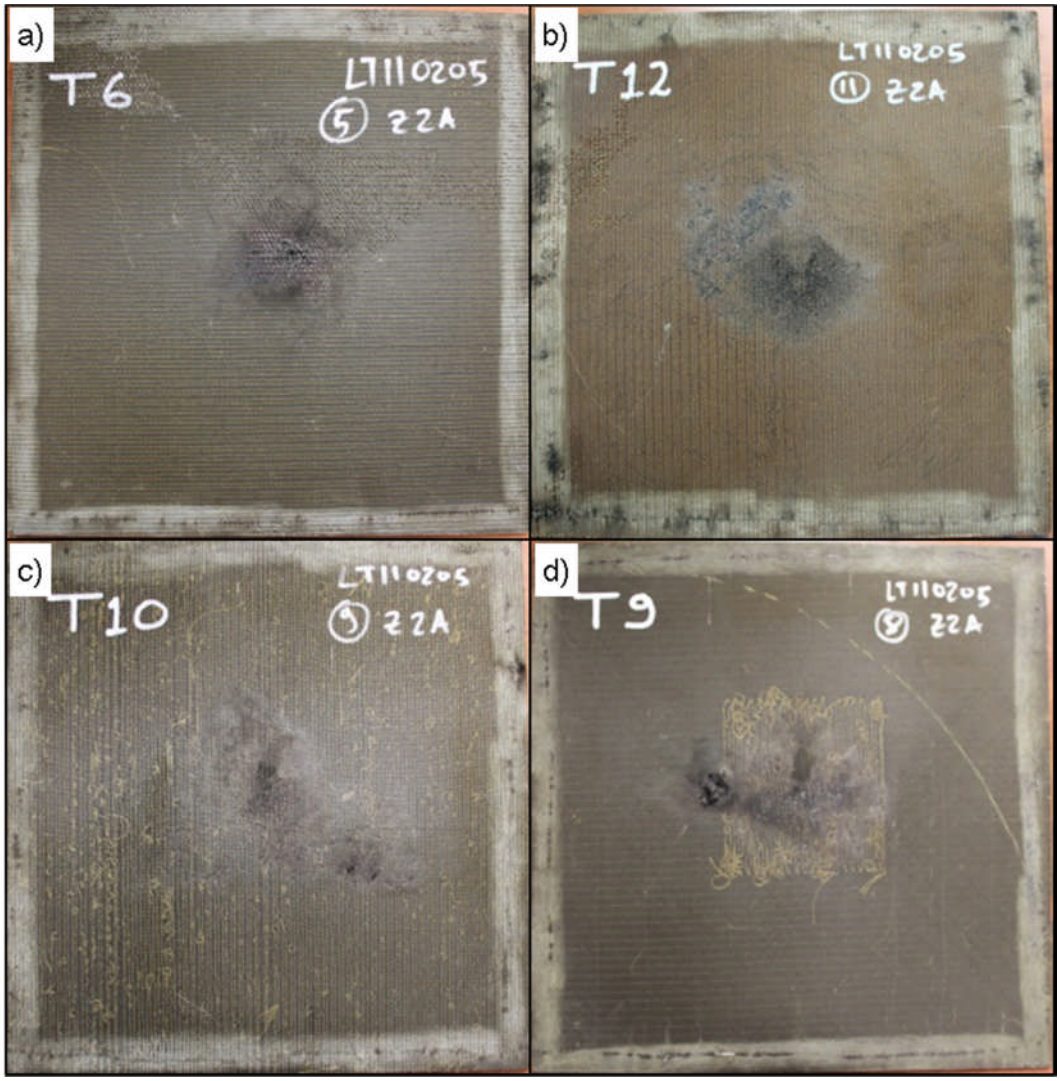

Figure 8-5 Panels after lightning strike: a) Fully glass tufted, b) glass tufted with copper mesh, c) fully stainless steel tufted and d) central square stainless steel tufted.

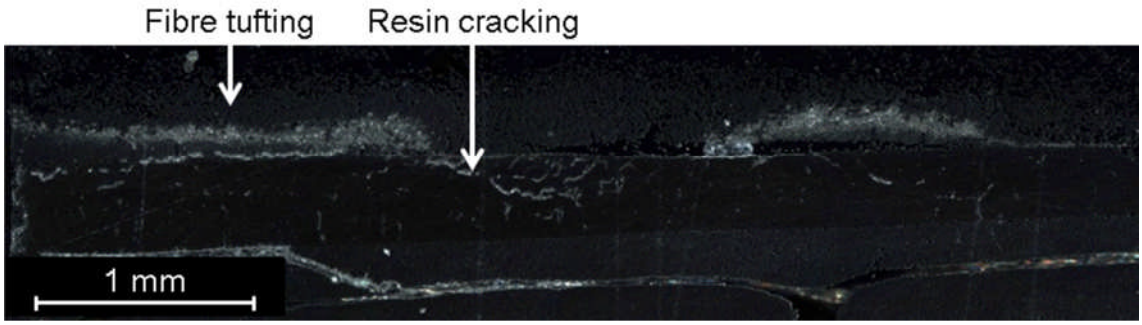

Figure 8-6 Micrograph of untufted control panel without copper mesh showing surface fibre tufting and resin cracking.

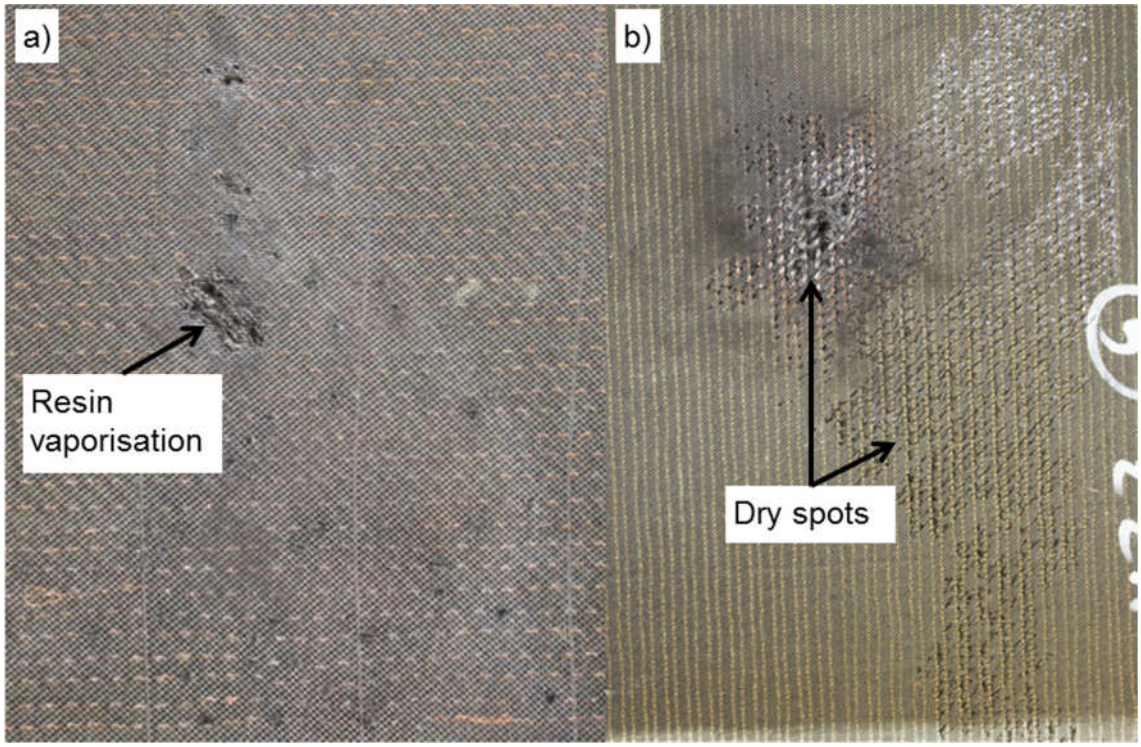

Figure 8-7 a) Resin vaporisation at lightning attachment location in copper tufted material and b) dry spots in fully glass tufted panel without copper mesh.

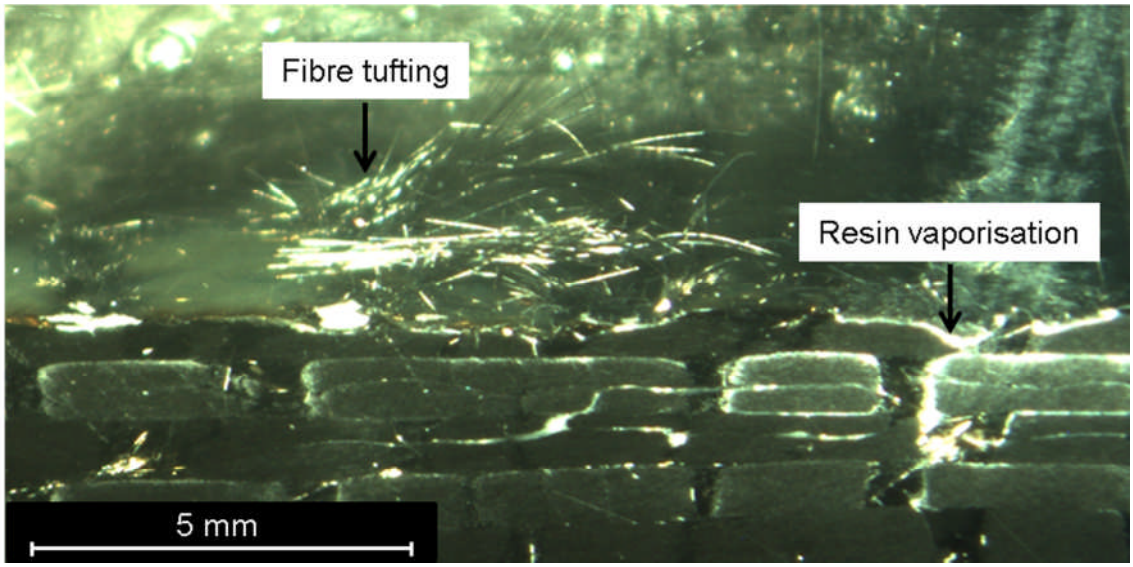

Figure 8-8 Micrograph of fully carbon tufted material without copper mesh showing small areas of fibre tufting and resin burn off.

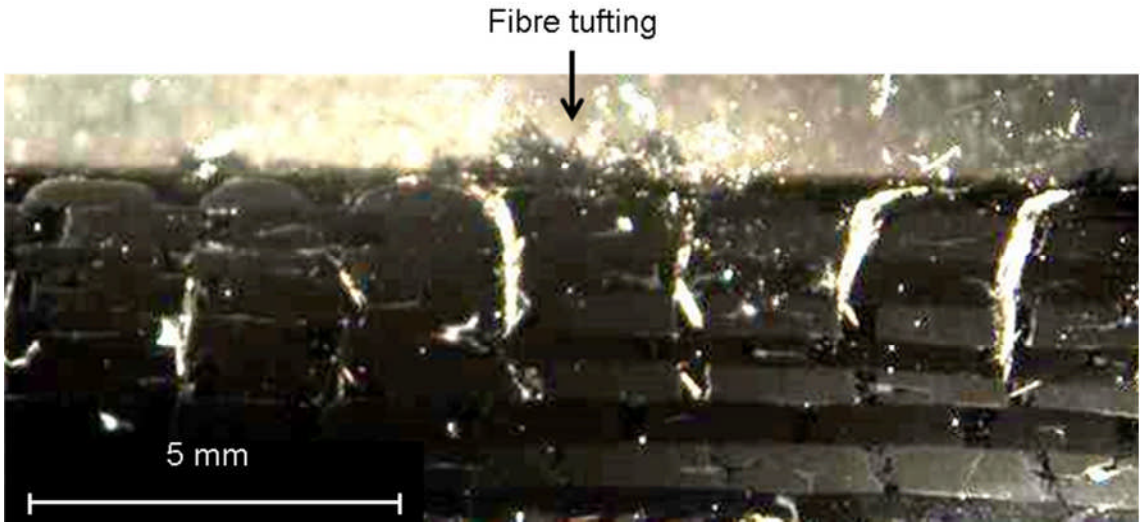

Figure 8-9 Example of fibre tufting in fully stainless steel tufted panel which also occurred in glass and central square carbon tufted panels.

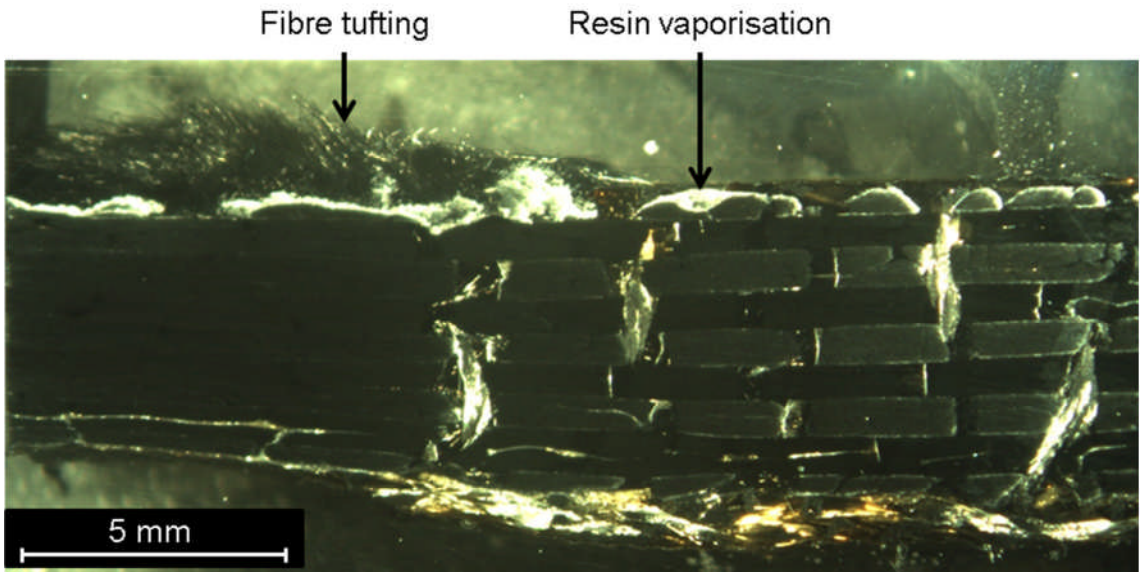

Figure 8-10 Panel containing a stainless steel tufted central square with resin burn off and fibre tufting on untufted surface.

In order to determine the extent of internal and surface damage the panels were analysed using C-scan. Figure 8-11 shows the C-scan results of the entire panels with the central damage caused by the lightning strike in white, whilst Figure 8-12 shows the C-scan results with the panels in white and the damage in black in order to emphasise the size of the damage. In general, the bi-axial fabric and the high tuft density lead to many resin rich areas. These areas are shown as white spots in Figure 8-11 and are independent of the lightning strike.

As shown in Figure 8-11a the resin rich areas form a square pattern around the central damage region following the fabric fibres, whilst in Figure 8-11c the resin rich areas form a long white stripe on the left side of the damage caused by the copper tufts. Equivalently, Figures 8-11h and 8-11b, g, and i show irregular patterns outside the central damage, all caused by resin rich regions generated by the tufting. The central carbon and stainless steel tufted material (Figure 8-11e, j) were scanned twice, each time with different settings for the untufted and tufted area adapting the frequency of the ultrasound due to the different sound absorption response of the two areas. The damage size results shown in Figures 8-11 and 8-12 are summarised in Figure 8-13. C-scanning does not distinguish between surface vaporisation/burn off and internal damage. The internal damage was determined by microscopy of cross sections of the panels as shown in Figure 8-6 and Figures 8-8 – 8-10. The results reported distinguish between surface damage, such as resin burn off, vaporisation of the copper mesh and tuft seams, and internal damage, such as resin vaporisation at larger scale, fibre tufting and damage to the tufts. Generally, the type of damage governs the residual mechanical properties of the material and the two types cannot be compared directly as internal damage is critical for structural integrity. In the untufted control material without copper mesh the damage extents to an area of 4100 mm^2 (4% of the panel) as shown in Figures 8-12a and 8-13a. The central square stainless steel tufted material (Figure 8-12j) displays surface damage and internal damage next to the tufted area.

The copper mesh on the untufted material (Figure 8-12b) changes the type of damage from surface and internal, as occurred for the equivalent material without mesh, to solely surface damage reducing the damage size. The high conductivity of the copper tufts leads to very limited amount of resin burn off on the surface of the copper tufted material (Figure 8-12c) resulting in the smallest damage area among all configurations tested. The carbon tufted panel without copper mesh (Figure 8-12d) shows of the largest surface damage. However, this can be still considered a significant improvement compared to the damage size of the untufted control material without copper mesh. The damage area of the central square carbon tufted material (Figure 8-12e) is 1020 mm^2 (1.0%).

However, some of the energy is dissipated through off centred secondary strokes. Copper mesh protection of the carbon tufted material reduces the damage size, as shown in Figure 8-12f which is equivalent to the level reached in unprotected copper tufted material. In contrast to the untufted material with copper mesh, the carbon tufts conduct the current through-the-thickness in addition to in-plane dissipation via the copper mesh, reducing significantly the overall damage. The test results are in line with the through-the-thickness conductivity results for the fully tufted materials without copper mesh.

The glass tufted panel without copper mesh (Figure 8-12g) shows a damage area of 1330 mm^2 (1.3%). As observed in Figure 8-5a, the dry spots in the centre of the panel lead to direct conduction of the current through the fabric fibres, mimicking a conductive lightning strike protection and leading to resin burn off and very limited fabric tufting. The glass tufted material with copper mesh (Figure 8-12h) shows a damage size larger than that of the glass tufted material without copper mesh, since no manufacturing defects were present affecting the lightning strike performance. The damage size is equivalent to that of the control panel with copper mesh since the insulating glass tufts do not affect significantly the lightning strike performance. Despite the small internal damage of the stainless steel tufted panel (Figure 8-12i), C-scanning reveals a damage size of 3170 mm^2 (3.1%). The reason is the off centred return strokes on the stainless steel tufted panel extending beyond the central region. Overall, the conductivity measurements of the tuft materials, presented in section 8.2.1, are in line with the lightning strike performance of the copper, carbon and stainless steel tufted material. The high conductivity of the copper wire reduces the surface damage compared to the fully carbon and stainless steel tufted materials without copper mesh. Also, the stainless steel tufted material has a lower damage area than the fully carbon tufted material as a result of the higher conductivity of the stainless steel thread compared to the carbon thread.

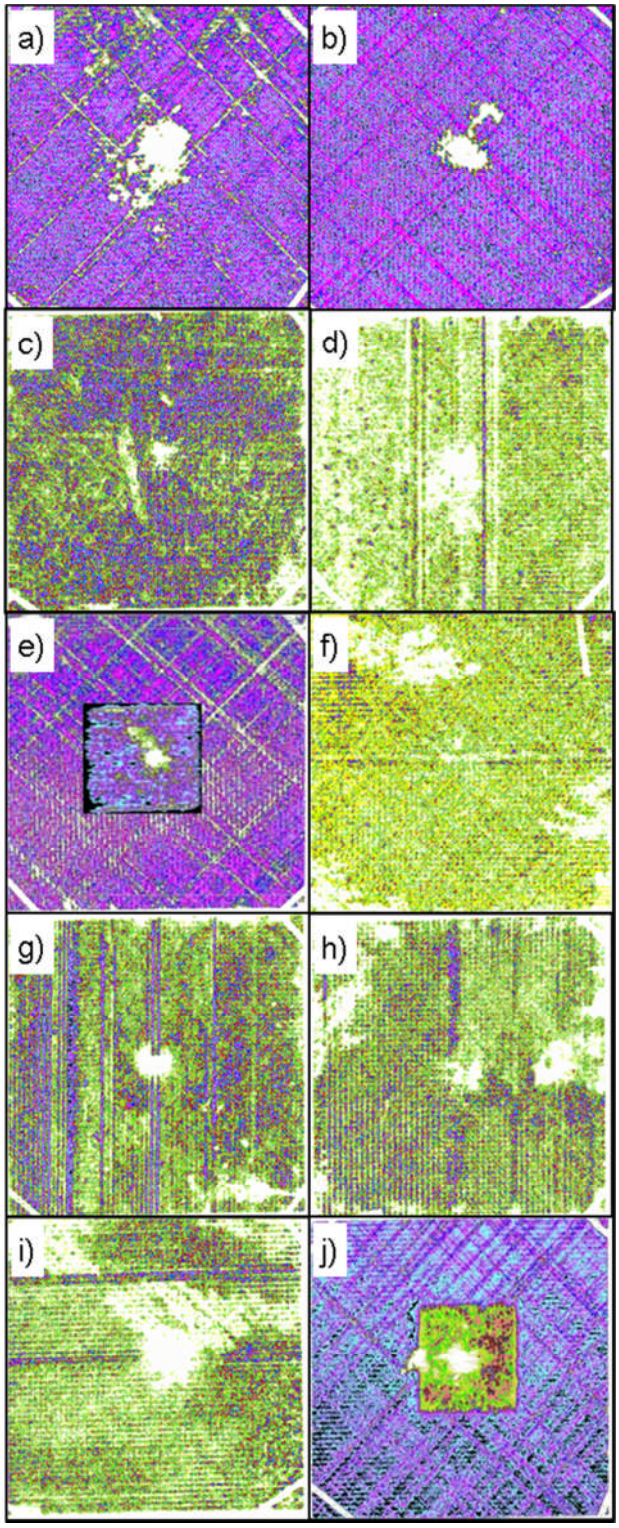

Figure 8-11 C-scan results of panels subjected to lightning strike: a) plain control, b) control with copper mesh, c) copper tufted, d) fully carbon tufted e) central square carbon tufted, f) carbon tufted with copper mesh, g) fully glass tufted, h) glass tufted with copper mesh, i) fully stainless steel tufted and j) central square stainless steel tufted.

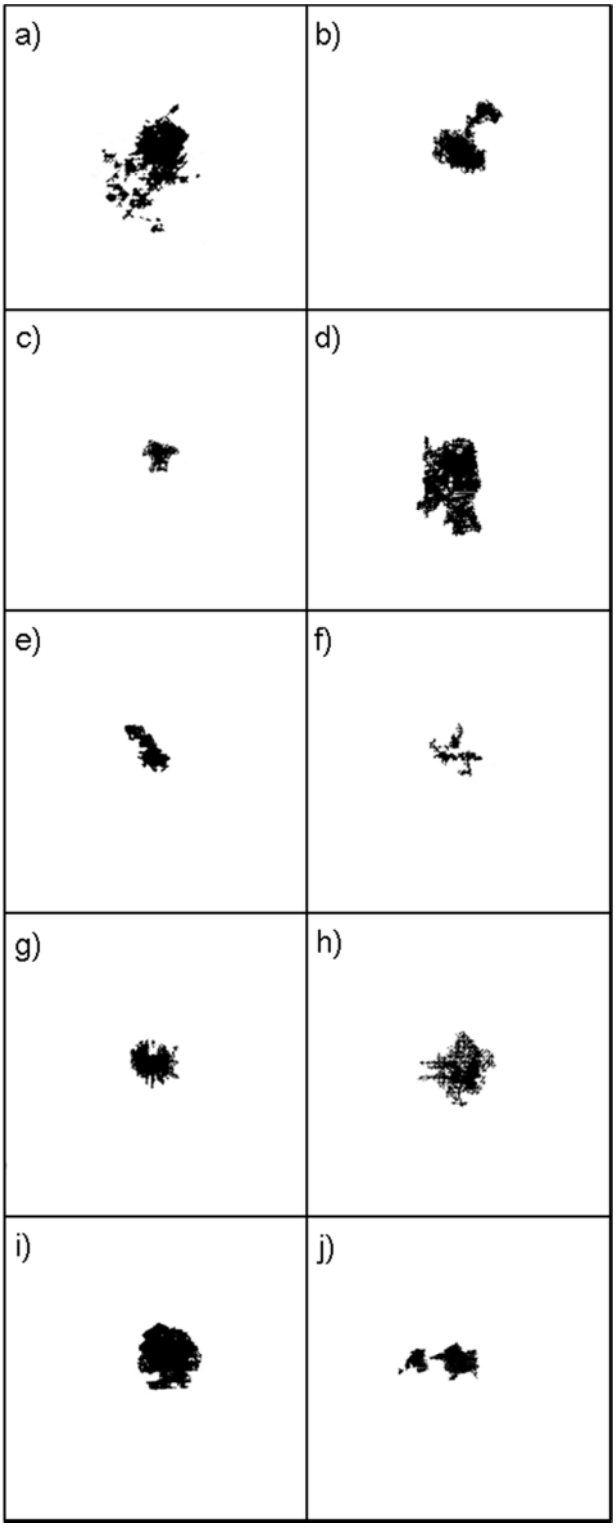

Figure 8-12 C-scan results after lightning strike in white with damages in black: a) plain control, b) control with copper mesh, c) copper tufted, d) fully carbon tufted, e) central square carbon tufted, f) carbon tufted with copper mesh, g) fully glass tufted, h) glass tufted with copper mesh, i) fully stainless steel tufted and j) central square stainless steel tufted.

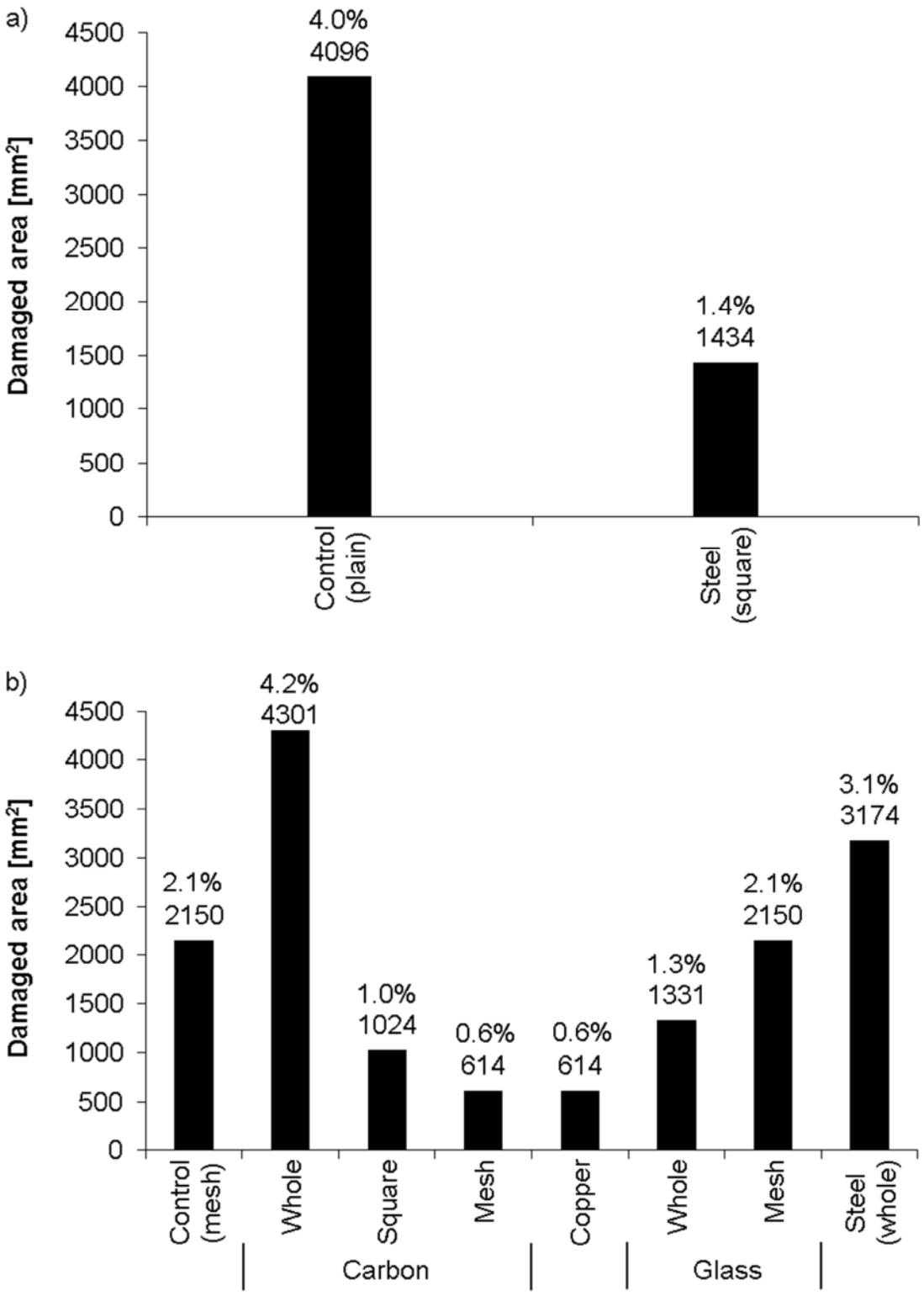

Figure 8-13 Size of damaged area and percentage related to the entire panel size: a) internal damage and b) surface damage.

8.4 Conclusions

The through-thickness conductivity of tufted materials increases with increasing conductivity of the tuft material. The increase is up to 250 times for copper tufted laminates compared to untufted composites. Tufting does not affect the conductivity in the in-plane direction significantly. However, in the case of copper tufting, the overlapping loops of the copper tufts contribute to the in-plane conductivity.

The lightning strike performance is improved significantly by tufting using conductive materials. In the case of copper tufts the size of the damage area is reduced by about 75% compared to untufted composites with copper mesh protection. Furthermore, the damage type changes from internal to surface damage due to the presence of tufting, when compared with unprotected, untufted laminates. The copper mesh improves the lightning strike protection by 40% for carbon tufted and 48% for untufted panels in terms of damage area size.

9 General discussion

This chapter discusses the results obtained in this study and their broader meaning for the mechanical and electrical performance of tufted composites. The findings are used in the context of overcoming the challenges to tuft the tail cone (section 4.2) and to answer the research questions proposed in section 4.5.

9.1 Mechanisms contributing to delamination performance

This section summarises the relation of the failure mechanisms described in sections 5.1.3, 5.2.2, 6.2 and 7.3. The findings, such as the lower crack initiation toughness for tufted materials as noted in the corresponding sections and unintentional fibre misalignment and its effect on the delamination performance, are discussed.

9.1.1 Failure mechanism of tufted composites

Generally, tufting increases the delamination toughness of composites in mode I by bridging delamination cracks and arresting the crack propagation. The increased delamination performance is accompanied by typical features, such as resin rich areas and fabric fibre misalignment, undulation and breakage around the tufts potentially reducing the in-plane properties of tufted materials. During mode I delamination testing the resin in the tufts is crushed due to untwisting yarns, whilst the thread debonds from the surrounding composite or resin, followed by a rotational movement, due to twisting, and axial elongation. Energy is required for the tuft translational and rotational movement as well as for the debonding and crushing of the resin. This energy is accumulated during the process increasing the crack energy release rate. Once the tufts rupture the accumulated energy is released and the crack propagates until it is arrested by subsequent tuft rows.

The performance of tufts is influenced by the tuft material and its mechanical properties, such as ultimate strength and strain. High strain increases the number of activated tuft rows, compared to tuft materials with low strain, raising the potential for energy accumulation and increasing the crack energy release

rate. Low strain can be compensated by high strength which increases the crack bridging loads and delamination resistance. An ideal tufting thread may combine the properties of the copper wire and the aramid thread representing a high ultimate strength accompanied by a large strain. In regard to the results shown in Figure 5-1 the stress-strain curve of the thread would be between the stress-strain curves of aramid and copper. This would result in several tuft rows (up to six) being active, comparable to copper tufts, and simultaneously further increasing the crack tip closure traction due to the high strength comparable to aramid tufts. By heat treatment of metallic threads the ductility is increased maintaining the ultimate strength. This may result in a thread material combining the advantageous mechanical properties and further improving the delamination performance compared to aramid, stainless steel and copper.

Tufting enhances fibre bridging contributing to the delamination resistance. Fabric fibres attached to the thread are lifted, whilst the thread elongates, breaking the non-structural stitches. The tuft performance and magnitude of fibre bridging is also affected by the base laminate. A high amount of binder increases the resin/fabric interface suppressing the tuft performance. However, fibre bridging is enhanced as fibres attach to the elongating tufts being lifted during delamination.

Materials with different tuft depths show different delamination performance: the delamination resistance increases with decreasing tuft depth. In materials with a high tuft depth, the tufts are constrained more by the surrounding composite leading to limitations in tuft movement (rotation and elongation) and rupture of the tuft below its ultimate strength and strain. At low tuft depth the tuft debonding crack, starts at the specimen delamination plane and propagates along the tuft, debonding the entire tuft loop leading to interfacial shear and frictional pull-out of the tuft. These shear loads are the main energy consuming mechanism increasing the delamination resistance. This has also been found to be the most energy consuming mechanism for Z-pins during mode I delamination tests [27]. At high tuft depth the tuft/composite interface strength is higher than the tensile strength of the tuft causing tuft rupture and a lower delamination toughness compared to low tuft depths. Based on these findings

the failure mechanism changes at a certain tuft length. However, the ultimate strain of the tuft materials is an important factor concerning the tuft depth. The tuft depth may not have an effect on the delamination performance for brittle materials, such as the stainless steel thread, as the threads may reach the relatively low ultimate strain in composites with high tuft depths rendering the effect of tuft depths insignificantly.

Figure 9-1 illustrates schematically the relationship between delamination toughness and tuft depth for different tuft materials and constructions. Zone 1+3 represents pure shear during pull-out of extremely short tufts once the crack reaches the tuft location. The length of the tufts is below 1 mm for the tuft materials and intermediately bindered preform used in this study. The delamination toughness can be assumed to increase linearly with increasing tuft length due to linear increase of the interface causing shear stresses. The linear relation continues in zone 1+2+3 where shear and tuft elongation take place at first, followed by frictional pull-out of the tuft accompanied by fibre bridging leading to maximum crack energy release rate (solid line).

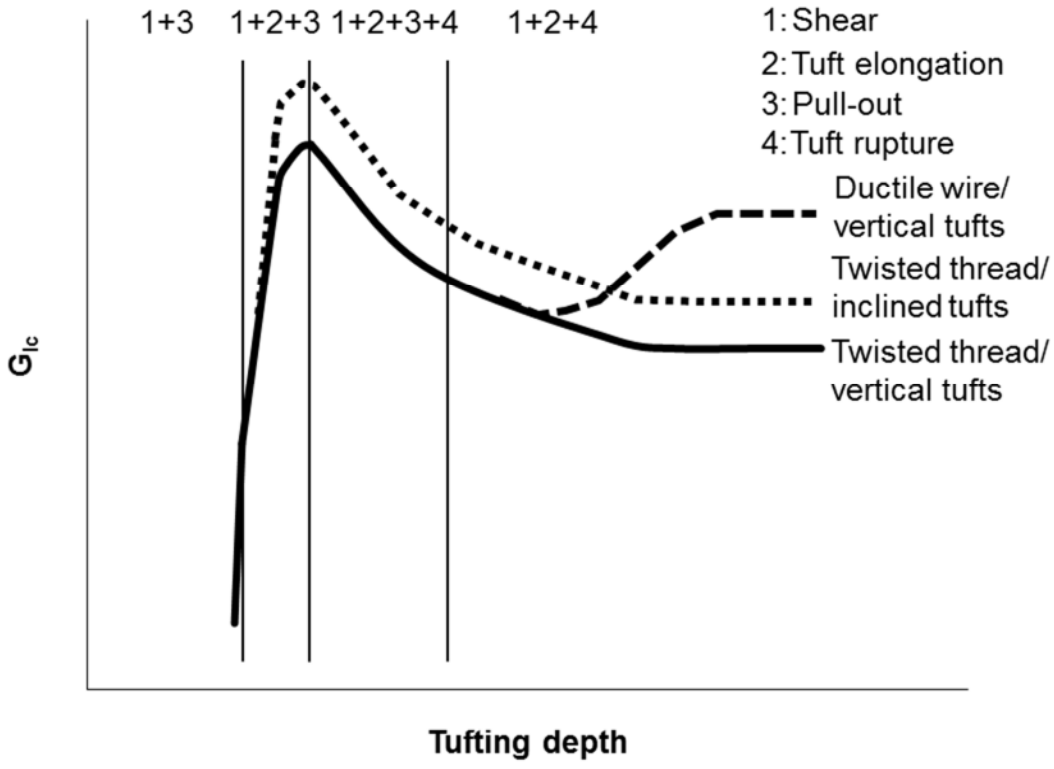

Figure 9-1 Dependence of delamination toughening mechanisms on tufting depth.

Increasing the tuft depth may lead to shear, tuft elongation and tuft rupture with subsequent pull-out of the ruptured tuft and fibre bridging causing additional shear stresses, as represented by zone 1+2+3+4. Such an event may occur if the tuft has a certain length, so that the debonding crack reaches the outermost ply leading to tuft elongation of the vertical tuft section, but due to the bend of the tuft loop stress concentration may lead to rupture before the crack debonds the tuft loop. The ruptured tuft is then pulled-out of the composite. The delamination toughness is lower compared to zone 1+2+3 as the friction is lower due to a shorter tuft section being pulled-out. Increasing the tuft length within zone 1+2+3+4 decreases the delamination resistance as the debonding crack does not reach the outermost ply and the tuft section pulled-out decreases up to a tuft length corresponding to zone 1+2+4. In that zone the first part is described by a decreasing delamination toughness due to a decreasing tuft section debonding from the composite leading to reduced shear stresses, tuft elongation and rupture at the delamination plane. The second part is represented by a relatively consistent delamination toughness (solid line) caused by debonding, elongation and relatively small amount of shear stresses of a relatively short tuft section with subsequent rupture at the delamination plane due to tuft compression by the surrounding composite. The dashed line represents tuft depth dependence of untwisted ductile materials (vertical tufts) which are not affected by the surrounding composite. The tuft length of 1.0 mm using aramid, stainless steel and copper tufts in intermediately bindered fabric material, as used in this study (section 6.1.1), corresponds to zone 1+2+3, whilst the stainless steel is closer to zone 1+3 and aramid closer to zone 1+2+3+4. The tuft length of 2.6 mm using aramid and stainless steel corresponds to zone 1+2+4 (solid line) with aramid being closer to zone 1+2+3+4 than stainless steel. Indeed, the stainless steel is relatively close to the flat section as the tuft depth of 5.2 mm leads to a similar delamination toughness. Aramid tufts with a depth of 5.2 mm correspond to the centre of the decreasing section in zone 1+2+4 as the delamination toughness is lower compared to the 2.6 mm tuft depth. The copper wire with a tuft depth of 2.6 mm corresponds to the decreasing section in zone 1+2+4 before the dashed line

starts, whilst the copper wire with a tuft depth of 5.2 mm is on the dashed line leading to an increased delamination toughness compared to the tuft depth of 2.6 mm. This is due to the fact that the copper wire is affected less by the surrounding composite, being free to move and leading to larger displacements. However, the maximum strain of a material leads to a plateau region for the dashed line. The ultimate strain of the tuft materials is an important factor concerning the tuft depth. The tuft depth may not have an effect on the delamination performance for brittle materials, such as the stainless steel thread, as the threads may reach the relatively low ultimate strain in composites with high tuft depths neglecting the effect of low tuft depths.

Although very low tuft depths, such as 1.0 mm, show improved delamination performance compared to larger tuft depths, the robustness is reduced. Short tufts are susceptible to pull-out during handling of the preform and depending on the tuft material the friction between the fabric and the thread may not be sufficient to hold the thread in place. In addition, the reliability and repeatability of the delamination performance of short tufts is also reduced as the frictional pull-out (main failure mechanism) depends on the friction between tuft and composite and may change from tuft to tuft. This confirms the high variability in test results as shown in Table 6-1. Regarding the tufting process to implement low tuft depths, the resistance for the needle to penetrate the preform is minimal. This suggests that a needle with reduced diameter may be used decreasing the fabric fibre misalignment and increasing the friction between the thread and the composite. Furthermore, the in-plane properties may be deteriorated less as a thinner needle leads to reduced fibre crimp, misalignment and breakage and resulting resin rich areas.

The 4 mm and 8 mm deep aramid tufted highly bindered material contain similar delamination toughness corresponding to the flat part of the solid line in zone 1+2+4. In general, a high amount of binder may decrease the span of the zones leading to the start of the consistent delamination toughness at a lower tuft depth. The high amount of binder increases the resin/tuft interface strength reducing the tuft elongation and suppressing the effect of tufts. However, the large amount of binder increases the resin toughness and fibre bridging. Hence,

depending on the tuft material and tuft depth the curve for the highly bindered preform material may be shifted vertically compared to the solid line.

The main failure mechanisms for angled tufting are similar to those illustrated in Figure 9-1. In addition, resin ploughing occurs which constitutes a major mechanism for enhancing the delamination resistance. During mode I delamination inclined tufts (twisted threads) rotate and plough into the resin. Transferring this mechanism to the schematic in Figure 9-1, ploughing may start in zone 1+2+3 following the dotted line. The magnitude of ploughing depends on the bending behaviour of the tufting materials and the angle. A ductile copper wire elongates and bends at the delamination plane, rather than rotating and ploughing into the resin, whilst the relatively rigid aramid and stainless steel threads show increased resin ploughing for an angle of 45°. Increasing the angle, i.e. reducing the inclination should reduce ploughing so that the delamination resistance approaches the delamination performance of vertical tufts. Decreasing the angle may have counteracting effects on the failure mechanism and delamination toughness. Ploughing may be increased as highly inclined tufts rotate during mode I loading increasing the delamination resistance. However, at high inclinations stress concentration sites may be caused, bending the tuft at the delamination plane and the ratio of tensile and shear loads in tufts changes with shear prevailing. Relatively thin tufting threads or wires are susceptible to shear loads, due to low shear strength, leading to rupture at lower loads and a reduction of delamination performance. A ductile material, such as the copper, may still not plough at small angles; however, bending at the delamination plane would be increased causing stress concentration in the tuft and leading to rupture at lower loads reducing the delamination resistance.

In general, the likelihood that tufts fail under mode II loading conditions is higher than under mode I as delamination is mainly caused by bending of composite structures. The contribution of tufts to the delamination toughness in mode II is lower than in mode I due to the relatively low shear strength of tuft threads. It is assumed that the dependence on the tuft depth is less prominent compared to mode I. A tuft pull-out may increase the delamination toughness, compared to

mode I, caused by shear and friction. However, once the failure mechanism changes to shear failure the tuft depth may not affect the delamination resistance as elongation of tufts is relatively small in contrast to mode I.

9.1.2 Tuft misalignment

Tuft inclination may also occur unintentionally during manufacture affecting the delamination performance as reported in the case of conventional stitching [59]. The steps of separating the tufted preform from the tufting support, placing the preform into the RTM mould, compressing it in the mould and infusion can potentially lead to movements of single layers of the carbon fabric and tuft crimping. Meso-structural analyses of tufted specimens showing different degrees of misalignment of initially vertical tufts are presented in Figure 9-2. The stainless steel thread (Figure 9-2a) shows misalignments of 12° in the centre of the composite and up to 72° at the outermost ply (loop side), whilst the inclination of the copper wire (Figure 9-2b) is 45° in the centre and 13° at the outermost ply (loops side). The nominal tuft length can be doubled by such misalignments. Long tufts may also increase the thickness of the preform and add additional weight. It is assumed that the degree of unintentional inclination depends, among others, on the bending stiffness and compression limit of the tufting material. A tuft material with a higher bending stiffness than the dry fabric fibres, such as the copper wire, tends to rotate due to preform compression, pushing fibres away, rather than buckle. A conventional fibrous thread (e.g. stainless steel) instead, buckles and crimps in through-the-thickness direction, inclining close to the outer surfaces where the lateral movement of single plies is enhanced. Such misalignments can have detrimental effects on the delamination toughness depending on the direction applied loads act. This may be avoided by compressing the preform during the tufting process in order to allow insertion of shorter tufts. However, as mentioned for angled tufting, the misalignment may also increase the delamination toughness. Unintentional inclination may not be consistent throughout the tuft rows, each affecting differently the delamination performance.

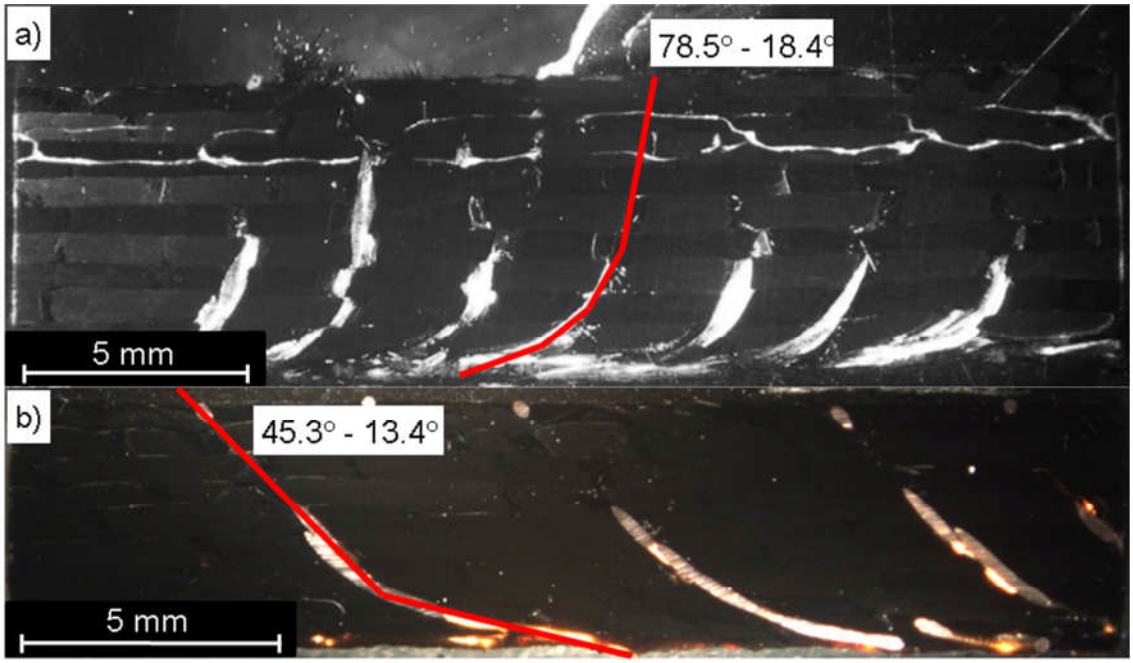

Figure 9-2 Tuft angles in composites with ±45 lay-up: a) stainless steel thread and b) copper wire.

In mode II such misalignments may improve the delamination toughness if the load is applied, so that tufts are loaded in the axial direction. However, unintentional misalignments are irregular and cannot be controlled. The direction of the inclination is important, as tufts may buckle if the structure is loaded against the nap, whilst loading with the nap the tufts are loaded axially potentially improving the delamination toughness.

In general, unintentional tuft misalignment may have a crucial effect on applications if the misalignments are not detected. The delamination performance of structures may be lower than estimated and may lead to catastrophic failure when in service. Straighten up of misaligned tufts may lead to minor delamination. However, for applications where, for example, aerodynamics is of importance minor delaminations have a large effect on the air flow and loads act differently, compared to the undamaged structure, potentially resulting in major damage.

9.1.3 Crack initiation toughness of untufted and tufted materials

The crack initiation toughness of tufted materials is lower than that of the untufted control material, as described in section 5.1.2. This trend is also

present for the delamination results of intermediately bindered specimens with different tuft depths (section 6.1.1) and angled tufts (section 7.1). The reason may be that the resin layer in the delamination plane of tufted materials is thinner, compared to untufted material, due to increased preform thickness as a result of tufting leading to higher compression of the preform inside the RTM mould. A reduced resin layer leads to constraints in the plastic deformation of the resin caused by adjacent fabric plies, which occurs in front of the crack tip during propagation, decreasing the delamination toughness [313]. Considering the von Mises yield criterion and the equation for equivalent tensile stress using principal stresses, the mode I stress fields and plane strain state the plastic zone size can be calculated and expressed in polar coordinates as follows [314]:

$$r(\theta) = \frac{1}{4\pi}\left(\frac{K_{Ic}}{\sigma_{YS}}\right)^2 \left[(1-2\nu)^2(1+\cos\theta) + \frac{3}{2}\sin^2\theta\right] \quad \textbf{9-1}$$

with

$$K_{Ic} = \sqrt{\frac{G_{Ic}E}{(1-\nu^2)}} \quad \textbf{9-2}$$

where r and θ are the radius and the angle polar coordinates, respectively, K_{Ic} the critical stress intensity factor in mode I, σ_{YS} the yield strength of the resin, ν the Poisson's ratio of the resin, G_{Ic} the critical crack energy release rate in mode I of the resin and E the Young's modulus of the resin. The result of the calculation is presented in Figure 9-3, assuming a yield strength of 120 MPa [315], a Poisson's ratio of 0.35 [316], a stress intensity factor of 0.79 MPa√m and a delamination toughness of 216 J/m^2 of the cured resin [317] and a resulting modulus of 2.5 GPa.

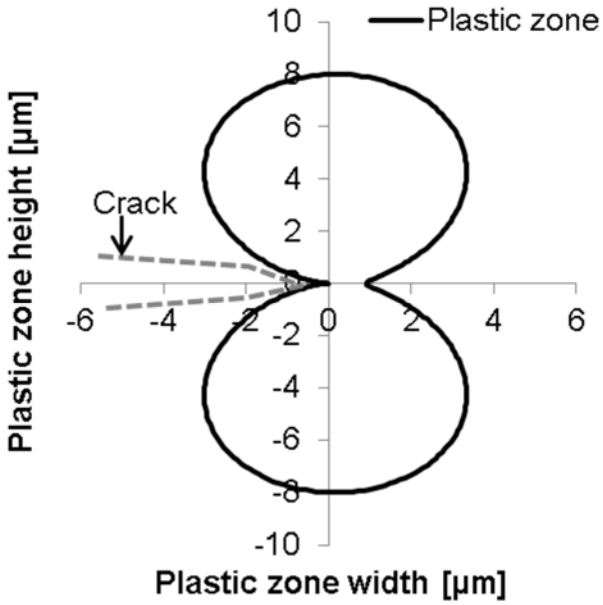

Figure 9-3 Plastic zone size in front of crack tip during delamination.

Figure 9-3 shows the shape of the plastic zone, with a total height of approximately 16 µm. The crack initiation in the DCB tests occurs at the end of the PTFE crack starter film which has a thickness of 10 µm. Assuming that the resin layer at that location has the same thickness as the crack starter film the plastic deformation in the thickness direction (plastic zone height) is constrained by the fabric plies at the delamination plane reducing the delamination resistance. Greater preform compression in the RTM mould, due to tufting, may lead to a reduction in resin layer thickness, further increasing the constraints of the plastic deformation in the resin and, thus, reducing the crack initiation toughness of tufted materials. However, the first tuft row is placed 15 mm away from the crack starter film and may not affect the resin layer thickness at crack initiation. Measuring the resin layer at the cross section of an untested tufted and untufted DCB specimen using microscopy can give more information about the effect of tufting on the thickness of the resin layer. The difference in crack initiation toughness between the highly bindered tufted and untufted materials (section 6.1.2) can be considered as insignificant, considering the standard deviations, as the crack starter film is thicker (13 µm) and the compression in the VARTM process is lower compared to the RTM leading to probably similar thicknesses in resin layer.

9.1.4 Superposition of material and tuft response

The effect of tufting on the mechanical properties of tufted materials can be explained to a degree by superimposing the incremental crack energy release rates contributed by the resin and the tufts. This is carried out by integrating the fracture surface stresses of untufted materials, obtained by the bridging law, and the tuft loads per unit area over the opening displacements at their corresponding locations. The contribution to the delamination performance by the tufts is based on the thread and wire tensile test results. This leads to the assumption that pure tuft elongation with subsequent rupture is the main energy consuming mechanism. However, in most of the experiments tuft elongation was accompanied by rotational movements due to thread twisting, fabric fibre bridging, shear and friction with the surrounding composite. Also the model does not consider pull-out of tufts for short tuft depths and resin ploughing for inclined tufts. Such failure mechanisms and the effect of the surrounding composite may be taken into account using data from single-tuft miniature specimens tested in mode I. These specimens contain a PTFE film in the entire mid-plane allowing direct measurement of loads and displacements caused by tuft debonding, elongation and rotation with subsequent rupture of long vertical tufts, representing the tuft behaviour in mode I delamination more precisely than thread tensile tests. However, they are complicated and time consuming to manufacture due to the small size of the specimens (20 × 20 mm) and the fact that a PTFE film is laid-up over the entire delamination plane. In addition, the tests are not standardised increasing the potential for unreliable results. The contribution of the composite, its interactions with the tufts and the effect on the delamination toughness may be also predicted using finite element methods (FEM) or an analytical approach considering the micromechanics of delamination loading. However, this may be difficult to implement as the contribution of shear stresses between tufts and composite is not well known.

The predicted superimposed R-curves reach a fully developed bridging zone represented by a consistent plateau. This is due to the tufts considered as a continuum neglecting crack arrest and propagation represented by increases in delamination resistance during tuft bridging and decreases after tuft rupture.

Taking this into account by subtracting the energy, which is added previously by tuft bridging, leads to increases and decreases of delamination toughness at the fully developed bridging zone similar to the experimental results. This can be carried out semi-analytically or numerically (FEM).

9.2 Electrical properties and corrosion of metal tufts

This section discusses the improvements in electrical performance due to tufting and potential problems related to the potential generation of galvanic corrosion.

9.2.1 Lightning strike performance and electrical conductivity of tufted materials

The lightning strike performance of tufted and untufted composites was tested carrying out Zone 2A lightning strike tests (section 3.3.3). The results are in line with electrical through-thickness conductivity test results (section 8.2.2), showing an improvement in conductivity and lightning strike performance of composites with increasing conductivity of the tuft material. The high conductivity of copper, stainless steel and carbon leads to decreased surface and internal damage, compared to untufted materials and materials tufted with electrically inert materials, as reported in section 8.3. Highly conductive copper mesh placed on the top of the composite structures does not affect the through-thickness conductivity, but increases the lightning strike protection by conducting the current along the surface through the mesh reducing the surface and internal damages of composites. In addition, the weight of common copper meshes is around 195 g/m^2, whilst that of the copper tufts is approximately 1 kg/m^2 considering a total wire length per tuft of 20 mm (4 mm panel thickness, 3 mm loop length and a square tuft pattern with 3 mm distance). The stainless steel and carbon thread add a weight of around 540 g/m^2 and 310 g/m^2, respectively. The lightning strike protection may be a trade-off between a moderate protection with lower weight addition by the copper mesh and high lightning strike protection accompanied by a greater amount of weight caused by conductive tufts. Misalignment, as shown in Figure 9-2, affects the conductivity test results: the measured resistance was related to a tuft length

corresponding to the specimen thickness. However, due to the misalignment the length may be doubled increasing the actual through-thickness conductivity of tufted composites compared to the measured values.

9.2.2 Potential corrosion of metal tufted composites

Lightning strike protection of composites using metal meshes is subject to galvanic corrosion. If the metal mesh is in contact with the conductive carbon fibres both the metal and the composite may corrode in an environment of humid air, moisture or salty water. Aluminium is highly susceptible to corrosion and is, therefore, used with an insulating layer, such as glass fibres, between the metal and the carbon composite. In contrast, copper is more noble than aluminium and less reactive leading to reduced corrosion [302]. Carbon is the more cathodic material compared to metals causing the metal to corrode, rather than the composite [302]. Galvanic corrosion causes damage mainly in the metal mesh, but also in the composite. If the damage is not addressed the metal and the composite can dissolve deteriorating the mechanical integrity of the structure. Furthermore, damaged metal meshes may not conduct sufficiently the current of a lightning strike, increasing the potential for crucial damage of the composite structure. Such problems can be transferred to metal tufts: the copper wire inside the composite may corrode due to the reaction with hydrogen gas, coming from the resin and generated in voids and cracks around the tufts inside the composite [318]. The corrosion may lead to damage of the tufts decreasing their load bearing capability and delamination performance of the composite structure as well as the lightning strike protection if the current is not conducted through broken or oxidised tufts. In contrast to metal meshes, the corrosion of tufts inside the composite is not visible and easily detectable. Non-destructive testing methods for composite may provide images of damaged tufts. Stainless steel tufts decrease the potential for corrosion, compared to copper, as the alloy contains chromium protecting against corrosion by developing a chromium oxide surface. Nevertheless, tufting materials may be coated with non-conductive materials, preventing corrosion with the surrounding composite. The ultimate strain of the coat would need to be as high as that of the tuft material or higher in order to prevent cracking during tuft elongation.

Cracking of the coat may provide access to gasses or moisture to the tufts leading to corrosion. However, coating may affect the electrical conductivity of tufts and the entire structure. The tufts need to provide an attachment point for the current generated by lightning strike. In order to use other metals as tufting material, requirements have to be fulfilled corresponding to the mechanical properties, such as tensile strength, stiffness and ultimate strain, and a relatively high conductivity with low susceptibility to corrosion. These criteria may be fulfilled by passivated titanium and its alloys, providing a significant high tensile strength of 1 GPa and stiffness of 115 GPa as a bulk material [319] and resistance to corrosion [320]. Passivation is provided by enhancement of the titanium oxide layer protecting the metal against corrosion [321]. However, the electrical conductivity of titanium as bulk material is lower than that of copper and stainless steel.

9.3 Potential applications using tufting for mechanical and electrical improvements

Metal tufts and their functionality of improving the delamination performance and the lightning strike performance of composite structures, may be applied to any structure confronted to high loads and outdoor conditions, such as wind turbines, aircrafts and automobiles. The highest loads in wind turbines are the centrifugal loads in blades, i.e. in the blade longitudinal direction. Tufts should be orientated in that direction to exploit their maximum performance. However, tufts are usually inserted through-the-thickness of the blade skin, orientated in perpendicular direction experiencing shear loads corresponding to mode II without improving the delamination toughness. A possibility to load the tufts mainly in tension is the inclination of the tufts by a relatively high angle. Wind turbines also suffer from lightning strikes and high amount of moisture, especially in off-shore installations. Metal tufts may improve the delamination resistance and simultaneously protect the turbine blades against lightning strikes. The high amount of moisture increases the risk of corrosion leading to the need of tufts using metals with surface treatment, such as passivation or coating. In the automotive industry the mechanical performance is more important than the electrical leading to the possibility of using non-metallic tufts,

such as carbon or aramid thread. Depending on the part to be reinforced and its application on the car the loads may act differently. A bumper, as mentioned in section 2.4, is subject to impact loading leading to compression of the tufts, whilst a composite roof may be loaded in tension, compression or shear. Larger surfaces, such as the roof, can be tufted with different inclinations to increase the load bearing capability in different directions. In aircrafts high loads are applied, especially during take-off and landing. However, tufting would be mainly applied to joints, such as stiffeners and ribs, to reinforce the skin-to-flange interface. The joints are usually loaded, so that the flanges are pulled-off acting in the tuft axial direction or in the stinger longitudinal direction leading to shear load in the tuft. Thus, tufts may be inserted with a certain angle to be loaded axially to withstand the shear loads. Using metal tufts or conductive carbon tufts can be used as lightning strike protection if the tuft seams or loops are accessible on the outer skin side for the lightning inducing the current in the tufts. The tufts and the surface have to be protected against corrosion as aircrafts operate in humid conditions. Overall, the tufting parameters, such as pattern, depth and angle as well as the tuft material have to be adapted to the application and the loads acting. Therefore, certain information about the loads, obtained by simulation or experiments, is needed before designing the structure to apply the correct parameters.

Based on the overall performance (delamination resistance and electrical properties) the copper tufts inclined by 45° appear to be the most suitable reinforcement due to the relatively large improvement in delamination resistance of composite structures and lightning strike protection. The use of inclined tufts needs to be carried with introduction in different directions, making sure that the benefits of tufting are present in loading and crack propagations in all directions on the delamination plane. Depending on the purpose of the application and if lightning strike protection is required the tufts may be inserted fully, for the conductivity of current, or partially. However, fully tufted materials facilitate the tufting process as the tufted materials can be infused afterwards, whilst partially tufted materials have to be covered with fabric plies before infusion.

10 Conclusions and recommendations for further research

10.1 Conclusions

The main conclusions of this study are as follows:

- The stainless steel thread and the copper wire are capable of reinforcing composite structures significantly;
- The lightning strike performance is improved significantly by tufting using conductive material leading to a reduced damage area size by up to 75% for copper tufts compared to untufted composites with copper mesh protection;
- The strain energy release rate increases with decreasing tufting depth by up to 410% for aramid, 270% for stainless steel and 360% for copper tufted material compared to untufted material;
- The delamination resistance increases with a tuft insertion angle of 45°, compared to vertical tufts, by up to 30% for aramid and copper and 90% for stainless steel, due to resin ploughing in aramid and stainless steel tufted materials around the tufts and friction between inclined copper tufts and the resin during elongation;
- The use of a CAD-file enables automated blind tufting of complex geometries to be carried out;
- The amount of binder alters the delamination properties of composite structures, with and without tufts due to the increased resin/fibre interface strength.

Detailed conclusions can be summarised as follows:

<u>Tufting of complex structures:</u>

- Only the aramid thread is able to withstand the loads of the tufting process in highly bindered material;
- In order to facilitate thread insertion and reduce the resistance by the bindered fabric a heat source can be used activating the binder and softening the fabric;

- The estimated costs and increase in weight show that tufting may have the potential to replace metal fasteners. The aramid thread may reduce the weight and costs of composite structures in contrast to metal fasteners.

Tuft and preform material:

- The tensile properties of impregnated tufting threads and wire decrease due to additional constrains in inter-thread movements caused by the cured composite;
- The tensile properties depend on the state of the tuft material: the copper wire is ductile, whereas the twisted stainless steel thread is brittle;
- The tuft material and its tensile properties have a high impact on the delamination toughness of composite structures: the copper wire has a low tensile strength and significant high ultimate strain causing several tuft rows to bridge the crack opening simultaneously, leading to high delamination toughness and progressive failure, whilst the stainless steel thread has a higher strength but is more brittle than the copper wire, leading to lower delamination toughness and more abrupt crack propagation;
- Fibre bridging and breakage of non-structural stitching increases with tufting and contributes to an increase in delamination toughness.

Tuft depth:

- The aramid thread shows clear tufting depth dependence in contrast to the brittle stainless steel thread and ductile copper wire; the brittleness of stainless steel eliminates the tufting depth effect for long tuft lengths, whilst the copper wire elongates more with increasing tuft depth;
- Increasing the tufting depth results in greater constraints in the deformation of the tufting thread and a decrease in delamination resistance;
- The mobility of the tufting thread is of importance for the full exploitation of tuft performance;
- An increasing thread elongation in tufted materials enhances fibre bridging and the contribution of non-structural stitching to a further increase of strain energy release rate;
- The tuft depth affects the failure mechanism: specimens with short tufts fail by frictional pull-out of tufts, whilst longer tufts elongate and rupture.

Superposition:

- Superimposing the base laminate delamination behaviour with the thread tension response is capable of predicting the contribution of the resin and tufts to the crack energy release rate in the form of surface fracture stress and tuft elongation with subsequent rupture, respectively;
- The tuft density, thread diameter and different preform materials are taken into account for the prediction of the delamination toughness, whilst the tuft depth and inclination lead to contradicting results compared to experiments due to the non-consideration of failure mechanisms, such as shear between tufts and the surrounding composite and resin ploughing.

Electrical properties:

- The through-thickness conductivity of tufted materials increases with increasing conductivity of the tuft material by up to 250 times for copper tufted laminates compared to untufted composites;
- Tufting does not affect the in-plane conductivity significantly. In the case of copper tufting, the overlapping loops of copper tufts contribute to the in-plane conductivity;
- Tufting changes the damage type from internal to surface damage, when compared with unprotected, untufted laminates.

Potential application of tufting:

- Tufting can improve mechanical and electrical properties of composite structures simultaneously compared to unreinforced composites, depending on the tuft material, its electrical and mechanical parameters and tuft parameters.

10.2 Recommendations for further research

The delamination tests with different tuft materials showed that the ultimate strength and strain are important regarding the delamination toughness of tufted materials. Further tuft materials can be explored, such as titanium in the form of a fibrous thread or a very thin wire. In addition, heat treatment of the stainless steel thread can be applied to increase its ductility maintaining its ultimate strength. This could lead to the activation of more tuft rows and improve the delamination performance of steel tufted composites.

The different crack initiation toughness for untufted and tufted materials can be explained by analysing micrographs of the cross sections of the materials. Measurements of the resin layer thickness at the delamination plane can provide a deeper insight on whether tufts affect the resin layer thickness and the crack initiation toughness or if the first tuft row is too far from the crack starter film to affect the initiation toughness.

The delamination test results of materials with different tuft depths lead to the assumption that the delamination toughness is unchanged beyond a certain tuft depth. This needs to be validated by further delamination tests of tufted materials with tuft depths larger than 5.2 mm.

Tufting with a higher preform compression may prevent tuft misalignment caused by preform handling and compression during resin infusion. Cross sectional micrographs of materials tufted with different compression loads may give more information about the effect of preform compression on the tuft misalignment.

The behaviour of angled tufts was described by delamination tests of materials incorporating tufts inclined by 45°. The failure mechanism of materials tufted with lower angles, such as 30° or 22.5° can provide more information if a trend in delamination toughness is present dependent on the tuft inclination. A trend would enable predictions of the delamination toughness. Furthermore, mode II, mixed mode and in-plane tests can be carried out in order to determine if inclined tufts have a detrimental or improving effect on mode II or mixed mode delamination test results or in-plane properties. This can be expanded to the

insertion of tufts with positive and negative inclinations in order to know if the tuft direction affects the results.

The superposition of the preform material and tuft response can be extended by introducing tufts as discrete representation for energy accumulation and release simulating tuft bridging and rupture. The use of single-tuft delamination test results may be a more accurate representation of tuft behaviour than thread tensile tests leading to predicted results closer to experimental results.

The through-the-thickness electrical conductivity of tufted composites could be predicted by an analytical model considering every single tuft as a resistor. Therefore, the conductivity of a single tuft in a composite has to be determined by manufacturing single-tuft specimens.

The lightning strike performance was carried out on tufted panels without paint which is usually used in aircrafts or wind turbines. Lightning strike tests on painted and tufted panels can be carried out to investigate the effect of the paint on tufted panels. If titanium is used for tufting it would be relevant to know the effect of titanium tufts on the lightning strike performance of composites. Galvanic corrosion tests can be carried out on metal tufted composites. It is not clear if fibrous metal threads corrode to the same extent as bulk materials and what the effect is on the delamination toughness.

REFERENCES

[1] Bunsell AR, Renard J. Fundamentals of Fibre Reinforced Composite Materials: IOP Publishing Ltd, Bristol, UK, 2005.

[2] Boeing Commercial Airplanes. Aero. 2006, http://boeing.com/commercial/aeromagazine;(accessed January 2014).

[3] Airbus S.A.S. Intelligent and aerodynamic airframe. 2013, http://www.a350xwb.com/advanced/fuselage;(accessed January 2014).

[4] Airbus S.A.S. A350XWB-S15 Spirit Delivery 012012. 2012, http://www.airbus.com/galleries/photo-gallery/dg/idp/26681-a350xwb-s15-spirit-delivery-012012/?share=1;(accessed January 2014).

[5] Huang S, Richey R, Deska E. Cross reinforcement in a GR/EP laminate. American Society of Mechanical Engineers, Winter Annual Meeting, San Francisco, USA, 1978. p.1978.

[6] Krasnov V, Kuznetsov V, Maksakov AY. Automated method of transverse reinforcement of composites by short fibers. Mechanics of Composite Materials 1987;23(3):356-361.

[7] Tomashevskii V, Shalygin V, Romanov D, Sitnikov SY. Transversal reinforcement of composite materials using ultrasonic vibrations. Mechanics of Composite Materials 1988;23(6):769-772.

[8] Tomashevskii V, Sitnikov SY, Shalygin V, Yakovlev V. A method of calculating technological regimes of transversal reinforcement of composites with short-fiber microparticles. Mechanics of Composite Materials 1989;25(3):400-406.

[9] Freitas G, Magee C, Boyce J, Bott R. Service tough composite structures using the Z-direction reinforcement process. Proceedings of the 9th DoD/NASA/FAA Conference on Fibrous Composites in Structural Design, Lake Tahoe, Nevada, USA, 1991. p.1223-1229.

[10] Boyce JS, Freitas GA, Magee CL, Fusco TM, Harris JJ, Kunkel E. Ultrasonic fastening system and method, Patent WO 98/29243 1998.

[11] Mouritz A. Review of z-pinned composite laminates. Composites Part A: Applied Science and Manufacturing 2007;38(12):2383-2397.

[12] Dell'Anno G. Effect of tufting on the mechanical behaviour of carbon fabric/epoxy composites. PhD Thesis, School of Applied Sciences, Cranfield University, 2007.

[13] Treiber JWG. Performance of tufted carbon fibre/epoxy composites. PhD Thesis, School of Applied Sciences, Cranfield University, 2011.

[14] Freitas G, Magee C, Dardzinski P, Fusco T. Fiber insertion process for improved damage tolerance in aircraft laminates. Journal of Advanced Materials(USA) 1994;25(4):36-43.

[15] Rugg K, Cox B, Ward K, Sherrick G. Damage mechanisms for angled through-thickness rod reinforcement in carbon–epoxy laminates. Composites Part A: Applied Science and Manufacturing 1998;29(12):1603-1613.

[16] Chang P, Mouritz AP, Cox BN. Fracture and fatigue properties of z-pinned composite lap joints. IFC11 - International Congress on Fracture, Turin, Italy, 2005.

[17] Chang P, Harris E, Kootsookos A, Cox B, Mouritz A. Improved elevated temperature properties of z-pinned composite lap joints. Proceedings of the 4th Australasian Congress on Applied Mechanics, Melbourne, Australia, 2005. p.499-504.

[18] Chang P, Mouritz A, Cox B. Properties and failure mechanisms of pinned composite lap joints in monotonic and cyclic tension. Composites Science and Technology 2006;66(13):2163-2176.

[19] Lander JK. Designing with z-pins: locally reinforced composite structures. PhD Thesis, School of Applied Sciences, Cranfield University, 2008.

[20] Tao Y, Jiao G, Wang B, Chang Y. Effect of Z-pins' diameter, spacing and overlap length on connecting performance of CMC single lap joint. Acta Mechanica Solida Sinica 2008;21(5):461-471.

[21] Koh T, Isa M, Chang P, Mouritz A. Improving the structural properties and damage tolerance of bonded composite joints using z-pins. Journal of Composite Materials 2012;46(26):3255-3265.

[22] Son H, Park Y, Kweon J, Choi J. Fatigue behaviour of metal pin-reinforced composite single-lap joints in a hygrothermal environment. Composite Structures 2014;108:151-160.

[23] Ko M, Kweon J, Choi J. Fatigue characteristics of jagged pin-reinforced composite single-lap joints in hygrothermal environments. Composite Structures 2015;119:59-66.

[24] Clarke A, Greenhalgh E, Meeks C. Enhanced structural damage tolerance of CFRP primary structures by z-pin reinforcement. Proceedings of 44th AIAA/ASME/ASCE/AHS/ASC Structures, Structural Dynamics, and Materials Conference, Norfolk, Virgina, 2003. p.1-11.

[25] Li Y, Li W, Zhang X, Xiao J. Bending Performance of Polymer Composites Single Lap Joints Reinforced by Z-pin. Journal of Materials Engineering 2015;43(2):26-34.

[26] Cartié DD, Dell'Anno G, Poulin E, Partridge IK. 3D reinforcement of stiffener-to-skin T-joints by Z-pinning and tufting. Engineering Fracture Mechanics 2006;73(16):2532-2540.

[27] Troulis E. Effect of Z-Fiber® pinning on the mechanical properties of carbon fibre/epoxy composites. PhD Thesis, School of Applied Sciences, Cranfield University, 2003.

[28] Grassi M, Clarke A, Khermiri N, Gaitonde M. Analysis of through-thickness reinforcements effect on the failure modes of a composite rib foot. , Rhodes, Greece, 2004. p.1-10.

[29] Greenhalgh E, Lewis A, Bowen R, Grassi M. Evaluation of toughening concepts at structural features in CFRP—Part I: Stiffener pull-off. Composites Part A: Applied Science and Manufacturing 2006;37(10):1521-1535.

[30] Koh T, Feih S, Mouritz A. Experimental determination of the structural properties and strengthening mechanisms of z-pinned composite T-joints. Composite Structures 2011;93(9):2222-2230.

[31] Bianchi F, Koh T, Zhang X, Partridge I, Mouritz A. Finite element modelling of z-pinned composite T-joints. Composites Science and Technology 2012;73:48-56.

[32] Koh T, Isa M, Feih S, Mouritz A. Damage tolerance of z-pinned composite joints. Proceedings of 28th International Congress of the Aeronautical Sciences (ICAS), Brisbane, Australia, 2012. p.23-28.

[33] Koh T, Feih S, Mouritz A. Strengthening mechanics of thin and thick composite T-joints reinforced with z-pins. Composites Part A: Applied Science and Manufacturing 2012;43(8):1308-1317.

[34] Park Y, Lee B, Kweon J, Choi J, Choi I. The strength of composite bonded T-joints transversely reinforced by carbon pins. Composite Structures 2012;94(2):625-634.

[35] Koh T, Isa M, Feih S, Mouritz A. Experimental assessment of the damage tolerance of z-pinned T-stiffened composite panels. Composites Part B: Engineering 2013;44(1):620-627.

[36] Nanayakkara A, Feih S, Mouritz A. Improving the fracture resistance of sandwich composite T-joints by z-pinning. Composite Structures 2013;96:207-215.

[37] Ji H, Kweon J, Choi J. Fatigue characteristics of stainless steel pin-reinforced composite hat joints. Composite Structures 2014;108:49-56.

[38] Mouritz A. Structural properties of z-pinned carbon-epoxy T-joints in hot-wet environment. Journal of Composite Materials 2014;48(23):2905-2914.

[39] Ma YE, Du YH. Bridge effects of Z-pin on damage evolution of Z-pin reinforced composite T-joint: Experiment and simulation. ICCM20 - 20th International Conference on Composite Materials, Copenhagen, Denmark, 2015.

[40] Partridge I, Cartie DD, Bonnington T. Manufacture and performance of z-pinned composites. In: Advani SG, Shonaike GO, editors. Advanced Polymeric Materials, Structure Property Relationships. USA: CRC Press, 2003.

[41] Hall, T. Automation of Z-Fiber for complex shapes. Composites Manufacturing Technology Center cmtc.scra.org/pubs/fall_2002.pdf;(accessed January 2012).

[42] Cartié DDR, Troulis M, Partridge IK. Delamination of Z-pinned carbon fibre reinforced laminates. Composites Science and Technology 2006;66(6):855-861.

[43] Rezai A, Cartié D, Partridge I, Irving P, Aston T, Negre P, Langer J. Interlaminar damage resistance of Z-FibreTM reinforced structural CFRP. ICCM 13 - 13th International Conference on Composite Materials, Beijing, China, 2001.

[44] Cartié DDR, Partridge IK. Delamination behaviour of Z-pinned laminates. ICCM12 - 12th International Conference on Composite Materials, Paris, France, 1999.

[45] Evans D. Transverse reinforcement methods for improved delamination resistance. International Sampe Symposium and Exhibition. 1989;34:271-282.

[46] Graftieaux B, Rezai A, Partridge I. Effects of z-pin reinforcement on the delamination toughness and fatigue performance of unidirectional AS4/8552 composite. ECCM9 – 9th European Conference on Composite Materials, Brighton, UK, 2000.

[47] Troulis M, Cartié D, Bartattoni L, Partridge I. Z-pinned woven laminates: interlaminar fracture results and pinning quality considerations. Sixth International Conference on Deformation and Fracture of Composites (DFC6), Manchester, UK, 2001.

[48] Rugg K, Cox B, Massabo R. Mixed mode delamination of polymer composite laminates reinforced through the thickness by z-fibers. Composites Part A: Applied Science and Manufacturing 2002;33(2):177-190.

[49] Liu H, Yan W, Mai Y-W. Z-Pin bridge force in composite delamination. In: Blackman BRK, Pavan A, Williams JG, editors. Fracture of polymers, composites and adhesives II: Elsevier Science, 2003.

[50] Liu H, Yan W, Yu X, Mai Y. Experimental study on z-pinned DCB mode I delamination. Proceedings of Structural Integrity and Fracture International Conference (SIF'04), Brisbane, Australia, 2004. p.229-234.

[51] Partridge I, Cartié D, Troulis M, Grassi M, Zhang X. Evaluating the mechanical effectiveness of z-pinning. Proceedings of The SAMPE Technical Conference, 2004.

[52] Robinson P, Das S. Mode I DCB testing of composite laminates reinforced with z-direction pins: a simple model for the investigation of data reduction strategies. Engineering Fracture Mechanics 2004;71(3):345-364.

[53] Mouritz A. Delamination properties of z-pinned composites in hot–wet environment. Composites Part A: Applied Science and Manufacturing 2013;52:134-142.

[54] Stringer L, Hiley M. Through-Thickness Reinforcement of Composite: Z-Pinning, Stitching, and 3D Weaving. ICCM14 - 14th International Conference on Composite Materials, San Diego, USA, 2003.

[55] Mouritz AP. Review of z-pinned composite laminates. Composites Part A: Applied Science and Manufacturing 2007;38:2383-2397.

[56] Creative Commons Attribution-Share Alike 3.0 Australia. RAAF (A44-222) FA 18F Super Hornet landing. https://en.wikipedia.org/wiki/Royal_Australian_Air_Force#/media/File:RAAF_%28A44-222%29_FA_18F_Super_Hornet_landing.jpg;(accessed July 2015).

[57] Collantine, K. http://www.f1fanatic.co.uk/?attachment_id=59699, 2012;(accessed July 2015).

[58] Sweeting RD, Thomson RS. The effect of thermal mismatch on Z-pinned laminated composite structures. Composite Structures 2004;66(1):189-195.

[59] Mouritz AP, Cox BN. A mechanistic interpretation of the comparative in-plane mechanical properties of 3D woven, stitched and pinned composites. Composites Part A: Applied Science and Manufacturing 2010;41:709-728.

[60] Cartié DDR. Effect of Z-FibresTM on the Delamination Behaviour of Carbon Fibre/Epoxy Laminates. PhD Thesis, School of Applied Sciences, Cranfield University, 2000.

[61] Lenzi F, Riccio A, Clarke A, Creemers R. Coupon Tests on z-Pinned and Unpinned Composite Samples for Damage Resistant Applications. Macromolecular Symposia: Wiley Online Library, 2007. p. 230-237.

[62] Chang P, Mouritz AP, Cox BN. Properties and failure mechanisms of pinned composite lap joints in monotonic and cyclic tension. Composites Science and Technology 2006;66:2163-2176.

[63] Mouritz A, Chang P, Cox B. Fatigue properties of Z-pinned aircraft composite materials. 25th International Congress of the Aeronautical Sciences, Hamburg, Germany, 2006.

[64] Mouritz A. Tensile fatigue properties of 3D composites with through-thickness reinforcement. Composites Science and Technology 2008;68(12):2503-2510.

[65] Cui Y, Qi D, Wen Y, Li C, Yan Y. Experiment and simulation study on tensile properties of Z-pinned composite laminates. Hangkong Xuebao/Acta Aeronautica et Astronautica Sinica 2010;31(12).

[66] Mouritz A, Chang P. Tension fatigue of fibre-dominated and matrix-dominated laminates reinforced with z-pins. International Journal of Fatigue 2010;32(4):650-658.

[67] Chun H, Son J, Kang K, Byun J, Um M, Lee S. Prediction of elastic properties for woven z-pinned composites. Composites Part B: Engineering 2014;64:59-71.

[68] Knaupp M, Scharr G. Manufacturing process and performance of dry carbon fabrics reinforced with rectangular and circular z-pins. Journal of Composite Materials 2014;48(17):2163-2172.

[69] Chang P, Mouritz A, Cox B. Properties and failure mechanisms of z-pinned laminates in monotonic and cyclic tension. Composites Part A: Applied Science and Manufacturing 2006;37(10):1501-1513.

[70] Mouritz A. Compression properties of z-pinned composite laminates. Composites Science and Technology 2007;67(15):3110-3120.

[71] Son J, Chun HJ, Kang K, Lee H, Byun JH, Um M, Lee S, Kim BS. Effect of Z-Pin on the through-the-Thickness Strength of Woven Composite Laminates. Advanced Materials Research: Trans Tech Publications, 2010. p.47-50.

[72] Dickinson L, Farley G, Hinders M. Prediction of effective three-dimensional elastic constants of translaminar reinforced composites. Journal of Composite Materials 1999;33(11):1002-1029.

[73] Steeves CA, Fleck NA. In-plane properties of composite laminates with through-thickness pin reinforcement. International Journal of Solids and Structures 2006;43:3197-3212.

[74] Huang H, Waas AM. Compressive response of Z-pinned woven glass fiber textile composite laminates: Experiments. Composites Science and Technology 2009;69(14):2331-2337.

[75] Isa M, Feih S, Mouritz A. Compression fatigue properties of z-pinned quasi-isotropic carbon/epoxy laminate with barely visible impact damage. Composite Structures 2011;93(9):2269-2276.

[76] Chenghu L, Ying Y, Ping W, Desheng Q, Yonghai W. Study on compressive properties of Z-pinned laminates in RTD and hygrothermal environment. Chinese Journal of Aeronautics 2012;25(1):64-70.

[77] Mouritz A. Design dilemma for z-pinned composite structures. Proceedings of the 27th Congress of the International Council of the Aeronautical Science (ICAS). Nice, 2010. p.19-24.

[78] Liu W, Jiao GQ, Zhang WX, Zhang WM. Interlaminar shear property of z-pins reinforced woven ceramic matrix composites. Advanced Materials Research: Trans Tech Publications, 2011. p.1608-1612.

[79] Brown AS. Cutting composite costs with needle and thread. Aerospace America 1997;35(11):24. p.24-25.

[80] Karal M. AST Composite Wing Program-Executive Summary. NASA Report, vol NASA-CR-2001-210650, 2001.

[81] Ogale A, Mitschang P. Tailoring of textile preforms for fibre-reinforced polymer composites. Journal of Industrial Textiles 2004;34(2):77-96.

[82] Morales A. Structural stitching of textile preforms. Proceedings of 22nd International SAMPE Technical Conference, Boston, USA, 1990. p.1217-1230.

[83] Mouritz AP, Cox BN. A mechanistic approach to the properties of stitched laminates. Composites Part A: Applied Science and Manufacturing 2000;31:1-27.

[84] Mouritz AP, Leong KH, Herszberg I. A review of the effect of stitching on the in-plane mechanical properties of fibre-reinforced polymer composites. Composites Part A: Applied Science and Manufacturing 1997;28A:979-991.

[85] Sawyer JW. Effect of stitching on the strength of bonded composite single lap joints. AIAA Journal 1985;23(11):1744-1748.

[86] Lee C, Liu D. Tensile strength of stitching joint in woven glass fabrics. Journal of Engineering Materials and Technology 1990;112(2):125-130.

[87] Tada Y, Ishikawa T. Experimental evaluation of the effects of stitching on CFRP laminate specimens with various shapes and loadings. Key Engineering Materials: Trans Tech Publications, 1991. p.305-316.

[88] Jain LK, Leong K, Mai Y, Tong L. Effect of through-thickness stitching on the fatigue life of composite single-lap joints. Applied Composite Materials 1998;5(6):399-409.

[89] Tong L, Jain L, Leong K, Kelly D, Herszberg I. Failure of transversely stitched RTM lap joints. Composites Science and Technology 1998;58(2):221-227.

[90] Glaessgen E, Raju I, Poe C. Analytical and experimental studies of the debonding of stitched and unstitched composite joints. Journal of Composite Materials 2002;36(23):2599-2622.

[91] Aymerich F. Experimental investigation into the effect of edge stitching on the tensile strengthand fatigue life of co-cured joints between cross-ply adherends. Advanced Composites Letters 2004;13(3):151-161.

[92] Reeder J, Glaessgen E. Debonding of stitched composite joints under static and fatigue loading. Journal of Reinforced Plastics and Composites 2004;23(3):249-263.

[93] Aymerich F, Onnis R, Priolo P. Analysis of the fracture behaviour of a stitched single-lap joint. Composites Part A: Applied Science and Manufacturing 2005;36(5):603-614.

[94] Aymerich F, Onnis R, Priolo P. Analysis of the effect of stitching on the fatigue strength of single-lap composite joints. Composites Science and Technology 2006;66(2):166-175.

[95] Wang D, Chen G, Li Z, Kou C. Bearing strength analysis of single mechanically fastened joint in stitched laminates. Journal of Reinforced Plastics and Composites 2006;25(7):711-724.

[96] Wood MD, Tong L, Luo Q, Sun X, Katzos A, Rispler AR. Failure of stitched composite L-joints under tensile loading–experiment and simulation. Journal of Reinforced Plastics and Composites 2009;28(6):715-742.

[97] Bogdanovich AE, Dannemann M, Döll J, Leschik T, Singletary JN, Hufenbach WA. Experimental study of joining thick composites reinforced with non-crimp 3D orthogonal woven E-glass fabrics. Composites Part A: Applied Science and Manufacturing 2011;42(8):896-905.

[98] Kadlec M, Hron R, Grieser T. Damage tolerance of composite T-sections made of cost-effective carbon fibre preforms. International Journal of Structural Integrity 2015;6(1):90-106.

[99] Jegley DC. Improving strength of postbuckled panels through stitching. Composite structures 2007;80(2):298-306.

[100] Poe C, Dexter H, Raju I. Review of the NASA textile composites research. Journal of Aircraft 1999;36(5):876-884.

[101] Jiao Y, Li J, Sun Q. Analysis on bending damage mode of stitching joint 3D braided composites. Journal of Solid Rocket Technology 2010;33(1):104-107.

[102] Motsch N, Magin M. Influence of structural stitching on composite T-joint strength. ICCM20 - 20th International Conference on Composite Materials, Copenhagen, Denmark, 2015.

[103] Holt D. Future composite aircraft structures may be sewn together. Automotive Engineering 1982;90(7):46-49.

[104] Kumari S, Sinha P. Effects of transverse stitching and hygrothermal environment on composite wing T-joints. Journal of Reinforced Plastics and Composites 2003;22(18):1705-1728.

[105] Yang T, Zhang J, Mouritz A, Wang C. Healing of carbon fibre–epoxy composite T-joints using mendable polymer fibre stitching. Composites Part B: Engineering 2013;45(1):1499-1507.

[106] Liu D. Photoelastic study on composite stitching. Experimental Techniques 1990;14(1):25-27.

[107] Hamilton S, Schinske N. Multiaxial stitched preform reinforcements. Proceedings of Structural Composites: Design and Processing Technologies: 6th Annual Advanced Composites Conference, Detroit, USA, 1990. p.433-434.

[108] Chen L, Ifju PG, Sankar BV. A novel double cantilever beam test for stitched composite laminates. Journal of Composite Materials 2001;35(13):1137-1149.

[109] Dexter HB, Funk JG. Impact resistance and interlaminar fracture toughness of through-the-thickness reinforced graphite/epoxy. Proceedings of 27th Structures, Structural Dynamics and Materials Conference, San Antonio, USA, 1986. p.700-709.

[110] Guénon VA, Chou T, Gillespie Jr JW. Toughness properties of a three-dimensional carbon-epoxy composite. Journal of Materials Science 1989;24(11):4168-4175.

[111] Su KB. Delamination resistance of stitched thermoplastic matrix composite laminates. Proceedings of Symposium of Advances in Thermoplastic Matrix Composite Materials, Bal Harbour, USA, 1989. p.279-300.

[112] Hashemi S, Kinloch A, Williams J. The effects of geometry, rate and temperature on the mode I, mode II and mixed-mode I/II interlaminar fracture of carbon-fibre/poly (ether-ether ketone) composites. Journal of Composite Materials 1990;24(9):918-956.

[113] Palmer R. Techno-economic requirements for composite aircraft components. In NASA. Langley Research Center, Proceedings of FIBER-TEX 1992: The Sixth Conference on Advanced Engineering Fibers and Textile Structures for Composites, Philadelphia, USA, 1993. p.305-341.

[114] Aboura Z, Benzeggagh M, Billaut F, Dambrine B. Mode I interlaminar failure of stitched textile composites materials: proposition of predictive reinforcement model. Proceedings of ICCM10 - 10th International Conference on Composite Materials, Whistler, Canada, 1995. p.109-116.

[115] Dransfield K, Bader M, Baillie C, Mai Y. The effect of cross-stitching with an aramid yarn on the delamination fracture toughness of CFRPs. Proceedings of 3rd International Conference on Deformation and Fracture of Composites (DFC3), Surrey, UK, 1995. p.27-29.

[116] Jain LK, Mai Y. Recent work on stitching of laminated composites-theoretical analysis and experiments. Proceedings of ICCM11 – 11th International Conference on Composite Materials, Gold Coast, Australia 1997. p.25-51.

[117] Mouritz A, Gallagher J, Goodwin A. Flexural strength and interlaminar shear strength of stitched GRP laminates following repeated impacts. Composites Science and Technology 1997;57(5):509-522.

[118] Sharma S, Sankar B. Effect of stitching on impact and interlaminar properties of graphite/epoxy laminates. Journal of Thermoplastic Composite Materials 1997;10(3):241-253.

[119] Dransfield KA, Jain LK, Mai Y-. On The Effects of Stitching in CFRPs-I. Mode I Delamination Toughness. Composites Science and Technology 1998;58:815-827.

[120] Jain LK, Dransfield KA, Mai Y. Effect of reinforcing tabs on the mode I delamination toughness of stitched CFRPs. Journal of Composite Materials 1998;32(22):2016-2041.

[121] Watt A, Goodwin A, Mouritz A. Thermal degradation of the mode I interlaminar fracture properties of stitched glass fibre/vinyl ester composites. Journal of Materials Science 1998;33(10):2629-2638.

[122] Mouritz A, Baini C, Herszberg I. Mode I interlaminar fracture toughness properties of advanced textile fibreglass composites. Composites Part A: Applied Science and Manufacturing 1999;30(7):859-870.

[123] Ishai O. Interlaminar fracture toughness of selectively stitched thick carbon fibre reinforced polymer fabric composite laminates. Plastics, rubber and composites 2000;29(3):134-143.

[124] Mattheij P, Gliesche K, Feltin D. 3D reinforced stitched carbon/epoxy laminates made by tailored fibre placement. Composites Part A: Applied Science and Manufacturing 2000;31(6):571-581.

[125] Mouritz A. Ballistic impact and explosive blast resistance of stitched composites. Composites Part B: Engineering 2001;32(5):431-439.

[126] Rong MZ, Zhang MQ, Liu Y, Zhang ZW, Yang GC, Zeng HM. Effect of stitching on in-plane and interlaminar properties of sisal/epoxy laminates. Journal of Composite Materials 2002;36(12):1505-1526.

[127] Tong L, Mouritz A, Bannister MK. 3D Fibre Reinforced Polymer Composites: Elsevier Science Ltd, 2002.

[128] Warrior N, Turner T, Robitaille F, Rudd C. The effect of interlaminar toughening strategies on the energy absorption of composite tubes. Composites Part A: Applied Science and Manufacturing 2004;35(4):431-437.

[129] Wood MDK, Sun X, Tong L, Katzosb A, Rispler A. The Effect of Stitch Distribution and Stitch Pattern on Mode I Delamination Toughness of Stitched Laminated Composites. In: Ye L, Mai Y-, Su Z, editors. Composite Technologies for 2020: Woodhead Publishing, 2004.

[130] Tsai G, Chen J. Effect of stitching on mode I strain energy release rate. Composite Structures 2005;69(1):1-9.

[131] Zhao HP, Li RKY, Feng XQ. Experimental investigation of interlaminar fracture toughness of CFRP composites with different stitching patterns. Key Engineering Materials: Trans Tech Publications, 2005. p.189-194.

[132] Hamitouche L, Tarfaoui M, Vautrin A. Experimental and numerical analysis of mode I interlaminair delamination of a stitched laminated

composite. ICCM16 - 16th International Conference on Composite Materials, Kyoto, Japan, 2007.

[133] Iwahori Y, Ishikawa T, Watanabe N, Ito A, Hayashi Y, Sugimoto S. Experimental investigation of interlaminar mechanical properties on carbon fiber stitched CFRP laminates. Advanced Composite Materials 2007;16(2):95-113.

[134] Solaimurugan S, Velmurugan R. Progressive crushing of stitched glass/polyester composite cylindrical shells. Composites Science and Technology 2007;67(3):422-437.

[135] Velmurugan R, Solaimurugan S. Improvements in Mode I interlaminar fracture toughness and in-plane mechanical properties of stitched glass/polyester composites. Composites Science and Technology 2007;67(1):61-69.

[136] Wood MD, Sun X, Tong L, Katzos A, Rispler AR, Mai Y. The effect of stitch distribution on Mode I delamination toughness of stitched laminated composites–experimental results and FEA simulation. Composites Science and Technology 2007;67(6):1058-1072.

[137] Solaimurugan S, Velmurugan R. Influence of in-plane fibre orientation on mode I interlaminar fracture toughness of stitched glass/polyester composites. Composites Science and Technology 2008;68(7):1742-1752.

[138] Rys T, Sankar BV, Ifju PG. Investigation of fracture toughness of laminated stitched composites subjected to mixed mode loading. Journal of Reinforced Plastics and Composites 2009;29(3):422-430.

[139] Plain KP, Tong L. The effect of stitch incline angle on mode I fracture toughness–Experimental and modelling. Composite Structures 2010;92(7):1620-1630.

[140] Tan KT, Watanabe N, Sano M, Iwahori Y, Hoshi H. Interlaminar Fracture Toughness of Vectran-stitched Composites-Experimental and Computational Analysis. Journal of Composite Materials 2010;44(26):3203-3229.

[141] Hess H, Himmel N. Structurally stitched NCF CFRP laminates. Part 1: Experimental characterization of in-plane and out-of-plane properties. Composites Science and Technology 2011;71(5):549-568.

[142] Ghafari-Namini N, Ghasemnejad H. Effect of natural stitched composites on the crashworthiness of box structures. Materials & Design 2012;39:484-494.

[143] Muruganandhan R, Murali V. Mode-I Fracture and Impact Analysis on Stitched and Unstitched Glass/Epoxy Composite Laminate. Procedia Engineering 2012;38:2207-2213.

[144] Yang T, Wang C, Zhang J, He S, Mouritz A. Toughening and self-healing of epoxy matrix laminates using mendable polymer stitching. Composites Science and Technology 2012;72(12):1396-1401.

[145] Pingkarawat K, Wang C, Varley R, Mouritz A. Effect of mendable polymer stitch density on the toughening and healing of delamination cracks in carbon–epoxy laminates. Composites Part A: Applied Science and Manufacturing 2013;50:22-30.

[146] Pingkarawat K, Wang CH, Varley RJ, Mouritz AP. Healing of fatigue delamination cracks in carbon–epoxy composite using mendable polymer stitching. Journal of Intelligent Material Systems and Structures 2014;25(1):75-86.

[147] Pingkarawat K, Mouritz A. Stitched mendable composites: Balancing healing performance against mechanical performance. Composite Structures 2015;123:54-64.

[148] Ravandi M, Teo WS, Tran LQN, Yong MS, Tay TE. Effect of through-the-thickness stitching and fibre architecture on the interlaminar properties of flax/epoxy laminates. ICCM20 - 20th International Conference on Composite Materials, Copenhagen, Denmark, 2015.

[149] Dransfield KA, Jain LK, Mai Y. On the effects of stitching in CFRPs—I. Mode I delamination toughness. Composites Science and Technology 1998;58(6):815-827.

[150] Dransfield KA, Baillie CA, Mai Y. The Mode II delamination fracture toughness of stitched CFRPs. Proceedings of Second Pacific International Conference on Aerospace and Technology; Sixth Australian Aeronautical Conference, Barton, Australia,1995. p.211-218.

[151] Sankar BV, Sharma SK. Mode II delamination toughness of stitched graphite/epoxy textile composites. Composites Science and Technology 1997;57(7):729-737.

[152] Jain LK, Dransfield KA, Mai Y-. On The Effects of Stitching in CFRPs-II. Mode II Delamination Toughness. Composites Science and Technology 1998;58:829-837.

[153] Massabò R, Mumm DR, Cox B. Characterizing mode II delamination cracks in stitched composites. International Journal of Fracture 1998;92(1):1-38.

[154] Wood MD, Sun X, Tong L, Luo Q, Katzos A, Rispler A. A new ENF test specimen for the mode II delamination toughness testing of stitched woven CFRP laminates. Journal of Composite Materials 2007;41(14):1743-1772.

[155] Herwan J, Kondo A, Morooka S, Watanabe N. Effects of stitch density and stitch thread thickness on mode II delamination properties of Vectran stitched composites. Plastics, Rubber and Composites 2014;43(9):300-308.

[156] Herwan J, Kondo A, Morooka S, Watanabe N. Effect of stitching parameter on mode II delamination properties of vectran stitched composites. ECCM16 – 16th European Conference on Composite Materials, Seville, Spain, 2014.

[157] Vandermey, N.E., Morris, D., Masters, J.E. Damage development under compression-compression fatigue loading in a stitched uniwoven graphite/epoxy composite material. Interim Report, Virginia Polytechnic Institute and State University, Blacksburg, United States, 1991;No.86.

[158] Shim S, Ahn K, Seferis JC, Berg AJ, Hudson W. Cracks and microcracks in stitched structural composites manufactured with resin film infusion process. Journal of Advanced Materials 1995;26(4):48-62.

[159] Klopp K, Moll K, Wulfhorst B. Stitching technology for technical textiles and composites. Technische Textilien 2000;43(4):E 67-E 67.

[160] Chiu C, Cheng C. In-plane permeability of stitched MMWK laminates in resin transfer molding. Journal of Reinforced Plastics and Composites 2002;21(5):391-408.

[161] Talvensaari H, Ladstätter E, Billinger W. Permeability of stitched preform packages. Composite structures 2005;71(3):371-377.

[162] Rieber G, Mitschang P. 2D Permeability changes due to stitching seams. Composites Part A: Applied Science and Manufacturing 2010;41(1):2-7.

[163] Kang TJ, Lee SH. Effect of stitching on the mechanical and impact properties of woven laminate composite. Journal of Composite Materials 1994;28(16):1574-1587.

[164] Herszberg I, Bannister MK. Tensile properties of thin stitched carbon/epoxy composites. Proceedings of 5th Australian Aerospace Conference, Barton, Australia, 1993. p.213-218.

[165] Reeder JR. Stitching vs. a toughened matrix: compression strength effects. Journal of Composite Materials 1995;29(18):2464-2487.

[166] Furrow KW, Loos AC, Cano RJ. Environmental effects on stitched RTM textile composites. Journal of Reinforced Plastics and Composites 1996;15(4):378-419.

[167] Mouritz A. Flexural properties of stitched GRP laminates. Composites Part A: Applied Science and Manufacturing 1996;27(7):525-530.

[168] Larsson F. Damage tolerance of a stitched carbon/epoxy laminate. Composites Part A: Applied Science and Manufacturing 1997;28(11):923-934.

[169] Mouritz A, Gallagher J, Goodwin A. Flexural strength and interlaminar shear strength of stitched GRP laminates following repeated impacts. Composites Science and Technology 1997;57(5):509-522.

[170] Takatoya T, Susuki I. In-plane and Out-of-plane Characteristics of Three-dimensional Textile Composites. Journal of Composite Materials 2005;39(6):543-556.

[171] Hess H, Roth Y, Himmel N. Elastic constants estimation of stitched NCF CFRP laminates based on a finite element unit-cell model. Composites Science and Technology 2007;67(6):1081-1095.

[172] Matthew J. Hiley, Graeme Stringer. A Comparison of Through-Thickness Reinforcement Methods: Z-pinning and Stitching. ICCM16 - 16th International Conference on Composite Materials, Kyoto, Japan, 2007.

[173] Bilisik K, Yolacan G. Experimental off-axis tensile characterization of multistitched woven nano composites. Fibers and Polymers 2014;15(3):614-624.

[174] Bilisik K, Yolacan G. Off-axis tensile properties of multistitched plain woven E-glass/polyester composites. Fibers and Polymers 2014;15(3):589-598.

[175] Yudhanto A, Watanabe N, Iwahori Y, Hoshi H. Effect of stitch density on fatigue characteristics and damage mechanisms of stitched carbon/epoxy composites. Composites Part A: Applied Science and Manufacturing 2014;60:52-65.

[176] Harris H, Schinske N, Krueger R, Swanson B. Multiaxial stitched preform reinforcements for RTM fabrication, 36th Int. SAMPE Symp.(15–18 April 1991). p.521-535.

[177] Wu E, Wang J. Behavior of stitched laminates under in-plane tensile and transverse impact loading. Journal of Composite Materials 1995;29(17):2254-2279.

[178] Pang F, Wang C, Bathgate R. Creep response of woven-fibre composites and the effect of stitching. Composites Science and Technology 1997;57(1):91-98.

[179] Karahan M, Ulcay Y, Karahan N, KUŞ A. Influence of Stitching Parameters on Tensile Strength of Aramid/Vinyl Ester Composites. Materials Science 2013;19(1):67-72.

[180] Bilisik K, Yolacan G. Warp and weft directional tensile properties of multistitched woven fabric E-glass/polyester nano composites. Fibers and Polymers 2014;15(5):1051-1061.

[181] Mignery L, Tan T, Sun C. The use of stitching to suppress delamination in laminated composites. Proceedings of ASTM Symposium on Delamination and Debonding of Materials, Pittsburgh, USA, 1985. p.371-385.

[182] Mouritz A. The damage to stitched GRP laminates by underwater explosion shock loading. Composites Science and Technology 1995;55(4):365-374.

[183] Khan MS, Mouritz A. Fatigue behaviour of stitched GRP laminates. Composites Science and Technology 1996;56(6):695-701.

[184] Pang F, Wang CH. A creep study on stitched fibre/resin composites. Proceedings of First Australasian Congress on Applied Mechanics: ACAM-96, Australia: Institution of Engineers, Melbourne, Australia, 1996. p.357-361.

[185] Markus Schneider, C.K. Carbon Fibre Yarn for Structural Reinforcement of Composites and Textile Applications. Lecture, Techtextil Frankfurt, 2005.

[186] Weimer C, Mitschang P. Aspects of the stitch formation process on the quality of sewn multi-textile-preforms. Composites Part A: Applied Science and Manufacturing 2001;32(10):1477-1484.

[187] Aymerich F, Priolo P, Sun C. Static and fatigue behaviour of stitched graphite/epoxy composite laminates. Composites Science and Technology 2003;63(6):907-917.

[188] Mouritz A. Fracture and tensile fatigue properties of stitched fibreglass composites. Proceedings of the Institution of Mechanical Engineers, Part L: Journal of Materials Design and Applications 2004;218(2):87-93.

[189] Zhao N, Rödel H, Herzberg C, Gao S, Krzywinski S. Stitched glass/PP composite. Part I: Tensile and impact properties. Composites Part A: Applied Science and Manufacturing 2009;40(5):635-643.

[190] Karahan M, Ulcay Y, Karahan N, KUŞ A. Influence of Stitching Parameters on Tensile Strength of Aramid/Vinyl Ester Composites. Materials Science 2013;19(1):67-72.

[191] Yudhanto A, Watanabe N, Iwahori Y, Hoshi H. Effect of stitch density on tensile properties and damage mechanisms of stitched carbon/epoxy composites. Composites Part B: Engineering 2013;46:151-165.

[192] Du X, Xue F, Gu Z. Experimental study of the effect of stitching on strength of a composite laminate. Proc. Int. Symp. on Composite Materials and Structures: Technomic Lancaster, PA, 1986. p.912-918.

[193] Herszberg I, Weller T, Leong K, Bannister M. The residual tensile strength of stitched and unstitched carbon/epoxy laminates impacted under tensile load. Proceedings of First Autralasian Congress on Applied Mechanics: ACAM-96, Melbourne, Australia, 1996. p.309-314.

[194] Kamiya R, Chou T. Strength and failure behavior of stitched carbon/epoxy composites. Metallurgical and Materials Transactions A 2000;31(13):899-909.

[195] Aymerich F, Priolo P, Sun C. Static and fatigue behaviour of stitched graphite/epoxy composite laminates. Composites Science and Technology 2003;63(6):907-917.

[196] Xiaoquan C, Al-Mansour AM, Zhengneng L, Chenghe K. Compression strength of stitched laminates after low-velocity impact. Journal of Reinforced Plastics and Composites 2005;24(9):935-947.

[197] Beier U, Fischer F, Sandler JK, Altstädt V, Weimer C, Buchs W. Mechanical performance of carbon fibre-reinforced composites based on stitched preforms. Composites Part A: Applied Science and Manufacturing 2007;38(7):1655-1663.

[198] Zheng Y, Cheng X, Yasir B. Effect of stitching on plain and open-hole strength of CFRP laminates. Chinese Journal of Aeronautics 2012;25(3):473-484.

[199] Yudhanto A, Watanabe N, Iwahori Y, Hoshi H. Effect of stitch density on fatigue characteristics and damage mechanisms of stitched carbon/epoxy composites. Composites Part A: Applied Science and Manufacturing 2014;60:52-65.

[200] Kullerd SM, Dow MB. Development of stitched/RTM composite primary structures. Proceedings of The Sixth Conference on Advanced Engineering Fibers and Textile Structure for Composites, Philadelphia, USA, 1992. p.115-140.

[201] Yudhanto A, Watanabe N, Iwahori Y, Hoshi H. The effects of stitch orientation on the tensile and open hole tension properties of carbon/epoxy plain weave laminates. Materials & Design 2012;35:563-571.

[202] Palmer RJ, Dow MB, Smith DL. Development of stitching reinforcement for transport wing panels. Proceedings of First NASA Advanced Composites Technology Conference, Part 2, Seattle, USA, 1991. p.621-646.

[203] Adanur S, Gongalareddy S. Compressive properties of stitched woven fibreglass fabric reinforced composite sections for civil engineering applications. Proceedings of ICCM3 - Third International Conference on Composites Engineering, New Orleans, USA, 1996. p.49-50.

[204] Gunnion AJ, Scott ML, Thomson RS, Hachenberg D. Thickness effects on the compressive stiffness and strength of stitched composite laminates. Composite structures 2004;66(1):479-486.

[205] Han H, Li H, Li K, Yue Z. Damage to thickness-reinforced C/C laminates by low-energy impact. Carbon 2004;42(14):3033-3036.

[206] Scarponi C, Perillo A, Cutillo L, Foglio C. Advanced TTT composite materials for aeronautical purposes: Compression after impact (CAI) behaviour. Composites Part B: Engineering 2007;38(2):258-264.

[207] Xiaoquan C, Baig Y, Zhonghai L. Effects of hygrothermal environmental conditions on compressive strength of CFRP stitched laminates. Journal of Reinforced Plastics and Composites 2011;30(2):110-122.

[208] Lubowinski S, Poe Jr C. Fatigue characterization of stitched graphite/epoxy composites. Proceedings of FIBER-TEX Conference, Greenville, USA, 1987. p.253-271.

[209] Dow MB, Smith DL. Damage-tolerant composite materials produced by stitching carbon fabrics. Proceedings of International SAMPE Technical Conference, Covina, USA, 1989. p.595-605.

[210] Farley GL, Smith BT, Maiden J. Compression response of thick layer composite laminates with through-the-thickness reinforcement. Journal of Reinforced Plastics and Composites 1992;11(7):787-810.

[211] Farley GL, Dickinson LC. Removal of surface loop from stitched composites can improve compression and compression-after-impact strengths. Journal of Reinforced Plastics and Composites 1992;11(6):633-642.

[212] Caneva C, Olivieri S, Santulli C, Bonifazi G. Impact damage evaluation on advanced stitched composites by means of acoustic emission and image analysis. Composite Structures 1993;25(1):121-128.

[213] Jenq S, Sheu S. High strain rate compressional behavior of stitched and unstitched composite laminates with radial constraint. Composite Structures 1993;25(1):427-438.

[214] Palmer R. Techno-economic requirements for composite aircraft components. In NASA. Langley Research Center, Proceedings of FIBER-TEX 1992: The Sixth Conference on Advanced Engineering Fibers and Textile Structures for Composites, Philadelphia, USA, 1993. p.305-341.

[215] Furrow K, Loos A, Cano R. Environmental effects on stitched RTM uniwoven composites. Proceedings of 39th International SAMPE Symposium and Exhibition, Anaheim, USA, 1994. p.813-825.

[216] Jain L, Dransfleld K, Mai Y, Baillie C. Improvement of interlaminar properties in advanced fibre composites with through-thickness reinforcement. Cooperative Research Centre for Aerospace Structures Ltd., CRC-AS TM94012 1994.

[217] Reeder JR. Comparison of the compressive strengths for stitched and toughened composite systems, Technical Report vol. 109108: National Aeronautics and Space Administration, Langley Research Center, 1994.

[218] Herszberg I, Leong K, Bannister M. The effect of stitching on the impact damage resistance and tolerance of uniweave carbon/epoxy laminates. Proceedings of Fourth International Conference on Automated Composites, 1995. p. 53-60.

[219] Kedward K. Compression damage tolerance of stitched composites. Proceedings Joint applied mechanics and materials summer meeting, Los Angeles, USA, 1995.

[220] Leong K, Herszberg I, Bannister M. Impact damage resistance and tolerance of stitched carbon epoxy laminates. Proceedings of Second Pacific International Conference on Aero-Space Science and Technology/Sixth Australian Aeronautical Conference, Melbourne, Australia, 1995. p.605-612.

[221] Leong K, Herszberg I, Bannister M. An investigation of fracture mechanisms of carbon epoxy laminates subjected to impact and compression-after-impact loading. International Journal of Crashworthiness 1996;1(3):285-294.

[222] Sharma S, Sankar B. Sublaminate buckling and compression strength of stitched uniweave graphite/epoxy laminates. Journal of Reinforced Plastics and Composites 1997;16(5):425-434.

[223] Yang B, Kozey V, Adanur S, Kumar S. Bending, compression, and shear behavior of woven glass fiber–epoxy composites. Composites Part B: Engineering 2000;31(8):715-721.

[224] Hosur M, Adya M, Vaidya U, Mayer A, Jeelani S. Effect of stitching and weave architecture on the high strain rate compression response of affordable woven carbon/epoxy composites. Composite structures 2003;59(4):507-523.

[225] Byun J, Song S, Lee C, Um M, Hwang B. Impact properties of laminated composites with stitching fibers. Composite structures 2006;76(1):21-27.

[226] Beier U, Fischer F, Sandler JK, Altstädt V, Weimer C, Spanner H, Buchs W. Evaluation of preforms stitched with a low melting-temperature thermoplastic yarn in carbon fibre-reinforced composites. Composites Part A: Applied Science and Manufacturing 2008;39(5):705-711.

[227] Yudhanto A, Watanabe N, Iwahori Y, Hoshi H. Compression properties and damage mechanisms of stitched carbon/epoxy composites. Composites Science and Technology 2013;86:52-60.

[228] Hahn HT, Tsai SW. Introduction to composite materials, vol. 1: CRC Press, Lancaster, USA, 1980.

[229] Cholakara M, Jang B, Wang C. Deformation and failure mechanisms in 3D composites. Proceedings of the 34th International SAMPE Symposium and Exhibition, Reno, USA, 1989. p.8-11.

[230] Farley GL. A mechanism responsible for reducing compression strength of through-the-thickness reinforced composite material. Journal of Composite Materials 1992;26(12):1784-1795.

[231] Herszberg I, Loh A, Bannister M, Thuis H. Open hole fatigue of stitched and unstitched carbon/epoxy laminates. Proceedings of ICCM11 - 11th International Conference on Composite Materials, Gold Coast, Australia, 1997. p.V-138-V-148.

[232] Yudhanto A, Iwahori Y, Watanabe N, Hoshi H. Open hole fatigue characteristics and damage growth of stitched plain weave carbon/epoxy laminates. International Journal of Fatigue 2012;43:12-22.

[233] Portanova M, Poe C, Whotcomb JD. Open hole and postimpact compressive fatigue of stitched and unstitched carbon-epoxy composites. Composite materials: Testing and design. 1992;10:37-53.

[234] Mayadas A, Pastore C, Ko FK. Tensile and shear properties of composites by various reinforcement concepts. Advancing Technology in Materials and Processes, The 30th National SAMPE Symposium and Exhibition, Anaheim, USA, 1985. p.1284-1293.

[235] Adanur S, Tsao YP. Stitch bonded textile structural composites. 50 Years of Progress in Materials Science and Technology: 26th International SAMPE Technical Conference, Atlanta, Georgia, 1994. p.25-34.

[236] Byun J, Lee C, Song S, Lee S, Kim B, Joe C. Stitching effect on flexural and interlaminar properties of MWK textile composites. ICCM15 - 15th International Conference on Composite Materials, Durban, South Africa, 2005.

[237] Mitschang P, Ogale A. Effect of sewing threads on interlaminar shear strength and flexural bending strength of stitched non-crimp carbon fabric laminates. Advanced Composites Letters 2006;15(6):199-206.

[238] Koziol M. Effect of thread tension on mechanical performance of stitched glass fibre-reinforced polymer laminates–experimental study. Journal of Composite Materials 2013;47(16):1919-1930.

[239] Koziol M. Experimental study on the effect of stitch arrangement on mechanical performance of GFRP laminates manufactured on a basis of stitched preforms. Journal of Composite Materials 2012;46(9):1067-1078.

[240] Huang T, Jiao GQ, Xu TT. Tensile and shear properties of stitched laminates in hygrothermal environment. Key Engineering Materials: Trans Tech Publications, 2006. p.1753-1756.

[241] Cox B, Massabo R, Mumm D, Turrettini A, Kedward K. Delamination fracture in the presence of through-thickness reinforcement. Proceedings of ICCM11 – 11th International Conference on Composite Materials, Gold Coast, Australia, 1997. p.1-159.

[242] Sun Y-, Thurm T. CNC-stitching machine tool for preform production. International SAMPE Technical Conference, 2004. p.1053-1062.

[243] Wittig J. Recent development in the robotic stitching technology for textile structural composites. International Sampe Technical Conference, 2001. p.540-550.

[244] Klopp K, Moll K, Wulfhorst B. Stitching Process With One-Sided Approach of the Textile for the Production of Reinforcing Textiles for

Composites and Other Technical Textiles. TexComp 5 - The 5th International Conference on Textile Composites, Leuven, Belgium, 2000.

[245] Grundmann T, Gries T, Kordl MT, Corves B. Robot-supported joining of reinforcement textiles with one-sided sewing heads. Technische Textilien 2006;49(4):E200-E201+262-263.

[246] Kordi, M.T., Mbarek, T., Hüsing, M., Corves, B. Systematical development of a one-sided sewing machine for robot-supported 3D-sewing by automated manufacture of fibre reinforced composite structures. VDI Berichte 2007(1971):477-495.

[247] Trabelsi W, Michel L, Othomene R. Effects of stitching on delamination of satin weave carbon-epoxy laminates under mode I, mode II and mixed-mode I/II loadings. Applied Composite Materials 2010;17(6):575-595.

[248] Plain KP, Tong L. An experimental study on mode I and II fracture toughness of laminates stitched with a one-sided stitching technique. Composites Part A: Applied Science and Manufacturing 2011;42(2):203-210.

[249] Bigaud J, Aboura Z, Verger S. Study and analysis of the mechanical behaviour of reinforced stitching stiffeners. ECCM16 - 16th European Conference on Composite Materials, Seville, Spain, 2014.

[250] Leduc C, Joncas S, Leclerc J-. Effect of process parameters on damage tolerance of carbon epoxy laminate preformed using one-sided stitching. ECCM16 - 16th European Conference on Composite Materials, Seville, Spain, 2014.

[251] Song Y, Khellil K, Abour Z, Ouahsine A. Influence of one side stitching on the permeability of composite reinforced by transverse sewing. ECCM16 – 16th European Conference on Composite Materials, Seville, Spain, 2014.

[252] Thurm T. Applications of one-sided stitching techniques for resin infusion preforms and structures. SAMPE Journal 2005;41(1):64-67.

[253] Filsinger J, Dittmann R, Bischoff T. Nähen als Textile Preform-Technik zur Herstellung von Faserverbundstrukturen für Luftfahrtanwendungen am Beispiel der A380 Druckkalotte. München: Deutsche Luft-und Raumfahrtkongress 2003. p.17-20.

[254] Grundmann TC. Economic production of fibre-reinforced-plastic (FRP) parts by automated production of textile preforms. Mitteilungen / Institut für Textiltechnik 2007;53.

[255] Gripp, S., Spiegel, R. Vielkanal-Ultraschallprüfung in Kontakttechnik - eine neuartige Prüftechnologie setzt sich durch. DGZfP-Jahrestagung, ZfP in Anwendung, Entwicklung und Forschung, Mainz, 2003.

[256] Schiebel P, Herrmann A. Textile preform technologies in the aviation sector - chances and challenges for the automotive sector. Proceedings

of Industrial Fabrics Association International - Advanced Textiles Europe Conference, Berlin, Germany, 2008.

[257] Sickinger C, Herrmann A. Structural stitching as a method to design high-performance composites in future. Proceedings of TechTextil Symposium, Frankfurt am Main, Germany, 2001.

[258] Dell'Anno G, Partridge IK, Cartié DDR, Hamlyn A, Chehura E, James SW, Tatam RP. Automated manufacture of 3D reinforced aerospace composite structures. International Journal of Structural Integrity 2012;3(1):22.

[259] Dell'Anno G, Treiber J, Partridge I. Manufacturing of composite parts reinforced through-thickness by tufting. Robotics and Computer-Integrated Manufacturing 2015;37:262-272

[260] Dell'Anno G, Cartié DD, Partridge IK, Rezai A. Exploring mechanical property balance in tufted carbon fabric/epoxy composites. Composites Part A: Applied Science and Manufacturing 2007;38(11):2366-2373.

[261] Colin de Verdiere M, Pickett AK, Skordos AA, Witzel V. Effect of tufting on the response of non-crimp fabric composites. Proceedings of ECCOMAS Thematic Conference on Mechanical Response of Composites, Porto, Portugal, 2007. p.12-14.

[262] Colin de Verdiere M, Pickett A, Skordos A, Witzel V. Evaluation of the mechanical and damage behaviour of tufted non crimped fabric composites using full field measurements. Composites Science and Technology 2009;69(2):131-138.

[263] Colin de Verdiere M, Skordos A, May M, Walton A. Influence of loading rate on the delamination response of untufted and tufted carbon epoxy non crimp fabric composites: Mode I. Engineering Fracture Mechanics 2012;96:11-25.

[264] Colin de Verdiere M, Skordos A, Walton A, May M. Influence of loading rate on the delamination response of untufted and tufted carbon epoxy non-crimp fabric composites/Mode II. Engineering Fracture Mechanics 2012;96:1-10.

[265] Koissin V, Ruopp A, Lomov SV, Verpoest I, Witzel V, Drechsler K. On-surface fibre-free zones and irregularity of piercing pattern in structurally stitched NCF preforms. Advanced composites letters 2006;15(3):81-88.

[266] Koissin V, Kustermans J, Lomov SV, Verpoest I, Nakai H, Kurashiki T, Hamada K, Momoji Y, Zako M. Structurally stitched woven preforms: experimental characterisation, geometrical modelling, and FE analysis. Plastics, Rubber and Composites 2009;38(2-4):98-105.

[267] Koissin V, Kustermans J, Lomov SV, Verpoest I, Van Den Broucke B, Witzel V. Structurally stitched NCF preforms: Quasi-static response. Composites Science and Technology 2009;69(15):2701-2710.

[268] Henao A, Carrera M, Miravete A, Castejón L. Mechanical performance of through-thickness tufted sandwich structures. Composite Structures 2010;92:2052-2059.

[269] Deconinck P, Capelle J, Bouchart V, Chevrier P, Ravailler F. Delamination propagation analysis in tufted carbon fibre-reinforced plastic composites subjected to high-velocity impact. Journal of Reinforced Plastics and Composites 2014;33(14):1353-1363.

[270] Henao A, Guzmán de Villoria R, Cuartero J, Carrera M, Picón J, Miravete A. Enhanced Impact Energy Absorption Characteristics of Sandwich Composites through Tufting. Mechanics of Advanced Materials and Structures 2015;22(12):1016-1023.

[271] Carvelli V, Tomaselli VN, Lomov SV, Verpoest I, Witzel V, Van den Broucke B. Fatigue and post-fatigue tensile behaviour of non-crimp stitched and unstitched carbon/epoxy composites. Composites Science and Technology 2010;70(15):2216-2224.

[272] Cartié DD, Dell'Anno G, Poulin E, Partridge IK. 3D reinforcement of stiffener-to-skin T-joints by Z-pinning and tufting. Engineering Fracture Mechanics 2006;73(16):2532-2540.

[273] Mills A, Jones J. Investigation, manufacture, and testing of damage-resistant airframe structures using low-cost carbon fibre composite materials and manufacturing technology. Proceedings of the Institution of Mechanical Engineers, Part G: Journal of Aerospace Engineering 2010;224(4):489-497.

[274] Herkt M, Middendorf P, Less C, Riedel W, Maier G, Drechsler K. Dynamic strength testing of 3D-reinforced T-joints. Proceedings of ICAS 2006 – 25th Congress of International Council of the Aeronautical Sciences, Hamburg, Germany, 2006.

[275] Kratz J, Clegg H, Dell'Anno G, Partridge IK. Improving the damage tolerance of composite joints with tufting. ICCM20 - 20th International Conference on Composite Materials, Copenhagen, Denmark, 2015.

[276] Harman D, Grove S, Summerscales J. The economics of through-thickness fibre reinforcement using single sided robotic tufting. ECCM16 – 16th European Conference on Composite Materials, Seville, Spain, 2014.

[277] Cranfield University. Composite landing gear brace for Boeing 787 Dreamliner – first in the market for Messier-Bugatti-Dowty. http://impact.ref.ac.uk/CaseStudies/CaseStudy.aspx?Id=17852;(accessed July 2015).

[278] Ogale A, Weimer C, Mitschang P. Selection of sewing threads for preform manufacturing. Advanced Composites Letters 2005;13(4):199-206.

[279] ADVITAC. Advanced Integrated Tail Cone. http://www.advitac eu;(accessed August 2015).

[280] Hexcel. HexFlow® RTM 6, Product Data sheet. http://www.hexcel com/Resources/DataSheets/RTM-Data-Sheets/RTM6_global pdf;(accessed October 2015).

[281] Huntsman. Araldite®420 A/B, Data sheet. Publication No A 161 d GB, https://www.silmid.com/MetaFiles/Silmid/0f/0fe65000-9138-4ebb-8e64-4829b5a52e13 pdf 2000;(accessed October 2015).

[282] Military Standard 1757A, Lightning qualification test techniques for aerospace vehicles and hardware. Department of Defense, United States of America, 1983.

[283] DuPont®. Kevlar technical guide. http://www.dupont.co.uk/content/dam/dupont/products-and-services/ fabrics-fibers-and-nonwovens/fibers/documents/ Kevlar_Technical_Guide.pdf;(accessed October 2015).

[284] Ross RB. Metallic materials specification handbook: Springer Science & Business Media, Glasgow, UK, 2013.

[285] British Stainless Steel Association. Elevated temperature physical properties of stainless steels. http://www.bssa.org.uk/topics.php?article=139;(accessed October 2015).

[286] Jenkins WD, Digges TG, Johnson CR. Tensile Properties of Copper, Nickel, and 70-Percent-Copper-30-Percent-Nickel and 30-Percent-Copper-70-Percent-Nickel Alloys at High Temperatures. Journal of Research of the National Institute of Standards and Technology 1957;58(4):201-211.

[287] Kuhn H, Medlin D. ASM Handbook. Volume 8: Mechanical Testing and Evaluation. ASM International, Member/Customer Service Center, Novelty, USA, 2000.

[288] Rollett A, Humphreys F, Rohrer GS, Hatherly M. Recrystallization and related annealing phenomena: Elsevier, Oxford, UK, 2004.

[289] Rice JR. A path independent integral and the approximate analysis of strain concentration by notches and cracks. Journal of applied mechanics 1968;35(2):379-386.

[290] Larsson A. The interaction between a lightning flash and an aircraft in flight. Comptes Rendus Physique 2002;3(10):1423-1444.

[291] Mall S, Ouper B, Fielding J. Compression strength degradation of nanocomposites after lightning strike. Journal of Composite Materials 2009;43(24):2987-3001.

[292] Gou J, Tang Y, Liang F, Zhao Z, Firsich D, Fielding J. Carbon nanofiber paper for lightning strike protection of composite materials. Composites Part B: Engineering 2010;41(2):192-198.

[293] Gagné M, Therriault D. Lightning strike protection of composites. Progress in Aerospace Sciences 2013;64:1-16.

[294] Advisory Circular FAA. Protection of aircraft electrical/electronic systems against the indirect effects of lightning. Circular 20-136A, http://www.faa.gov/documentLibrary/media/Advisory_Circular/AC%2020-136A_Final.pdf, 2006;(accessed October 2015).

[295] Volland H. Handbook of atmospheric electrodynamics, vol. 2: CRC Press, Boca Raton, USA, 1995.

[296] Fisher FA, Plumer JA, Perala RA. Aircraft Lightning Protection Handbook, Springfield, USA, 1989.

[297] Sweers G, Birch B, Gokcen J. Lightning Strikes: Protection, inspection, and repair. AERO Quarterly.GTR 2004;12(4):19-28.

[298] Haynes KK, Clark M. Lightning strike protection: novel nonwoven technology. JEC composites 2006(24):32-33.

[299] Welch J. Repair design, test and process considerations for lightning strike. Presentation at 3rd FAA/EASA/Boeing/Airbus Joint Workshop on Safety and Certification, Amsterdam, Netherlands, 2007.

[300] Kawakami H, Feraboli P. Lightning strike damage resistance and tolerance of scarf-repaired mesh-protected carbon fiber composites. Composites Part A: Applied Science and Manufacturing 2011;42(9):1247-1262.

[301] Klomp-de Boer R, Smeets M. Lightning strike behaviour of thick walled Resin Transfer Moulded parts using various Lightning Strike Protection concepts. National Aerospace Laboratory NLR, Technical Report No. NLR-TP-2013-402, Amsterdam, Netherlands, 2013.

[302] Zhang B, Patlolla VR, Chiao D, Kalla DK, Misak H, Asmatulu R. Galvanic corrosion of Al/Cu meshes with carbon fibers and graphene and ITO-based nanocomposite coatings as alternative approaches for lightning strikes. The International Journal of Advanced Manufacturing Technology 2013;67(5-8):1317-1323.

[303] Hirano Y, Katsumata S, Iwahori Y, Todoroki A. Artificial lightning testing on graphite/epoxy composite laminate. Composites Part A: Applied Science and Manufacturing 2010;41(10):1461-1470.

[304] Gardiner G. Lightning strike protection for composite structures. High performance composites. http://www.compositesworld.com/articles/lightning-strike-protection-for-composite-structures, 2006;(accessed October 2015).

[305] Chemartin L, Lalande P, Peyrou B, Chazottes A, Elias P, Delalondre C, Cheron B, Lago F. Direct effects of lightning on aircraft structure: analysis of the thermal, electrical and mechanical constraints. Journal Aerospace Lab 2012(5):p.1-15.

[306] Morgan J. Thermal Simulation and Testing of Expanded Metal Foils Used for Lightning Protection of Composite Aircraft Structures. SAE International Journal of Aerospace 2013;6(2):371-377.

[307] Black S. Lightning strike protection strategies for composite aircraft. High-Performance Composites. http://www.compositesworld.com/articles/lightning-strike-protection-strategies-for-composite-aircraft, 2013;(accessed October 2015).

[308] Reid G. Mechanical damage to aircraft structures from lightning strikes. Proceedings of the Institution of Mechanical Engineers, Part G: Journal of Aerospace Engineering 1993;207(1):1-14.

[309] Brosius D. Boeing 787 update. High Performance Composites. http://www.compositesworld.com/articles/boeing-787-update, 2007;(accessed October 2015).

[310] Fernandez Reia Da Costa E. Liquid moulding of carbon nanoparticle filled composites. PhD Thesis, School of Applied Sciences, Cranfield University, 2011.

[311] Matula RA. Electrical resistivity of copper, gold, palladium, and silver. Journal of Physical and Chemical Reference Data 1979;8(4):1147-1298.

[312] Ho CY, Chu T. Electrical resistivity and thermal conductivity of nine selected AISI stainless steels. CINIDAS Report 45, West Lafayette, USA, 1977.

[313] Singh S, Partridge I. Mixed-mode fracture in an interleaved carbon-fibre/epoxy composite. Composites Science and Technology 1995;55(4):319-327.

[314] Anderson TL, Anderson T. Fracture mechanics: fundamentals and applications: CRC press, Boca Raton, USA, 2005.

[315] Gerlach R, Siviour CR, Petrinic N, Wiegand J. Experimental characterisation and constitutive modelling of RTM-6 resin under impact loading. Polymer 2008;49(11):2728-2737.

[316] Appleby-Thomas G, Hazell P, Stennett C. The variation in lateral and longitudinal stress gauge response within an RTM 6 epoxy resin under one-dimensional shock loading. Journal of Materials Science 2009;44(22):6187-6198.

[317] Morelle X, Lani F, Melchior M, Andre S, Bailly C, Pardoen T. The elasto-viscoplasticity and fracture behaviour of the RTM6 structural epoxy and impact on the response of woven composites. ECCM15 – 15th European Conference on Composites Materials, Venice, Italy, 2012.

[318] Mehdi, Y. Galvanic Corrosion of Metals Connected to Carbon Fiber Reinforced Polymers. Corrosionpedia, https://www.corrosionpedia com/2/1556/corrosion/galvanic-corrosion-of-metals-connected-to-carbon-fiber-reinforced-polymers, 2015;(accessed October 2015).

[319] Howatson AM. Engineering tables and data: Springer Science & Business Media, London, UK, 2012.

[320] Lütjering G, Williams JC. Titanium, vol. 2: Springer, Berlin, Germany, 2003.

[321] Oshida Y. Bioscience and bioengineering of titanium materials: Elsevier, Oxford, UK, 2010.

APPENDICES

Appendix A – Technical drawing of plinth designed for tufting of the tail cone

Figure A-1 shows the technical drawing of the new plinth designed for the elevation of the robot in order to increase its envelope.

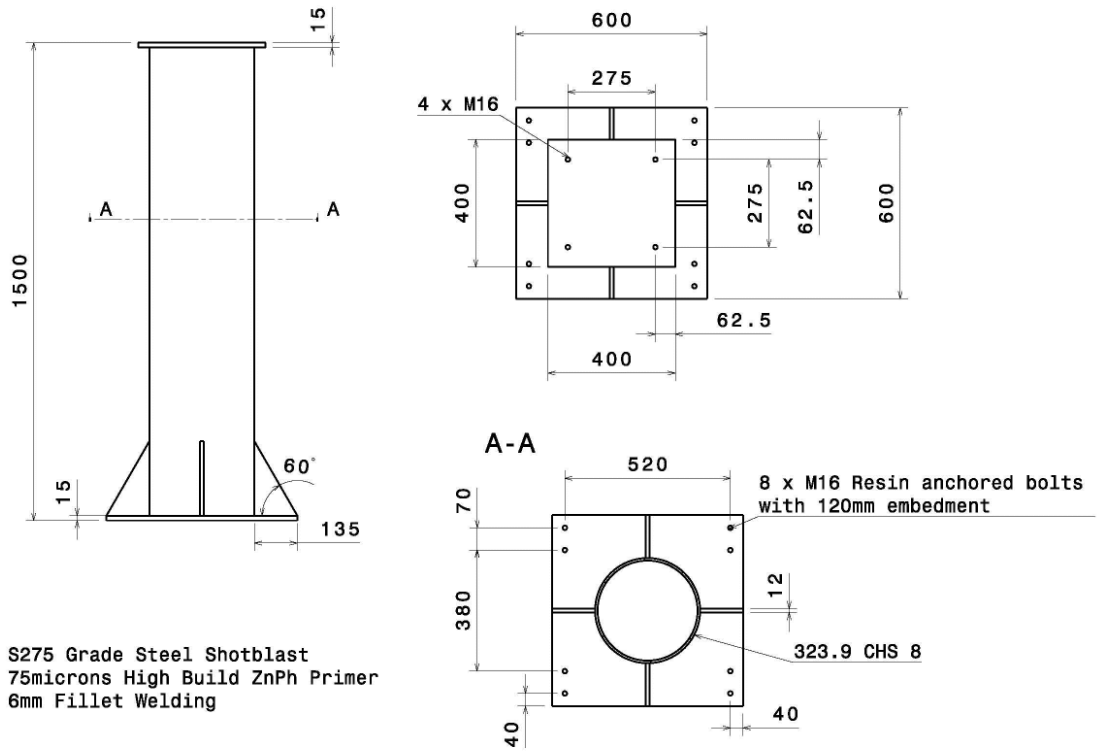

Figure A-1 Technical drawing of new plinth.

Appendix B – Example code for generation of tuft insertion points in CATIA

The presented in Listing B-1 code is an example of the generation of tuft insertion points along a single tuft row of a stiffener flange.

```
Language="VBSCRIPT"
Sub CATMain()

i=1

Set partDocument1 = CATIA.ActiveDocument
Set part1 = partDocument1.Part
Set hybridShapeFactory1 = part1.HybridShapeFactory
Set hybridBodies1 = part1.HybridBodies
Set hybridBody1 = hybridBodies1.Item("Tufting")
Set hybridShapes1 = hybridBody1.HybridShapes

for j=540 to 641 step 1
z=j+102

Set hybridShapePointOnCurve1 = hybridShapes1.Item("Point."+CStr(j))
Set reference1 = part1.CreateReferenceFromObject(hybridShapePointOnCurve1)
Set hybridShapePointOnCurve2 = hybridShapes1.Item("Point."+CStr(z))

Set reference2 = part1.CreateReferenceFromObject(hybridShapePointOnCurve2)

Set hybridShapePointBetween1 = hybridShapeFactory1.AddNewPointBetween(reference1,
reference2, 0.500000, 1)

Set parameters1 = part1.Parameters
Set hybridShapeSurfaceExplicit1 = parameters1.Item("Surface.772")

Set reference3 = part1.CreateReferenceFromObject(hybridShapeSurfaceExplicit1)

hybridShapePointBetween1.Support = reference3
hybridBody1.AppendHybridShape hybridShapePointBetween1
part1.InWorkObject = hybridShapePointBetween1
part1.Update

Next
i=i+1
End Sub
```

Listing B-1 Script for automated generation of tuft insertion points in CATIA.

Appendix C - Tuft coordinate transformation routine

The code in Listing C-1 was developed to transform the virtual created tuft insertion point coordinates into the robot coordinate system.

```
Option Base 1
Option Explicit
Dim XYZo(3) As Variant
Dim RxRyRz(3, 3) As Variant
Dim Rx(3, 3) As Variant
Dim Ry(3, 3) As Variant
Dim Rz(3, 3) As Variant
Dim Pi As Double
Dim vSmall As Double
Private Sub LoadTransf_Click()
Dim RobotX() As Variant, RobotY() As Variant, RobotZ() As Variant
Dim GeomXYZ() As Variant
Dim LinestXTmp() As Variant, LinestYTmp() As Variant, LinestZTmp() As
    Variant
Dim phi As Double, theta As Double, psi As Double
Dim counter As Long
counter = 1
While (Sheet2.Cells(2 + counter, 1) <> "")
   ReDim Preserve RobotX(counter)
   ReDim Preserve RobotY(counter)
   ReDim Preserve RobotZ(counter)
   ReDim Preserve GeomXYZ(3, counter)
   RobotX(counter) = Sheet2.Cells(2 + counter, 6)
   RobotY(counter) = Sheet2.Cells(2 + counter, 7)
   RobotZ(counter) = Sheet2.Cells(2 + counter, 8)
   GeomXYZ(1, counter) = Sheet2.Cells(2 + counter, 1)
   GeomXYZ(2, counter) = Sheet2.Cells(2 + counter, 2)
   GeomXYZ(3, counter) = Sheet2.Cells(2 + counter, 3)
   counter = counter + 1
Wend
LinestXTmp = Application.LinEst(RobotX, GeomXYZ)
LinestYTmp = Application.LinEst(RobotY, GeomXYZ)
LinestZTmp = Application.LinEst(RobotZ, GeomXYZ)
XYZo(1) = LinestXTmp(4)
XYZo(2) = LinestYTmp(4)
XYZo(3) = LinestZTmp(4)
RxRyRz(1, 1) = LinestXTmp(3)
RxRyRz(1, 2) = LinestXTmp(2)
RxRyRz(1, 3) = LinestXTmp(1)
RxRyRz(2, 1) = LinestYTmp(3)
RxRyRz(2, 2) = LinestYTmp(2)
RxRyRz(2, 3) = LinestYTmp(1)
RxRyRz(3, 1) = LinestZTmp(3)
RxRyRz(3, 2) = LinestZTmp(2)
RxRyRz(3, 3) = LinestZTmp(1)
phi = Atn(RxRyRz(3, 2) / RxRyRz(3, 3)) * 180 / Pi
theta = Application.Asin(-RxRyRz(3, 1)) * 180 / Pi
psi = Atn(RxRyRz(2, 1) / RxRyRz(1, 1)) * 180 / Pi
If Err(RxRyRz, phi, theta, psi) < vSmall Then
```

```
   GoTo 110
End If
If Err(RxRyRz, phi, theta, 180 + psi) < vSmall Then
   psi = 180 + psi
   GoTo 110
End If
If Err(RxRyRz, 180 + phi, theta, psi) < vSmall Then
   phi = 180 + phi
   GoTo 110
End If
If Err(RxRyRz, 180 + phi, theta, 180 + psi) < vSmall Then
   phi = 180 + phi
   psi = 180 + psi
   GoTo 110
End If
If Err(RxRyRz, phi, 180 - theta, psi) < vSmall Then
   theta = 180 - theta
   GoTo 110
End If
If Err(RxRyRz, phi, 180 - theta, 180 + psi) < vSmall Then
   theta = 180 - theta
   psi = 180 + psi
   GoTo 110
End If
If Err(RxRyRz, 180 + phi, 180 - theta, psi) < vSmall Then
   phi = 180 + phi
   theta = 180 - theta
   GoTo 110
End If
If Err(RxRyRz, 180 + phi, 180 - theta, 180 + psi) < vSmall Then
   phi = 180 + phi
   theta = 180 - theta
   psi = 180 + psi
   GoTo 110
End If
110:
Rx(1, 1) = 1
Rx(1, 2) = 0
Rx(1, 3) = 0
Rx(2, 1) = 0
Rx(2, 2) = Cos(Pi / 180 * phi)
Rx(2, 3) = -Sin(Pi / 180 * phi)
Rx(3, 1) = 0
Rx(3, 2) = Sin(Pi / 180 * phi)
Rx(3, 3) = Cos(Pi / 180 * phi)
Ry(1, 1) = Cos(Pi / 180 * theta)
Ry(1, 2) = 0
Ry(1, 3) = -Sin(Pi / 180 * theta)
Ry(2, 1) = 0
Ry(2, 2) = 1
Ry(2, 3) = 0
Ry(3, 1) = Sin(Pi / 180 * theta)
Ry(3, 2) = 0
Ry(3, 3) = Cos(Pi / 180 * theta)
Rz(1, 1) = Cos(Pi / 180 * psi)
Rz(1, 2) = -Sin(Pi / 180 * psi)
Rz(1, 3) = 0
Rz(2, 1) = Sin(Pi / 180 * psi)
```

```
Rz(2, 2) = Cos(Pi / 180 * phi)
Rz(2, 3) = 0
Rz(3, 1) = 0
Rz(3, 2) = 0
Rz(3, 3) = 1
End Sub
```

Listing C-1 Coordinate transformation code.

Appendix D – Code for automated tufting process

The code presented in Listing D-1 was developed so that the robot interface software is able to read the transformed coordinates and to move the tufting needle to the corresponding tuft insertion point.

```
Private Sub Move_Click()
ProcID = Shell("C:\Documents and Settings\e15562\Desktop\kcwin.EXE", 1)
CommandString = "do draw " + XBox.Text + " ," + YBox.Text + " ," + ZBox.Text + " ," +
RxBox.Text + " ," + RyBox.Text + " ," + RzBox.Text + " ,"
SendKeys CommandString, True
SendKeys "{ENTER}", True
newHour = Hour(Now())
newMinute = Minute(Now())
newSecond = Second(Now()) + 3
waitTime = TimeSerial(newHour, newMinute, newSecond)
Application.Wait waitTime
SendKeys "%FX", True
newHour = Hour(Now())
newMinute = Minute(Now())
newSecond = Second(Now()) + 1
waitTime = TimeSerial(newHour, newMinute, newSecond)
Application.Wait waitTime
SendKeys "{ENTER}", True
Call populate(PointBox.Text + 1)
End Sub
Private Sub UserForm_Activate()
Pi = Application.Pi()
vSmall = 0.0000001
Call populate(1)
Call LoadTransf_Click
End Sub
Public Sub populate(Row)
PointBox.Text = Sheet1.Cells(Row + 1, 1)
XBox.Text = Sheet1.Cells(Row + 1, 2)
YBox.Text = Sheet1.Cells(Row + 1, 3)
ZBox.Text = Sheet1.Cells(Row + 1, 4)
RxBox.Text = Sheet1.Cells(Row + 1, 5)
RyBox.Text = Sheet1.Cells(Row + 1, 6)
RzBox.Text = Sheet1.Cells(Row + 1, 7)
End Sub
Function Err(Rot, ph, the, ps)
Err = Abs(Rot(1, 1) - R11(ph, the, ps))
Err = Err + Abs(Rot(1, 2) - R12(ph, the, ps))
Err = Err + Abs(Rot(1, 3) - R13(ph, the, ps))
Err = Err + Abs(Rot(2, 1) - R21(ph, the, ps))
Err = Err + Abs(Rot(2, 2) - R22(ph, the, ps))
Err = Err + Abs(Rot(2, 3) - R23(ph, the, ps))
Err = Err + Abs(Rot(3, 1) - R31(ph, the, ps))
Err = Err + Abs(Rot(3, 2) - R32(ph, the, ps))
Err = Err + Abs(Rot(3, 3) - R33(ph, the, ps))
End Function
Function R11(ph, the, ps)
R11 = Cos(the * Pi / 180) * Cos(ps * Pi / 180)
```

```
End Function
Function R12(ph, the, ps)
R12 = -Cos(ph * Pi / 180) * Sin(ps * Pi / 180) + Sin(ph * Pi / 180) * Sin(the * Pi / 180) * Cos(ps * Pi / 180)
End Function
Function R13(ph, the, ps)
R13 = Sin(ph * Pi / 180) * Sin(ps * Pi / 180) + Cos(ph * Pi / 180) * Sin(the * Pi / 180) * Cos(ps * Pi / 180)
End Function
Function R21(ph, the, ps)
R21 = Cos(the * Pi / 180) * Sin(ps * Pi / 180)
End Function
Function R22(ph, the, ps)
R22 = Cos(ph * Pi / 180) * Cos(ps * Pi / 180) + Sin(ph * Pi / 180) * Sin(the * Pi / 180) * Sin(ps * Pi / 180)
End Function
Function R23(ph, the, ps)
R23 = -Sin(ph * Pi / 180) * Cos(ps * Pi / 180) + Cos(ph * Pi / 180) * Sin(the * Pi / 180) * Sin(ps * Pi / 180)
End Function
Function R31(ph, the, ps)
R31 = -Sin(the * Pi / 180)
End Function
Function R32(ph, the, ps)
R32 = Sin(ph * Pi / 180) * Cos(the * Pi / 180)
End Function
Function R33(ph, the, ps)
R33 = Cos(ph * Pi / 180) * Cos(Pi / 180 * the)
End Function
```

Listing D-1 Tufting control code.